Reaction-bonded silicon carbide for nuclear fusion blanket applications

Alexander Leide

St Anne's College

Department of Materials

University of Oxford

DPhil Thesis

Trinity Term 2019

Abstract

Reaction-bonded silicon carbide has properties which make it useful for certain components of a nuclear fusion reactor, but its response to irradiation has not been studied since early work suggested its unsuitability. Modern commercially available samples of RB-SiC, along with some novel samples prepared in-house were investigated to identify links between microstructure and radiation and mechanical performance.

2.5 displacements per atom (dpa)and 0.25 dpa of radiation damage were introduced using ion implantation at 300 °C and 750 °C. The radiation-induced changes to mechanical properties were investigated using nanoindentation, chemical defects by Raman spectroscopy, and structural defects by electron backscatter diffraction.

Residual stresses were found to strongly influence the micromechanical properties of reaction-bonded SiC. Radiation changes these stresses leading to the degradation of macroscopic mechanical properties. Further investigation of these residual stresses found they are caused by radiation swelling of silicon carbide. This swelling is constrained by the unirradiated layer in ion irradiation experiments, creating a lateral stress which increases the apparent toughness and hardness, as assessed by nanoindentation. This constrained swelling effect appears to significantly influence the mechanical properties measured by nanoindentation of ion implanted layers.

Ion irradiation appears unable to recreate defects created by neutron irradiation. The lateral swelling stress prevents chemical bonds reaching their equilibrium length, possibly hindering their evolution. The choice of implanted ion also appears to influence defects in SiC; self-ions change the local chemistry and defect structures.

Acknowledgements

I would like to thank my supervisors Prof. David Armstrong, Prof. Richard Todd, and Prof. Steve Roberts for their guidance throughout the project. Dave for his advice and enthusiasm for pretty pictures and videos, Richard for lively discussions about residual stresses, cracks, and Raman spectroscopy, and Steve for his wealth of knowledge on ceramics and radiation damage which inspired this project.

The MFFP, Ceramics, and Micromechanics research group members have all provided invaluable advice on my experiments and results and helped with many of my questions. My time in the Yano-Yoshida group at Tokyo Institute of Technology was a highlight of these past four years, thanks to the members of the group who helped me and made me welcome.

Various members of the department who have not been mentioned in the thesis deserve thanks for their help along the way: Tony Wheeler, Pete Flaxman, Jenny Holter, Gareth Hughes, Graham Wyatt, and Paula Topping. Rebecca Bradford deserves special thanks; it would be considerably more difficult for any of us to finish our DPhils without her help. Also, thanks to the staff at CCFE who have been involved in my project: Dr Yiqiang Wang, Dr Mike Gorley, Chris Smith, and Kate Breech. Thanks to Dr Nianhua Peng at Surrey Ion Beam Centre for running the ion implantation experiments.

Members and friends of the corner office have made DPhil life good fun with lively chats, lots of coffee and cake, and strange food brought back from our travels. It has been a pleasure to share the Fusion CDT DPhil experience with John and Carmen.

Thank you to my mum for her support over these years and looking after me when I’m at home. Thanks to my family and friends for giving me distractions from research when I needed them, and reminders of life outside of the Oxford Bubble.

Contents

Abstract 2

Acknowledgements 3

Contents.. 4

1 Introduction 9

1.1 Nuclear Fusion 9

1.2 Silicon carbide 12

1.2.1 Silicon carbide for nuclear fusion applications 15

1.3 Aims of this thesis 21

2 Literature Review 23

2.1 Processing reaction-bonded silicon carbide 23

2.1.1 Shape forming 23

2.1.2 Reactive melt infiltration 24

2.2 Radiation damage 36

2.2.1 Radiation damage in ceramics 37

2.2.2 Radiation defects in SiC 41

2.2.3 Macroscopic radiation swelling 58

2.2.4 Radiation studies of reaction-bonded SiC (RB-SiC) 60

2.3 Micromechanical testing 67

2.3.1 Nanoindentation of irradiated SiC 67

2.4 Residual stress measurements 75
2.4.1 Raman spectroscopy of RB-SiC 75
2.4.2 SEM digital image correlation 76
2.4.3 Microcantilever deflection and ion beam layer removal 77
2.5 Summary of literature and problems to solve 79
3 Materials 81
3.1 Commercially available materials 81
3.2 Self-made materials 81
3.2.1 Conventional RB-SiC 81
3.2.2 Metal-silicide RB-SiC 83
3.3 Summary of RB-SiC materials studied 85
4 Methods 86
4.1 Specimen preparation 86
4.2 Ion implantation 88
4.3 Nanoindentation 92
4.4 Raman spectroscopy 94
4.4.1 Radiation damage and defects 94
4.4.2 Residual stress measurements 96
4.5 Electron microscopy 99
4.5.1 SEM imaging 99
4.5.2 Electron-backscatter diffraction (EBSD) 101

4.5.3 Focussed ion beam tomography 105

4.5.4 Microcantilever residual stress measurements 106

4.5.5 Micropillar swelling digital image correlation 108

4.6 Atomic Force Microscopy (AFM) 111

5 Results 112

5.1 RB-SiC microstructures 112

5.1.1 In-house RB-SiC microstructure 112

5.1.2 Metal silicide RB-SiC 113

5.1.3 Commercial RB-SiC 117

5.1.4 Processing-induced residual stresses 122

5.1.5 Unirradiated nanoindentation cracking 125

5.2 Radiation damage 144

5.2.1 Radiation-induced changes to hardness and modulus of single crystals 144

5.2.2 Radiation-induced changes to hardness and modulus of RB-SiC 147

5.2.3 Radiation changes to nanoindentation deformation 151

5.2.4 Microstructural changes 160

5.2.5 Radiation-induced swelling 182

5.2.6 Radiation-induced residual stresses/strains 186

5.2.7 Stress release in microcantilevers 194

6 Discussion 209

6.1 Processing RB-SiC 209

6.2 Radiation-induced defects 210

6.2.1 Optical and SEM contrast 216

6.2.2 GND density and EBSD pattern quality 217

6.3 Radiation swelling and residual stresses 220

6.4 Radiation effects on mechanical properties 226

6.4.1 Ion implantation effect on RB-SiC micromechanical properties 236

6.5 Radiation-enhanced oxidation 237

6.6 Residual stress in RB-SiC 240

6.6.1 As processed 240

6.6.2 After ion implantation 241

7 Conclusions and recommendations for further work 245

7.1 Radiation defects in SiC and Silicon 245

7.2 Identification of radiation induced changes 245

7.3 Effectiveness of ion implantation 248

7.4 Replicating in-service environments 250

7.5 Future materials for fusion reactors 252

7.5.1 Suitability of reaction-bonded silicon carbide for a fusion reactor breeder blanket 252

7.5.2 Recommendations for material improvements 253

8 Appendices 254

8.1 Videos 254

8.2 Phase diagrams 254

References 257

List of figures reproduced with permission 279

1 Introduction

1.1 Nuclear Fusion

Nuclear fusion is a sustainable form of clean energy created by combining two light atomic nuclei to form a heavier one, the same process as occurs in stars. Fuels are plentiful, and there are no radioactive products to dispose of, although the tritium fuel itself is radioactive and some structural components will be activated by transmutations. To achieve this on Earth, a plasma of deuterium and tritium is heated to high energy in a reactor until their electrostatic repulsion is overcome and they fuse into helium, releasing a 14.1 MeV neutron. The walls of the device capture this neutron; its kinetic energy is converted to heat and into electricity via steam turbines. However, achieving fusion is a huge challenge for scientists and engineers, and is still decades away from commercial realisation.

The most developed reactor concept is the tokamak, a toroidal vacuum vessel where the plasma is held using magnetic coils and heated by induction, radio waves, and energetic neutral particles injected into the plasma. Toroidal and poloidal magnetic coils create a net helical field in the plasma to circulate ions from the outside to the inside of the plasma to improve particle confinement, reducing energy loss and improving plant efficiency. The aim is to improve confinement to such an extent that fusion energy is sufficient to sustain the plasma without the need for external heating.

A large international project is underway in France to build ITER (International Thermonuclear Experimental Reactor), the most advanced tokamak and the most complex machine ever built. Figure 1-1 shows a schematic cross-section of Iter, highlighting the complexity of the machine and its scale. Further support systems and diagnostics will be connected to the machine externally and are not shown in the figure.

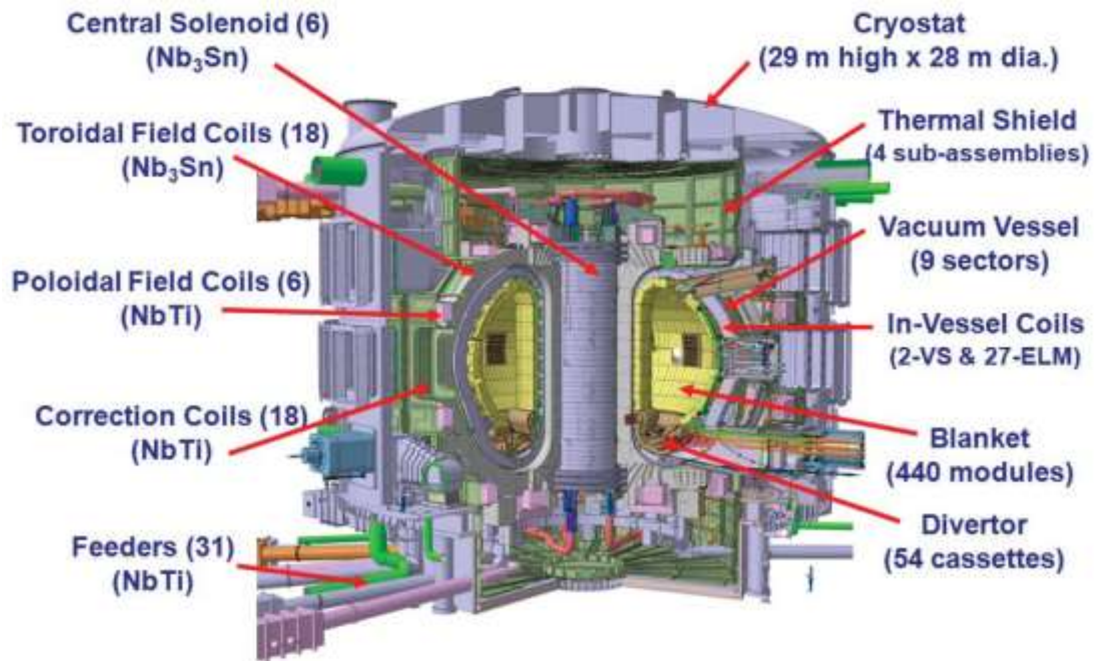

Figure 1-1: Schematic of Iter showing key components. Adult human for scale in bottom right (Credit © ITER Organization, http://www.iter.org/) [1]

Most of these components will require advanced materials due to the extreme conditions required to achieve fusion [2]. These include the highest temperature gradient in the universe (>200 million degrees at the centre of the plasma to 4.2 K liquid helium cooled superconductors in a few metres), extreme neutron irradiation, plasma sputtering and erosion, and corrosion from coolants and molten breeding materials. Neutron irradiation is particularly challenging for materials scientists as it causes atomic displacement cascades leading to defects and swelling, nuclear transmutations to hydrogen and helium gas products or new atomic species including radioactive isotopes, sputtering, and phase changes [3,4]. Thus, the material properties change during use, and these changes must be predicted and accounted for in the reactor design or mitigated through advanced material design.

Alternative reactor concepts exist such as stellarators, and inertial confinement fusion [5]. Both these techniques are currently behind tokamaks in terms of technological readiness but are still being actively researched. The material challenges for stellarators

and other magnetic confinement fusion (MCF) devices are much the same as for tokamaks; however, inertial confinement fusion (ICF) devices operate under significantly different conditions. The structural material requirements for an ICF reactor are expected to be easier for various reasons: the pulsed nature of the device allowing time for materials to anneal, larger reactor dimensions spread radiation across a larger area, and a point source of radiation favouring implantation over sputtering, and the neutron energy spectrum can be softened by the higher fuel density or by filling the chamber with gas [5–7]. Figure 1-2 shows the simulated effect of these features on the primary knock-on atom energy of iron in the chamber walls of a theoretical MCF reactor and a theoretical ICF reactor [8]. Additionally, the softer neutron spectrum reduces gas production by subduing (n, α) and (n, β) reactions. In the case of SiC, this halves the gas production rate relative to an MCF reactor, gas products being a contributor to high temperature swelling and embrittlement in SiC [9]. Although there are material benefits to ICF reactors, the same materials cannot necessarily be used within the requirements for low activation. Due to the different neutron spectrum causing different atomic transmutations, some elements which would be low activation in an MCF environment are high activation in ICF, including tungsten and iron [6].

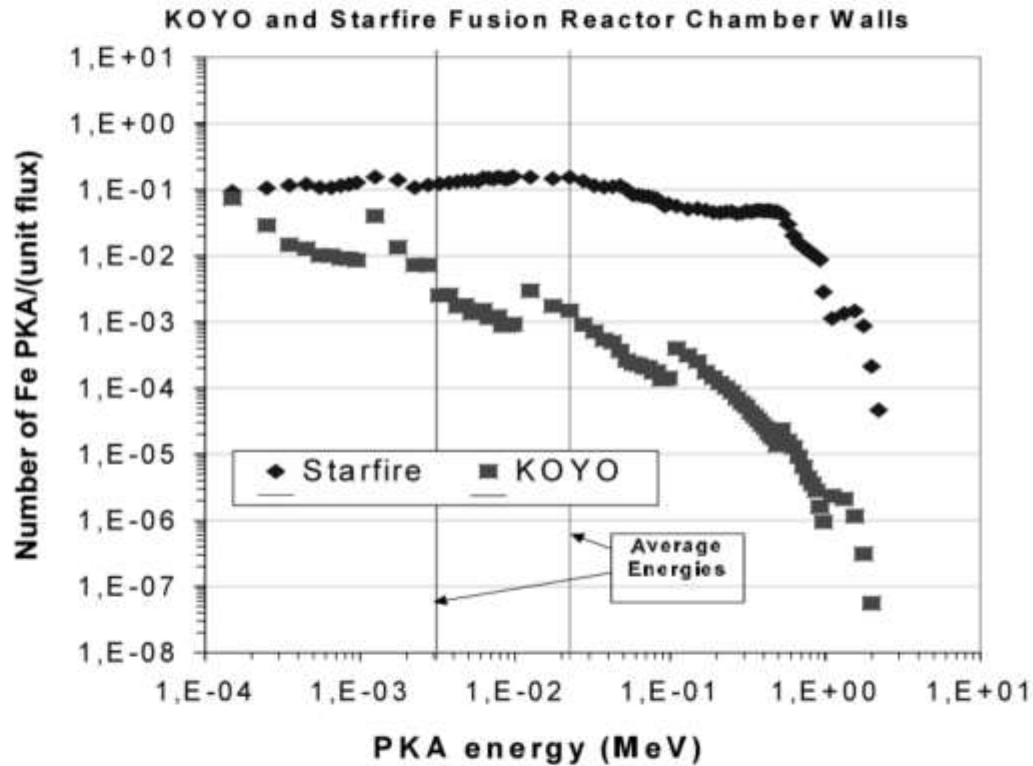

Figure 1-2: Simulated PKA energies for the Starfire (MCF) and KOYO (ICF) fusion reactor concepts. ICF has a lower average PKA energy in chamber walls [8].

Tokamak MCF is the focus of most materials research as it is closest to technological readiness. ICF has many more hurdles to overcome from both a basic science and engineering perspective before targeted materials research is prioritised.

1.2 Silicon carbide

Silicon carbide is a covalently bonded ceramic material that is most commonly found as hexagonal α-SiC consisting of mostly 4H and 6H polytypes and including other hexagonal and rhombohedral polytypes. Cubic 3C β-SiC is produced by low temperature processing such as chemical vapour deposition (CVD). Due to the strong directional covalent bonding (~8% ionic character [10]), it is very hard and brittle making it difficult to form into shapes and complex components. Its most common use is as an abrasive due to its high hardness and very low cost in powder form. SiC components are used

industrially where its wear resistance, high temperature strength, dimensional stability, low density, and chemical inertness are useful.

Silicon carbide components can be monolithic, or fibre reinforced composites. The microstructures and properties are strongly dependent on the processing used to make that component. A brief overview of the forms of SiC and processing techniques is given below, along with typical microstructures.

Sintered silicon carbide is made by sintering SiC powders at temperatures greater than 2000°C typically with the "ABC" sintering aids (aluminium, boron, carbon). Consolidation of the green body is by solid state diffusion, leading to dimensional changes and some residual porosity. Shapes must be relatively simple due to the macroscopic dimensional changes during sintering. Sintering aids remain as impurities.

Hot pressed SiC uses pressure in addition to heat to consolidate SiC particles into a component. Compared to sintered SiC, it can have reduced porosity, a slightly lower sintering temperature, or reduced sintering additives. Shapes are dependent on the directions pressure can be applied, whether uniaxial or hydrostatic, and properties may be anisotropic.

Reaction-bonded silicon carbide is made by infiltrating a green body of SiC and carbon powders with molten silicon [11]. The molten silicon reacts with carbon to form silicon carbide *in-situ*, bonding the original silicon carbide powders together. Any remaining porosity (typically ~12%) is filled with residual silicon, creating a fully-dense two-phase object (Figure 1-3). Reaction-bonding is a near net-shape process, meaning complex shapes can be made with thin internal sections. It is fast and cost effective compared to sintering, and large components can be made. This material will be discussed more in this literature review.

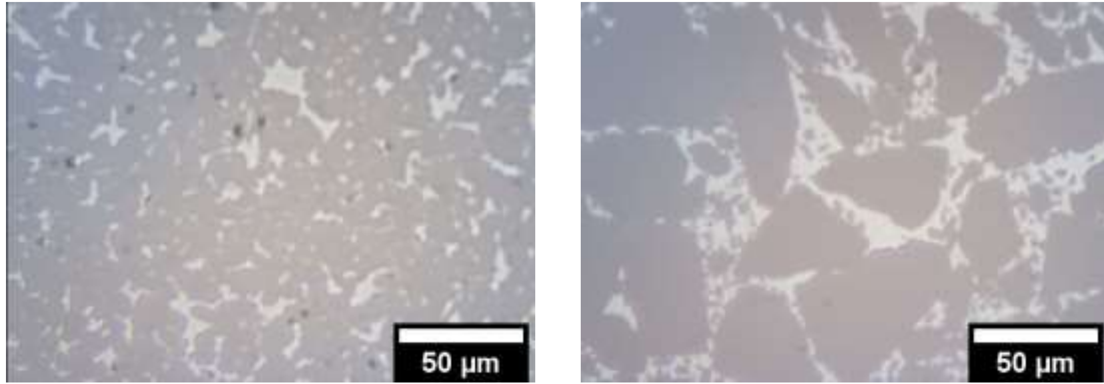

Figure 1-3: Optical micrographs of typical RB-SiC microstructures. REFEL on the left, Starceram Si on the right

Silicon carbide fibre reinforced silicon carbide composites (SiC_f/SiC) are made by weaving bundles of fibres into shapes, followed by densification of the gaps between the weaves. The fibres are coated with interlayers such as carbon or boron nitride to give weak interfaces, and control their pull-out properties, giving pseudo-ductile failure and a higher macroscopic fracture toughness than monolithic SiC. Densification could be by polymer infiltration and pyrolysis (PIP) [12], chemical vapour infiltration (CVI) [13], reactive melt infiltration (RMI) [14], or nano infiltration and transient eutectic (NITE) [15]. Typical microstructures are shown in Figure 1-4. Of these composites, CVI and NITE SiC have been developed for nuclear applications, and CVI SiC appears to be the better material due to the nanocrystalline β-SiC matrix without detrimental oxide sintering aids.

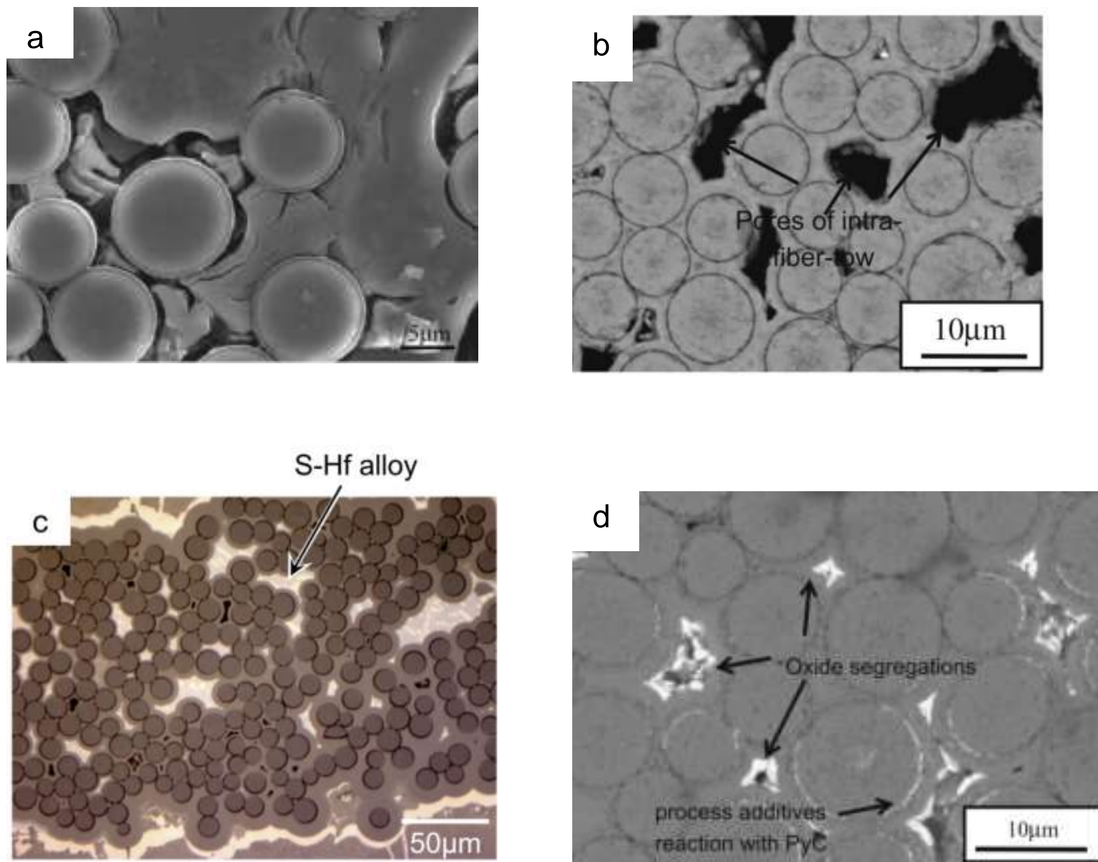

Figure 1-4: Typical microstructures of SiC/SiC composites fabricated by different techniques. a) PIP [16]*, b) CVI* [17]*, c) RMI* [18]*, d) NITE* [17]

1.2.1 Silicon carbide for nuclear fusion applications

Silicon carbide has been discussed in a fusion context for decades, always as a desired material and always far from application. It is particularly desirable as it is low activation allowing hands on maintenance within 10 days of reactor shut down, chemically inert, creep resistant, has a low thermal expansion coefficient, and maintains its strength to high temperatures (>1300 °C) [9,19,20].

Initially silicon carbide was considered for plasma facing components (PFC) as the low Z-number elements would have a smaller effect on plasma contamination and radiative energy loss compared to heavier metal alternatives, and the erosion rate is lower than for graphite or carbon/carbon composites [21,22]. Further experimentation focussing on fusion conditions identified that irradiation induced degradation of thermal conductivity

and fracture strength make the thermal shock resistance of silicon carbide unacceptably poor for PFC applications where plasma instabilities could be catastrophic [23]. Recently, test samples of CVD SiC on graphite have been exposed to plasma in the DIII-D tokamak and were found to have no additional cracking or flaking after exposure to steady state and ELMy (edge localised mode, a type of plasma disruption similar to a solar flare) plasmas compared with the as-processed condition [24]. This exploratory re-visit of SiC as a PFC was somewhat positive in its conclusions, although much more work will need to be done to compare to the studies done in the 80s and 90s [23].

Although SiC was ruled out as a PFC material, it still has attractive properties for breeder blankets where the risk of thermal shock is reduced, and gas bubble formation is lower. The benefits of SiC over other candidate blanket materials such as ferritic steels and vanadium alloys, lie in improved safety and plant efficiency [25–28]. The blanket of a fusion reactor is a structural component on which the first wall tiles attach, provides radiation shielding, and must provide a method of tritium breeding, and energy extraction.

If fusion is to be self-sufficient, tritium must be bred from the interaction between lithium and neutrons, providing more fuel for the fusion reaction plus an excess to build the tritium inventory for starting new fusion reactors and to account for tritium decay [29]. Silicon carbide is an effective tritium permeation barrier so will reduce tritium retention in blanket components [30]. Lithium can be in the form of solid ceramic pebbles, a molten lead-lithium alloy, or a molten salt, such as FLiBe. SiC is likely to be applied to the molten concepts allowing high temperature operation where its chemical inertness and high temperature strength are necessary. In addition, for liquid metal systems SiC is used as an electrical insulator to reduce the impact of magnetohydrodynamic effects [31–33].

Several prototype breeder blanket modules are being developed for testing in ITER, which can broadly be categorised as solid ceramic breeder, or liquid breeders [34]. Some

of these designs include SiC as a minor component for flow channel inserts (FCI), as in the case of the dual functional lithium-lead blanket (DFLL) test blanket module (TBM) being developed in China (Figure 1-5) [31], and the US dual-coolant lead-lithium (DCLL) design (Figure 1-6) [35]. In DFLL molten lead lithium is both the breeder and coolant/heat transfer medium, while in DCLL helium is an additional coolant/heat transfer medium. The main structural material for these prototypes is reduced activation ferritic/martensitic steel [36].

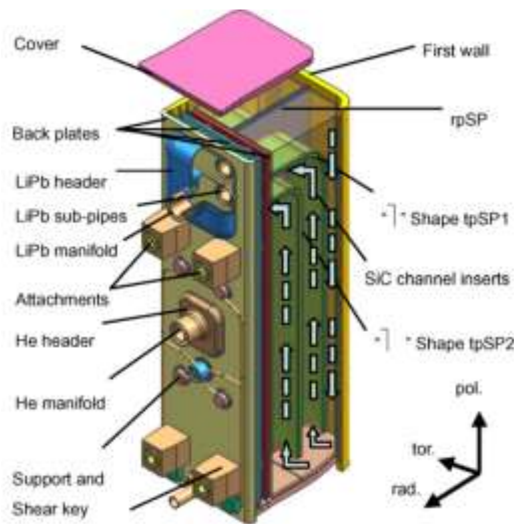

Figure 1-5: Structure of the Iter DFLL-TBM showing SiC as a flow channel insert [31]

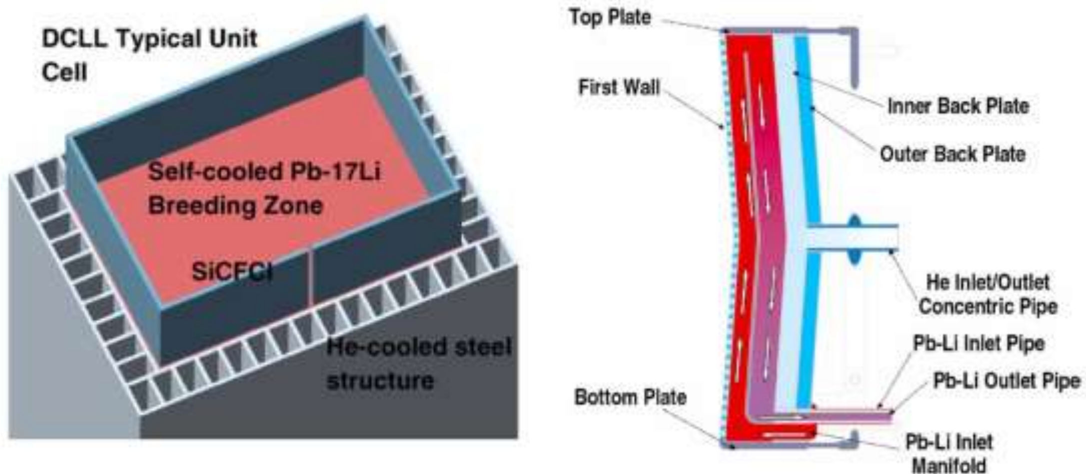

Figure 1-6:Structure of the Iter DCLL-TBM with a SiC flow channel insert [35]

Current DEMO blanket designs are similar to the ITER prototypes and based on EUROFER steel with SiC only used as a flow channel insert for the molten PbLi designs [37]. The design requirements for a SiC FCI are different to using SiC structurally; mainly that instead of thermal conductivity, the FCI should be thermally insulating (~7 W/mK), and the mechanical property requirements are much lower (>25 MPa bending strength) [38,39]. A research program through Eurofusion has developed a porous SiC material with a dense CVD SiC coating which meets these requirements for an FCI, although no radiation testing has been reported [40,41]. All the processing stages are commercially viable with existing technology, and it is significantly cheaper than SiC_f/SiC, meaning it is likely to be used during the ITER TBM testing period, and possibly in a DEMO with a structural steel water-cooled lithium-lead blanket [39,42].

The dense CVD SiC coating protects the porous SiC underneath from corrosion by molten lithium-lead in static corrosion tests at 700 °C for 1000 hours, however in combination with erosion this coating may not be suitable as some parts detached from the porous bulk during post-corrosion handling [39].

For technologically aggressive post-DEMO power plant designs such as the European Power Plant Conceptual Study (PPCS) designs C and D, or the ARIES Advanced Conservative Tokamak designs (ACT-1 and ACT-2), SiC will have to become a structural material for molten lead-lithium blankets [43,44]. All these designs call for SiC_f/SiC and require further material development to meet the design requirements.

Various post-ITER blanket design concepts exist using SiC as the main structural material, both for DEMO and future advanced high temperature fusion devices, both MCF [26,45–48] and ICF [49]. The TAURO self-cooled lead-lithium blanket design is shown in Figure 1-7 [48]. The TAURO design extends to structurally using SiC/SiC faced with tungsten armour as a PFC material. This could cause problems due to different radiation-

induced swelling and thermal expansion coefficients between SiC and tungsten leading to cracking [19].

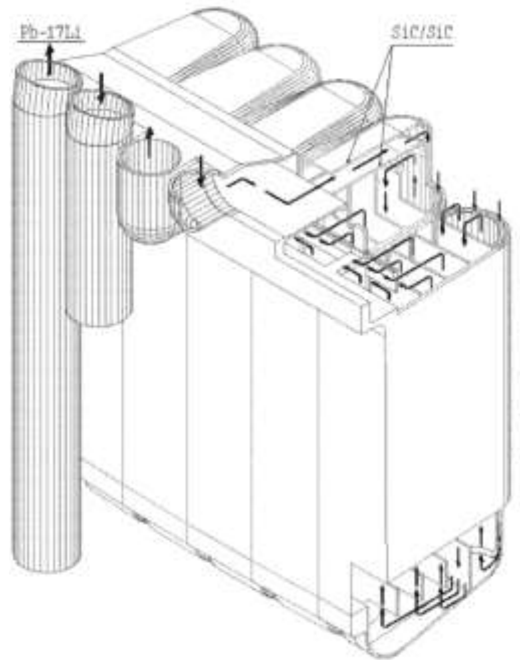

Figure 1-7: TAURO outboard blanket using SiC/SiC as a structural material [48]

With molten lead-lithium designs it is vital that no open porosity is present as corrosion has been observed to be catastrophic in porous SiC [40]. A protective CVD SiC layer over SiC_f/SiC is proposed as a solution, however differential anisotropic radiation swelling is foreseen to be an issue, potentially resulting in fracture at the interface between monolith and composite [50].

While a helium cooled ceramic pebble breeder blanket such as the DREAM conceptual design won't be susceptible to molten metal corrosion, a dense SiC layer is still required for helium and tritium hermeticity which may be susceptible to the same differential swelling fracture at the monolith-composite interface [26].

Table 1-1 from Giancarli *et al.* summarises some of the design parameters for SiC as a structural material in a self-cooled lithium lead blanket such as TAURO, and a helium cooled pebble-bed blanket such as DREAM [26]. The final column lists typical properties

of SiC_f/SiC composites when the article was written in 2002. While work has continued to progress on improving processing and mechanical properties of SiC_f/SiC, no significant progress has been made on improving thermal conductivity, and porosity beyond what is reported here [16,51,52].

Table 1-1: Design parameters for two blanket types incorporating SiC structurally, along with typical measured values of SiC/SiC composites [26]

Key SiC_f/SiC properties and parameters[a]	SCLL blankets (agreed values)	DREAM blanket	Typical measured value
Density	≈ 3000 kg/m^3	2500 kg/m^3	≈ 2500 kg/m^3
Porosity	≈ 5%	≈ 10%	≈ 10%
Young's modulus	200–300 GPa	≈ 200 GPa	≈ 200 GPa
Poisson's ratio	0.16–0.18	0.20	0.18
Thermal expansion coefficient	≈ 4 × 10^{-6}/°C	3.3 × 10^{-6}/°C	4 × 10^{-6}/°C
Thermal conductivity in plane (1000 °C)	≈ 20 W/m K (EOL)	15 and 60 W/m K (EOL)	≈ 15 W/m K (BOL)
Thermal conductivity through thickness (1000 °C)	≈ 20 W/m K (EOL)	15 and 60 W/m K (EOL)	≈ 7.5 W/m K (BOL)
Electrical conductivity	≈ 500/Ω m (under irradiation)	Not applicable	≈ 500/Ωm (out of irradiation)
Tensile strength	300 MPa	300 MPa	300 MPa
Trans-laminar shear strength	–	–	200 MPa
Inter-laminar shear strength	–	–	44 MPa
Maximum allowable tensile Stress	Not used[a]	200 MPa[a]	Unknown[a]
Maximum allowable temperature (swelling basis)	≈ 1000 °C	≈ 1100 °C	≈ 1000 °C
Maximum allowable interface temperature with breeder	≈ 1000 °C (flowing)	–	≈ 800 °C (static)
Minimum allowable temperature (thermal conductivity basis)	≈ 600 °C	≈ 600 °C	≈ 600 °C
Cost	≤ $400/kg	–	≈ 10 times larger

Joining ceramics is always a significant challenge, and researchers have been working on joining nuclear and aerospace grades of SiC_f/SiC for many years [53–55]. For practically joining components on-site, one would want a fast, pressureless process and to avoid needing a vacuum heat treatment. Of the joining processes summarised in Table 1-2, glass-ceramic and metallic brazes allow this, and are broadly similar to conventional metal brazing. The properties of the joints should be carefully controlled to match thermal expansion coefficients and radiation-induced swelling. The glass-ceramic composition can be optimised for thermal expansion, but radiation swelling is unknown for these compositions. Based on preliminary neutron irradiation and mechanical characterisation, these glass ceramic joints appear promising.

Table 1-2: Methods of joining SiC from Katoh et al.[54]

Table 1
Methods of joining SiC-based materials.

Method	Process condition	Material/phase in joint	Typical strength	Irradiation performance	Refs.
Solid state diffusion bonding	1200–1500 °C, 3–50 MPa	Ti_3SiC_2, $Ti_5Si_3C_x$, TiC, $TiSi_2$	Up to ~150 MPa shear	This work	[29,31,69]
	1500 °C, 3–17 MPa	$Mo_5Si_3C_x$, Mo_2C, what phase	~150 MPa DNS[1] shear	Unknown	[11]
	1500 °C, ~17 MPa	WC, W_2C, W_5Si_3	Not reported	Unknown	[31]
Transient eutectic-phase joining	1500–1900 °C, 5–20 MPa	SiC, Al–Y–O	Up to ~300 MPa tensile	Expectedly good	[15]
Glass-ceramic joining	1375 °C, pressureless	Mullite, cristobalite, keivyite	~100 MPa 4PB[2]	No degradation at a few dpa reported	[37]
	1480 °C, pressureless	$CaO–Al_2O_3$	~100 MPa torsional shear	This work	[10,37]
Metallic braze-based joining	~1400 °C, pressureless	Si, MSi_2 (M = Ti, Cr)	~100 MPa 4 PB or shear	Unknown	[70–72]
	~1000 °C, pressureless	Si, Al_4C_3	Not reported	No degradation at milli-dpa reported	[47]
Si–C reaction bonding	~1425 °C, pressureless	SiC, Si	Up to ~250 MPa 4 PB	Unknown	[18,21]
MAX-phase joining	~1450 °C, 30–40 MPa	Ti_3SiC_2, SiC	~400 MPa 4 PB	This work	[55]
Polymer-derived SiC joining	1000–1400 °C, pressureless	Si–O–C (–N)	Up to tens MPa, SLO[3] shear	Expectedly unstable	[57,73]
Selective area CVD	1000–1500 °C, pressureless	SiC	Not reported	Expectedly stable	[28]

[1] Double-notch shear.
[2] Four-point bending.
[3] Single-lap offset shear.

Based on the design concepts in the previous paragraphs, silicon carbide will allow high-temperature thermodynamic cycles, improving plant efficiency and the commercial viability of fusion. Using the Brayton helium gas cycle rather than the Rankine steam cycle is expected to give thermal efficiency between 51-64% at temperatures between 850°C and 1250°C [56]. These temperatures are above the operating temperature of advanced steels and vanadium alloys, which are the other candidate materials for a high temperature blanket.

In summary, silicon carbide has desirable properties for a structural material in advanced high temperature fusion reactor blankets, but both scientific and engineering challenges remain for implementing this material structurally.

1.3 Aims of this thesis

Reaction-bonded SiC was identified as an alternative form of SiC which solves many of the engineering challenges of using SiC_f/SiC composites. Its radiation response has not been studied since the early 1990s after early reports suggested its unsuitability. A revisit of this material using modern techniques may identify possibilities for improving this material, or where it may be usefully applied in a fusion reactor or other radiation environment.

Introduction

Initially the project centred around linking microstructure to micromechanical properties and the effect of ion implantation on these. The project evolved from this once it was identified that there were significant internal stresses in reaction-bonded silicon carbide (RB-SiC) as-processed, and these change under ion irradiation. The origin of the radiation changes to residual stresses became a significant part of the project, leading to measurements of swelling and radiation stresses in single crystals of SiC, along with identifying and interpreting fundamental radiation defects.

2 Literature Review

2.1 Processing reaction-bonded silicon carbide

Reaction-bonded SiC was first made in the 1950s [57] and was developed as a commercial material soon after. As it was commercialised very quickly, most development in processing techniques has been kept as an industrial secret. In general, materials made in public research labs have been inferior to those developed by industry as they have iteratively improved the technique over decades. Academic research has generally focussed on novel techniques including additive manufacture and reducing silicon content (section 2.1.2).

From personal discussions with Dr Nikolaos Katsikis, head of research at H.C. Starck Ceramics GmbH (a large German manufacturer of refractory metals and high performance ceramics including RB-SiC [58]), their customers are mainly asking for larger, more complex shaped components, regardless of excess silicon content. The applications where RB-SiC is currently used tend not to require high strength, but for them to fill a certain space or geometry. This has led to industry concentrating research on additive manufacture and joining rather than microstructural and mechanical property improvement.

2.1.1 Shape forming

Conventional powder processing techniques can be applied to form green bodies which can be densified by reactive melt infiltration. These include slip casting, uniaxial pressing, hydrostatic pressing, extrusion, or additive manufacture depending on the desired component. All these techniques have been used successfully to make RB-SiC components.

Since reaction-bonding is a near net-shape process, the dimensions and shape of the green body will be close to that of the final product. This minimises expensive diamond machining of the ceramic component after firing.

The key requirements for the green body are:

- Open porosity to allow silicon infiltration without blockages
- A source of carbon to react with silicon into SiC
- Structural strength to allow final shaping and handling before firing

Once a green body has been prepared, the sample is melt infiltrated to densify the component.

2.1.2 Reactive melt infiltration

2.1.2.1 Silicon

Liquid phase infiltration is by capillary action of molten silicon into the porous medium. The capillary action of silicon to form RB-SiC is effective in allowing large components to be formed; however, the mechanism of this capillary action is disputed. Some reports claim that molten silicon wets carbon very well with a low contact angle which allows strong capillary action to force silicon into pores [59]. However the literature values for wetting angles vary considerably depending on the form of carbon, from as low as 3° for rough graphite to 50° for vitreous carbon, which makes prediction of capillary effects difficult [60,61]. An alternative view from more recent work is that the capillary force is due to wetting of molten Si on newly formed SiC at a contact angle around 35° [61–63]. Thus, the rate limiting process for silicon infiltration is the formation rate of new SiC. This mechanism fits more closely to experimental observations of infiltration rate than based on the Washburn equation (2-1) which ignores reactivity (Figure 2-1). The Washburn equation gives infiltration height (h) as a function of time (t), effective pore

radius (r), surface tension (σ), viscosity (μ), equilibrium contact angle (θ). This gives a parabolic infiltration profile, however the experimental infiltration height (black line in Figure 2-1) is linear, as determined by the rate of the reaction forming silicon carbide [62]. As new SiC forms, the surface tension and effective pore radius are changing. If these changes can be accurately determined, the infiltration height equation could be modified to reflect this. With the exothermic nature of the Si+C reaction (see 2.1.2.3), the viscosity of silicon will also change. Alternatively, tortuous pore pathways and reactive blockages may explain the slower observed infiltration rate in experiments as these are not taken into account in the Washburn equation. It is difficult to compare these calculations to experiments as real pore structures are non-uniform.

$$h^2 = \frac{r\sigma\cos\theta}{2\mu}t \quad (2\text{-}1)$$

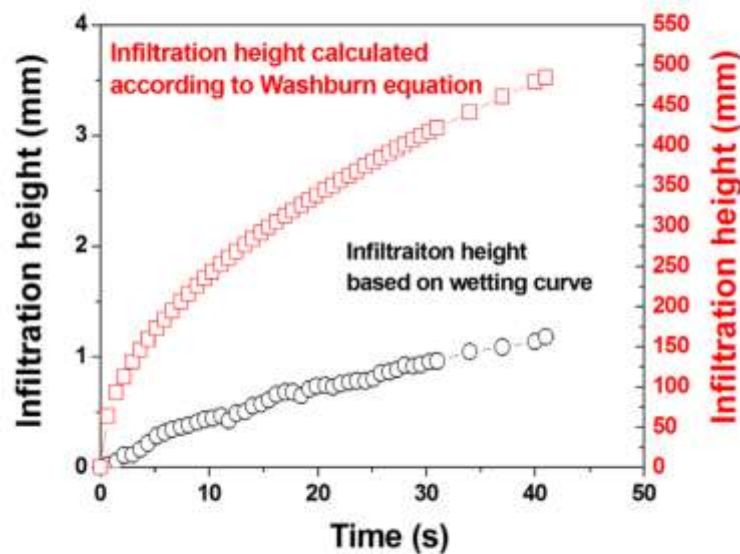

Figure 2-1: Infiltration heights into porous carbon based on wetting curve which includes Si + C reaction, and from Washburn equation based on viscosity of silicon [62]

Si becomes less viscous at higher temperatures which was thought to be the mechanism behind further penetration into the sample with temperature [59,64,65]. Instead, the further and faster silicon penetration at higher temperatures could be attributed

to faster transformation of carbon into SiC. Some experiments use an overpressure of argon in the furnace to reduce silicon evaporation. This results in shallower penetration as the pressure of gas-filled pores opposes the rising silicon front in addition to altering the contact angle of silicon [66].

Silicon is difficult to penetrate into pores less than 1 μm in diameter due to reactive blockages so the pore size is very important in making RB-SiC [67,68]. Some basic modelling of Si infiltration and reaction into idealised pores has been carried out with limited experimental validation [69,70]. This limit makes it difficult to reduce the residual silicon and size of silicon regions without introducing closed porosity.

2.1.2.2 Silicon alloys

In order to improve high temperature mechanical properties, researchers have tried to reduce the residual silicon content by replacing silicon with a refractory metal silicide. Most commonly, the alloy system has been Si-Mo [68,71–76] however, other alloys have been used including Si-Ti [72], Si-Al [77], Si-Cu [77], Si-Mo-Cr [64], Si-Mo-Al [64], Si-Mo-B [64], Si-Mo-Ti [64], Si-Nb [78], and Si-Zr [79,80].

Silicon alloys with lower melting points than pure silicon are being researched to lower the manufacturing costs of SiC_f/SiC composites by melt infiltration using Si-Hf, Si-Ti, and Si-Al [14,18,81]. Cheaper amorphous SiC fibres such as Tyranno ZMI have low thermal stability and begin to degrade around 1100°C so expensive crystalline fibres must be used for pure silicon melt infiltration at temperatures at least 1450°C. For melt infiltration, an additional CVD coating of SiC is applied to protect the boron nitride interlayer, however cracks in this SiC allow silicon to reach the fibre or interlayer which can significantly degrade the properties [14]. Bending strength at both high temperature and room temperature was improved by infiltrating Tyranno ZMI SiC_f/SiC with Hf-Si at a

1375°C rather than Si at 1450°C (Figure 2-2 top). Both are an improvement over expensive crystalline fibres using a BN+SiC multi-layer CVD interphase and infiltrated with Si at 1450°C (Figure 2-2 bottom) [82]. Composite infiltration using Si-Ti alloy at 1375 °C reduced the fraction of damaged fibres to 2% from 13% when pure silicon was used at 1450 °C [14]. Of course, there are further variables in the processing which could contribute to the strength variation.

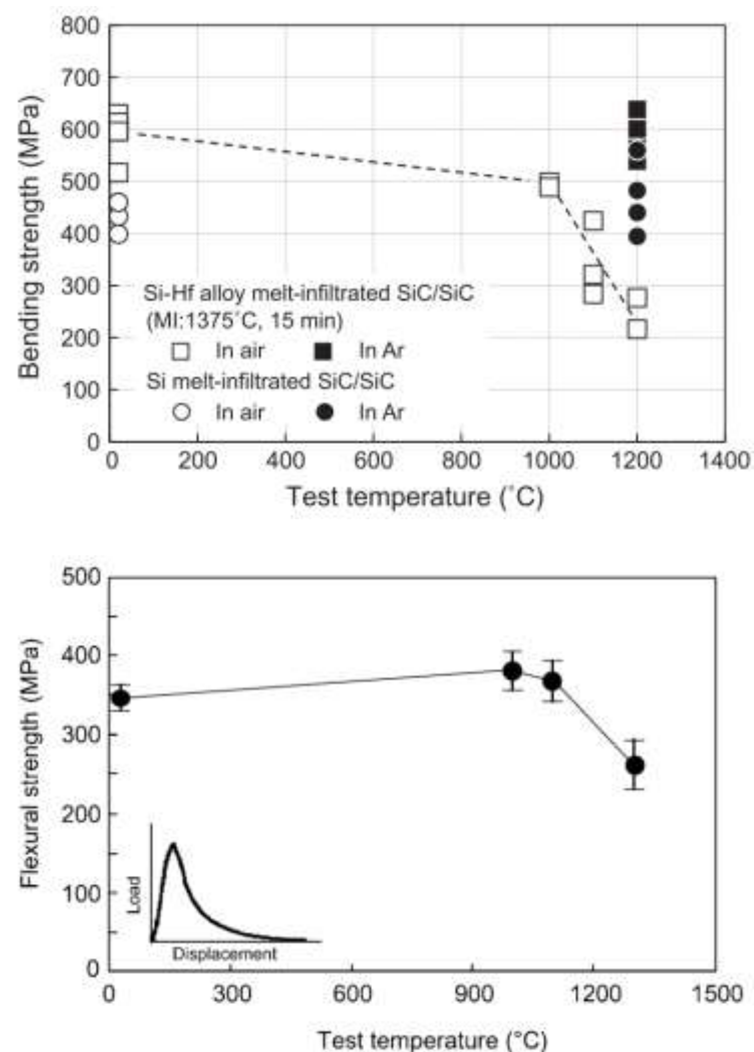

Figure 2-2: 3-point bending strength of Si infiltrated composite and Si-Hf infiltrated composite at room and elevated temperatures (top) [18] *3-point bending strength of Si-infiltrated composite with crystalline fibres and BN interphase (bottom)* [82].

Compared to silicon, silicon alloys do not wet the surface of SiC or carbon as well, reducing the depth of infiltration into the preform. The contact angle tends to increase with

reducing silicon content [77]. To counteract this, the reaction dwell time and temperature are increased which would cause damage to amorphous SiC fibres if this was carried out on a composite preform [77].

In multi-phase materials, thermal expansion of the individual phases must be considered. The difference between silicon and SiC is small, so traditional RB-SiC maintains its strength until close to the Si melting point. Raj has recently studied the thermal expansion of SiC, silicon, and various silicides for applications in SiC fibre-reinforced composites for gas turbines [83]. As can be seen in Figure 2-3 the thermal expansion of silicides is high and would be expected to cause mismatch stresses across interfaces, and crack growth as temperature is increased. This prompted work to use Si_3N_4 to counteract the high thermal expansion coefficient of silicides using a rule of mixtures approach [83]. This has the obvious drawback of the mismatch between silicide and silicon nitride being much larger than the mismatch between silicide and silicon carbide, so the mismatch stresses will be even higher.

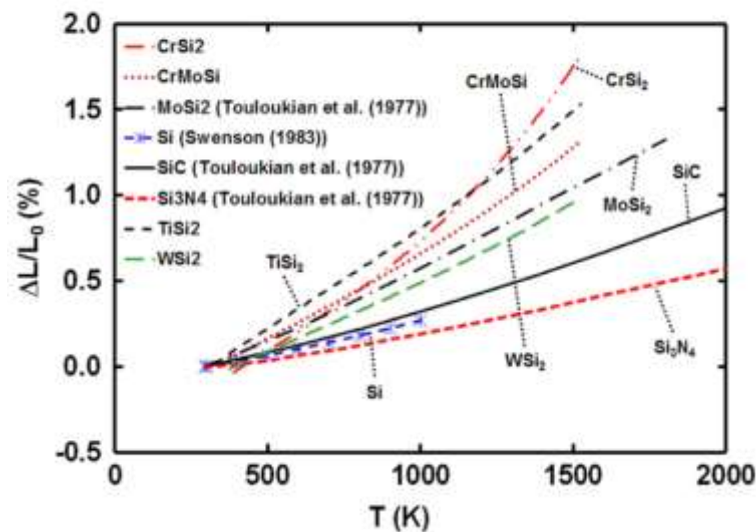

Figure 2-3: Thermal expansion coefficients of SiC, Si, Si_3N_4 and various silicides [83]

When $MoSi_2$ was used instead of silicon a lower room temperature strength is observed due to microcracking during cooling after silicide infiltration, with improved high

temperature strength above the brittle-ductile transition of the silicide phase (Figure 2-4) [73]. In these experiments, conventional RB-SiC was prepared, followed by evaporating the residual Si and melt infiltration of $MoSi_2$ so that the SiC microstructures were the same in both cases. The only difference is the extra heat treatment to the SiC as outlined in Figure 2-5.

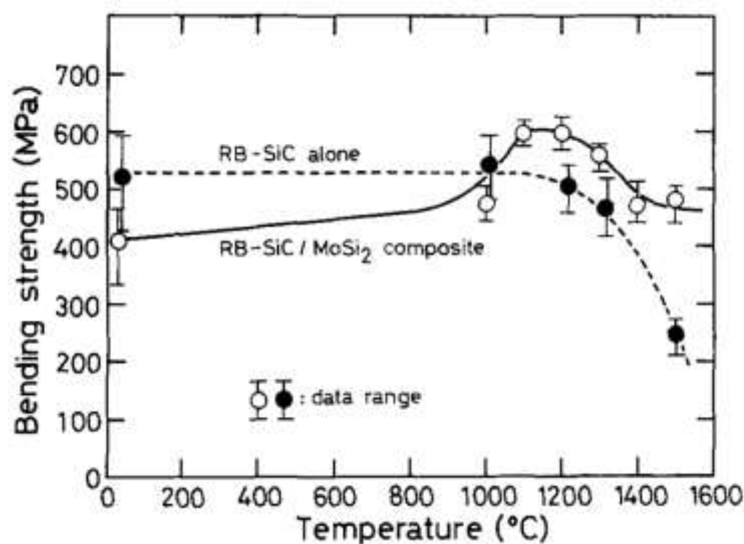

Figure 2-4: 3-point bending strength of RB-SiC with residual Si, and RB-SiC where residual silicon is replaced with $MoSi_2$ [73]

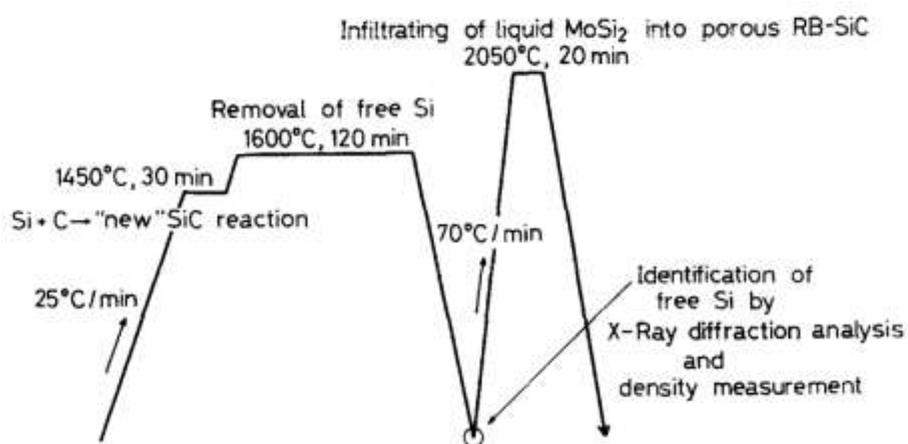

Figure 2-5: Process for forming RB-SiC followed by melt infiltration of $MoSi_2$ [73]

The silicides have brittle-ductile transitions, which, if they are below the operating temperature, can reduce the effect of thermal expansion mismatch and improve the mechanical properties compared to silicon. In a radiation environment, the brittle-ductile

transition temperature increases as defects are formed [3,4]. With thermal cycling of a nuclear reactor, thermal expansion mismatch could cause component failure.

For the fusion applications, low activation metal silicides have been identified as WSi_2, $TiSi_2$, and $CrSi_2$ [84]. The thermal expansion of these materials is high (Figure 2-3), however ductility at the proposed blanket operating temperature may counteract this. $TiSi_2$ has a brittle-ductile transition temperature around 805°C [85], and while no literature data is available for WSi_2 nor $CrSi_2$ the brittle to ductile transition temperature (BDTT) is expected to be in the region of 800-1000°C based on that of the other refractory silicides such as $MoSi_2$ [86].

No irradiation studies have been carried out on RB-SiC formed with silicides, nor on silicides themselves. Indeed, their application to a nuclear environment has not been considered in the literature.

2.1.2.3 SiC formation and growth

While the equilibrium phase diagram for silicon and carbon is very simple (Appendix 8.2), the reaction processes in reaction bonded SiC are complicated and debated. Three distinct mechanisms have been proposed to explain the formation of SiC from molten silicon and carbon during reaction bonding, although some authors differ on small details within each mechanism:

1. Dissolution of carbon into molten silicon, diffusion, and precipitation away from the dissolution site [59,87–90].
2. Heterogeneous formation of a SiC layer, followed by growth by diffusion of C or Si through the SiC layer [63,70,91,92].
3. Heterogeneous formation of a SiC layer on carbon, followed by spallation of this layer and repeated formation of new SiC [93,94].

Mechanism 1 is the only one developed from observations of reaction-bonded SiC containing SiC particles. Ness & Page used quenches from 1650°C at different stages during production of REFEL SiC to explain the reaction process as follows [59]:

1. Carbon dissolves in molten silicon as it rises through the compact.
2. Carbon diffuses through molten silicon to locally cooler areas behind the front of rising silicon.
3. Carbon becomes supersaturated and precipitates heterogeneously on original α-SiC particles. The formation of SiC is exothermic, raising the temperature locally allowing more carbon to dissolve [88].
4. During cooling remaining carbon in the silicon precipitates as isolated β-SiC particles.

Dissolving carbon into silicon is endothermic at 247 kJ/mole, while the formation of SiC from carbon and silicon is exothermic at -115 kJ/mole, making the whole process of formation of silicon carbide from a solution of carbon in silicon -362 kJ/mole [89]. This causes the local temperature rise widely reported, with temperatures reaching 2200 °C [59,87,93,95–98]. This temperature rise increases the solubility of carbon in silicon setting up a concentration gradient in addition to temperature gradients. As shown in Figure 2-6, dissolved carbon has diffused to cooler regions above and below the eroded area, where it has precipitated out as SiC [97].

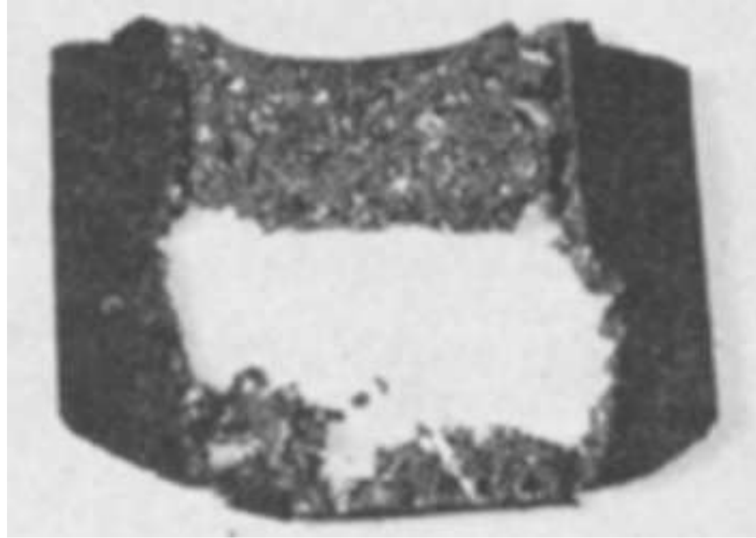

Figure 2-6: Eroded graphite crucible with SiC formed top and bottom. The centre region with eroded walls was at 2300°C while top and bottom were at 1800°C [97]

The original SiC grains act as nucleation sites for heterogeneous formation of SiC, which deposits as an epitaxial layer [59,87]. The polytype of this layer is uncertain and may depend on processing conditions. Sawyer and Page interpret it as α-SiC formed at a lower than equilibrium temperature due to the seeding effect of the α grains [87]. Using transmission electron microscopy (TEM), Ness and Page identified mostly α-SiC with some β proposing that SiC deposits as β then transforms to α due to the temperature increase of the reaction [59]. Hase *et al.* claim it is wholly β binding α grains together [94]. It is however agreed that fine-grained silicon carbide formed during cooling from supersaturated carbon in silicon is β-SiC.

In mechanism 2, Li & Hausner, and Gern & Kochendörfer describe the initial SiC formation as “instantaneous” and “immediate”, with growth by diffusion through this SiC layer [63,70]. Li & Hausner describe the initial SiC layer formation by a small amount of carbon dissolving in molten Si and precipitating heterogeneously on the carbon surface within 1s. This forms approximately a 4 μm layer very quickly, and further growth is by diffusion of carbon through the SiC layer. A discontinuous SiC layer as shown by “SiC layer II” in Figure 2-7 is explained by some of the original dissolved carbon precipitating

on the SiC layer during cooling of the sample [63]. Although the mechanism described is the same, Li & Hausner base theirs on experiments by melting Si on glassy carbon, while Gern & Kochendörfer use the reaction to inform modelling of Si infiltration through porous carbon [63,70].

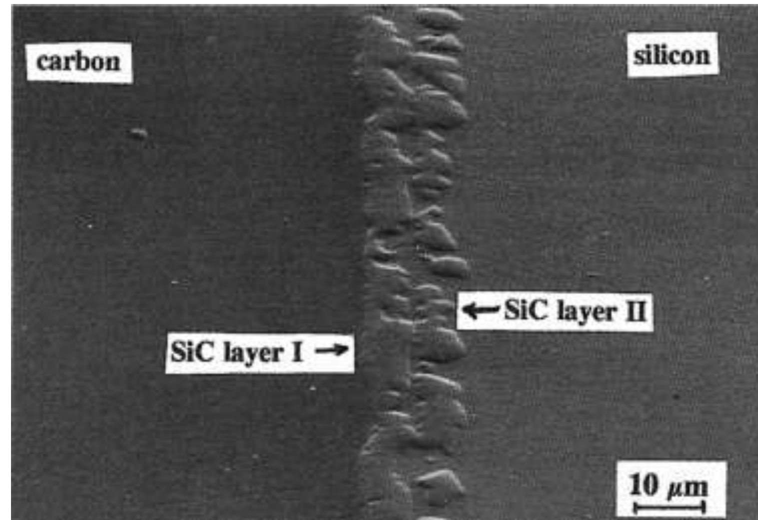

Figure 2-7: SiC layer I is formed heterogeneously on a glassy carbon surface within a few minutes of reaction. SiC layer II is formed by precipitation of dissolved carbon on the SiC layer during cooling [63].

Mechanism 3 proposed by Favre *et al.* is a modification of mechanism 2 based on experiments with molten silicon in two types of carbon crucible: polycrystalline graphite, and glassy carbon [93]. The work attempted to isolate SiC growth from pore infiltration kinetics by only reacting on the surface of impermeable glassy carbon, and comparing that to the reaction in porous graphite. The formation rate and saturation of SiC layer thickness supports mechanism 2 of heterogeneous nucleation of SiC, then growth by diffusion. The SiC layer on carbon is 4 μm thick after 5 minutes of reaction (in agreement with Li & Hausner [63]), and saturates around 10 μm within 30 minutes. However, with further heating a layer of SiC formed on the surface and isolated SiC regions were found within the solidified silicon (Figure 2-8). This thicker (approximately 150 μm) layer and the isolated SiC is attributed to regions of the SiC layer on carbon breaking off and floating away into the silicon, upon which the exposed carbon surface quickly regrows a SiC layer.

No such isolated SiC was observed in the porous carbon, possibly due to the molten silicon being less turbulent within pores so there was no surface break-off.

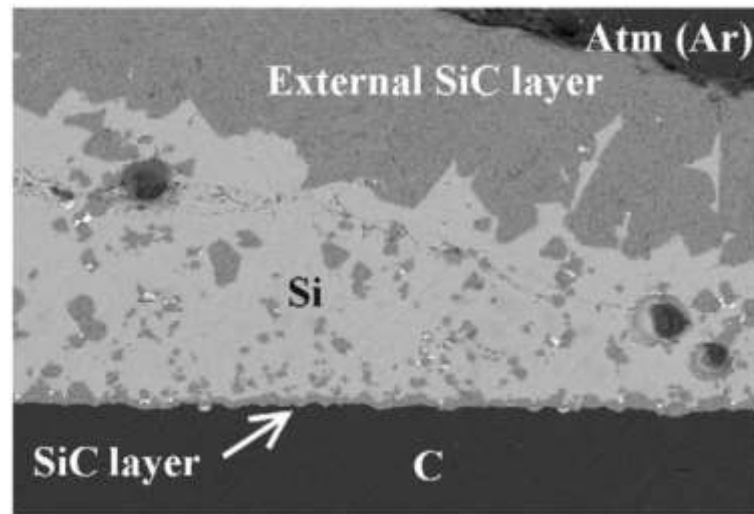

Figure 2-8: Glassy carbon in contact with molten Si for 24 hours at 1600C. 10 µm layer of SiC on the surface of carbon, and approximately 150 µm SiC layer on the surface of Silicon [93]

Mechanisms 2 and 3 are proposed based on reactions between molten silicon and carbon alone. These attempts to isolate the C-Si reaction and study it in more controlled conditions have potentially altered it. One variable of importance is the form of carbon used. Hase *et al.* observed that different sources of carbon reacted differently depending on crystal size and orientation within the powders, degree of crystallinity, and powder size [94]. The form of carbon in RB-SiC is typically carbon black, pyrolytic carbon derived from organics, or graphite. These will react differently to each other, and also in different conditions of temperature and atmosphere [99].

For reaction bonding, the amount of carbon is important for determining how much secondary reaction formed SiC is created to bond the original SiC grains together. Optimal reaction forming results in a denser and stronger material. Too much carbon, and some will be left unreacted resulting in weakening of the material, as shown in Figure 2-9 [100]. In this paper by Li *et al.,* the resulting material is relatively weak, possibly because the starting carbon powder size is very large at 40 µm, leaving the cores unreacted.

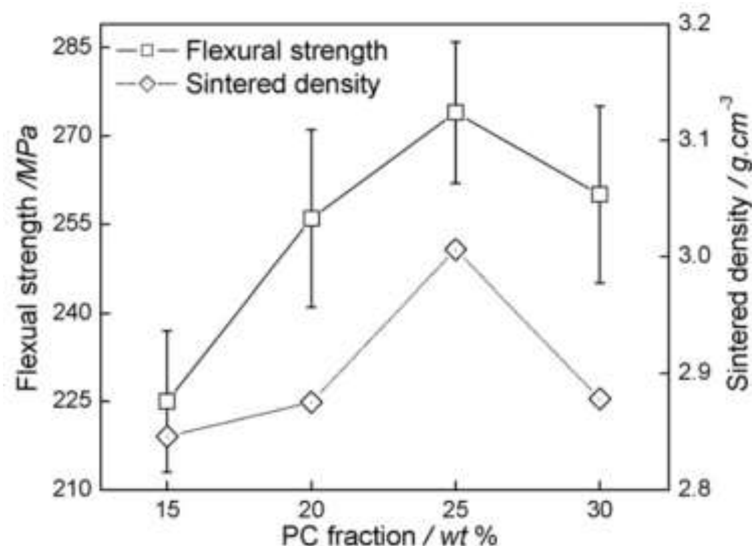

Figure 2-9: Impact of carbon content on strength and density [100]

The amount of reaction formed SiC, and thus the amount of carbon necessary for a dense and strong body is also dependent on the green density, which is a function of pore distribution, and starting particle size. More carbon makes silicon infiltration more difficult due to reactive blocking of the pores, so consideration of the final product dimensions must be made. The report by Phillips & Hutchings gives a qualitative review of effects of particle size, green density, and carbon content on properties of RB-SiC [101]. In general, a carbon content of 20-25 wt% is optimal consisting of fine particles. Suyama *et al.* developed a high strength RB-SiC by systematic investigation of starting particle size and residual silicon [102]. The highest strength material was made using 500 nm SiC particles with a low volume of small residual silicon, which was reduced using a higher carbon content (Figure 2-10). This material is called "New Technology SiC" and is made by Toshiba for mirrors in space telescopes [103]. No other form of RB-SiC has reached strengths similar to this material, and no testing or characterisation has been reported other than published by Toshiba themselves.

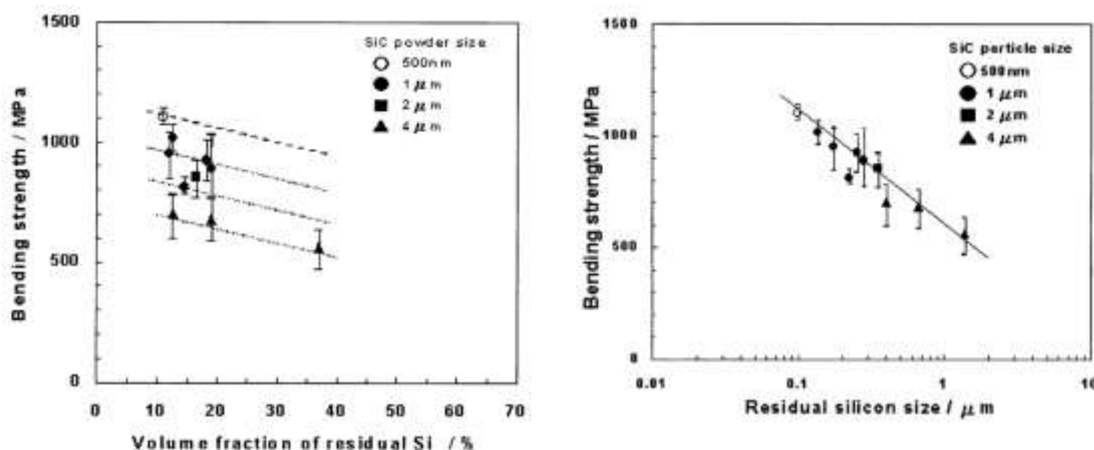

Figure 2-10: Dependence of bending strength with residual silicon content and SiC particle size, and with size of residual silicon pools [102]

Based on this literature review, processing RB-SiC is very complicated with many inter-related variables. Silicon infiltration and silicon carbide formation seem to depend on the specific material being made, whether it is a reaction bonded SiC starting from SiC powder particles, or reaction formed SiC from an initial carbon body. It also appears to depend on the form of carbon, and processing atmosphere. Processing parameters have a strong influence on the properties of the material, but improving properties is a trade off with the size of the component.

2.2 Radiation damage

This section will outline the evolution of radiation damage in SiC starting with a general overview of some of the issues in studying radiation damage in ceramics, then SiC more specifically in section 2.2.2. This will begin from atomistic simulations of the initial displacement cascades and individual defects, then onto relevant experimental measurements of defects and swelling. At this stage no distinction is made between SiC polytypes as their structures are very similar, and neutron irradiations are mainly considered. Macroscopic and mechanical properties are dominated by microstructural

features, so discussion of these will be limited to RB-SiC only. A separate discussion on ion implantation and micromechanical testing will follow.

2.2.1 Radiation damage in ceramics

Radiation effects on ceramics have generally been studied less than for metals as most nuclear reactor designs predominantly make use of metals for their known reliable properties [3]. As reactor designs become more aggressive, in particular for fusion, ceramics become interesting for some of their superior properties over metals [104]. However, ceramics are a wide class of materials and radiation damage processes in ceramics are more complicated than in metals for several reasons [10,105–109]:

- Covalent ceramics are not close-packed and have preferred interatomic bond lengths and angles/directions
- Defects can be charged, and charge can be transferred during irradiation with charged particles
- Ceramics are structurally and chemically ordered; thus, defects are structural and/or chemical
- Different atomic species have different displacement energies, so one sub-lattice can receive more displacements per atom (dpa) than another. Using controlled energy irradiation it is possible to preferentially displace one atomic species up to the point of amorphisation [110]

Characterising defects in ceramics is rather complicated as chemical defects are difficult to relate to structural defects directly. Structural defects tend to be measured by diffraction methods, and the use of Bragg’s law and crystallographic periodicity whereby a TEM can be used to identify “black-spot” defects, dislocations and stacking faults, or changes to lattice parameter and interplanar spacing. Chemical defects are investigated by

spectroscopy and give an integral of the interaction volume of the spectroscopy technique. Neither of these classes of technique can give information on the intermediate-range radiation-induced damage, ie the effect of individual defects on the structure of the crystal lattice which is where modelling is particularly useful. Modelling must always be related to experimental measurements to validate it.

Conventionally, radiation defects are considered in terms of crystallographic defects; vacancies, interstitials, etc [3]. For ceramics with directional, ordered, chemical bonding, radiation-induced changes to these bonds are also an appropriate measure of radiation damage which can be characterised. Since spectroscopic measurements of chemical bonding are mostly insensitive to crystallographic symmetry and whether an atom is sat on a lattice site, it is often useful to consider structures in terms of bonds rather than lattice sites.

An alternative to symmetry-based approaches to structure is to use topology based approaches where the crystal is considered a network of bonds connecting nodes (atoms) [111]. Crystallography, while it can be experimentally related to diffraction experiments, can sometimes obfuscate interesting features of structures. The crystallographic unit cells shown in Figure 2-11 (a) and (b) for 6H- and 3C-SiC are clearly vastly different and respond differently to diffraction experiments. However, topologically, 6H- and 3C-SiC are very similar (Figure 2-12, to be discussed more in the following paragraphs), and one would expect only small differences in terms of radiation defects. Silicon, diamond, and 3C-SiC are structurally identical apart from the occupation of lattice sites and bond lengths (Figure 2-11 (b) and (d)).

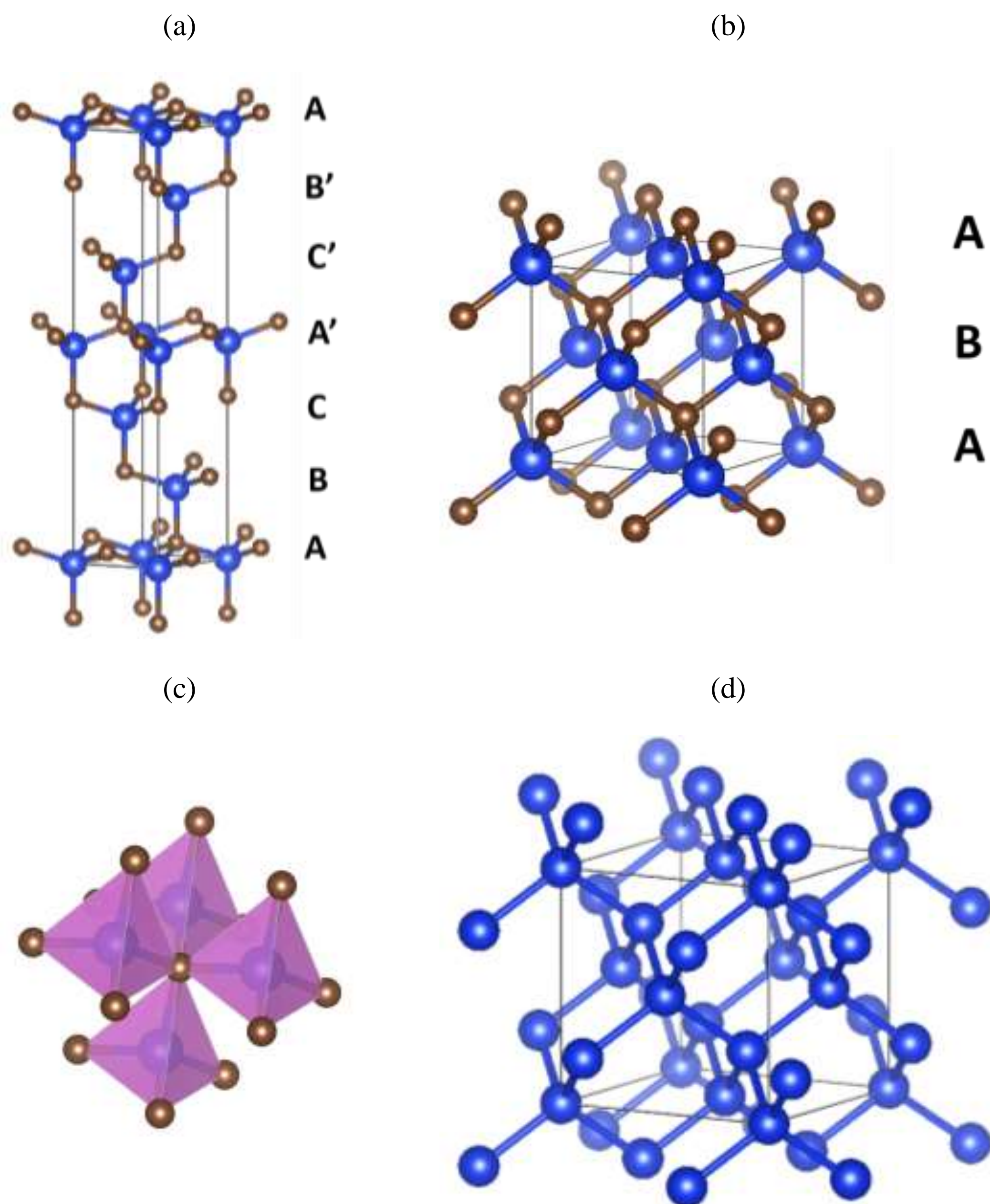

Figure 2-11: Crystallographic representations of atomic structures where brown circles are carbon atoms, and blue are silicon atoms. (a) unit cell of 6H-SiC showing staking sequence. (b) unit cell of 3C-SiC. (c) {4,4} connectivity of SiC_4 (CSi_4) tetrahedra. (d) crystal structure of cubic silicon. This is identical to the structure of 3C-SiC shown in (b), but with different site occupancy. Stacking of 3C-SiC is typically written as ABC when viewed along [110] *in analogy to the ABC layers in hexagonal polymorphs viewed along* $[11\bar{2}0]$. In this case the unit cell has been oriented to show similarity to the standard view of silicon.

Topological approaches are particularly useful in ceramics where bonds are directional, and the structure is not close-packed so mathematically can be considered a sparse network. The network is defined in terms of its structural unit (polytope), and how these polytopes are connected. For example, the polytope of SiC is a tetrahedron containing four vertices, and each vertex has 4 polytopes connected to it (Figure 2-11 (c)), so is

described as a {4,4} structure [111–113]. Variation in the order of stacking of these {4,4} structural units leads to the different polytypes of SiC. Si_3N_4 and SiO_2 are also tetrahedral, but connected with three, or two tetrahedra at a vertex, so are {4,3} and {4,2} networks respectively. This description only describes the ideal connectivity of bonds in the network - it says nothing about defects nor the specific structural polytype. An additional structural identifier is required.

Topological networks can be described by primitive rings which are the shortest rings made by bonds in the network. The primitive rings which emanate from and return to a node form the "local cluster" which is analogous to a unit cell (Figure 2-12 shows local clusters for 6H- and 3C-SiC), but can be defined in both crystalline, defected, and amorphous structures where crystallographic unit cells fail. A defect will change the size of the primitive rings, thus when local clusters are enumerated in terms of their average size (number of atoms and size of rings), the defect can be identified. For example, a local cluster of SiC consists of 12 6-atom primitive rings. A vacancy in the network would break up twelve of the 6-atom primitive rings and introduce twelve 12-atom primitive rings. A tetrahedral interstitial provides a "short cut" to some rings, adding 6 4-atom primitive rings to the network. Hobbs and co-workers have successfully used this method to describe the structure of crystals, defective crystals, and aperiodic (amorphous) structures over many years including the investigation of radiation defects [111,114–118]. Unfortunately, no experimental technique directly probes structural topology so experimental validation of models is only ever indirect measurements of another property. Although no experimental techniques use topology directly, it is useful in the discussion of radiation damage to appreciate topological defects and their significance to the atomic structure of irradiated SiC.

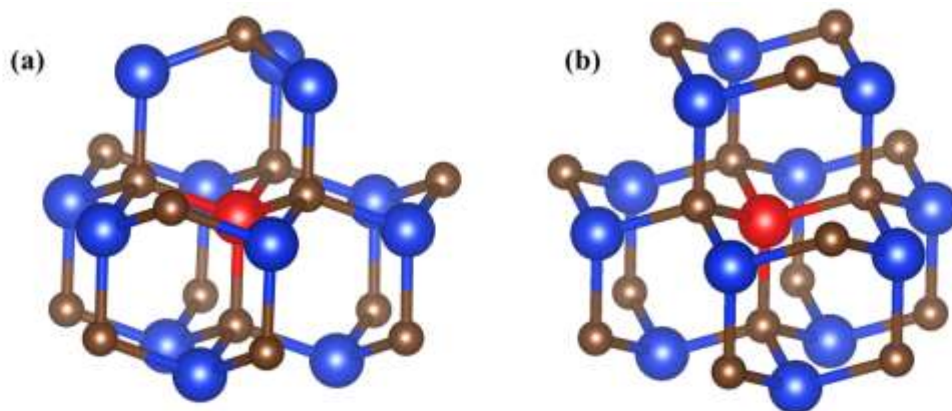

Figure 2-12: Local clusters of α- and β- SiC, emanating from the central red silicon atom. Brown is carbon, blue is silicon. [114]. *Note the similarity of these atomic structures compared to the crystallographic representations in Figure 2-11.*

2.2.2 Radiation defects in SiC

Nuclear grade silicon carbide is considered to be nanocrystalline chemical vapour infiltrated SiC_f/SiC composites or chemical vapour deposited 3C-SiC [55]. Models tend to consider 3C-SiC to fit into the framework of developing nuclear grade materials, however, fundamental experimental studies favour single crystals of 6H-SiC as single crystal 3C-SiC is very difficult to obtain. The literature discussed here is a combination of models and experiments where 6H- and 3C-SiC have been used. As explained above, the structure of 3C- and 6H-SiC is very similar on the scale of radiation defects. Snead *et al.* recently showed that under low temperature (~60 °C) neutron irradiation when defect annealing is minimal, single crystal 6H- and 3C-SiC behave identically to nanocrystalline CVD 3C-SiC in terms of swelling, point defects, and amorphisation [119]. It is only at temperatures where defect diffusion becomes significant that nanocrystalline CVD 3C-SiC shows a difference to micro-crystalline or single crystal 6H- or 3C-SiC due to the high density of defect sinks in CVD SiC. For these reasons, fundamental defects in 3C-SiC are considered alongside 6H-SiC until the microstructure become significant at which point the discussion focusses on reaction-bonded SiC.

As mentioned above, molecular dynamics (MD) simulations of SiC are complicated compared to metals, and do not capture the full effects of defects so caution should be used when interpreting MD results, in particular classical MD which must necessarily make classical assumptions which are not necessarily valid in ceramics and can result in significantly different defect structures compared to *ab initio* density functional theory (DFT)-based molecular dynamics [120].

Primary displacement damage in SiC and other covalent ceramics is anisotropic depending on bond strengths in different directions [108,121,122]. The threshold displacement energy most widely used for SiC is the minimum displacement energy of both carbon (21 eV) and silicon (35 eV) sublattices which is along [1$\bar{1}$00] and [000$\bar{1}$] directions respectively, but can rise to 65 eV for carbon along [000$\bar{1}$] and 120 eV for silicon along [0001] due to the orientation of nearest neighbour covalent bonds [122].

The anisotropy of displacement energy results in branched collision cascades with local damaged regions consisting of isolated point defects and clusters of point defects consisting of vacancies, interstitials, and anti-sites [123]. These crystallographic defects were identified using Wigner-Seitz cells on molecular dynamics simulations of cascades. When a point defect is identified using this technique, it does not fully account for the structural and chemical defects as the neighbouring atom environments are also changed [111]. For example, a C_{Si} anti-site has four C-C bonds, but also causes its 4 neighbouring carbon atoms to be defects as they now have 3 C-Si bonds, and 1 C-C bond. These neighbouring defected atoms are not captured as defects in a crystallographic definition of the structure (they are the correct atom types sat on their correct lattice site), these defects would only be counted when considering bonding [115]. This emphasises the importance of considering interatomic bonding defects when considering radiation damage in SiC. With further damage accumulation nearby point defects can have cumulative effects on

distorting the lattice to a point where a crystalline Wigner-Seitz reference cell struggles to identify topologically crystalline (but distorted) material and would over-estimate the amount of point defects [115]. A useful measure of defect accumulation in SiC is chemical disorder, defined as the ratio of homonuclear C-C bonds to heteronuclear C-Si bonds. This is sensitive to both crystallographic anti-sites and Frenkel pairs, and topological bonding defects, but is not reliant on crystal lattice sites [115,124]. This could be considered a measure of defects in a material structure in terms of interatomic bonds rather than occupation of lattice sites.

Chemical disorder (bond enumeration) has been shown to increase linearly with displacements (Figure 2-13) until the point of amorphisation at 0.15 molecular dynamic dpa (based on radial distribution functions) when Wigner-Seitz crystallographic defect counting no longer works. [106]. From Figure 2-13 one can also see that chemical disorder and enthalpy per atom are still evolving after the identification of the crystalline-amorphous transition, suggesting that the "amorphous" structure is still evolving, in agreement with other modelling of amorphous SiC [111,114,115] and Raman spectroscopy measurements of ion irradiated SiC [125]. Chemical disorder saturates in damaged, but not amorphous SiC due to dynamic annealing at higher temperatures – clearly chemical disorder is important in amorphisation processes in SiC [114,115]. Amorphous structures are identifiably different based on energetics and bond types, but also topologically identifiably different based on their local clusters [114,115]. Based on traditional crystallography or radial distribution functions, they would simply be classified as "amorphous". Amorphisation of silicon carbide has been extensively studied as it appears to be anomalously easy based on its structure [111], and it is of interest in ion implantation doping for semiconductor applications of SiC [126]. For the purposes of this literature review amorphisation will not be discussed in much more detail as it is only apparent below

a critical temperature between 300-500 K depending on radiation type which is out of the range of interest for the irradiations carried out in this work and the expected conditions in the fusion reactor blanket [115].

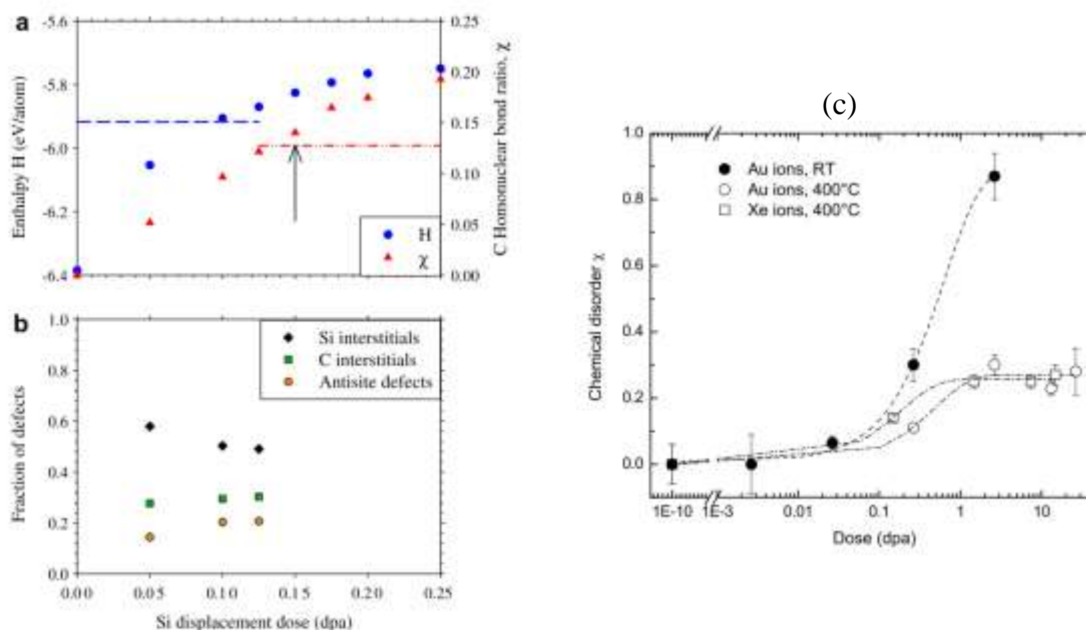

Figure 2-13: (a) evolution of enthalpy per atom and chemical disorder with dose during MD simulated displacements. Dashed lines are the enthalpy and chemical disorder values of a melt-quenched amorphous structure (b) Proportions of different point defects up to the point of amorphisation at 0.15 MD.dpa. Reproduced from [106] *(c) is experimental Raman measurements of chemical disorder showing the continued evolution of chemical disorder after room temperature amorphisation, while 400 °C irradiated SiC saturates in chemical disorder and does not amorphise* [125].

Li *et al.* used optimised classical molecular dynamics to calculate the excess volume of the different point defects in 3C-SiC (Table 2-1) [127]. All defects except C_{Si} anti-sites lead to an increase in volume of the simulation cell. While it is classical MD with a strong dependence on choice of interatomic potential, the optimisation process included benchmarking defect energies to DFT simulations. This excess volume is the origin of radiation swelling in the point defect regime.

Table 2-1: Excess point defect volumes in Å^3 from Li et al. [109] "AP" is anti-site pair, "DI" is di-vacancy

V_C	V_{Si}	C_{Si}	Si_C	C_{TC}	C_{TSi}	Si_{TSi}	Si_{TC}	AP	DI
2.68	1.85	-9.52	15.44	15.33	16.48	27.88	37.22	3.88	3.44

Beyond the scale of individual collision cascades, experimental techniques can be applied such as TEM and spectroscopy. Interstitials in irradiated SiC are relatively stable

and do not form clusters clearly resolvable in TEM [128]. The effect of isolated defects and small defect clusters is to expand the lattice parameter as measured by X-ray diffraction (XRD), which corresponds directly to macroscopic expansion at temperatures between 250 – 480 °C [129,130]. These small defect clusters are commonly known as "black spot defects" (BSD) due to their contrast in bright field TEM. BSDs are smaller than 5nm in size, but increase in number density with dose, and increase in size with temperature for both neutron and ion irradiations [131–133]. Until recently it was unclear what these black spot defects are – they were assumed to be either three-dimensional interstitial clusters [131,134] or small dislocation loops of unresolvable type [135]. However, recent high resolution-TEM and high angle annular dark field scanning transmission electron microscope (HAADF-STEM) combined with image simulation have revealed that they consist of a core vacancy cluster surrounded by interstitials [132,136]. Thus, there is an excess of isolated interstitials around the BSDs, while vacancies are clustered.

At neutron irradiation doses greater than ~10^{26} n/m^2 (~10 dpa) and temperatures above 480 °C interstitial dislocation loops are observed in addition to BSDs [130,137]. This is explained by the excess of isolated interstitials around BSDs diffusing into loops. At higher doses above 480 °C lattice parameter expansion is less than the macroscopic length expansion and XRD peaks broaden indicating the formation of small interstitial loops which increase in size with dose [129,130,135,138]. TEM after post-irradiation annealing shows that BSDs are still present and interstitial dislocation loops grow while lattice parameter and macroscopic length decrease with annealing up to 1200 °C due to recombination of Frenkel pairs by interstitial migration [130,138]. These annealing experiments indicate that there are more isolated vacancies than isolated interstitials after irradiation in this regime as the lattice parameter decreases below the unirradiated value

due to remaining vacancies after Frenkel pair recombination and interstitial loop growth [130,138,139]. Annealing at temperatures over ~1200 °C allows vacancies to migrate in addition to interstitials, allowing them to annihilate with small interstitial loops, and also to form voids at grain boundaries and a macroscopic volume expansion [135,137].

Post-irradiation annealing is a useful method to investigate defect migration energies and mechanisms to compare with atomistic simulations [123,139–142]. Annealing begins at temperatures above the irradiation temperature showing that the smaller saturated property changes with increasing temperature is due to dynamic annealing during irradiation [134,137,139,141]. Idris and Yamazaki [139,142] identified that below 950 °C annealing is by interstitial carbon and silicon diffusion to sessile vacancies less than 0.7 of the lattice parameter away, and ~75% of recovery of length can be achieved in this regime. Between 950 and 1150 °C interstitials become more mobile and can diffuse beyond next-nearest neighbour vacancy sites. Above 1150-1200 °C vacancies become mobile leading to grain boundary voids, consistent with the void swelling regime observed in high temperature irradiation experiments [130,143]. The exact activation energies for different defect migrations has been calculated using molecular dynamics and agrees well with the experimentally observed recovery regimes, although the modelling gives additional insight into the chemical environments and geometries of defects [144–146].

Studies on SiC samples which have been irradiated with self or similar mass ions show similar types of defects as neutron irradiation experiments as these ions tend to be substitutional. Light ions (protons, helium etc.) produce far fewer displacements so more need to be injected for a nominal dpa. This changes defect formation due to large numbers of injected interstitial atoms which may cluster or stabilise different defect types [147,148]. Most literature has used either silicon or carbon self-ions or inert gases, occasionally gold

has been used – the aim being to avoid chemical effects on the ion implantation. The effects of ion implantation will be studied more in the following sections

2.2.2.1 Raman spectroscopy of irradiated SiC

Silicon and silicon carbide are both "Raman active" materials meaning they have well defined collective atomic motion (phonon lattice vibrations) which can interact inelastically with incident light. A basic quantum explanation of Raman scattering is given below using Figure 2-14, but a more comprehensive description, including a classical explanation, can be found in ref [149].

Incident monochromatic light with frequency ω_i excites an electron to a higher energy level, 2. The excited electron can interact with a phonon of frequency ω_j being excited or de-excited to level 3 or 1 depending on whether the phonon is annihilated or created by this excited electron. The electron can return to the ground state, 0, by emitting a photon with energy $\omega_i \pm \omega_j$. $\omega_i + \omega_j$ is termed anti-Stokes scattering, and $\omega_i - \omega_j$ is Stokes scattering. The frequency difference of the emitted light, ω_j is the Raman shift [150]. This frequency shift is a fundamental measurement of the crystal lattice and is affected by crystal defects, and stresses. The unit "Raman shift" is the shift in frequency of the collected light compared to the incident light.

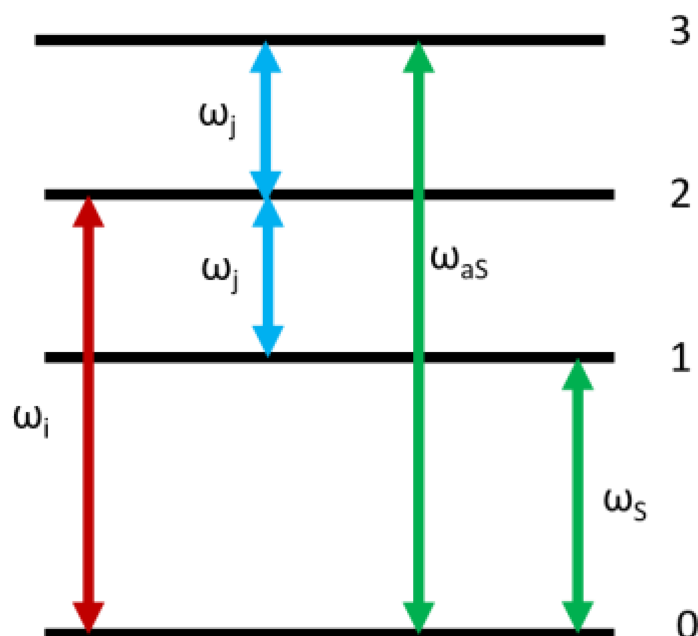

Figure 2-14: Basic energy level explanation of Raman spectroscopy.

Perfect crystalline silicon has three active phonon modes, two transverse optical (TO) along x= [100] and y = [010], and one longitudinal optic (LO) z = [001], all of which have a Raman shift of ~520 cm^{-1} in the unstressed state at room temperature (Figure 2-15) [149].

Silicon carbide is more complicated due to the presence of two atomic species and tall unit cells containing many atoms. Although the crystal symmetry is complicated, it allows Raman spectroscopy to identify different SiC polytypes [151,152]. In backscattering geometry 6H-SiC shows strong signals from transverse acoustic (TA 150 cm^{-1}), longitudinal optic (LO 967 cm^{-1}), and a triple peak for the three folded transverse optic (TO) modes at 767 cm^{-1}, 789 cm^{-1}, and 797 cm^{-1} (Figure 2-15). A broad, weak signal at 504 cm^{-1} is from longitudinal acoustic modes. There are also several very low intensity peaks corresponding to lower order phonon modes [151].

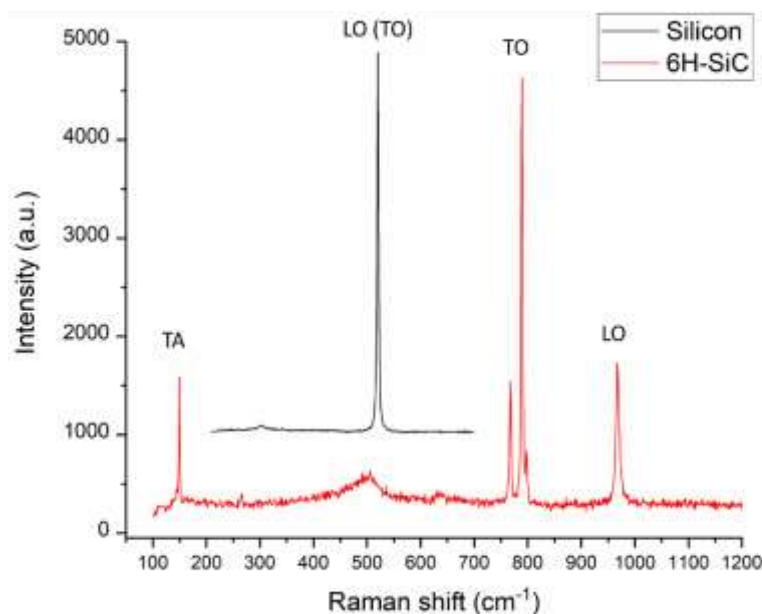

Figure 2-15: Reference Raman spectra of silicon and 6H-SiC single crystals with peaks labelled based on Refs. [149,151].

Raman spectroscopy has been used to identify defected bonding in damaged SiC with early research concentrating on elucidating different amorphous structures of SiC [153–156], and processing induced defects [157]. Only more recently has Raman spectroscopy been applied to radiation defects in SiC in the context of nuclear reactor applications. The power of this technique is that defects invisible in the TEM and diffraction experiments are identifiable which helps to develop radiation damage mechanisms [158].

The Raman spectrum of unirradiated SiC is shown in Figure 2-15 and contains sharp Si-C peaks as described above. Typical features of Raman spectra after irradiation are reduction in intensity and broadening of the characteristic Si-C peaks and the appearance of peaks corresponding to Si-Si and C-C bonding. These are apparent in all irradiation conditions and will be discussed in more detail below. Sorieul *et al.* and Chaâbane *et al.* summarised the peaks observed in irradiated SiC based on their observations and earlier literature (Table 2-2) and this has widely been used in the more recent literature for signal identification [125,159]. They cite Bolse *et al.* [153] for the 660

cm^{-1} peak of distorted SiC, however this paper makes no reference to the 660 cm^{-1} peak. A further literature search for appropriate identification of this peak found that it can be attributed to C-O-C vibrations in solid carbon dioxide with a tetrahedral structure [160].

Table 2-2: Identification of Raman signals in SiC from Sorieul et al. *and Chaâbane* et al. [125,159]

	Si-Si cm^{-1}	**Si-C cm^{-1}**	**C-C cm^{-1}**
Unirradiated	146	767	
	206	789	
	505	966	
Irradiated	~188	766, 789, 966	~1080 sp^3
	~260	~600, ~660* Distorted SiC	~1420 mixed sp^2/sp^3 D band
	~535	~870 Highly disordered SiC	~1600 sp^2 G band
		~933 Slightly disordered SiC	

Figure 2-16 shows the dose dependence on Raman spectra of neutron irradiated SiC. (a) and (b) are both very low temperature and low dose irradiations <100 °C, whereas (c) is most relevant for nuclear reactor conditions. These low temperatures are below the critical amorphisation temperature of SiC, so the structures (even at these low doses below the amorphisation dose) may not be representative of reactor-relevant structures, but could represent a highly damaged structure. With increasing dose, Raman signal reduces in intensity, with the Si-Si and C-C signals increasing in intensity relative to the Si-C signals. Figures (b) and (c) shows the appearance of G band carbon in addition to the D band [161]. The D/G ratio can indicate the extent of carbon ordering in the structure – higher G band intensity corresponds to extended ordered sp^2 carbon structures similar to graphite (graphene), although not necessarily ring shaped, while the D band is indicative of disordered C-C pairs or small chains [162]. The higher dose curve in (b) shows accumulation of C-C bonds at ~0.167 dpa without significant distortion of the Si-C bonds

indicating high chemical disorder within the crystalline lattice. The accumulation of C-C bonds has been shown to be a vital step in amorphisation of SiC, to the extent that it is possible to amorphise without inducing atomic displacements[1] [114,115]. This Raman spectrum is *not* indicative of amorphous SiC but the low temperature irradiation conditions suggest this sample may be on the way to amorphisation. As shown above, the types of radiation defects are strongly dependent on temperature due to dynamic annealing, hence the observed differences in Raman spectra.

[1] Chemical disorder introduces lattice strains in the SiC lattice as Si-Si and C-C bonds are different in length to Si-C. As local strain and energy accumulate it can become energetically favourable for C-C bonds to form sp^2 bond hybrids rather than sp^3. This introduces 3-fold coordination into the 4-fold tetrahedral SiC network, reducing connectivity. This can allow sufficient degrees of freedom for a highly strained and high energy crystal to lower its energy by rearranging into an aperiodic (amorphous) network without inducing atomic displacement damage.

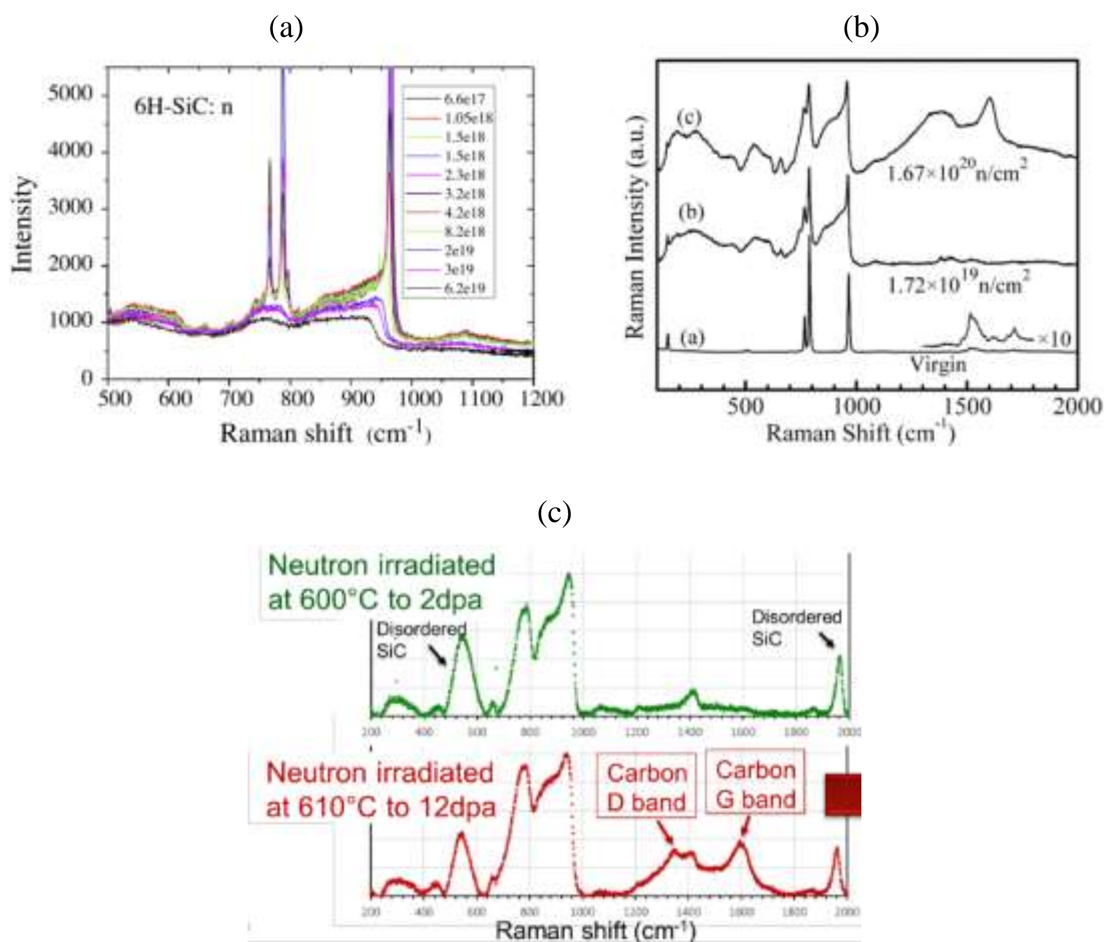

Figure 2-16: Raman spectra of neutron irradiated SiC showing dependence of dose on spectra. (a) is from irradiations of 6H-SiC at <50 °C from ref. [163], *(b) is from irradiations of 6H-SiC at <100 °C from ref.* [164]. *(c) is from irradiations of 3C-SiC at ~600 °C from ref.* [161] *1 dpa is ~1×10^{21}n/cm^2. The peak labelled "Disordered SiC" in (c) is incorrectly labelled by the authors, it is Si-Si*

Figure 2-17 shows the Si-C peaks of 3C-SiC neutron irradiated to various doses at reactor-relevant temperatures [158]. Both the TO and LO peaks are shifted to lower wavenumbers with increasing dose – this shift being reduced with increasing temperature. The shift to lower wavenumbers is indicative of tensile stress on the Si-C bonds, in agreement with the observed swelling characteristics of irradiated SiC. Peaks remain sharper with increased temperature, indicating less structural distortion. The 1.9 dpa 1180°C spectrum maintains sharp peaks with minimal tensile strain relative to the unirradiated spectrum. At this temperature vacancies are mobile, and it appears that structurally SiC tetrahedra are able to dynamically anneal towards their unirradiated state. Unfortunately, this paper does not report on C-C nor Si-Si bonding. This irradiation

condition is in the void swelling regime so point defects are mostly annealed, volumetric swelling is from grain boundary bubbles/voids and larger interstitial dislocation loops and black spots.

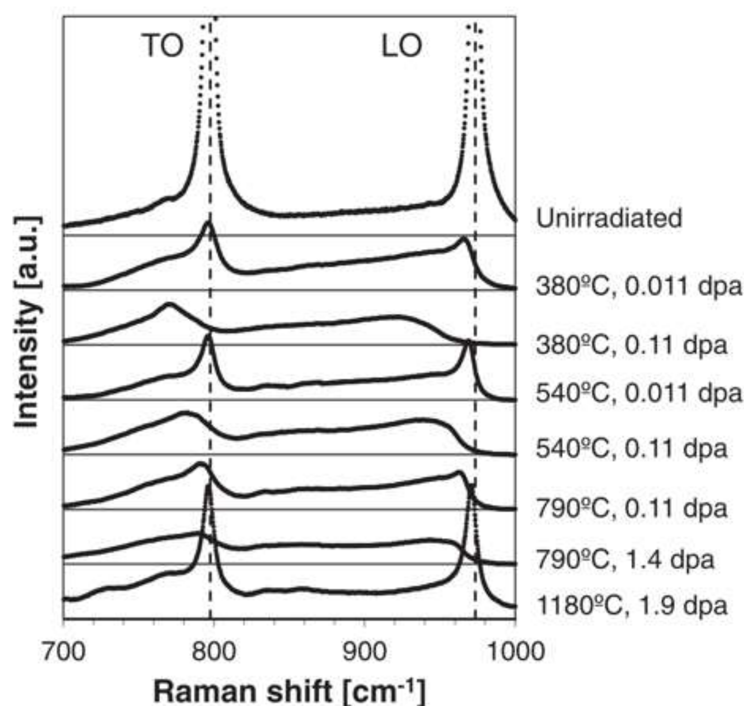

Figure 2-17: High temperature neutron irradiated 3C-SiC Raman spectra from ref. [158].

Raman spectroscopy has commonly been used with ion implanted samples as the probed depth of confocal Raman microscopy is similar to the damaged depth of ion implantation. The paper by Chen *et al.* is the only direct comparison of neutron irradiations matched with similar nominal dpa ion irradiations [165]. They chose silicon and carbon ions to reduce chemical effects but based on their Raman spectra these ions may have exacerbated the chemical effects (Figure 2-18). In Figure 2-18, The peak dpa of C-3 and C-4 approximately match the dpa of neutron-1 (0.1 dpa), and the plateau dpa of Si-4 and Si-5 approximately match the dpa of neutron-1 (0.1 dpa) and neutron-2 (0.2 dpa) respectively. The general form of the ion irradiated spectra matches the neutron irradiated spectra with the broadening of Si-C peaks and appearance of Si-Si and C-C peaks. Two significant differences exist: 1. Si-C peaks are not shifted to as low wavenumbers as with

neutron irradiations indicating less tensile strain on Si-C bonds. 2. carbon ion irradiation produces more intense D and G band signals than neutron irradiation, while Si ion irradiation only produces a D band signal. There appears to be no difference to the Si-Si bonding. These irradiations were carried out at low doses and approximately room temperature, so similarly to discussed above, the defects may be different to those expected in nuclear applications of SiC. This work does identify a potential issue in the choice of ions for ion implantation to replicate neutron irradiations.

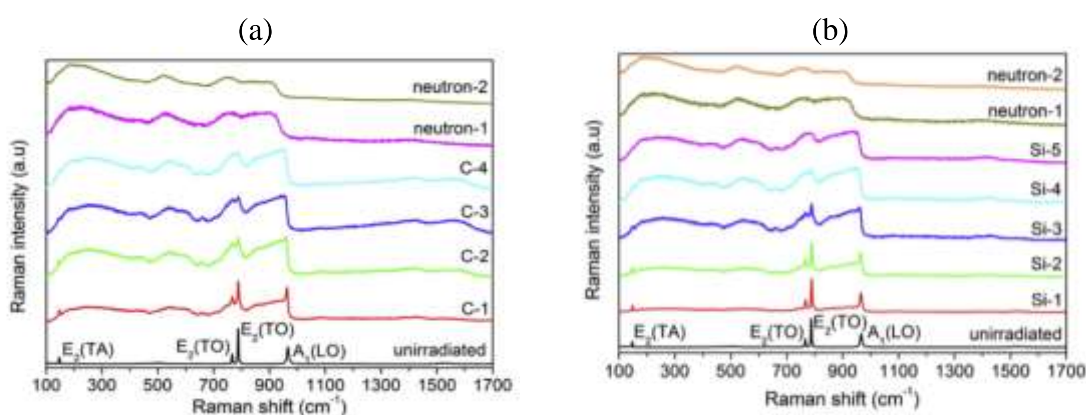

Figure 2-18: Comparison of Raman spectra produced by 50 °C neutron irradiations and room temperature (a) carbon ion and (b) silicon ion implantations in 6H-SiC. C-3 and C-4 approximately match the dpa of neutron-1, and Si-4 and Si-5 approximately match neutron-1 and neutron-2 respectively. From [165].

Subsequent work in the group of Chen *et al.* correlated the small reduction in Raman wavenumber of the Si-C peaks in ion irradiated SiC to significant lateral residual stresses due to constrained swelling identified by high resolution XRD, and the implications for this on nanoindentation measurements [165,166].

The group at Commissariat à l'énergie atomique (CEA) have collected Raman spectra of irradiated 6H-SiC with 4 MeV carbon, gold, and xenon ions at 400 °C at the same fluence of 10^{16} ions/cm^2 with corresponding nominal peak damage of 1.6, 2.64, and 1.48 dpa respectively (Figure 2-19) [125,159]. It is worth noting that the plateau damage region of carbon ion implantation is only 0.06 dpa, while the heavy gold and xenon ions do more damage up to the peak, although the level is unreported. Figure 2-19 (a) with

carbon ions shows stronger and sharper D band C-C signals than Au and Xe implantation in (b), and also a peak at ~1080 cm^{-1} corresponding to sp^3 carbon atoms. σ bonds formed by sp^3 C-C bonds are weakly resonant with visible exciting light, so although the signal is small, it may correspond to a significant number of bonds of these type [162]. sp^3 C-C bonding is not observed in Au and Xe ion implantations so the signal may be due to using carbon ions for the implantation. UV laser excitation would be required to investigate sp^3 bonding quantitatively. This 400 °C 1.6 dpa carbon ion implantation maintains less distorted peaks than the room temperature 0.1 dpa carbon ion implantation in Figure 2-18. At 400 °C carbon interstitials are mobile allowing dynamic annealing and less structural damage. The first order Si-C peaks have been cropped from the graph in Figure 2-19 (a) but remain sharper after the irradiation than the peaks in (b) with the LO signal being relatively higher than the TO signals [159].

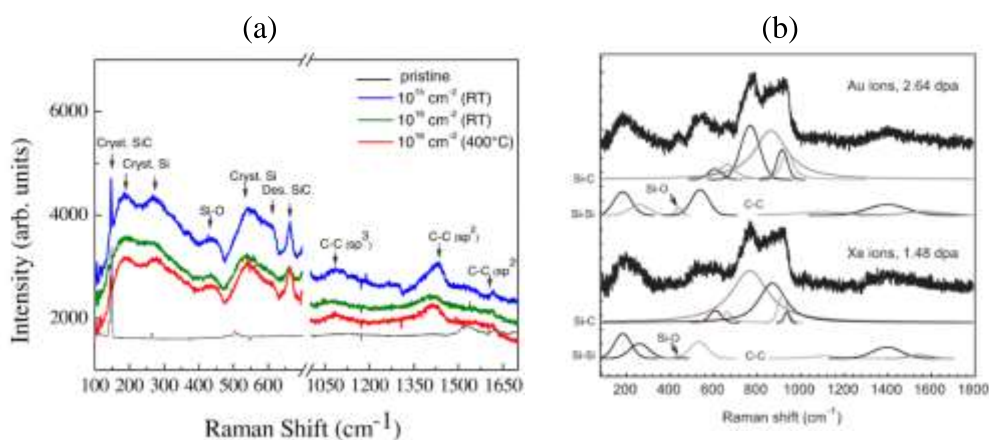

Figure 2-19: Comparison of Raman spectra of 6H-SiC irradiated with (a) C ions 1.6 dpa 400 °C (red line) [159], *and (b) Au and Xe ions at comparable dpa also at 400 C* [125]

Dual beam ion implantations have shown a synergistic effect of displacement damage with helium ions stabilising different defects compared to silicon ions [147]. The effect appears complex, but carbon-carbon defects appeared more strongly in Raman spectra with helium implanted alongside silicon ions than with silicon ions alone. This is possibly due to helium sitting substitutionally in the vacancy of a carbon Frenkel pair, preventing carbon recombining with its nearby vacancy, leading to the stronger C-C signal.

The final relevant Raman spectroscopy investigation of ion implanted SiC is the 4 MeV Kr ion implantation at relevant temperatures and high doses between 14 and 70 peak dpa shown in Figure 2-20 [129]. There appears to be little difference between 14 and 70 dpa on Raman spectra – the damaged structure has reached saturation in this “point defect damage regime”. The room temperature spectra (1 & 2) show amorphisation which is unsurprising at these very high doses. At 300 °C carbon interstitials are mobile at short distances and a broad peak corresponding to D and G band C-C is seen with highly damaged Si-Si and Si-C peaks. At 500 °C Si interstitials are mobile and can recombine at short distances leading to the sharpening of Si-Si and Si-C peaks. As carbon atoms have additional recombination opportunities above 500 °C the relative intensity of C-C bonding appears to reduce and the D band is relatively more intense than the G band, indicating more C-C pairs or short defected chains than extended C-C chains or rings. The nominal 14 dpa in this work is closest to the 12 neutron dpa of Koyanagi *et al.* [161] and in the same temperature regime of point defects, black spots, and small dislocation loops, with C and Si short range diffusion but not vacancy diffusion. Si-Si and Si-C peaks are reasonably well replicated using ions, however, the C-C structure is noticeably different without the higher intensity G band.

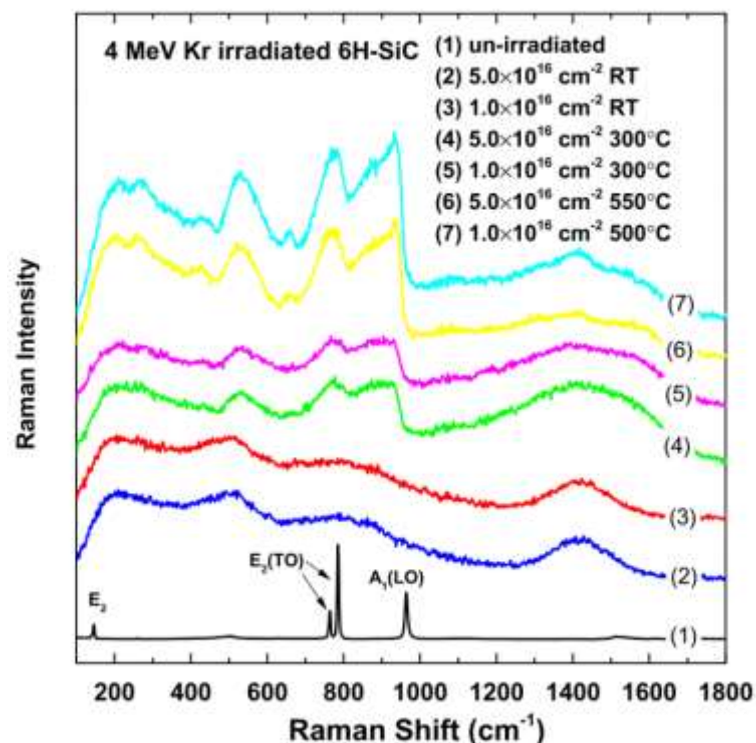

Figure 2-20: Kr ion implantation of 6H-SiC with temperature and dose dependence. There appears to be very little difference between 14 and 70 peak dpa doses. Increasing temperature sharpens Si-Si and Si-C peaks while the D band of C-C becomes more intense than the G band. Room temperature irradiation amorphises SiC [129]

The work on Raman spectroscopy characterisation of radiation damage indicated ion implantation conditions can be tailored to closely replicate neutron damage in terms of Si-Si and Si-C defects, however the C-C defects appear difficult to replicate. Ultraviolet (UV) Raman spectroscopy may be necessary to fully characterise the C-C defects as visible laser Raman does not satisfactorily excite sp^3 bonded carbon.

No ion implantation has been able to replicate the swelling of neutron irradiations, assessed by peak shifts to lower wavenumbers. This is a fundamental problem of ion irradiation of a thin layer on a thick substrate. The slight left-shift of ion implanted Raman spectra may be due to vertical, out of plane swelling within the interaction volume as it is an average signal.

2.2.3 Macroscopic radiation swelling

After neutron irradiation, it is possible to measure geometric changes of macroscopic samples using a micrometer, or by density measurements using the Archimedes method, as long as suitable active-sample handling facilities are available. This safety restriction has generally restricted the literature in this field.

As discussed above, radiation defects in SiC contribute to volumetric swelling. This swelling saturates after a fairly low dose (< 1dpa), so swelling is mostly determined by temperature (Figure 2-22) [50]. Macroscopic swelling has been categorised into three mechanisms determined by the irradiation temperature (see Figure 2-21 and Figure 2-22):

1. Amorphisation with ~10.8% swelling at less than 300-500 K [115]
2. Point defect swelling which saturates at <3%, reducing with temperature up to ~1150 °C [143]
3. >~1150 °C Void swelling due to vacancy diffusion increasing with temperature

The mechanisms of these three swelling regimes were discussed above.

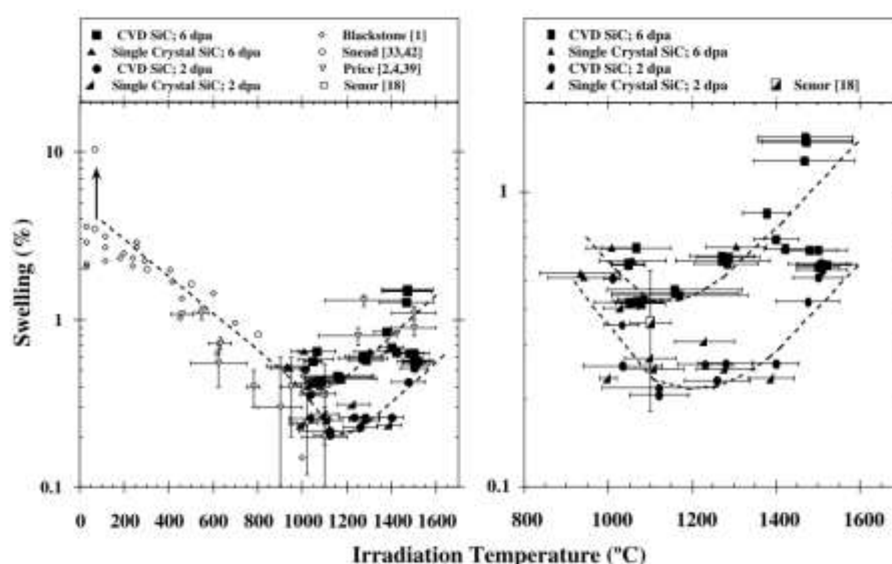

Figure 2-21: Swelling as a function of temperature for neutron irradiated SiC [143]

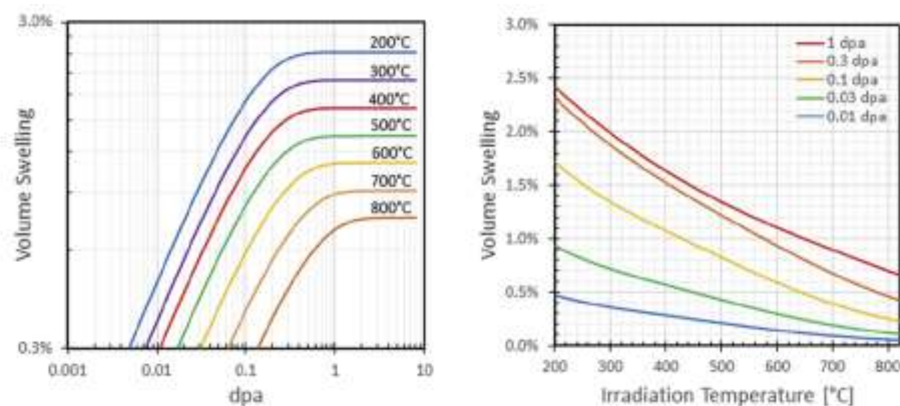

Figure 2-22: Dimensional swelling of neutron irradiated SiC based on a model fitted to experimental data [50]

Idris *et al.* found that composites swell less than monolithic CVD-SiC and NITE-SiC, and samples with oxide sintering aids swell more as residual oxide phases amorphised [167]. The lower swelling of composites compared to monolithic SiC which had nominally the same microstructure as the matrix of the composites was attributed to slightly lower swelling in the fibres relative to the matrix. This is likely to be due to more defects in the fibre (stacking faults, impurities, grain boundaries etc.) which act as defect sinks. The composite made by electrophoretic deposition [168] performed better than CVI SiC/SiC from HyperTherm High Temperature Composites (now Rolls-Royce), and the NITE SiC/SiC (Kyoto University) performed worst.

Ceramics with non-cubic crystal structures have shown anisotropic radiation swelling along their <a> and <c> axes [169]. This has been proposed in hexagonal forms of SiC however a recent review of the literature along with new experiments has shown that single crystal 6H- and 3C-SiC undergo almost identical volumetric swelling under low temperature neutron irradiation, and the <a> and <c> lattice parameters of 6H-SiC swell isotropically [119]. In the same work, Snead *et al.* showed that single crystal silicon did not undergo swelling during high dose neutron irradiation at 60 °C.

2.2.4 Radiation studies of reaction-bonded SiC (RB-SiC)

A little reported fact is that RB-SiC was used as a prototype fuel element in the Windscale Advanced Gas Reactor (AGR), although records of this seem to have mostly been lost [170]. Kennedy and Shennan give an overview of the UKAEA nuclear reaction-bonded SiC research effort in their declassified report from 1974 to complement the Forrest *et al.* article about REFEL processing [11]. Certain details are missing pertaining to the exact processing and experimental conditions, which either were commercial secrets or remained classified. Initial plans for development of a British high temperature reactor in the early 1960s were to modify the AGR design to use SiC fuel cladding rather than stainless steel and continue with CO_2 cooling. Instead, a new design based on helium-cooled graphite (the Dragon reactor) was selected as being more efficient, and the SiC development effort was stopped. The result of this research effort was REFEL SiC, which was commercialised for non-nuclear applications.

Various stages of fuel assembly development were undertaken, from uranium carbide microspheres forming an integral component of a solid fuel rod, to a lightly bonded bed of uranium carbide particles packed into thin-walled SiC tubes. Development then focussed on the SiC tubes and the fuel was replaced with conventional UO_2 pellets.

This research plan included 1080 individual RB-SiC fuel pins being placed into ten channels of the Windscale AGR, but this was not achieved. Prior to this, individual pins in sealed capsules, and a 28-pin mini-fuel element were irradiated in Windscale. In a 6-month production run, 11,000 REFEL tubes were produced for these experiments from a dedicated manufacturing plant. These were tested by ultrasound and X-rays, followed by proof testing which resulted in 19% being rejected. A predicted failure stress considering thermal stresses, neutron irradiation, and Weibull statistics concluded a failure probability of 2×10^{-6} for the design of REFEL fuel pins used with a peak design stress of 40 MPa.

One of the pins in the mini fuel element failed after three months which ended this experiment. By miniaturising the fuel element, the coolant became turbulent which increased the cooling efficiency, so the sample was irradiated at approximately 600 °C rather than the designed 800 °C. This lower temperature irradiation caused more degradation in thermal conductivity and strength than was considered in the design. This increased the thermal stress on the pin to 92 MPa with a 40% failure probability from Weibull statistics. New fuel pins were designed with a 1 mm wall thickness rather than 2 mm to reduce the temperature drop between the inner and outer edges of the tube wall. This reduced the design failure probability to 1×10^{-6}, however this was never tested as the research program was ended.

The report concludes that thin walled REFEL fuel cladding and fuel pins are viable. In non-radiation environments, the design stress could be increased by a factor of four for the same probability of failure. Although this is not a fusion environment, it is a positive sign for the use of reaction-bonded SiC in nuclear environments generally.

Although REFEL® SiC was developed by UKAEA (the name derives from **RE**actor **F**uel **EL**ement) it along with other forms of RB-SiC have not undergone many radiation studies after early investigations suggested its unsuitability. These studies are summarised in Table 2-3.

Table 2-3: Summary of radiation studies in RBSC

Type of RBSC	Temp	Dose	Measurements	Ref
REFEL	500 - 1300 °C	4-5×10^{25} n/m^2	Bending, thermal expansion, thermal conductivity	[170] 1974
Made by authors: 20μm grain, 10% Si	450 °C 650 °C	3×10^{25} n/m^2 E > 1 MeV	4-point bend, XRD	[171] 1974
NC-430	130 °C 800 °C electrons	2×10^{24} n/m^2 E > 1 MeV + 52 MeV electrons	Resistivity, 3-point bend, in-situ electron radiation, dimensions	[172] 1979
NC-430 (88.5% SiC, 8-10% Si, 0.4% Fe, 0.1% Al, C and pores)	140 °C	1.2×10^{25} n/m^2 E > 1 MeV (~2.6 dpa)	3-point bend, thermal conductivity	[173] 1981
NC-430	1100 °C 200 °C	1.2×10^{25}n/m^2 E > 1 MeV (~2.6 dpa)	3-point bend, resistivity, thermal conductivity	[174] 1981
NC-430 (8-10% Si)	740 °C	2.14×10^{26}n/m^2 E > 50 keV	4-point bend	[175] 1982
NC-430 (20-100 μm grains, 8-10% Si	140 °C 727 °C	1.2×10^{25} n/m^2 and 8.1×10^{25} n/m^2 E > 1 MeV (2.6 dpa - 20 dpa)	3-point bend, dimensions, thermal conductivity, resistivity, thermal cycling	[176] 1983
NC-430 (20-150 μm)	140 °C 727 °C	1.2×10^{25} n/m^2 and 8.1×10^{25} n/m^2 E > 1 MeV (2.6 dpa - 20 dpa)	TEM and XRD	[177] 1984
SE-10 (9% Si)	280 °C 600 °C 640 °C	8×10^{23} n/m^2 4.3×10^{24} n/m^2 6×10^{24} n/m^2 E > 1 MeV	4-point bend, indentation, dimensions, TEM	[178] 1990
Made by authors: 0.5 and 10 μm β-SiC powders with 17.1 vol% Si	RT	1.0×10^{16} ions/cm^2 2 MeV Au^{2+} (~13-45 dpa)	TEM, XRD, Raman spectroscopy, nano-indentation, thermal expansion	[179] 2016

Most of these investigations used Norton NC-430, which was more readily available than REFEL in America where most of these experiments were carried out. It has a larger grain size than REFEL, and much larger than the strongest RB-SiC made in labs, in addition to some unreacted carbon identified using TEM [177]. It is generally an inferior material.

The works of Corelli, Carey, Harrison and Malloy at Rensselaer Polytechnic Institute included some samples doped with 0.3 wt% boron so that their interaction with neutrons produced helium to simulate helium formation in fusion environments [173,176,177]. No other research has been done using boron doping to simulate helium formation in RB-SiC to compare to these results. Although an elegant way to introduce helium to the material, the samples doped with Boron during manufacturing were weaker, 234 MPa fracture strength at 1200°C rather than 270 MPa for un-doped NC-430 as it segregated to grain boundaries [176]. No room temperature strength is given.

REFEL SiC tested in-reactor at the Windscale AGR showed a temperature dependent reduction in strength shown in Table 2-4 below. The irradiated material shows an increase in strength with high temperature testing which could be attributed to annealing [170].

Table 2-4: Temperature dependent bending strengths (MPa) of irradiated REFEL [170]

Irradiation temperature (°C)	**Measurement temperature (°C)**				
	Room	**500**	**620**	**1100**	**1300**
Unirradiated	517	469		482	525
530 ± 20	362	320			
640 ± 20	331		354		
1120 ± 40	346			353	
1200-1400	320		320	334	367

The high quality SE-10 reaction-bonded SiC used by Iseki *et al.* compares favourably to other forms of commercially available monolithic SiC in strength as shown in Table 2-5 below [178]. Of concern is the wide standard deviation after irradiation, and reduction of Weibull modulus. This was found in all other work on RB-SiC, even in samples which had previously been proof-tested to remove the weakest in the Weibull distribution before irradiation [175].

Table 2-5: Room temperature mean fracture strengths of monolithic SiC before and after irradiation. (MPa) from Iseki et al.[178]

Material	**RB-SiC**	**Direct sintered**	**Hot pressed**
Before irradiation	530	430	360
Standard deviation	28	34	28
After irradiation (6×10^{24} n/m^2 at 640 °C)	370	350	390
Standard deviation	61	15	19
% change	-30	-20	+10

The reduction in strength is attributed to microcracks forming in the SiC-Si interface [173,174,176–178], although Matheney *et al.* did not observe these [172], nor did Liu *et al.* in the ion-irradiated samples [179]. The microcracking was observed using TEM, which neither of these studies used. The formation of microcracks is to accommodate the differential swelling between SiC and silicon. Matthews found that the SiC lattice parameter expanded 0.36% after irradiation while Si expanded by 0.04%. [171] Higher dislocation densities have been observed in SiC at SiC-Si interfaces caused by this differential swelling [177,178]. In Harrison and Corelli's experiments they claim dislocations are trapping sites for helium formed from boron, which stops helium coalescing into grain boundary bubbles as observed in other forms of SiC [177]. Iseki *et al.* did not have boron in their samples but consider that helium will pin dislocations reducing recombination by interstitial diffusion during annealing. They observed improved toughness after irradiation, which decreased after annealing in sintered SiC samples. This was attributed to increased dislocation density from radiation-induced dislocation loops allowing more plastic deformation at crack tips [178].

Studies of fracture surfaces show no significant change after irradiation. Fracture of large α-SiC grains remains transgranular, while fracture in residual silicon and small β-SiC grains remain intergranular [176]. Matthews identified silicon as the crack initiation site on a fracture surface of neutron irradiated RB-SiC which is the origin of SiC-Si microcracking as the cause of failure in RB-SiC [171].

Thermal conductivity decreases due to phonon scattering from defects: dislocations, stacking faults and vacancies [176]. It saturates after a dose of 4×10^{24} n/m^2 at 200 °C at 30% of the starting thermal conductivity in NC-430 [174], while REFEL saturates at half the thermal conductivity at a similar dose of about 10^{25} n/m^2 at the more relevant temperature of 800-1000 °C [170]. At higher temperatures, annealing brings thermal conductivity back towards unirradiated values as seen in Figure 2-23 [170]. At the proposed operating temperature of 800-1000 °C, thermal conductivity is just about over the recommendation from Table 1-1.

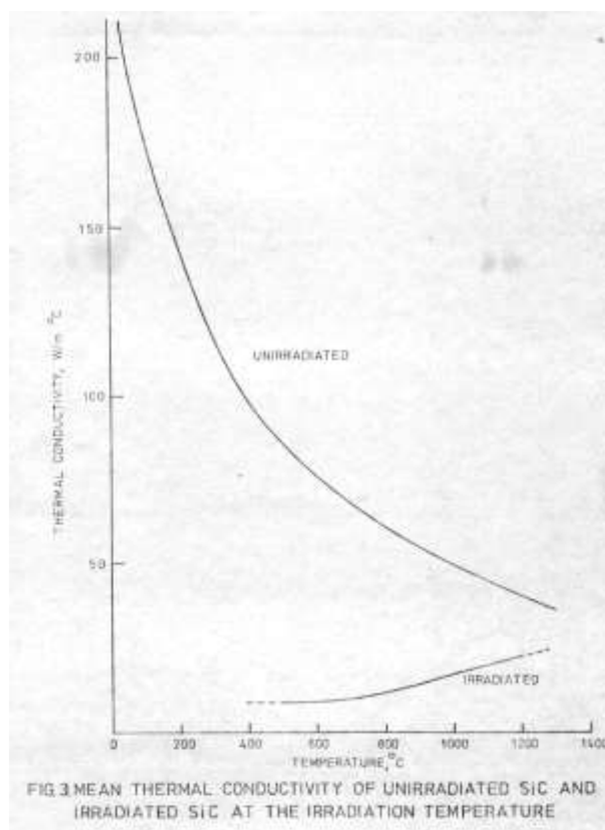

Figure 2-23: Thermal conductivity with temperature for unirradiated and irradiated REFEL [170]

Swelling of the samples saturates after a neutron fluence around 5×10^{24} n/m^3 [173,174,176]. In NC-430 samples without boron doping, swelling saturated at 1.5%, but samples with boron swelled by 7% volumetrically [173,174,176]. This is attributed to helium bubble formation as the expansion of α-SiC lattice parameter alone is much smaller.

Harrison and Corelli measured the volumetric lattice expansion after 30 minutes annealing at 1200°C as between 0.5-1.0% depending on dose, and Matthews measured ~1.2% volumetric expansion on the lower dose in his work before annealing [171,177]. Also before annealing, Iseki *et al.* found volumetric expansion of 1.5% with 280°C irradiation, while volumetric swelling reduced to 0.66% at 640°C even with almost an order of magnitude higher dose [178]. At the operating temperature of a fusion reactor, the saturation swelling will probably be less than reported here as temperature is dominant over increased dose. With annealing above the irradiation temperature, the volume can approach pre-irradiation values [178]. These swelling amounts are less than hot pressed SiC, and pressureless sintered SiC irradiated in the same conditions.

The recent study by Liu *et al.* shows a renewed interest in reaction bonded SiC for nuclear applications. In contrast to all other studies they used 2 MeV Au^{2+} ions at room temperature to irradiate their sample to amorphisation [179]. This is a fundamentally different damage mechanism to neutron irradiation, so comparison to the other papers is difficult. One of their conclusions is that RB-SiC is half as resistant to amorphisation relative to sintered polycrystalline SiC, with a critical dose of 0.1244 dpa compared to 0.25 dpa. They claim it is due to excess silicon atoms.

The radiation response of RB-SiC strongly depends on the starting material, and this has perhaps unfairly meant it has been dismissed as a nuclear material. Norton NC-430 which is most widely studied, and the self-made material by Matthews is poor quality, but has the most citations in the literature. The high-quality REFEL and SE-10 grades of RB-SiC are better starting materials and respond favourably compared to other forms of monolithic SiC to neutron irradiation.

2.3 Micromechanical testing

The intention of ion implantation is to replicate the properties of neutron irradiation in a quicker, controlled manner without activating the samples, allowing faster screening and development of new materials. Unfortunately, only a thin damaged layer is available for studying mechanical properties, so researchers are constrained to using micromechanical techniques. Since researchers with access to neutron irradiated samples are not constrained to micromechanical testing, they tend to use macroscopic tests which conform to engineering standards. In the case of ceramics, material strength is a function of specimen size through the Weibull relationship, so statistically relevant macroscopic testing needs to be carried out. This means there is very little literature of nanoindented neutron irradiated SiC to compare ion irradiations to, and what literature is available of neutron and ion irradiated SiC varies widely in terms of temperatures and doses. All nanoindentation measurements in the literature have been conducted at room temperature using Berkovich geometry indenters.

2.3.1 Nanoindentation of irradiated SiC

Literature data from ion and neutron irradiated SiC is summarised below, with all graphs using percentage mean hardening to normalise for different nanoindentation protocols and the unirradiated values of hardness. No results of amorphous SiC are included. The details of nanoindentation measurements are varied – some with full details of tip calibrations, measurement depths, and errors, others with no detail at all. Where errors are provided in the literature these have been replicated in the graphs here. Most unirradiated hardness values converge on ~38 GPa as the nanoindentation hardness of SiC with the exception of Kerbiriou *et al.* who measure 51 GPa for unirradiated 6H-SiC [180]. The large difference in this measurement puts their other measurements in doubt as it is

left unexplained. Doses are plotted on $\log_{10}$ axes to help differentiate similar dose experiments. Temperatures are the mean irradiation temperatures.

Three researchers have published nanoindentation results of neutron irradiated SiC summarised in Figure 2-24. Osborne [181] and Nogami [182] used CVD 3C-SiC samples as a surrogate for the matrix of CVI SiC_f/SiC composites while Chen [166] used 6H-SiC single crystals as part of their comparison with ion implantation. Osborne found that hardening saturated by ~1 dpa but was higher at 500 °C due to growth of interstitial dislocation loops. Nogami *et al.* meanwhile found no dependence on hardening with temperature above 100 °C. Chen *et al.* observed no hardening in their neutron irradiated samples at 0.1 and 0.2 dpa at ~50 °C. This result will be discussed in more detail below. It is worth pointing out that Osborne and Nogami's work is from the early days of nanoindentation. Nogami's measurements come with very large standard deviation error bars which significantly overlap the unirradiated hardness values (Figure 2-25).

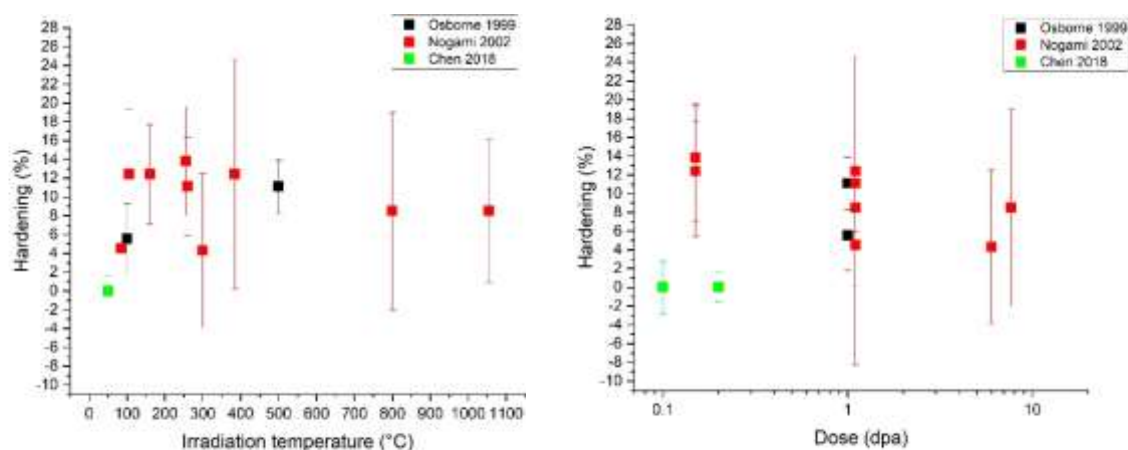

Figure 2-24: Literature values of nanoindentation hardening of neutron irradiated SiC. Data from [166,181,182]

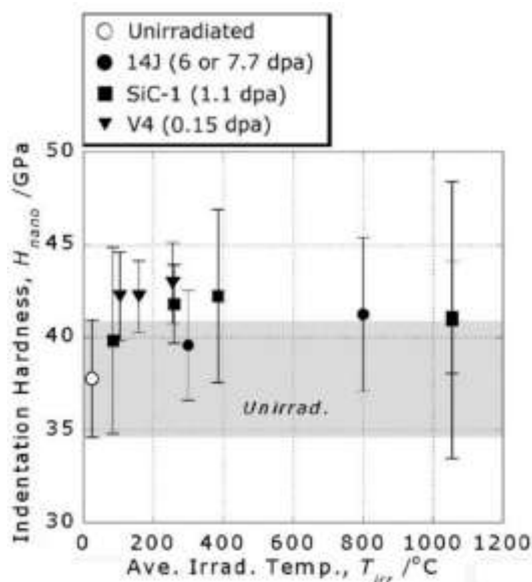

Figure 2-25: Nanoindentation hardness from Nogami et al. [182] *note the large error bars overlapping unirradiated hardness.*

Nanoindentation hardening at ~1 dpa as a function of temperature is shown in Figure 2-26 for neutrons and argon ions [183]. Hardening increases with temperature up to ~500°C then appears to fall due to enhanced defect recovery. With only one 1 dpa data point for ions it is difficult to spot if it fits the trend.

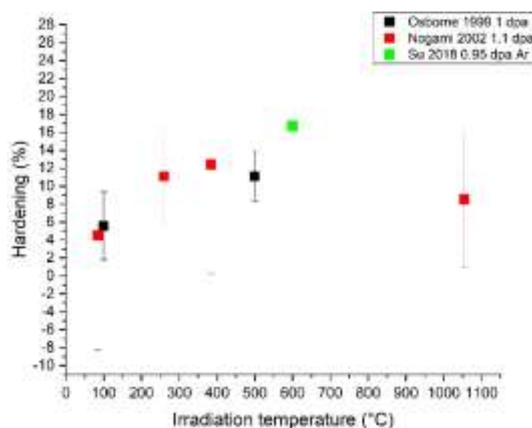

Figure 2-26: Nanoindentation hardening with temperature ~1dpa for neutrons and Argon ions

To extend the comparison of neutrons vs ions, all hardening data is summarised in Figure 2-27. Unfortunately, most ion implantations have been carried out at room temperature to study amorphisation – in these cases the data points presented are the highest dose measurements taken before amorphisation which should be approximately the

maximum radiation defect damage at temperatures above the critical amorphisation temperature. The initial observation is that ion implantation causes more hardening than neutrons for comparable temperatures and doses. Data from Kerbiriou *et al.* is circled as it may show deceptively low hardening due to their high unirradiated hardness value [180]. The purple and blue arrows are data points from Su *et al.* [183] which are at a reactor-relevant temperature. Their explanation for less hardening with a higher dose was that the high dose sample was held at 600 °C for a longer time to maintain the same dose rate, so it annealed more. This seems conflicting as dynamic defect annealing should be independent of time if damage has saturated and the dose rate is the same. If damage has not saturated, the higher dose should cause more hardening.

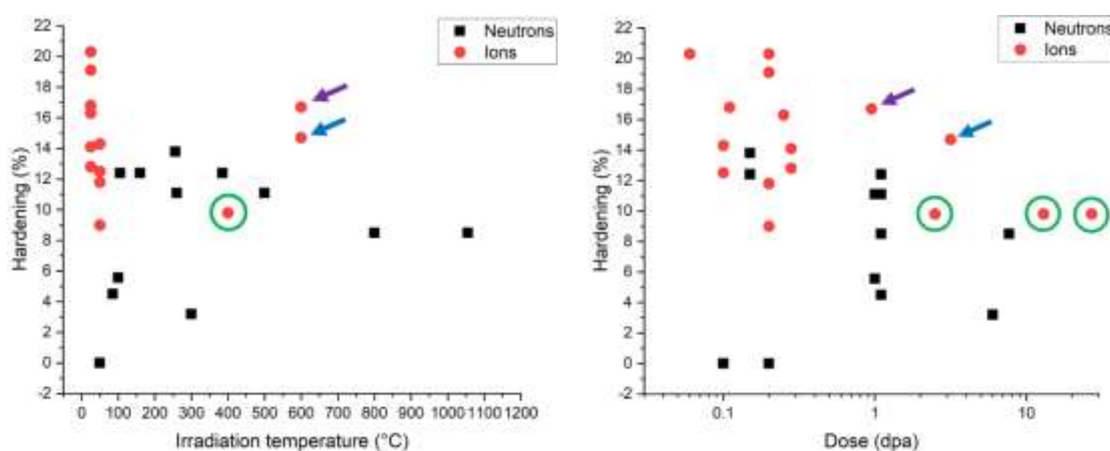

Figure 2-27: Hardening comparisons between neutron and ion irradiations. Measurements from Kerbiriou with very high unirradiated values are circled. Purple and blue arrows indicate corresponding data points from Su et al. [183]

Hardening from ion implantation as a function of dose or temperature and grouped by ion species is shown in Figure 2-28 with data from refs. [166,180,183–186]. Variation in hardening may be attributable to ion species, although no clear trend is apparent in this figure, perhaps due to variation in different researcher's techniques.

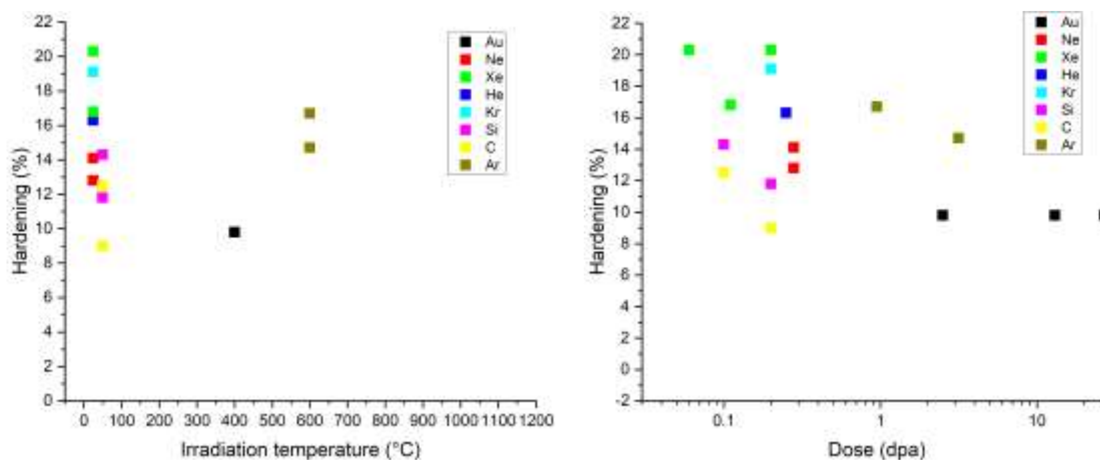

Figure 2-28: Hardening as a function of temperature and dose for ion implantations with different ions.

Yang *et al.* [186] have conducted systematic experiments comparing the effects of different ion species on nanohardness of irradiated SiC. Unfortunately, these experiments were conducted at low temperatures to study amorphisation so the highest dose before amorphisation is presented. The experimental nanoindentation methodology should be the same allowing reliable comparisons.

Table 2-6: Hardening for different inert gas ions implanted into 6H-SiC at room temperature from [186]. *The maximum dose before amorphisation is presented*

	He (0.25 dpa)	**Ne (0.28 dpa)**	**Kr (0.2 dpa)**	**Xe (0.11 dpa)**
Hardening	16.3%	12.8%	19.1%	16.8%

Chen *et al.* [166] conducted self-ion implantations to the same dose and at the same temperature as neutron irradiated 6H-SiC. They find no change in hardness of neutron irradiated SiC, but large changes with ion implantation which they explain by lateral residual stresses caused by constrained swelling. Comparing self-ions to inert gas ions at similar doses in Table 2-6, it appears that heavier ions cause more hardening than the neon ions which are intermediate in mass between carbon and silicon. Helium ion implantation appears to cause more hardening than its low mass would suggest based on this trend, but it may be due to helium stabilising different defects as discussed in reference [147] and also seen in tungsten [187].

Table 2-7: Nanoindentation hardening and modulus changes for neutron and self-ion irradiated 6H-SiC [166]

	n 0.1 dpa	Si 0.1 dpa	C 0.1 dpa	n 0.2 dpa	Si 0.2 dpa	C 0.2 dpa
Hardness	0	+14.3%	+12.5%	0	+11.8%	+9%
Modulus	-10.1%	-0.7%	-3%	-15.9%	-6.9%	-10.4%

Chen *et al.* [166] are one of the only groups to report on changes to elastic modulus, finding a large decrease with neutron irradiation and a much smaller decrease with ion implantation (Table 2-7). Their reduction in modulus for neutron irradiation is comparable to the reduction in modulus from Nogami *et al.* (Figure 2-29) [182]. Elastic modulus is reduced less at higher irradiation temperatures, and is similar to the unirradiated value when irradiated above 1000 °C. Nogami *et al.* found that the reduction in elastic modulus is linearly related to swelling in the point defect swelling regime. Chen *et al.* explain their small reduction in elastic modulus after ion implantation as being due to constrained swelling. As modulus is physically related to interatomic bond strength, bond density, and bond length, if swelling is reduced the change in elastic modulus should also be smaller. The modulus change is not related to constrained swelling stress, but to changes in bond length.

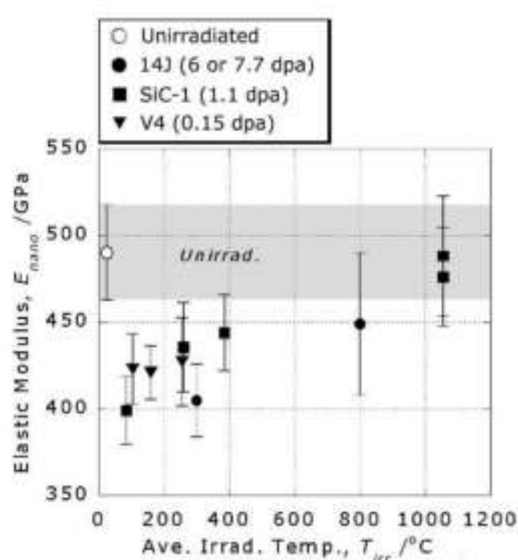

Figure 2-29: Elastic modulus as a function of temperature for neutron irradiated SiC from Nogami et al. [182]. *The legend refers to different neutron irradiation experiments*

Fracture toughness from nanoindentation of neutron irradiated SiC was measured by Nogami [182] and for ion irradiated SiC by Jiang [188]. Nogami found an unirradiated fracture toughness of 5.08 MPa√m which is approximately twice as high as the generally accepted fracture toughness of SiC. They attribute this to errors measuring crack length, but this seems insufficient to explain such a big error. They also use an equation derived for Vickers indents with some values from Vickers indentation, and some from Berkovich nanoindentation, which seems to be a bigger source of error. Although their values are likely to be incorrect, they find a decrease in fracture toughness with low temperature neutron irradiations, but an increase with irradiations above 800 °C (Figure 2-30). They attribute the increase in toughness at high temperatures to radiation induced dislocations and enhanced plasticity, or crack deflection or blunting from defect clusters, but do not explain the low temperature loss of toughness. At low temperatures defects are less mobile and do not form large mobile dislocation loops which may explain the lower fracture toughness.

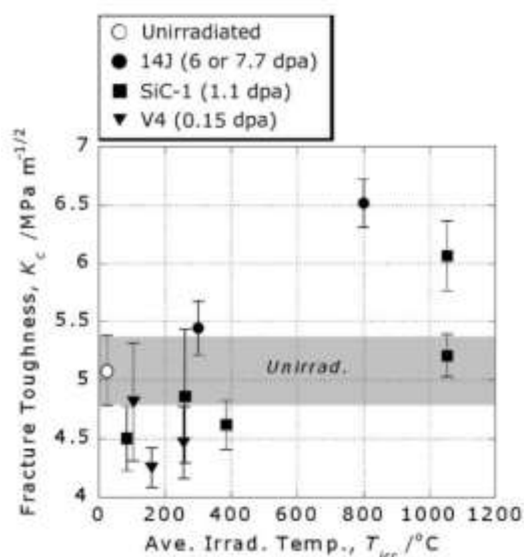

Figure 2-30: Indentation fracture toughness of neutron irradiated CVD SiC. Values are likely to be incorrect, but a reduction in fracture toughness with low temperature irradiation, and an increase in toughness at high temperatures can be seen [182].

Jiang *et al.* report fracture toughness of room temperature Xe ion implanted 4H-SiC, and the variation of strain (Figure 2-31) [188]. The toughness increases with dose up until amorphisation. It also increases with elastic out of plane strain. The authors explain this toughening as due to lateral compressive strain in the damaged layer. They do not say which equation is used in estimating fracture toughness, so the values may not be comparable to this work. A lateral residual stress should have an enormous effect on measured fracture toughness.

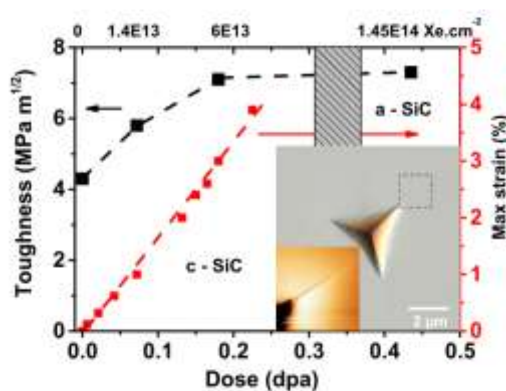

Figure 2-31: Nanoindentation fracture toughness and out of plane strain of room temperature Xe implanted SiC. The dashed box marks amorphisation [188]

To summarise, neutron irradiations appear to cause less hardening but a larger reduction in modulus than ion implantations. However, nanoindentation measurements of irradiated SiC appear to vary widely with differing reliability due to lack of experimental detail. Most of the ion implantations have been conducted at room temperature rather than reactor-relevant temperatures which may induce different radiation defect structures. Recent work comparing ions and neutrons is more useful, but until high temperature ion implantations are carried out in conjunction with complementary measurements of neutron irradiated SiC it is impossible to know if ion implantation can replicate neutron irradiation changes to micromechanical properties in SiC.

2.4 Residual stress measurements

2.4.1 Raman spectroscopy of RB-SiC

Two groups have previously studied processing-induced residual stresses in reaction-bonded SiC and melt infiltrated SiC_f/SiC composites using Raman piezo-spectroscopy. However, they obtained contradictory results. The work by Jannotti *et al.* found a tensile residual stress in silicon regions of reaction-bonded SiC and a compressive stress in reaction-bonded B_4C [189]. Their interpretation was based on thermal expansion mismatch between the phases with silicon having a smaller thermal expansion than SiC so would be placed into tension upon cooling, consistent with their experimental results. The average tensile stress in silicon was 240 MPa. This work used a 100x objective lens, allowing peak shift to be spatially mapped, showing a distribution where the edges of silicon regions were in less tension than the centre of the silicon regions, and in some geometries went into compression (Figure 2-32).

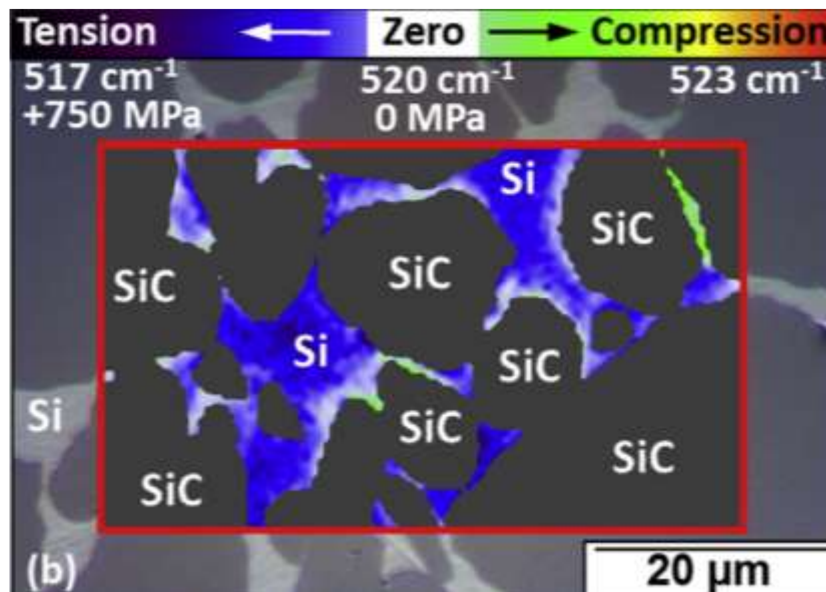

Figure 2-32: Residual stress map in silicon regions of RB-SiC [189]

The work by Wing *et al.* conversely finds a compressive residual stress in the silicon regions, averaging -1.8 GPa. [190,191]. Thermal expansion mismatch alone is

insufficient to cause residual stresses of the magnitude measured. Silicon is known to expand by 11% upon crystallisation, which when included in their modelling is enough to cause stresses of the magnitude measured by Raman piezospectroscopy. These measurements were made with a 20x objective, so were not spatially resolved, but provide an average of the stress in the volume covered by the laser spot, covering several silicon regions and SiC grains.

While Wing *et al.* give details of their peak fitting technique [190,191], no details are given in the paper by Jannotti *et al.* [189]. The individual spectra they give for the residual silicon phase shows significant asymmetry consistent with Fano resonances [192] caused by impurities. This makes the peak difficult to fit using the Renishaw Wire software used in their work, and from experience, the peak position is dragged to lower (tensile) wavenumbers during peak fitting of these asymmetric peaks. The silicon spectra from the materials studied by Wing *et al.* are symmetrical as with pure silicon, and the peak fitting curves appear a good fit [190,191].

2.4.2 SEM digital image correlation

Recent developments in FIB-SEM (dual focussed ion beam and scanning electron microscope) technology have allowed the miniaturisation of macroscale residual stress measurement techniques [193]. Ring-core drilling combined with digital image correlation (DIC) is similar to the micropillar swelling DIC used in this work (section 4.5.5) and will be outlined below.

Lunt and Korsunsky have published extensively on FIB ring-core DIC for residual stress measurement and the reader is referred to their articles for comprehensive details of the technique [193–196]. Briefly, a speckle pattern is applied to a region of interest (ROI) on a scale of a few microns, then an annular ring is milled to create a shallow micropillar.

Tracking the position of the speckles allows the strain tensor to be calculated as a function of milled depth as lateral strain is relieved. This allows the in-plane strain tensor to be calculated on the scale of microstructural features. This is an in-situ technique where the main sources of error are drift in the SEM, strain induced by FIB damage, and redeposition of FIB milled material onto the DIC surface [193]. This technique appears to still be in the development stages rather than being a routine tool. Displacement caused by image drift is inherently corrected in strain measurements using DIC as the technique tracks relative position of markers rather than absolute positions.

In-situ FIB-SEM DIC reduces error as the SEM settings can remain constant during the experiment. Ex-situ or long duration SEM DIC introduces additional error as microscope conditions can change over time [197]. Mello *et al.* recently published on the best practices for minimising errors between microscopy sessions [197]. In particular, the nominal SEM magnification may not be accurate. The main correction procedure they propose is to use a certified reference grid to calibrate the magnification of the acquired images without having to calibrate the microscope. Additionally, this reference grid can be used to generate a correction strain tensor to account for microscope distortions. This can be applied on top of DIC strain fields acquired in different SEM sessions. Unfortunately, this protocol was published after the DIC experiment in this work was conducted, but it should be followed in any subsequent long duration, or ex-situ SEM-DIC measurements.

2.4.3 Microcantilever deflection and ion beam layer removal

Surface strains can be measured in the SEM by DIC to calculate residual stresses with a planar tensor. The depth dimension of residual stress distribution is important to investigate in the context of multilayer thin films for the electronics industry or coatings for mechanical applications. By analogy, ion irradiated samples in this work can be crudely considered as a thin film on a substrate. Pippan and co-workers have developed the ion

beam layer removal (ILR) method which is described in detail in their papers, but will be discussed here in the context of bending microcantilevers (section 4.5.4) [198–200]. A rectangular cross-section cantilever is cut at the edge of a specimen containing depth varying residual stresses. The cantilever will bend upwards for a tensile residual stress in the surface, or downwards for a compressive residual surface stress. Subsequent thinning of a section of the cantilever causes deflections up and down depending on the stress profile of the layers. By measuring deflection of the cantilever as a function of milled depth, and with knowledge of the layer thicknesses and material properties, the depth profile of residual stress in the cantilever can be calculated analytically using Euler-Bernouli beam equations (Figure 2-33).

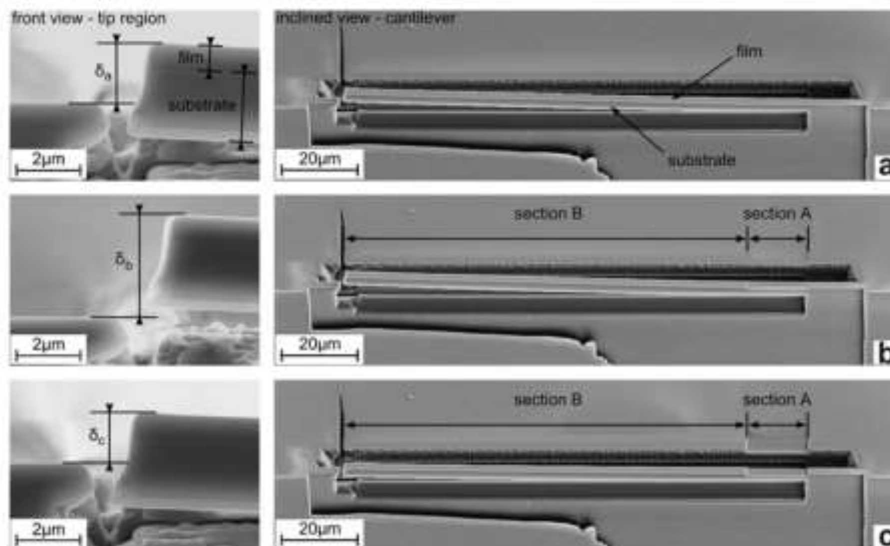

Figure 2-33: Outline of the IBL method from ref. [199]. *(a) rectangular cross-section cantilever is released by cutting off the end and deflects upwards due to tensile residual stress in the film. (b) & (c) An area (section A) of the cantilever is thinned and the deflection of the cantilever as a function of thinned depth is measured.*

The group at Leoben have optimised their sample processing to create rectangular cross-section cantilevers which greatly simplifies analytical calculations. The process uses an ion slicer and a masked area to remove a large area of material, however it requires a larger specimen and loses the ability to microscopically target cantilever fabrication [201]. The analytical calculation of residual stresses simplifies the situation by ignoring the relaxation of the cantilever base and across the cantilever width. This relaxation was found

to significantly reduce (~16%) the stresses within the cantilever compared to the unaffected base when the stresses were calculated using a finite element model including an elastic base, rather than analytically with a fixed cantilever end [201]. Since the stress distribution in the original material is of interest rather than the stress distribution in the cantilever, the reported stresses should be taken away from the region affected by stress relief i.e. in the cantilever base. This is quite routinely possible using finite element methods whereas an analytical calculation would quickly become complicated.

2.5 Summary of literature and problems to solve

While the community has investigated radiation effects in silicon carbide for decades, it has been done inconsistently, with different materials being studied in different radiation conditions using different techniques. This thesis (along with other researchers in the MFFP group) aims to investigate different types of SiC in the same ion irradiation conditions, namely single crystal and RB-SiC (this thesis), sintered SiC (Helen Pratt DPhil thesis), and SiC_f/SiC composite (Helen Pratt and Dr Yevhen Zayachuk).

Existing experimental literature appears to have focussed on presenting material properties and changes to these properties with little explanation as to *why* these changes occur. Underlying mechanisms are discussed in modelling literature, but are limited by the lack of experimental validation.

The aerospace and military armour literature identified that residual stresses can control the properties of ceramics. This has not significantly been discussed in the nuclear materials publications, so this will be investigated in more detail, along with the effects of radiation damage on residual stress. Once the effects of radiation damage on residual stress have been identified, it may be possible to engineer the microstructure to make a more radiation tolerant material by adjusting the secondary phase or grain size.

A significant challenge to using nuclear grade SiC is manufacturing, both making large complex components, and joining these into a machine. The premise of this research is to bypass this problem by using reaction-bonded SiC where these challenges have been solved or are more easily solvable. The challenge here is the lack of nuclear relevant knowledge of this material, which this thesis aims to contribute to. The aim is to understand the role of RB-SiC microstructure on mechanical properties and the radiation-induced changes to these properties. As well as identifying and measuring these changes, this thesis intends to explain why these changes occur.

Chemical defects in SiC are important and recent literature on Raman spectroscopy has begun to explore these in detail. An area which has not been investigated sufficiently is the chemical effect of ion implantation species which will be explored here.

While not intentionally investigated in this research, corrosion of SiC remains to be explored more by the community, in particular the combined effects of radiation damage plus a corrosive environment.

3 Materials

3.1 Commercially available materials

Two commercially available forms of RB-SiC were studied. REFEL (**Re**actor **F**uel **El**ement) SiC obtained from Goodfellow UK, and produced by TENMAT Advanced Materials Ltd. Representative samples of "StarCeram Si" manufactured by H.C. Starck Ceramics GmbH were obtained from Dr Nikolaos Katsikis.

The processing for both these materials is commercially sensitive, so the processing variables are not available to be investigated in detail here. Historic literature has investigated the processing of REFEL when it was a newly invented material, but it is not clear if the processing conditions will have changed. The microstructure of this REFEL sample appears to be the same as REFEL samples studied in the literature, apart from the special REFEL samples studied by Sawyer and Page [87]. The REFEL sample is made by extrusion of the green body into a 10 mm diameter rod, while the Starceram Si samples were cut from a sheet initially made by uniaxial pressing.

3.2 Self-made materials

3.2.1 Conventional RB-SiC

36 batches of slurry were mixed, then pressed or slip-cast in various conditions followed by melt infiltration with silicon to make 28 reacted bodies. Some green bodies were too weak and broke before they could be melt-infiltrated. Most of these reacted bodies were very porous and crumbly, but after iterative improvements a sample with useful regions for ion implantation and micromechanical testing was made following the recipe below:

Materials

1. Combine 63 wt% SiC powder (600 grit, d_{50} = 10.6 μm, H.C. Starck Gmbh) with 20 wt% carbon black (17 nm particle size, 200 m^2/g surface area, Monarch M700 Cabot corporation) and 17 wt% maple syrup (Sainsburys) in a ball milling bottle with ethanol and zirconia milling media.
2. Mill overnight (~20 hours).
3. Evaporate ethanol in a rotary evaporator to extract dried friable powder
4. Grind the extracted powder in a pestle and mortar and sieve the powder to break up agglomerates
5. Uniaxially press the powder at 100 MPa into discs
6. Line a lidded alumina crucible with graphite paper then coat with boron nitride spray.
7. Place the disc in the crucible on a bed of silicon powder (Silgrain HQ, Elkem ASA) then cover with excess silicon powder. The mass of silicon powder was ~1.4x the mass of the green body.
8. Melt infiltrate the silicon in 2.2×10^{-5} mbar vacuum at 1480 °C with a dwell time of 30 minutes before cooling
9. Brush off excess silicon

This recipe is based on the report by Phillips and Hutchings for the Atomic Energy of Canada Ltd. who tested various process parameters, in particular binders [101]. They found maple syrup to be the best binder, even compared to more conventional binders such as phenolic resins and other polymers. This is not entirely unreasonable as modern industrially produced Starceram RB-SiC uses a sugar/cellulose based binder and carbon source [202].

To make the residual silicon suitable for Raman stress mapping, Silgrain HQ was used which has a low impurity content based on the manufacturer’s data sheet. Elkem are

the main supplier of industrial silicon powder used for reactive melt infiltration so should make RB-SiC representative of industrially manufacturable materials. The Silgrain HQ grade is more expensive than the standard Silgrain CG grade which would typically be used commercially which has 99.6 wt% silicon. Since these experiments, Elkem now manufacture Silgrain Supreme with 99.995 wt% silicon which would have been more appropriate for these experiments.

Table 3-1: Typical impurity content of Elkem Silgrain HQ

	Si	**Fe**	**Al**	**Ca**	**Ti**	**P**	**B**
wt%	99.8	0.04	0.09	0.013	0.001	25 ppmw	30 ppmw

This recipe made a sample with dense regions of material suitable for ion implantation and micromechanical testing, but macroscopic residual porosity remained in the centre of the reacted disc.

3.2.2 Metal-silicide RB-SiC

One method to improve properties of RB-SiC discussed in the literature is to replace residual silicon with a metal silicide phase [14,73,75,203,204]. For application in a fusion environment, low activation silicides were chosen based on tungsten, chromium, and titanium [84].

These samples were processed in the Yano-Yoshida labs at Tokyo Institute of Technology based on their experience of melt infiltrating SiC with various metal silicides [18,73]. The recipe for the samples of WSi_2-Si and $CrSi_2$ RB-SiC is different to the recipe used in Oxford and is based on the materials and equipment in the lab at Tokyo Institute of Technology. No successful samples containing titanium were made. They were all cracked or exploded during the melt infiltration step (Figure 3-1 (a)). Several samples of Cr and W containing RB-SiC were processed using various conditions, but none were very

successful, containing lots of residual porosity or limited infiltration of the melted alloy. The recipes for the two samples which were tested further are outlined below, but neither sample was optimised to create materials suitable for bulk testing.

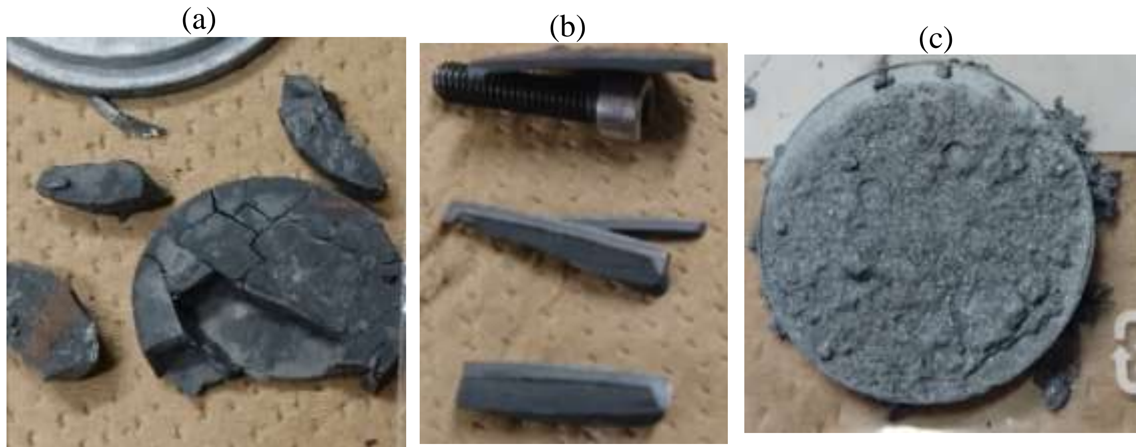

Figure 3-1: Samples after heat treatment (a) Si-Ti sample cracked and not infiltrated. (b) Si-Cr sample partially infiltrated, otherwise unreacted. (c) Si-W sample was intact and solidified powder was brushed off.

Green bodies were made by slip-casting 25 mm diameter disks from a slurry consisting of α-SiC powder (d_{50} 3 μm or 7.9 μm Fujimi Kenmazai Kogyo Co.,Ltd, Nagoya, Japan) with 20 wt% carbon black (80 nm, Asahi Carbon Co, Ltd) ultrasonically dispersed in distilled water with 2 wt% polyethyleneimine binder/cationic dispersant (PEI, MW ~10000, Wako Pure Chemical Industries, Ltd, Japan). These bodies were covered in powdered near-eutectic alloys of Si-13.2 at% Cr, and Si-4.4 at% W, prepared by vacuum arc melting pure metals (Si lump 99.99 %, Cr lump 99.95 %, and W lump 99.95 %, Goodfellow Cambridge Ltd, UK). Powder covered bodies were melt infiltrated inside BN coated graphite crucibles in a graphite resistance heated furnace (Fujidempa Hi-multi 5000) at 1500 ºC for the Si-Cr alloy, and 1700 ºC for the Si-W alloy, with holding times of 15 minutes, and heating rate of 20 ºC/min followed by furnace cooling. Phase diagrams for these alloys are given in Appendix 8.2. At these eutectic alloy compositions, the resulting phase consists of silicon plus $Cr(W)Si_2$. During the reactive melt infiltration silicon will react with carbon to form SiC. On cooling the remaining silicon will solidify

with a metal disilicide. The proportion of residual silicon and metal disilicide will depend on how much silicon us consumed by the reaction with carbon, and how much evaporates in the furnace.

Most samples made with Si-Cr alloy were un-infiltrated and cracked during processing, only one sample had partial infiltration, shown in Figure 3-1 (b), and was fairly dense and well reacted in the infiltrated region. Si-W infiltrated through the thickness of the sample but left behind some local porosity. Their microstructures will be discussed more in results section 5.1.2.

3.3 Summary of RB-SiC materials studied

Material name	**Notes**
REFEL	Commercially available from Tenmat. Highly connected SiC. Isolated silicon regions.
Starceram Si	Commercially available from H.C.Starck. Large isolated SiC grains. Continuous silicon with a dispersion of fine SiC grains.
In-house RB-SiC	In-house RB-SiC. Isolated fine grains in continuous silicon.
WSi_2-Si RB-SiC	In-house RB-SiC. Highly connected SiC. Isolated silicon and WSi_2.
$CrSi_2$-RB-SiC	In-house RB-SiC. Highly connected SiC. Isolated $CrSi_2$.

Representative optical micrographs of conventional RB-SiC are given in Figure 3-2 to show variation in grain size and silicon connectivity and how the different microstructures are complementary to this investigation.

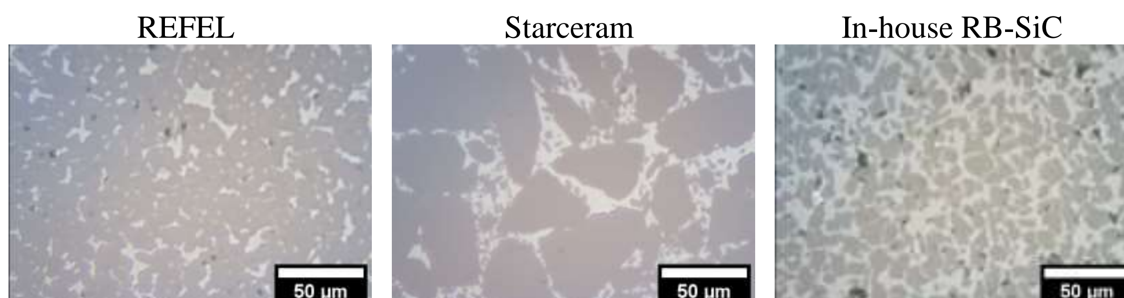

Figure 3-2: Optical micrographs of conventional RB-SiC taken with x20 objective

4 Methods

4.1 Specimen preparation

Small specimens of the sample materials were prepared for analysis from larger pieces, first by cutting using diamond saws, either a Buehler Isomet 5000 with a LC25 blade, or a Cayex Capco annular diamond saw depending on the geometry of the piece being cut. Typical sample sizes were approximately 10 mm × 5 mm × 3mm.

Cut specimens were mounted for grinding and polishing using a hot plate and wax, with several pieces of the same thickness mounted on one aluminium polishing holder to ensure uniform thickness and to minimise bevelling. The wax was piled up so that no sharp edges or corners of the samples were protruding to prevent damage to the polishing cloths.

Before the first stage of grinding, the specimens were coated in permanent marker so that it was visible when they had been ground flat and parallel as all the marker would be removed. Both sides of the specimens were ground flat and parallel so that a good contact could be made with specimen stubs for nanoindentation and microscopy, and a good thermal and mechanical contact could be made to the sample holders used for ion implantation.

The sequence of grinding and polishing was:

1. 55 µm diamond impregnated grinding disk with water
2. 35 µm diamond impregnated grinding disk with water
3. 15 µm diamond impregnated grinding disk with water
4. 9 µm diamond suspension sprayed on a Verdutex cloth dampened with water
5. 6 µm diamond suspension sprayed on a Verdutex cloth dampened with water
6. 3 µm diamond suspension sprayed on a Verdutex cloth dampened with water

7. 1 μm diamond suspension sprayed on a Verdutex cloth dampened with water
8. ¼ μm diamond suspension sprayed on a Verdutex cloth dampened with water

After each step the specimens were inspected with an optical microscope to see if scratches were aligned or removed. After ¼ μm diamond the optical finish was good, and microstructure was clearly visible in the SEM. Generally, EBSD patterns were acceptable. Attempts to improve EBSD pattern quality using ion polishing in a Gatan PECS (precision etching coating system) resulted in preferential etching of silicon which exposed the edges of SiC grains which milled preferentially, leading to unacceptable surface topology changes (Figure 4-1).

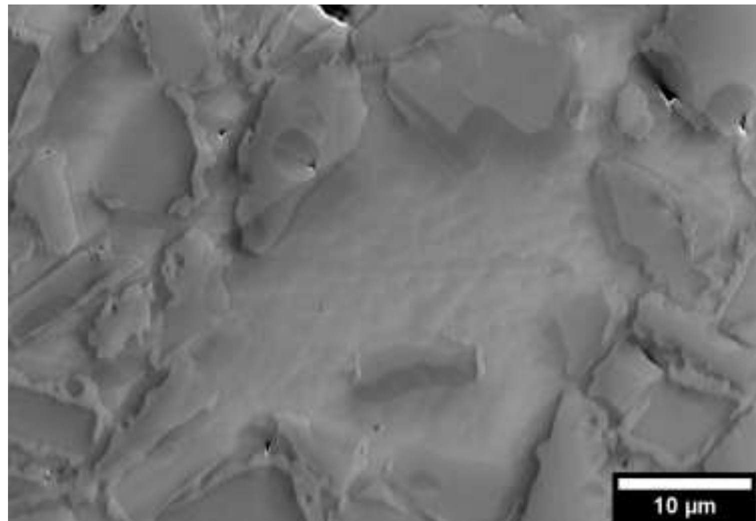

Figure 4-1: REFEL sample after PECS etching for 30 minutes with 3 kV 3°. Silicon was etched faster and exposed edges of SiC grains which were then etched quickly (SEM SE)

Single crystal (0001) 6H-SiC samples were obtained from Pi-Kem Ltd. already polished to an acceptable standard for all types of analysis. Small pieces were cleaved from larger samples using a diamond tipped scribe.

For nanoindentation, optical/Raman microscopy, and AFM, specimens were mounted on 12.5 mm aluminium stubs using Quickstick 135 mounting wax from South Bay Technology. The hot plate was set to 150°C and each sample was heated for less than 1 minute. No radiation damage annealing effects should occur in these conditions as it is

well below the irradiation temperature. For electron microscopy, samples were fixed to 12.5 mm aluminium stubs using conductive silver paint to ensure a conductive path to ground preventing charging.

4.2 Ion implantation

High energy ion implantation was used to introduce displacement damage to samples as a surrogate for neutron irradiation. Five sets of implantations were carried out:

	0.25 dpa Si+	2.5 dpa Si+	2.5 dpa Ne+
300 °C	✓	✓	✓
750 °C	✓	✓	×

The implantations were carried out at the Surrey Ion Beam Centre using the 2 MV Van de Graaff high energy implanter. The beam was scanned over a 75mm diameter area of a temperature-controlled stage on which the samples were mechanically mounted. Figure 4-2 shows the samples, sample rails, and sample plate of one of the implantation experiments. Washers and screws were used to clamp the samples to sample rails, ensuring part of the sample was blanked from the ion beam for post-irradiation analysis. Annealed copper washers were used to accommodate thermal expansion mismatch to avoid samples becoming loose and falling off or being overtightened and fracturing.

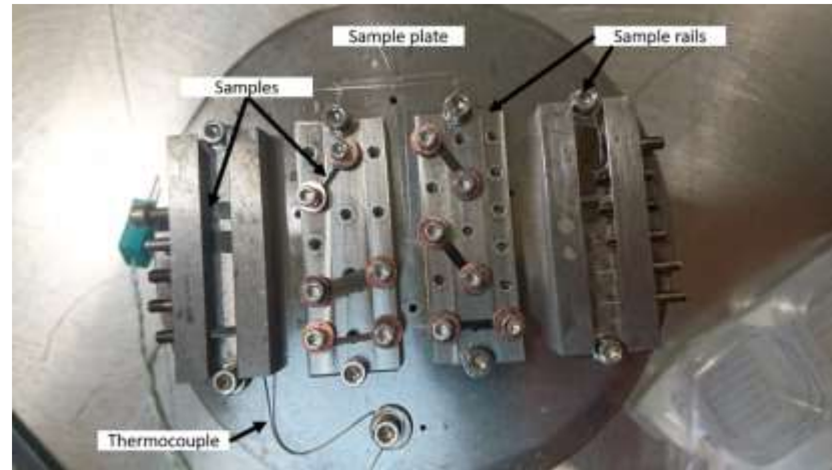

Figure 4-2: Samples mounted on sample rails fixed to the temperature-controlled stage for ion implantation.

The target chamber was maintained at high vacuum ~1×10^{-6} mbar. Temperature was controlled by two thermocouples, one fixed to one of the sample rails, and one fixed to the back of the sample plate near the heating element of the stage. The 300 °C implantations were controlled ±5 °C and 750 °C implantations to ±10 °C.

The implantation conditions used here are consistent with previous work on radiation damage in silicon carbide carried out in our group. Three ion implantation energies were chosen to give a flatter damage profile more suitable for micromechanical testing (Table 4-1 and Figure 4-3). Displacement damage can be accumulated over a wide depth range in a shorter time and at a lower total fluence than a comparable near-flat profile would be achieved using a single ion energy where the Bragg peak is avoided. The draw-back is that implanted ions will remain in the damaged region of material and may affect certain measurements.

Table 4-1: Ion fluences and energies. Low dose silicon implantations were 1/10th of these fluences.

Ion	Energy (MeV)	Fluence ($\times 10^{15}$ ions/cm^2)
Silicon	2.0	6.0
	1.0	4.0
	0.5	2.0
Neon	1.45	9.4
	0.72	6.1
	0.35	3.71

As a crude upper bound of the volume added by these ions, if all the implanted silicon ions were to solidify as crystalline silicon, the height added would be 2.405 nm, contributing to ~0.2 % strain in the implanted layer. In fact, the ions will implant as interstitials or substitutions in a strained lattice so the volume added will be considerably smaller than this.

The stopping and range of ions in matter (SRIM) [205] code was used to predict ion range and induced vacancies for each ion energy from which displacements per atom were calculated. Displacement energies for silicon and carbon in SiC were 35 eV and 21 eV respectively, with binding energies set to 0 eV [122]. The quick Kinchin-Pease model was used and run for 10,000 ions of each energy [206]. Target density was set to 3.21 g/cm^3. This calculation of dpa is intended to be consistent with other researchers for ease of comparison. It is a rough guide to induced damage and little to do with residual measured damage.

To investigate the chemical effect of implanting silicon ions into silicon carbide, inert gas ions were also used. Neon was chosen as it is the heaviest inert gas which could be implanted to the same depth as silicon ions using the 2 MV implanter at Surrey Ion Beam centre using a 1+ charge. By adjusting the fluence of neon ions, a damage profile

similar to that of the silicon ion implantation could be generated with the same peak damage and depth of damage (Figure 4-3). Multiply charged heavier ions could have been used, but it might have affected damage due to charge transfer and synergistic effects on charged defects (see section 2.2.1), and extracting higher charged ions is less efficient so the current will be lower.

To produce the damage profiles in Figure 4-3 the ion fluences were as shown in Table 4-1. The low dose silicon implantations were simply $1/10^{th}$ of these fluences to give 0.25 peak dpa. Beam current and integrated dose were measured at Surrey Ion Beam centre using Faraday cups to achieve these conditions.

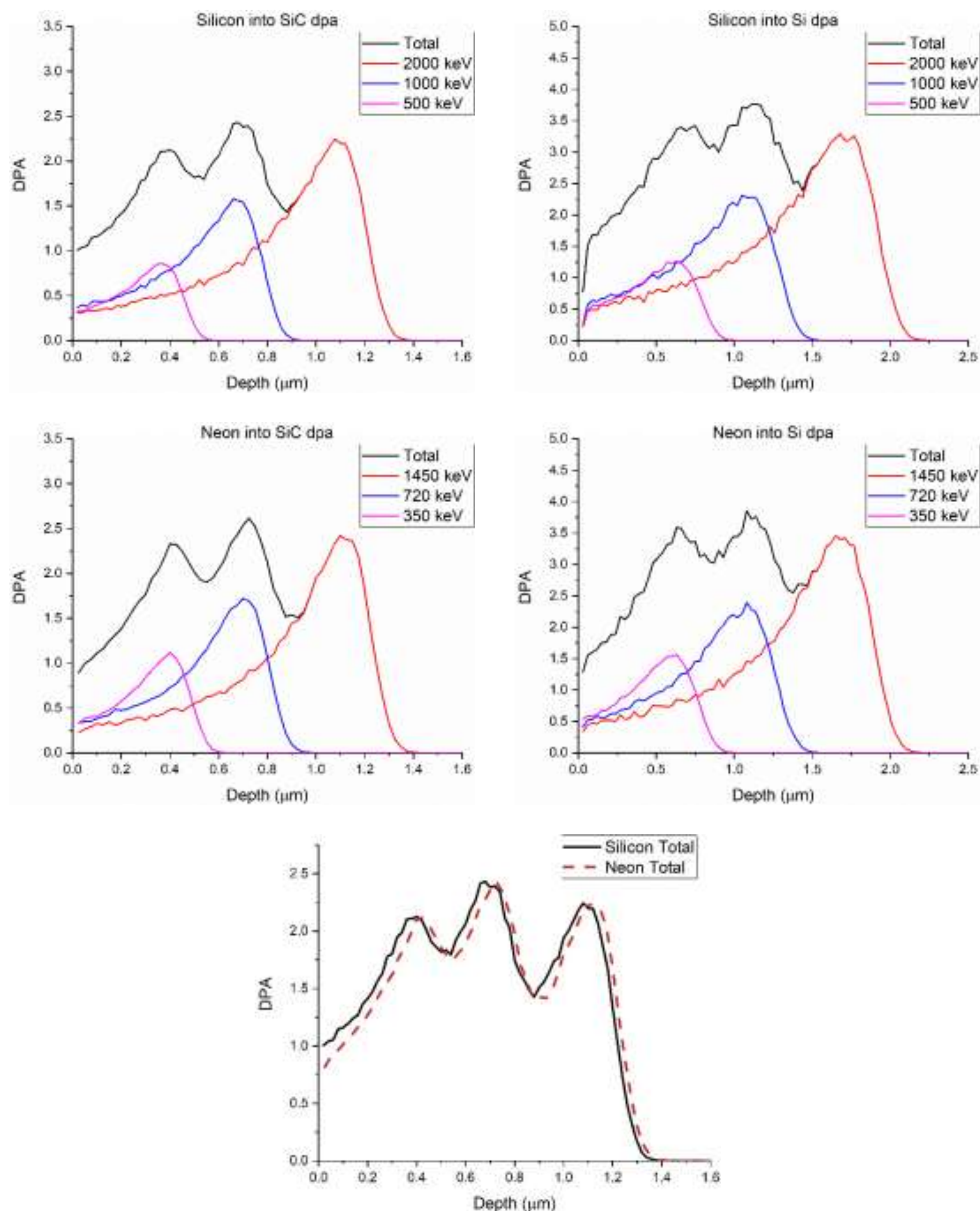

Figure 4-3: SRIM predicted dpa for silicon and neon ion implantations, with a comparison of 2.5 dpa silicon and neon damage profiles

4.3 Nanoindentation

Nanoindentation was carried out using an MTS Nanoindenter XP with a diamond Berkovich tip. The continuous stiffness method (CSM) was used to calculate mechanical properties. The CSM harmonic displacement was 2 nm with a frequency of 45 Hz and a strain rate of 0.05 s^{-1}. The tip and frame were calibrated based on the modulus of fused

silica before each batch of indents in a sample. As SiC is a hard material it was found that the tip calibration needed to be updated regularly. Each batch consisted of arrays of 500 nm and 1000 nm indents in unirradiated and irradiated regions of the same sample so that the tip calibration and condition, sample mounting, and environmental conditions were constant for comparing the effects of ion implantation. The drawback is that nanoindentation of different samples and radiation conditions would have been carried out with different tip calibrations, so the absolute values of hardness and modulus are not necessarily comparable; relative hardness and modulus changes should be compared. This appears to be important in analysis of nanoindentation measurements, especially in hard materials.

Fracture toughness from Berkovich nanoindents was calculated using the modified Laugier [207] equation from Dukino and Swain [208,209]:

$$K_c = x_v \left(\frac{a}{l}\right)^{1/2} \left(\frac{E}{H}\right)^{2/3} \frac{P}{c^{3/2}} \tag{4-1}$$

where K_c is the fracture toughness, a is indent impression radius from the centre of the impression to the corner, l is surface crack length, E is Young's modulus, H is hardness, P is maximum indenter load, and c, is the length from the centre of the indent impression to the crack tip, ie $a+l$. x_v is a fitting factor with a value 0.016. This equation is valid for the Palmqvist radial crack system with the fitting factor for Berkovich geometry derived from fitting to fracture toughness from conventional micro-Vickers indents [208]. It is a crude fitting technique which was used for micro indents, not nanoindents, yet appears to have been used for many years with this 0.016 fitting factor [210]. More recent fitting which used nanoindentation with cube corner and Berkovich tip geometries compared with fracture toughnesses from single edge notched beam measurements, along with investigation of sub-surface crack geometries, found a fitting factor for Berkovich

nanoindentation of $x_v = 0.022$ [210]. This 38% difference in x_v will propagate into 38% difference in fracture toughness from Berkovich nanoindentation. Fracture toughness in this work will be presented using 0.016 as the constant, with the value using 0.022 in parentheses.

It is worth mentioning that indentation fracture toughness equations are always fitted to a macroscopic fracture toughness measurement with some assumptions. The fracture process is fundamentally different, and crack geometry is unknown beneath an indent, so crack geometries must be assumed. For the low load nanoindents in this work it is assumed that Palmqvist cracking is appropriate, however it proved impossible to confirm this (see section 5.1.5.3). As such, fracture toughness values are likely to be unreliable, but are useful for comparisons.

4.4 Raman spectroscopy

4.4.1 Radiation damage and defects

Raman spectra were collected using a Renishaw RM1000 Raman spectrometer, coupled to an Olympus optical microscope with a 100x objective lens, NA=0.9. Acquisition times were 45s. A He-Ne laser with 633 nm wavelength was used as the coherent light source. The same objective lens was used to collect backscattered light, with the high intensity Rayleigh scattered light blocked by a notch filter. A diffraction grating with 1800 l/mm was used to diffract the Raman scattered light onto a CCD (charge-coupled device) detector. The diffraction grating can be rotated to change the spectral range of the measurement. Calibration of the spectrometer was checked before every experimental session using a silicon standard.

Silicon carbide is transparent to visible light, so it is important to use the confocal aperture when collecting Raman spectra [211]. To obtain confocal measurements, a

physical slit was set to 10 µm width, and a virtual slit at 90° to the physical slit was created by using a three pixel stripe of the CCD [212]. These slits create an aperture which will block out of focus light reaching the CCD. The confocal depth resolution was tested by running a depth series through z and measuring the intensity of silicon and silicon carbide peaks. Figure 4-4 shows that the confocal aperture corresponds to a depth resolution of < 1 µm, with a full-width half maximum of 0.4 µm. The depth offset between silicon and silicon carbide in Figure 4-4 is due to the minimum step size of the motorised stage. The laser spot focussed through a 100x objective is ~1 µm in diameter. The laser spot and depth intensity profile have Gaussian profiles with long "tails". While these are contributing to the detected signal their contribution is small compared to the high intensity region, so we assume that most of the signal is from within the damaged layer. The assumed volume where most (but not all) of the signal is detected from is ~1 μm^3.

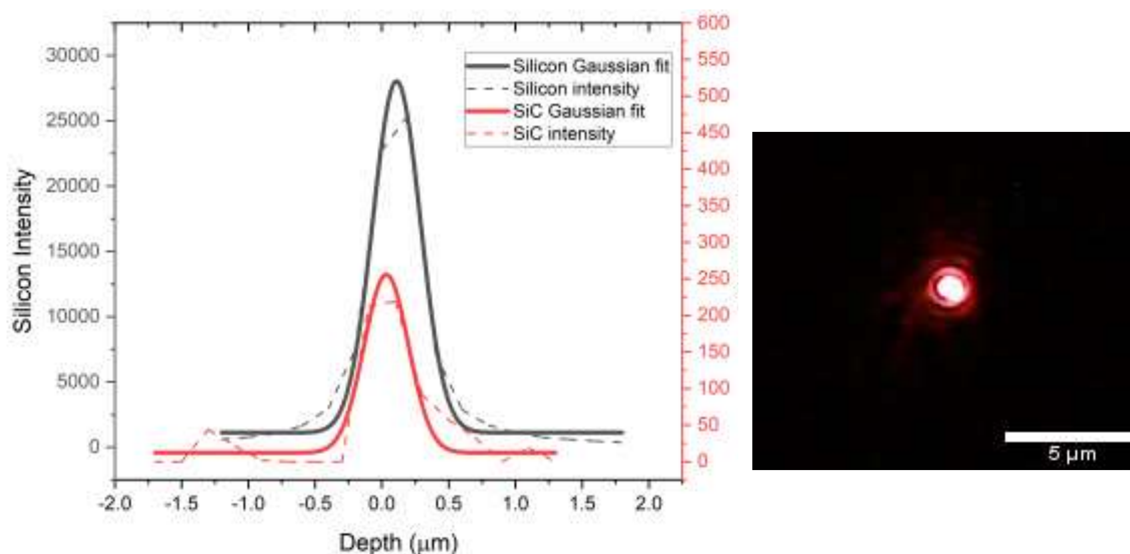

Figure 4-4: Confocal depth scan of silicon and silicon carbide intensities. Negative depths are above the sample surface. Laser spot focussed through a 100x objective lens. The samples were a large SiC grain in Starceram and a silicon single crystal.

In-situ annealing Raman spectroscopy experiments of ion irradiated single crystal SiC were carried out using the Witec Alpha 300R confocal Raman microscope in the Materials Research Facility at UKAEA. A Linkam TS1500 environmental stage was fitted

to the Raman microscope, allowing heating up to 1500 °C at 200 °C/min. A green 532 nm laser was used to acquire spectra through a 50x long focal length objective lens. The confocal aperture was the 50 μm optical fibre connecting the objective lens to the spectrometer, which achieves depth resolution ~ 1 μm. Spectra were acquired for 60s approximately every 2 minutes during the 1000 °C annealing experiment. The sample was placed in an alumina crucible on the heating stage with a quartz window. Long exposures were required as the long focal length collection optics are not as efficient as the x100 objective lens which would normally be used. Room temperature spectra acquired using the Witec microscope used a green laser operating at 10 mW, with 5 accumulations of 0.2s each. Spectra presented here are averaged over at least 5 positions.

4.4.2 Residual stress measurements

Elastic strain in a crystal changes interatomic bond length (and bond energies), so phonon frequencies will also be changed. This can be detected as a change to the Raman shift peak position for phonon modes in stressed samples. This has been predicted theoretically and observed experimentally in both silicon [213–215] and silicon carbide [216–219].

The effect of stress on Raman shift has been studied in silicon microelectronics and devices for many years [149,213,220–222], and more recently in residual silicon regions of reaction-bonded SiC [189–191].

Stress is linearly related to the shift in Raman peak position ($\Delta\omega$) by $\sigma = \Delta\omega \times R$ where R is a piezospectroscopic coefficient [190]. The shift in peak position is relative to an unstressed external standard. In this work the standards were a piece of single crystal (001) silicon and single crystal (0001) 6H-SiC. Unstressed 3C-SiC standards are difficult to acquire, so $\Delta\omega$ for 3C-SiC peaks is relative to literature values [151]. Spectra for each

of these reference materials were acquired using the spectrometers used in this work to avoid systematic errors. The spectrometer was always calibrated to a piece of single crystal silicon at the start of each experimental session.

The piezospectroscopic coefficient depends on stress state where: hydrostatic stress, $\sigma = \frac{\Delta\omega \times R}{3}$, and for biaxial stress $\sigma = \frac{\Delta\omega \times R}{2}$. The piezospectroscopic coefficients are summarised for the silicon LO peak at ~520 cm^{-1} in Table 4-2 and for 6H-SiC in Table 4-3. As no analyser is used the dependence of crystallography cannot be determined in these experiments.

Table 4-2: Piezospectroscopic constants for the silicon LO peak at 520 cm^{-1}

Stress state	Coefficient (MPa.cm)	Ref.
Hydrostatic ($\sigma_{xx} = \sigma_{yy} = \sigma_{zz}$)	-531.9±0.02	[214]
Unixial (σ_{xx})	-434	[149,223]
Biaxial ($\sigma_{xx} = \sigma_{yy}, \sigma_{zz} = 0$)	-434	[149,223]

The effects of mechanical and residual stresses on SiC Raman spectra have not been studied as extensively, and only in hydrostatic stress states using diamond anvil cells [217,224]. At typical mechanical pressures the relationship of Raman shift to stress is linear [217,225], but at ultrahigh pressures (12 GPa < P < 90 GPa), the relationship becomes quadratic [224]. DiGregorio and Furtak calibrated their piezospectroscopic coefficients for 6H-SiC using hydrostatic pressure, but consider it to be a coefficient for average stress across all directions so could be applied to other stress states including biaxial [217].

Table 4-3: Piezospectrocopic constants for 6H-SiC

Stress state	Coefficient (MPa.cm)	Ref.
Hydrostatic	-849.9 (6H-SiC TO peak ~789 cm^{-1}) -700.9 (6H-SiC LO peak ~970 cm^{-1})	[217] experimental [217] experimental
Uniaxial	-251.66 (3C-SiC TO peak ~796 cm^{-1})	[225] theoretical

As the exact stress state is unclear, all measurements of residual stress by Raman spectroscopy are presented in units of cm^{-1}, with a discussion of the stress state and the corresponding residual stress magnitudes based on the most appropriate piezospectroscopic coefficient.

The Renishaw RM1000 Raman microscope described above was used for some early mapping experiments, while later experiments used the new Witec microscope at the MRF which used a piezo stage for high spatial resolution mapping of irradiated RB-SiC samples and indents. The Witec microscope uses a more sensitive electron multiplying CCD (EMCCD) detector which enables very fast acquisition of Raman spectra, with spectral averaging of adjacent pixels to reduce noise.

Raman maps were acquired by scanning an area of the sample on a motorised stage and acquiring a spectrum at every defined step (pixel). Spectra can be analysed for peak intensity, area, and position, or compared to reference spectra for principal component analysis to identify and spatially map different phases or chemical features. For the case of residual stress mapping, the spectral position of peaks is of interest.

For each pixel in the map, curves are fitted to the spectrum using either Renishaw WiRE or Witec Project 5 software. Renishaw WiRE uses a mixed Gaussian-Lorentizian function from a previously acquired reference curve (.wxc file). The spectrum at each pixel is fitted based on this reference function. Witec Project 5 uses a Lorentz function and derives this function for every spectrum at each pixel in the map, rather than fitting to a

pre-defined reference function. This is much more computationally expensive and would take several minutes of processing on the 8-core PC. In both cases, the position of the maximum of the fitted curve was calculated and used as the position of the Raman shift at each pixel. To map silicon, the longitudinal optic phonon signal at ~520 cm^{-1} was used, and for silicon carbide the longitudinal optic and transverse optic signals at ~970 cm^{-1} and ~789 cm^{-1} were used.

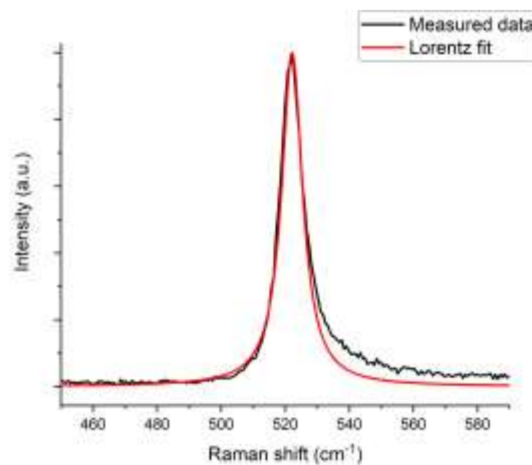

Figure 4-5: Lorentz fitting curve for a silicon region of in-house RB-SiC used for peak position mapping. The fit appears accurate for the peak position despite the slight asymmetry of the measured peak.

In these experiments the collected Raman signal was unpolarised so the change in Raman peak position corresponds to an average stress in the interaction volume. If an analyser was used with polarised light, the components of the stress tensor could be calculated [219].

4.5 Electron microscopy

4.5.1 SEM imaging

Scanning electron microscope images were acquired either using a Zeiss Merlin field emission SEM (FE-SEM) or a Zeiss Auriga dual beam focussed ion beam/SEM. Most images used secondary electrons (SE) which are generated near the sample surface so are

useful for high resolution imaging of surface topology. SEM images were acquired at 5 kV accelerating voltage.

Two detectors were used, either a conventional Everhart-Thornley detector (referred to as SEM-SE), or an in-lens detector (SEM in-lens). The Everhart-Thornley detector is placed to the side of the SEM column and detects mostly the SE2 signal by applying a positive bias to a Faraday cage to attract these low energy electrons. SE2 electrons are generated by back scattered electrons in the sample, so are slightly lower resolution than the SE1 signal generated by the incident electron beam. As the Everhart-Thornley detector is to one side of the specimen, topological contrast is clear, and can be enhanced by tilting the specimen.

The in-lens detector is placed inside the SEM column, just above the final magnetic pole piece. This detector collects SE1 electrons and a proportion of backscattered electrons, giving a mix of composition and topology contrast. Most important in this work is the geometry of the in-lens detector as it allows FIB cross-sections to be viewed while the specimen is tilted at 54° for FIB milling. The Everhart-Thornley detector is not in the line of sight of secondary electrons generated by the cross-section face so the image contrast is poor if the surface image contrast is good. A detailed comparison of Everhart-Thornley and in-lens detectors is given in reference [226].

Forescattered electron imaging was carried out in the Zeiss Merlin using the ARGUS system of the Bruker EBSD detector described in the next section. Three diodes placed below the phosphor screen are assigned “colours” in a red-green-blue system (Figure 4-6). Electrons diffracted by atomic planes will reach each diode in different proportions depending on crystallographic orientation, giving a false colour image depending on the RGB colour mixing. This is a quick imaging technique to give qualitative orientation-dependent microstructural images.

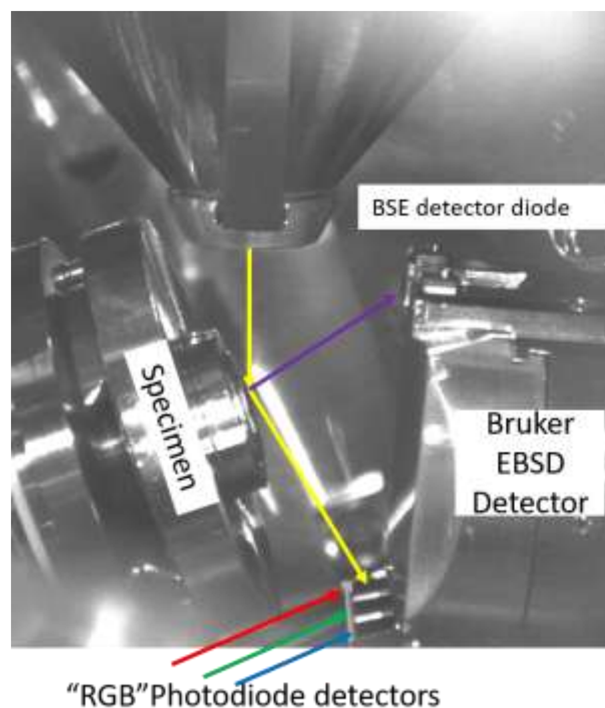

Figure 4-6: Chamber view of the Zeiss Merlin SEM showing the Bruker EBSD detector and ARGUS imaging diodes

4.5.2 Electron-backscatter diffraction (EBSD)

EBSD experiments were conducted using a Zeiss Merlin FE-SEM with a Bruker Quantax e-flash detector controlled using Bruker Esprit 2.1 software. Typical SEM conditions were 20 kV 20 nA with an acquisition time of 50 ms per pixel, although these were varied depending on experimental time constraints and pattern quality. Patterns were acquired with 800x600 pixel resolution and were all saved so that they could be analysed later using the high angular resolution (HR-EBSD) code, XEBSD developed at the Department of Materials, University of Oxford, and Imperial College, London.

The procedure for analysing EBSD patterns using high angular resolution is explained clearly in refs. [227,228], but will be summarised here. The simple concept is to compare EBSPs acquired from pixels in the map to a nominally unstrained reference pattern of the same crystal orientation. An applied strain will change interplanar angles which moves Kikuchi bands in the diffraction pattern. Additionally, crystal orientation

rotations will cause Kikuchi bands to move cooperatively across the screen. The diffraction pattern is segmented into 40 partially overlapping regions of interest, each of which undergoes a fast Fourier transform which is used for cross-correlation image analysis. The cross-correlation process creates a function with a peak, the position of which is the shift required to best overlay the region of interest to the corresponding reference ROI. From this a translation vector for each region of interest is calculated relative to the corresponding ROI in the reference pattern. With four or more translation vectors, a self-consistent deformation tensor for the diffraction pattern can be built up with components for strain and lattice rotations [229]. The anisotropic Hooke's law can be used to determine elastic stresses from strains with elastic constants from the Materials Project database [230,231]. Assuming traction free plane stress, the final ε_{33} strain component can be calculated [229].

Table 4-4: Elastic stiffness constants for 6H-SiC and silicon used for HR-EBSD elastic stress analysis. Values from the Materials Project [230,231]

6H-SiC	Silicon
$\begin{bmatrix} 501 & 111 & 52 & 0 & 0 & 0 \\ 111 & 501 & 52 & 0 & 0 & 0 \\ 52 & 52 & 553 & 0 & 0 & 0 \\ 0 & 0 & 0 & 163 & 0 & 0 \\ 0 & 0 & 0 & 0 & 163 & 0 \\ 0 & 0 & 0 & 0 & 0 & 191 \end{bmatrix}$	$\begin{bmatrix} 165 & 64 & 64 & 0 & 0 & 0 \\ 64 & 168 & 64 & 0 & 0 & 0 \\ 64 & 64 & 165 & 0 & 0 & 0 \\ 0 & 0 & 0 & 79.2 & 0 & 0 \\ 0 & 0 & 0 & 0 & 79.2 & 0 \\ 0 & 0 & 0 & 0 & 0 & 79.2 \end{bmatrix}$

The HR-EBSD analysis described above only accounts for elastic strain and stress. Plastic deformation by dislocations is more difficult to directly measure and calculate, but an indirect assessment based on deformation around dislocations can be conducted. As dislocations pile up, they contribute to a net lattice curvature due to the extra half-planes of atoms. Lattice rotations are measured from the diffraction pattern by HR-EBSD as described above. The spatial gradient of the lattice rotations can be related to the density of dislocations required to cause that lattice curvature (Figure 4-7) [232]. The measured

lattice curvature is a net effect of stored dislocations in the structure, not necessarily dislocations which have contributed to plastic deformation, and is a lower bound as dislocations of opposite sign will cancel out their effect on lattice curvature within a diffracting interaction volume [227]. If the measurement spacing is too large no net lattice curvature will be detected and geometrically necessary dislocation (GND) density cannot be calculated.

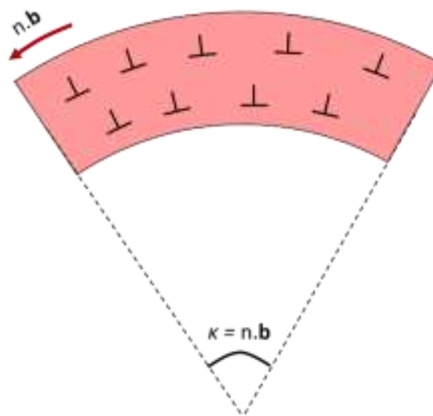

Figure 4-7: Schematic of lattice curvature κ *introduced by* n *dislocations with Burgers vector* **b**. *Based on the sketch in* [232]

Nye extended his derivation of curvature caused by a net density of dislocations into three dimensions as a tensor which can be solved based on lattice rotations and elastic strains measured using HR-EBSD [229,232]. With the angular and strain sensitivity of cross-correlation HR-EBSD, noise in GND maps is ~10^{12} m^{-2} [229].

Results from XEBSD stress analysis are presented graphically as plane stress tensors without the σ_{13} , σ_{23} , and σ_{33} components as these are zero (Figure 4-8). σ_{21} is symmetrical to σ_{12} so is also omitted for clarity.

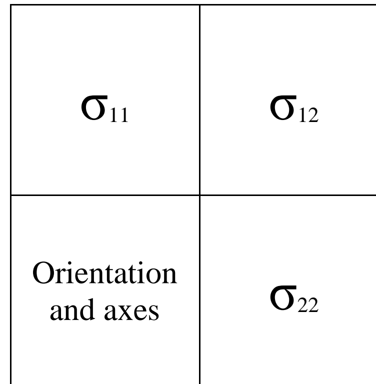

Figure 4-8: Layout of HR-EBSD maps in a plane stress tensor

For HR-EBSD of nanoindents the reference pattern is taken far from the indent, typically in the upper left of the map. HR-EBSD of nanoindents in irradiated regions is relative to a reference pattern taken away from the indent, but still in the irradiated region. As will be shown in the results section, this is *not* a stress-free position, so the maps are of stress relative to this position. For radiation boundary maps the reference is taken on the unirradiated side far from the boundary.

HR-EBSD is assumed to be plane stress, so the planar von Mises stress (equation (4-2) is plotted to more simply visualise residual elastic deformation around indents. Some maps are presented as mean planar biaxial stress ($(\sigma_{11} + \sigma_{22}) \div 2$).

$$\sigma_v = \sqrt{\sigma_{11}^2 - \sigma_{11}\sigma_{22} + \sigma_{22}^2 + 3\sigma_{12}^2} \tag{4-2}$$

There is some uncertainty in the depth the EBSD signal is coming from. Most literature assumes the signal is from the top 20-40 nm of the sample, however experiments by Wisniewski *et al.* suggest a proportion of the signal is coming from up to 150 nm into the surface [233,234]. In the high-quality patterns in this work, most of the signal in the high intensity bands will be coming from low-loss electrons scattered in the near surface (~40 nm) and maintaining >97% of their energy. Electrons scattered from deeper into the sample contribute to broad tails in the Kikuchi band as their energy is reduced and the

Bragg condition is changed. Since their contribution to the analysed patterns is small, the plane stress assumption still holds.

The peak in the cross-correlation function described above can be used as an indicator of the "quality" of an EBSD map through the quantity "peak height". This is the height of the cross correlation peak relative to autocorrelation where the cross-correlation process is applied to the reference image onto itself, resulting in perfect matching and a peak height of 1. In the case of lattice rotations, the Kikuchi pattern stays the same, but is moved cooperatively across the detector screen. Assuming nothing else has changed, this can be accommodated by a translation vector alone, so the peak height remains 1. When there is an elastic strain, angles in the Kikuchi pattern are changed so it is impossible for cross correlation to match the ROIs being assessed onto the reference ROI with a translation vector. The cross-correlation function has a broader peak, reducing its height thus the peak height is less than 1. Other alterations to the EBSD pattern being analysed such as background, broadened Kikuchi bands, lower intensity, all detract from autocorrelation, thus lowering the height of the peak in the cross-correlation function. The quantity "peak height" represents relative degradation to EBSD patterns caused by a combination of elastic strain and defects affecting diffraction such as dislocations and point defects or defect clusters.

4.5.3 Focussed ion beam tomography

To investigate sub-surface microstructure and crack paths some nanoindents were selected for 3D sectioning use the FIB slice and image technique. A Zeiss Auriga FIB/SEM was used for this, with a coarse trench milled away from the indent using 30 kV 4 nA to allow viewing with the SEM, followed by fine slicing at 30 kV 240 pA.

4.5.4 Microcantilever residual stress measurements

To measure residual stress in the ion implanted layer of silicon carbide, microcantilevers were milled using a Zeiss Auriga FIB/SEM. These microcantilevers were made slightly differently to microcantilevers used for conventional bend testing [235], as outlined below.

1. Coarse trench milling at 54° (30 kV, 4 nA)
2. Fine milling to make rough cantilever dimensions (30 kV, 1 nA)
3. Partially undercut at 24° to make a triangular cross-section “bridge” (30 kV, 600 pA). The geometry of the bridge was measured using the SEM at this point.
4. Cut off the end of the “bridge” using deposition mode at 54° (30 kV, 240 pA). A small section of the bridge is left at one end to use as a reference for the deflection measurements. Repeatedly image with the SEM to record the cantilever position as the material is removed.

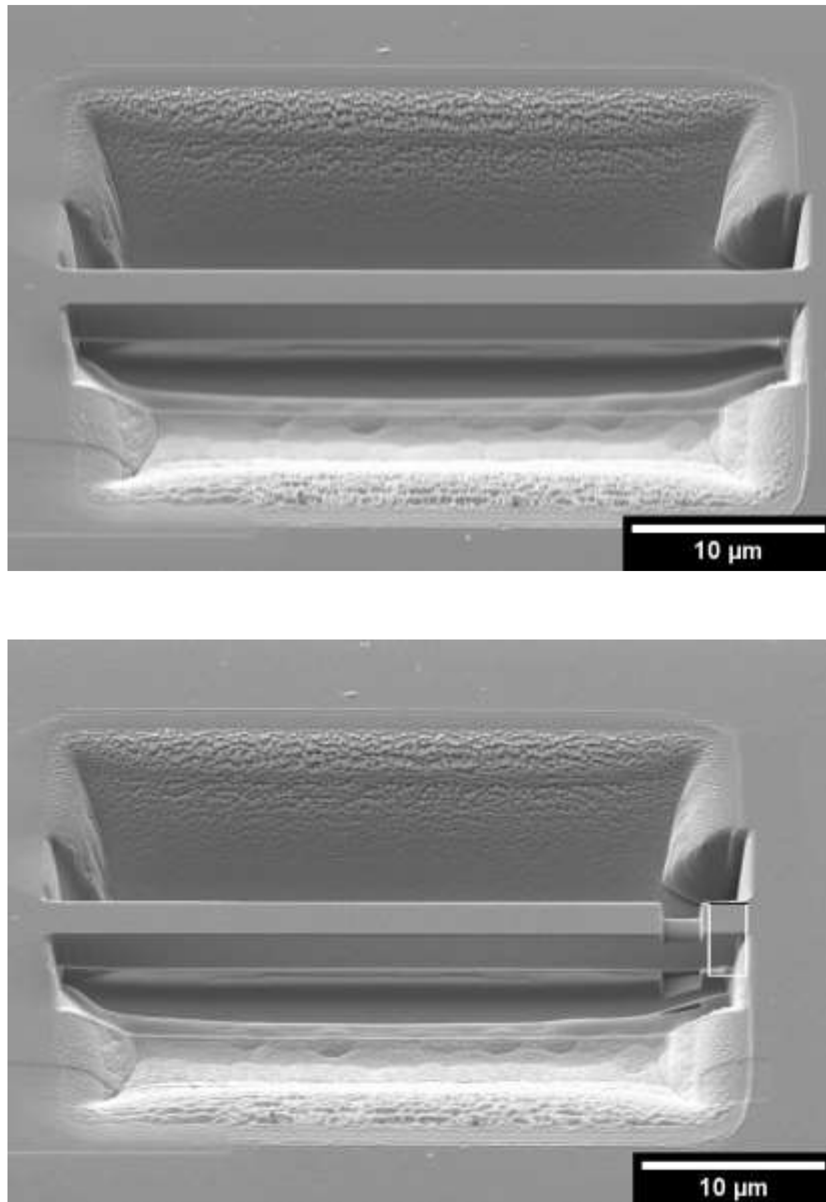

Figure 4-9: Micro "bridge" (top) being cut into a microcantilever (bottom) with a short section remaining for deflection comparison (SEM SE)

After the bridge was released into a cantilever, deflections were measured using high resolution SEM imaging at various tilts and tilt corrections to be used in the calculation of stress.

Stresses were calculated using a finite element model implemented in ABAQUS. The geometry of each cantilever was used, and a cantilever base was made large enough that the fixed edges did not impact on the cantilever. To simulate the ion implanted layer,

a layer with the nominal thickness of the damaged layer was segmented and given a thermal expansion coefficient of 1, where the rest of the model did not have a thermal expansion in the material properties. A temperature was applied to simulate radiation swelling until the cantilever bent to the experimentally measured displacement, then radiation-induced residual stresses could be calculated in the base of the cantilever.

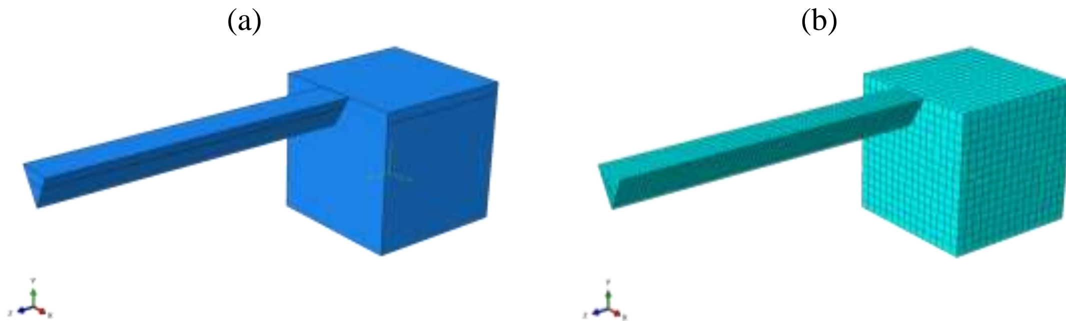

Figure 4-10: Finite element model for bending cantilevers (a) shows the "irradiated" upper layer given a thermal expansion coefficient of 1, and (b) shows the meshed component

4.5.5 Micropillar swelling digital image correlation

Micropillars were machined into single crystals of silicon and silicon carbide using a Zeiss Auriga gallium FIB/SEM. Rough milling was initially carried out at 30 kV 4 nA, followed by 30 kV 2 nA, 30 kV 1 nA, and 30 kV 600 pA. This resulted in pillars with near-parallel sides and sharp, well defined edges (Figure 4-11). Initially 5 pillars in each sample were planned with different diameters, however they are very time consuming to make, so only two of each were finished. The heights were intended to be deeper than the ion implantation depth so that the radiation-induced swelling wouldn't be laterally constrained by surrounding material, only the substrate.

Single crystal samples containing micropillars were implanted with neon ions in the 300 °C 2.5 dpa experiment.

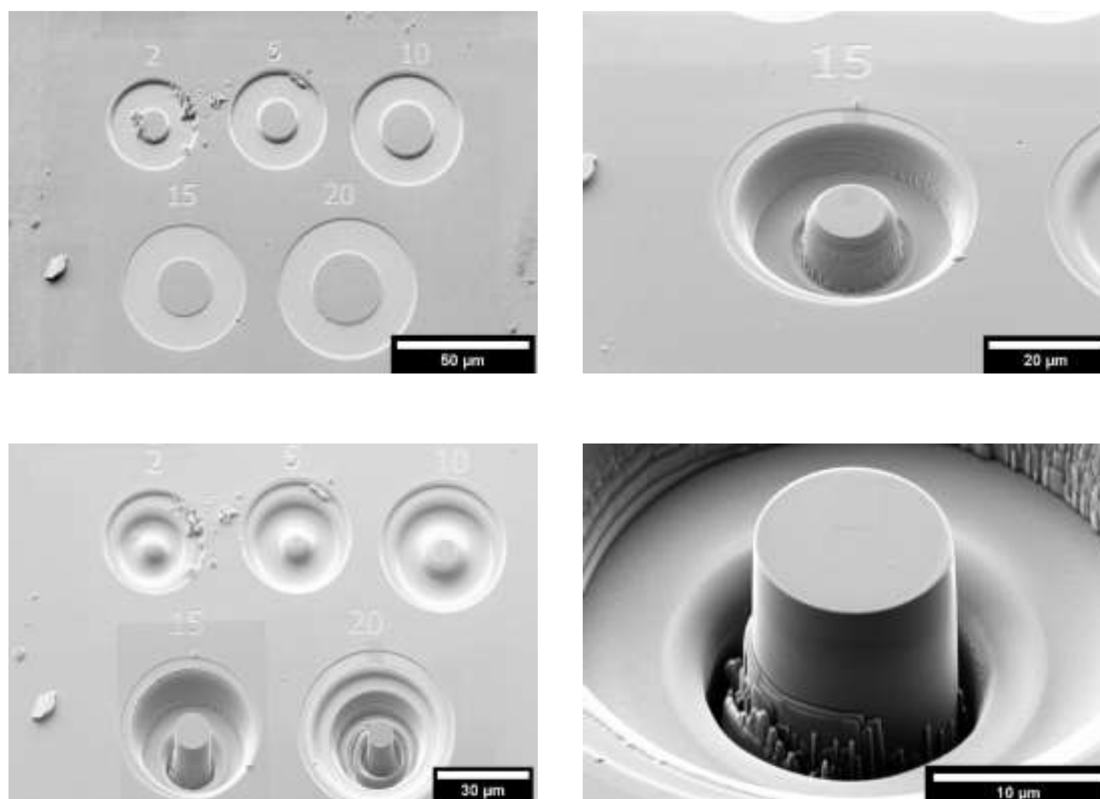

Figure 4-11: Micropillars during FIB milling (SEM SE)

Once the pillars were finished, a random speckle pattern was milled into the top. The pattern was made using the Zeiss Atlas Engine v5.1 software, with different sized ellipsoids randomly copy and pasted and translated. Approximately 3000 speckles were milled into the surface of each pillar using 15 kV 2 pA to 0.03 nC/μm^2. This was approximately the lowest dose which could be controllably applied to each speckle. Based on the software's material-dose calibrations, each speckle was approximately 5 nm deep. Cross-hair markers were milled so that the pillar could reliably be aligned in the FIB/SEM at the same orientation and position between different microscopy sessions and after the ion implantation (Figure 4-12).

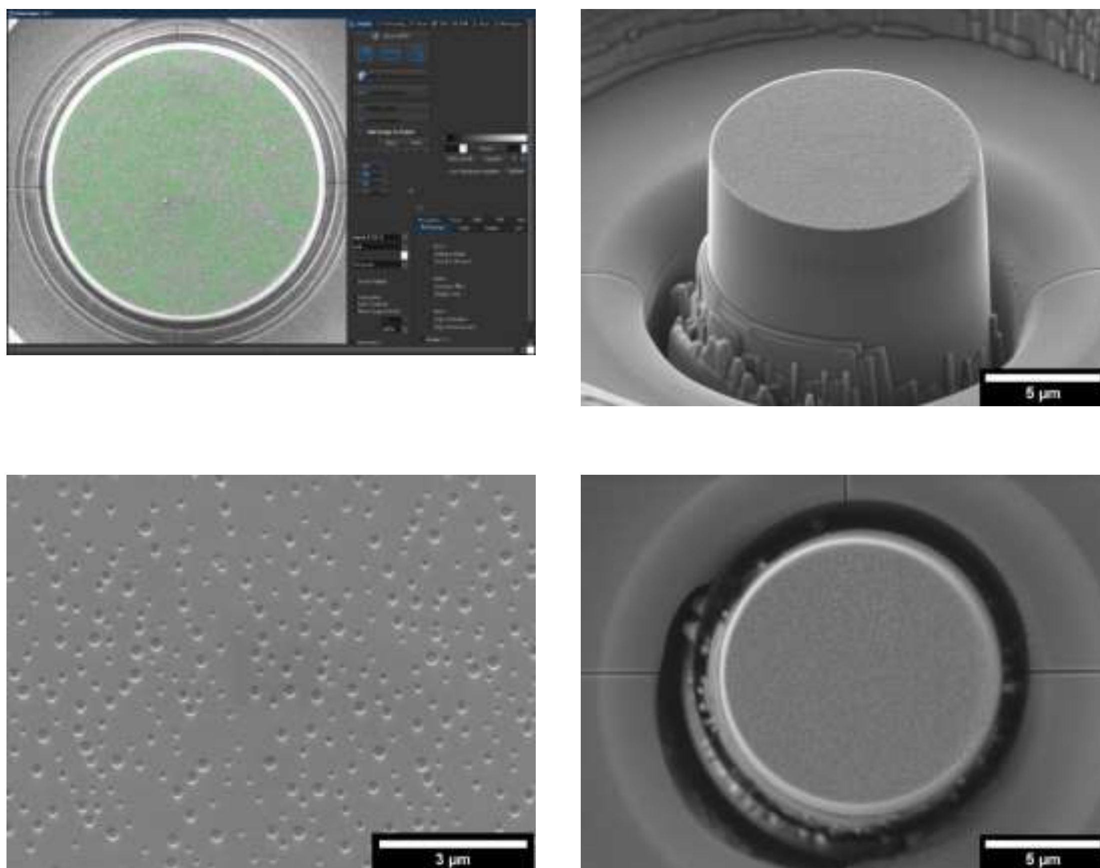

Figure 4-12: Milling of speckles and cross-hair markers for digital image correlation. (a) speckle pattern made using Atlas Engine Software. (b) speckled pillar. (c) close-up of speckle pattern. (d) final speckle-patterned pillar with cross-hair lines marked (SEM SE)

The effectiveness of the speckle pattern for digital image correlation swelling strain measurements was tested by editing the pre-irradiation images. GIMP 2.8.22 was used to crop the SEM image of the surface of the pillar, then artificially scale this image to 101% dimensions to the nearest pixel. >1% swelling is typically expected for irradiation of monolithic silicon carbide. This made a "before" and "after" image for DIC analysis.

NCORR Digital Image Correlation software was used for the DIC analysis [236]. As the speckles are rather large for the magnification, the subset radius and spacing were set to 60 pixels and 10 pixels respectively so that multiple features could be identified and tracked between subsets. Figure 4-13 shows the xx and yy strain results after the 101% scaling. DIC has sub-pixel resolution, so discrepancy in the DIC strains can be traced back to the initial dimensional swelling using GIMP. Based on this, the speckle pattern and DIC

analysis using NCORR appears suitable for measuring radiation-induced swelling strains in SiC.

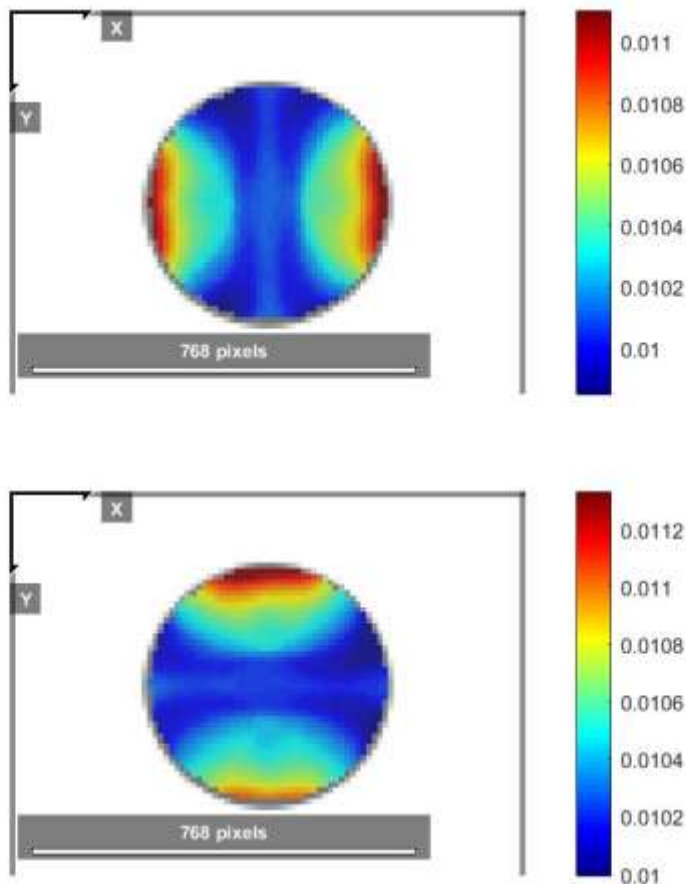

Figure 4-13: Results of DIC testing. (a) xx strain, (b) yy strain

4.6 Atomic Force Microscopy (AFM)

Atomic force microscopy was used to measure the height of the step caused by radiation-induced swelling in single-crystal SiC. The experiment was carried out by Nicola Flanagan of Oxford Materials Characterisation Service using an Agilent 5400 AFM with a Mikro Masch NSC35 tip in contact mode. The force constant of the tip was 4.5 N/m. Data was acquired using Keysight Picoview 1.20.2, and analysed using the software package Gwyddion 2.52 [237]. Line profiles of step height are calculated as averages across the boundary of a 40 x 40 μm area map.

5 Results

5.1 RB-SiC microstructures

5.1.1 In-house RB-SiC microstructure

Processing conditions were not optimised for making RB-SiC in-house, but useful samples for ion implantation and micromechanical testing were made. Processing details are given in the methods section.

Figure 5-1 shows the microstructure of the conventional in-house RB-SiC; the ARGUS image in particular shows that SiC grains are mostly isolated with few SiC-SiC grain boundaries. These micrographs are representative of the dense regions used for micromechanical testing and analysis.

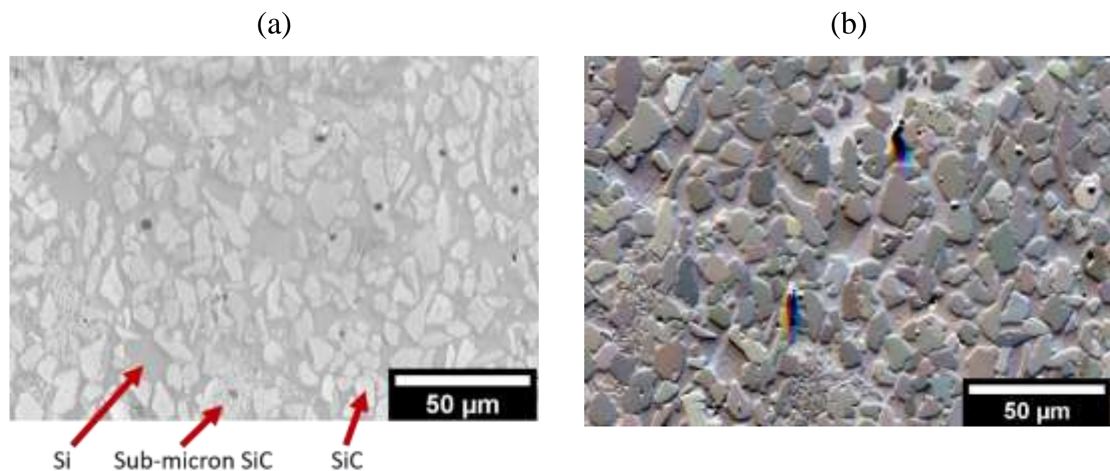

Figure 5-1: Microstructure of in-house RB-SiC (a) secondary electron image, (b) forescattered electron ARGUS image of the same area

Another difference in this microstructure to the commercial materials is the clusters of fine sub-micron SiC grains. The Raman spectrum of these sub-micron SiC grains is shown in Figure 5-2, and is dominated by the silicon signal, but the inset of Figure 5-2 shows details of the SiC region of the spectrum. The single peak at 797 cm^{-1} and the smaller one at 972 cm^{-1} are characteristic of 3C-SiC [151,152]. The broad peak around 950 cm^{-1} is

the second order TO resonance in silicon [238] which overlaps the 3C-SiC LO peak. These small grains are formed from reaction of carbon with silicon during the melt infiltration, but do not transform into 6H-SiC as there is no 6H-SiC substrate to seed this crystal structure [59,87]. This suggests these small SiC grains are formed from the direct conversion of carbon to SiC. The 3C-SiC TO peak is shifted to 797.4 cm^{-1} rather than the reference unstressed 3C-SiC peak position of 796 cm^{-1} [151]. This $\Delta\omega$ of +1.4 cm^{-1} corresponds to a hydrostatic compressive stress of -352.3 MPa [225]. The silicon peak at 522 cm^{-1} corresponds to a compressive stress of -354.7 MPa. The silicon peak is more symmetric than in commercial RB-SiC suggesting a lower impurity content.

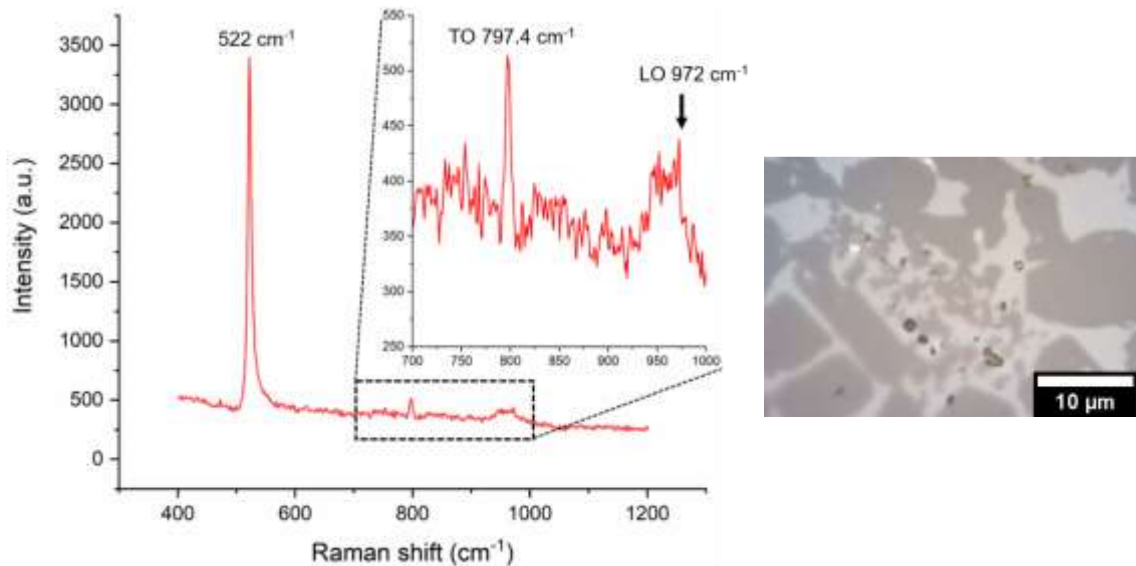

Figure 5-2: Raman spectrum from a region of sub-micron SiC grains in in-house RB-SiC. The main spectrum is dominated by the silicon signal. Inset is magnified on the SiC region of the spectrum. (100x optical micrograph)

5.1.2 Metal silicide RB-SiC

5.1.2.1 Si-Cr alloy

The Si-Cr sample shown in Figure 5-3 was infiltrated ~1.2 mm and remained porous apart from a 300 µm thick dense layer which was used for subsequent micromechanical testing and characterisation. Some alloy remained solidified on the surface after heat treatment.

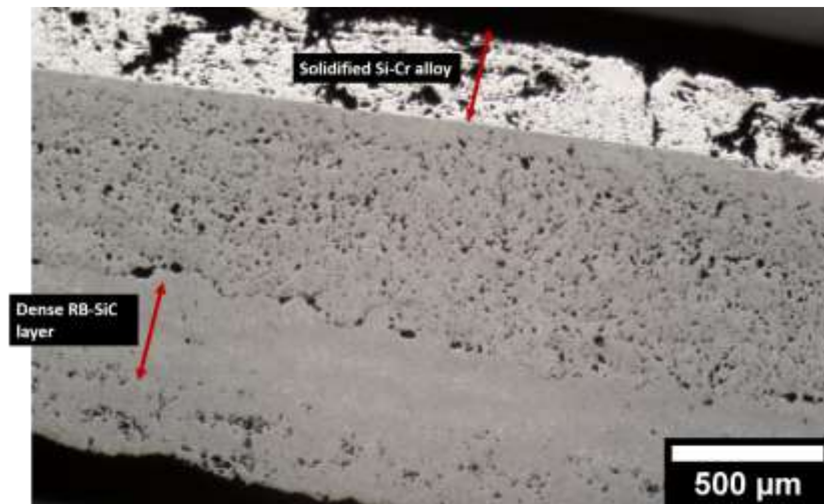

Figure 5-3: Optical micrograph of $CrSi_2$ RB-SiC. 2.5x objective

Remaining un-infiltrated alloy solidified with a eutectic microstructure showing secondary electron contrast between $CrSi_2$ and silicon (Figure 5-4).

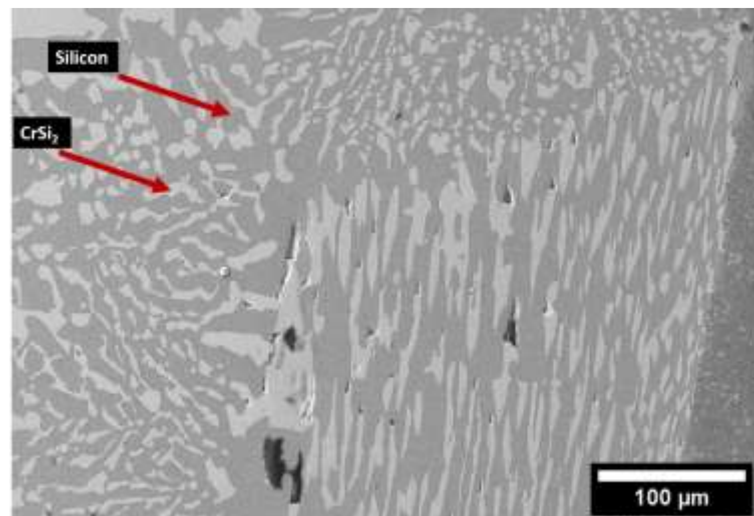

Figure 5-4: Solidified Si-Cr alloy on the surface of the RB-SiC sample. Darker contrast is silicon, lighter is $CrSi_2$. RB-SiC can be seen on the right (SEM SE)

Within the dense RB-SiC layer, only the brighter contrast from $CrSi_2$ could been seen (Figure 5-5). However, Raman spectra show that some crystalline silicon was still present in very small quantities based on the low intensity of the silicon peak compared to bulk silicon. The peaks assigned to $CrSi_2$ are based on measurements by Hermet *et al.* [239].

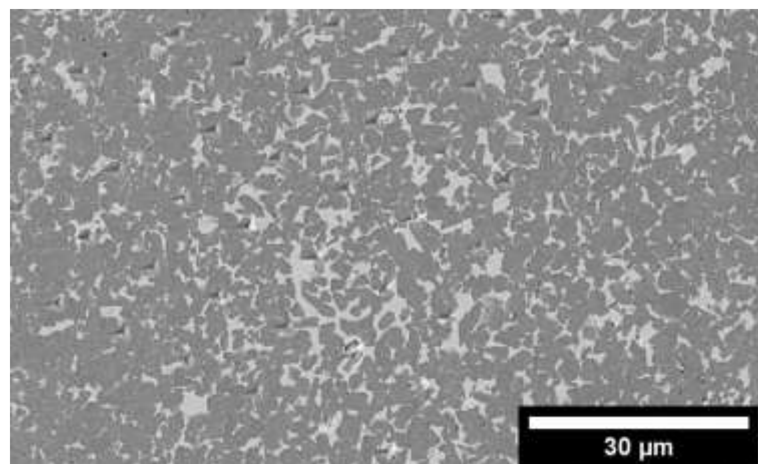

Figure 5-5: Dense $CrSi_2$ RB-SiC region including an array of nanoindents (SEM SE)

Based on image thresholding and analysis, the composition by area of the dense RB-SiC regions which were used for analysis is 80.3% SiC, 19.4% $CrSi_2$, and 0.3% porosity.

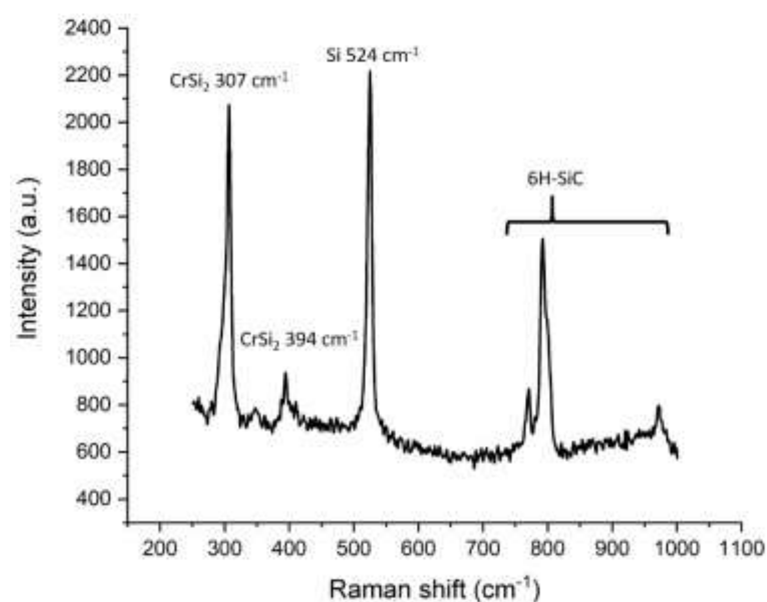

Figure 5-6: Raman spectrum of $CrSi_2$ in RB-SiC. A small quantity of crystalline silicon is present, and some 6H-SiC grains were included in the interaction volume

5.1.2.2 Si-W alloy

The Si-W alloy infiltrated the full thickness of the sample but there was residual porosity caused by reactive blockages (Figure 5-7). Bright WSi_2 regions are larger near the top surface, then evenly distributed in finer regions deeper into the sample.

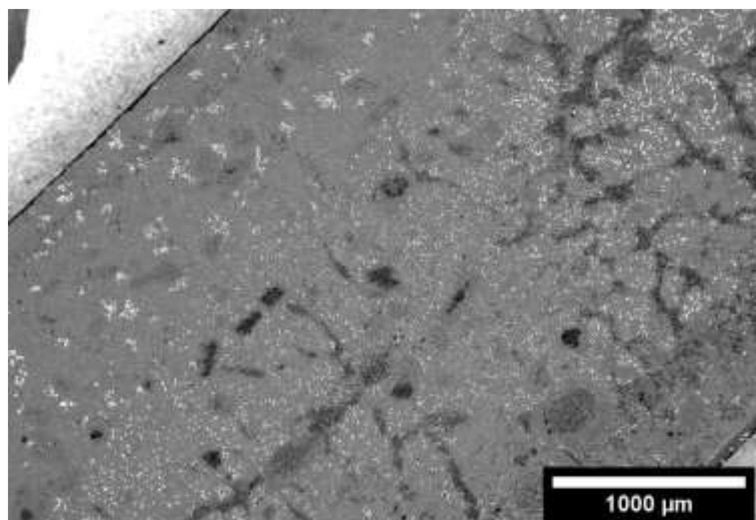

Figure 5-7: Low magnification overview of Si-W infiltrated RB-SiC. Bright regions are WSi_2, grey is SiC, black/dark grey is porosity (SEM SE)

Figure 5-8 clearly shows the effect of reactive blocking. A dense layer of SiC has formed during the C+Si reaction and closed the pathways preventing silicon reaching these regions.

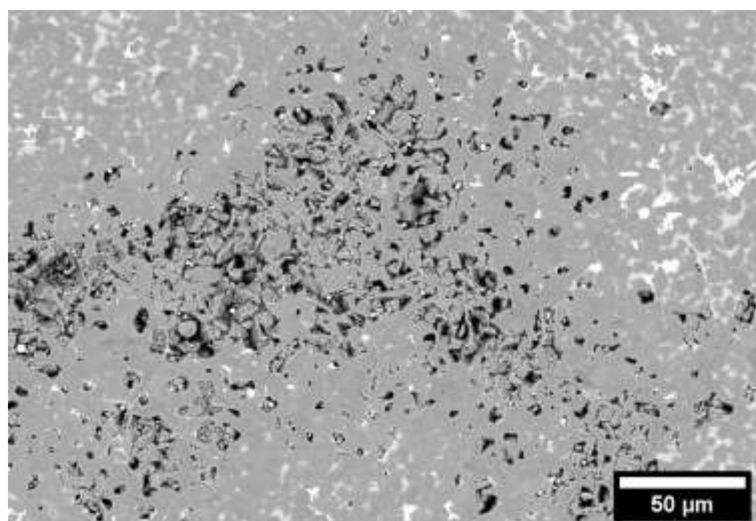

Figure 5-8: Porosity and reactive blockage in Si-W RB-SiC (SEM SE)

Looking inside the blocked porosity, one can see the “frozen” reaction between carbon and silicon and the formation of RB-SiC. Figure 5-9 (a) shows aligned lamellae of SiC growing on the surface of a SiC particle, seemingly seeded from carbon-black nanoparticles. On the grain in Figure 5-9 (b) the lamellae seem to have merged and are growing epitaxially.

(a)

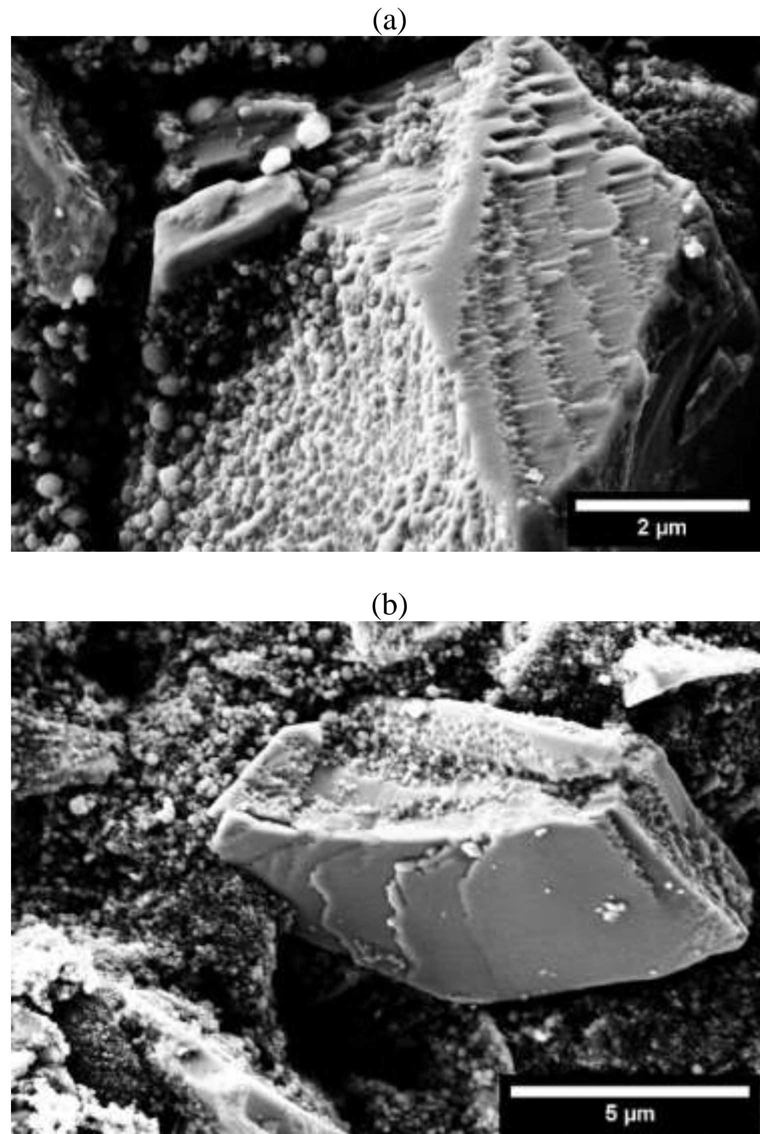

Figure 5-9: Partially formed RB-SiC inside a reactive blockage. Unreacted carbon black nanoparticles can be seen on the surface of larger SiC grains, and partial growth of reaction-formed SiC (SEM SE)

Typical dense regions used for measurements had an area fraction of 87% SiC, 3.5% WSi_2, and 9% Si, and 0.5% porosity.

5.1.3 Commercial RB-SiC

The microstructure of REFEL has been discussed in the literature in relation to the formation mechanism of RB-SiC [59,87]. Figure 5-10 (a) shows secondary electron imaging revealing a characteristic “core-shell” contrast in the SiC grains in REFEL (starting SiC grains with dark contrast with a layer of epitaxially deposited reaction-formed SiC with bright contrast). Backscattered electron images (Figure 5-10 (b)) are sensitive to

atomic mass and show clear contrast between SiC (dark) and Si (light), like optical imaging. Secondary electron yield in silicon has been shown to increase with p-type doping with boron [240]. With the aluminium and boron impurities in the residual silicon regions of commercial RB-SiC, it is likely that boron will be incorporated in reaction-formed SiC, increasing the secondary electron yield and causing the brighter “shell” contrast [87]. The p-type doping of both silicon and reaction-formed SiC explains why it is possible to use electrical discharge machining on REFEL and Starceram Si [202].

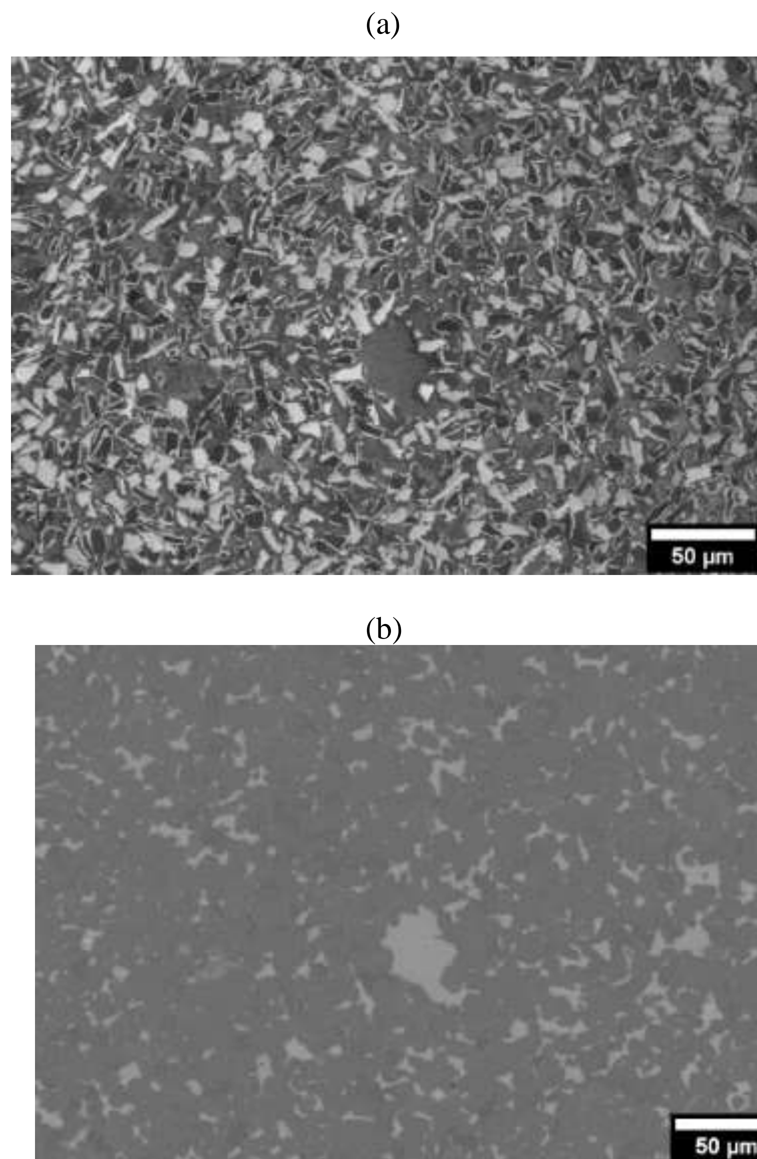

Figure 5-10: SEM images of the same region of REFEL (a) is secondary electron imaging, (b) is backscattered electron imaging

Figure 5-11 shows the same region of REFEL imaged using secondary and forescattered electrons. The colour contrast in the ARGUS image is due to the number of electrons being diffracted onto each of the "RGB" diode detectors, allowing grains to be clearly differentiated based on their crystallographic orientations. The "shell" around starting SiC grains is not visible in the ARGUS image, it is incorporated into the grain, so crystallographically it is the same structure and orientation as the core of these SiC grains. HR-TEM and selected area diffraction patterns in the literature have identified some remaining regions of untransformed 3C-SiC, and various polytypes of hexagonal and rhombohedral SiC in the reaction formed layers [87].

The ARGUS image in Figure 5-11 (b) also highlights the high connectivity of REFEL SiC grains, with most grain boundaries being SiC-SiC, and silicon regions are closed, surrounded by continuous SiC. In three dimensions, the silicon regions are mostly interconnected, based on literature experiments where silicon was evaporated and replaced with CaF_2 solid lubricant [241]

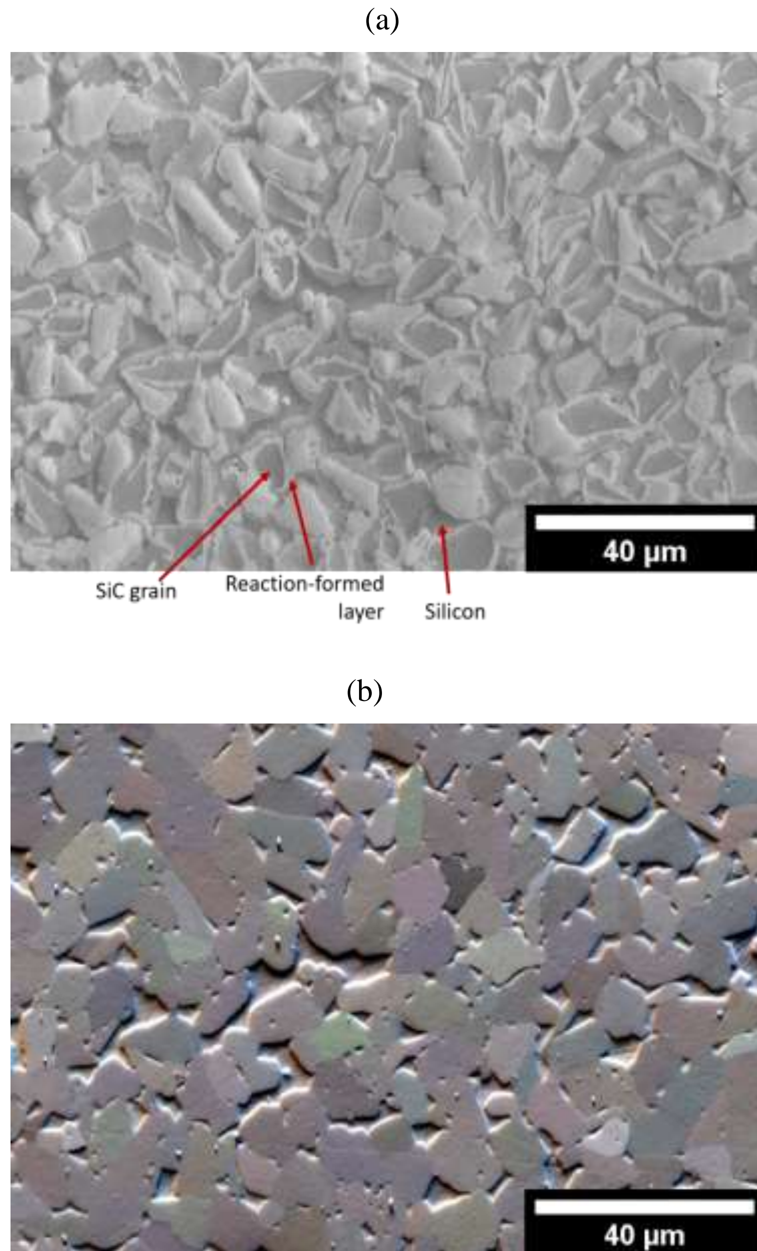

Figure 5-11: Microstructure of REFEL in the same area using (a) secondary electron, (b) forescattered electron ARGUS image

In contrast to REFEL, the ARGUS image of Starceram (Figure 5-12) shows the large proportion of small isolated SiC grains between larger SiC grains with a lower reaction-bonding connectivity.

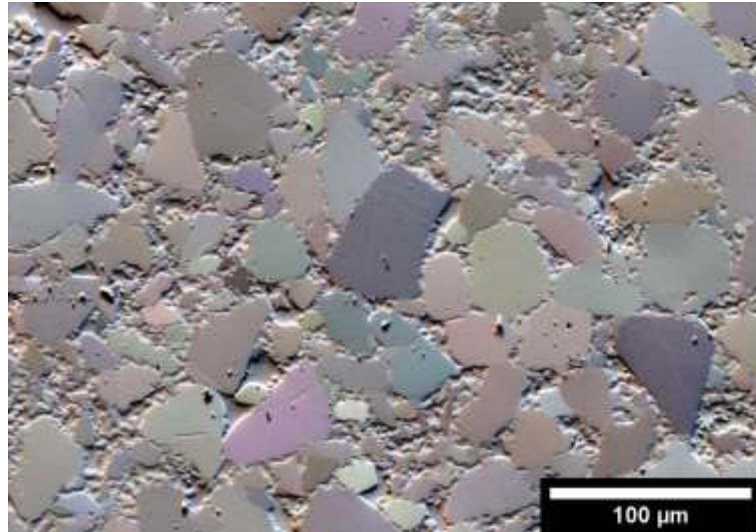

Figure 5-12: ARGUS forescattered electron image of Starceram microstructure

The commercial grades of RB-SiC use cheaper, impure silicon for the melt infiltration. Of the typical impurities, boron and aluminium are electron acceptors which contribute to Bright-Wigner-Fano resonances in silicon, and the Raman spectra seen in Figure 5-13 [192,242]. These dopants influence silicon peak position, along with the asymmetry. Extra boron could be introduced into silicon from boron nitride spray used to coat samples during processing to change the surface tension of silicon making it not wet the surface of the sample so that it can be ground off more easily after processing [202].

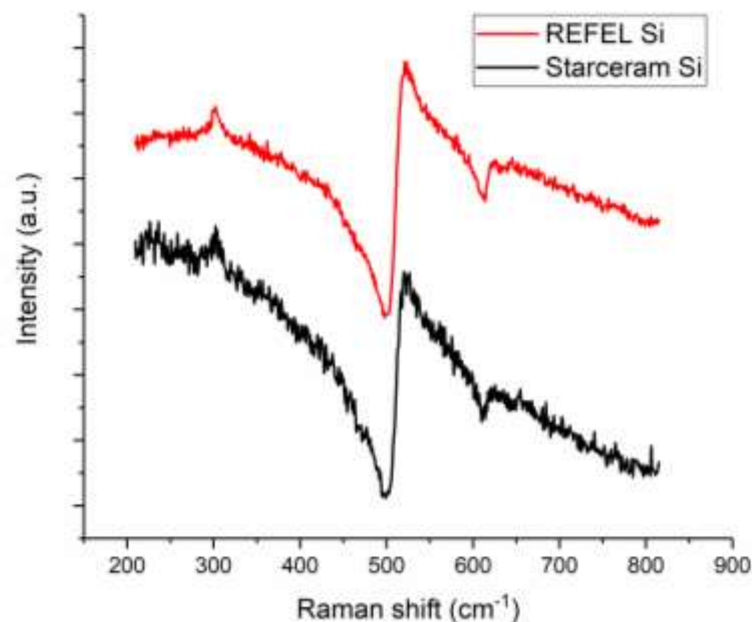

Figure 5-13: Raman spectra of residual silicon in commercial grades of RB-SiC.

One observation not previously mentioned in the literature is that the secondary electron contrast changes with working distance and sample tilt. Figure 5-14 shows 5 kV secondary electron images of unirradiated REFEL. Shortening the working distance from 13.5mm to 8 mm removes the “core-shell” contrast but tilting the specimen while at 8 mm brings back the contrast. It is unclear why the shell contrast is lost by changing working distance if it is caused by p-type boron doping and electronic structure changes.

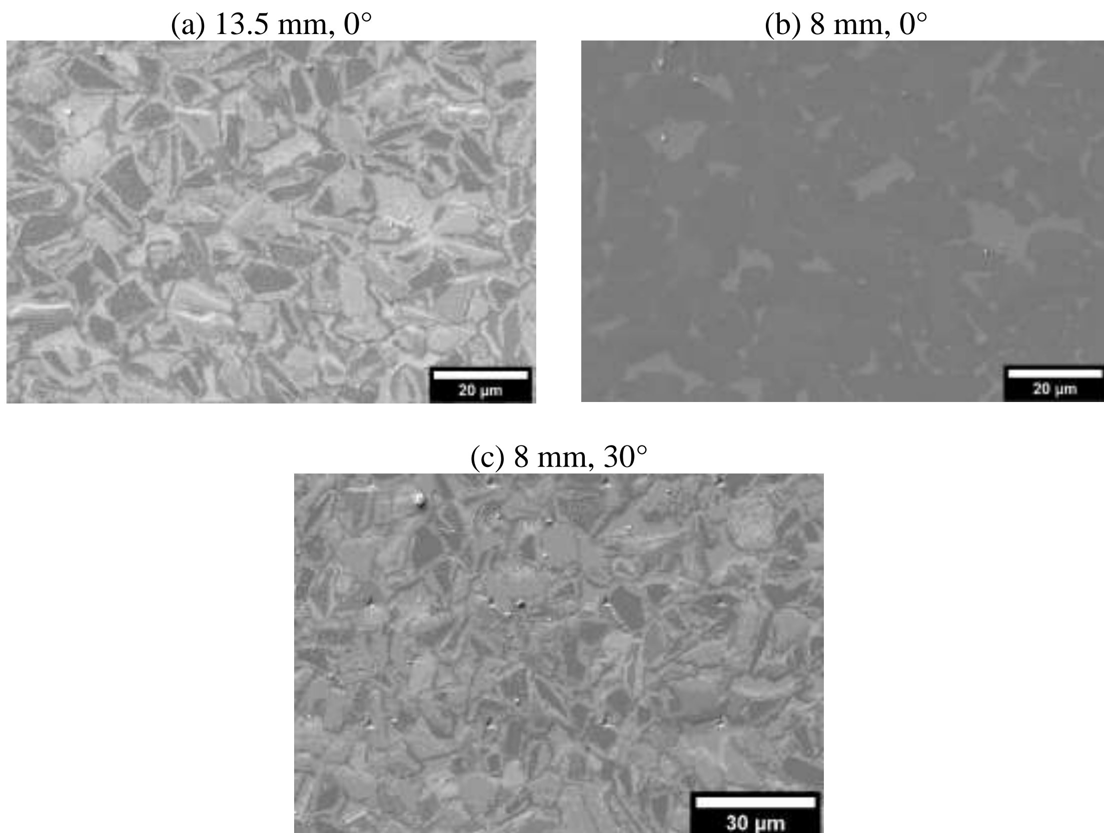

Figure 5-14: 5 kV secondary electron images of the same region of unirradiated REFEL, (a) is with working distance 13.5 mm, (b) is at working distance 8 mm. (c) 8 mm working distance, 30° specimen tilt. No changes were made to microscope condition.

5.1.4 Processing-induced residual stresses

During processing of RB-SiC, residual stresses can be introduced due to differential thermal expansion or phase changes [189,190]. These were investigated for the silicon phase using Raman spectroscopy mapping. Raman spectra were acquired along lines

(Figure 5-15) and areas (Figure 5-16) and using a reference curve to determine the position of the silicon LO peak, as described in section 4.4.2. The position of the silicon spectral peak is plotted for each pixel along the line, or in the area map.

Figure 5-15 shows linescans of silicon peak position in residual silicon regions of the in-house RB-SiC. The whole length of the line has a peak position greater than 520 cm^{-1} which corresponds to a residual compressive stress relative to the unstressed silicon standard. Close to the SiC grains at the start and end of the linescan, the peak position is closer to 520 cm^{-1} corresponding to a lower compressive stress. At the centre of the regions the peak position is at higher wave numbers corresponding to a more compressive stress. Regions (a) and (b) vary in the values of the silicon peak position suggesting that the magnitude of compressive stress will vary spatially within the sample. Linescan (a) is 10 µm long and has a maximum peak position of 523.8 cm^{-1} while linescan (b) is 5 µm long and has a maximum peak position of 522.9 cm^{-1}. This suggests that larger silicon regions could have higher compressive stresses at their centre.

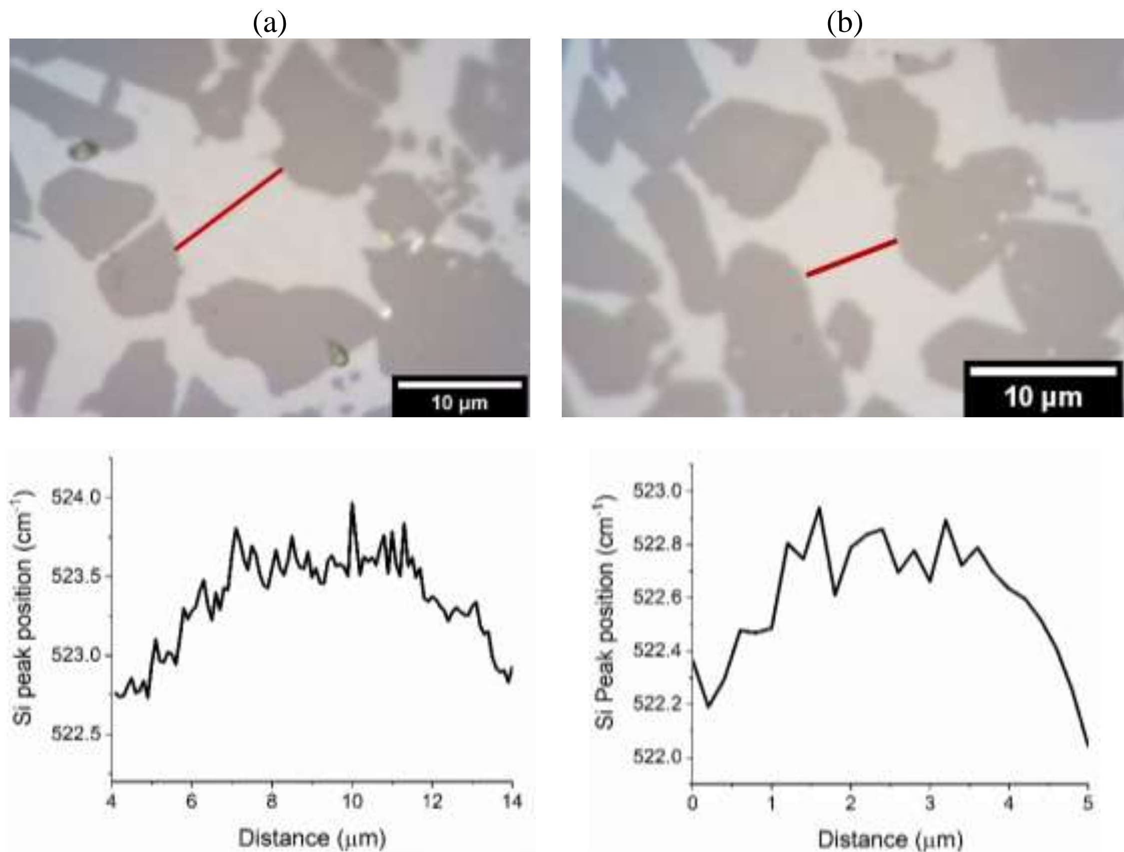

Figure 5-15: Linescan of Raman silicon peak position in residual silicon regions of in-house RB-SiC (100x optical)

Area scans of residual silicon regions of the in-house RB-SiC show the 2D spatial variation of silicon peak position. Figure 5-16 shows an area map of residual silicon, again showing that all the silicon has Raman peaks at wavenumbers greater than 520 cm^{-1} corresponding to compressive stress. At the edges of silicon regions, close to the SiC grains, the silicon wavenumber is lower, closer to 520 cm^{-1}. The silicon region in the upper left including small SiC grains has lower wavenumber Si peak positions than the larger silicon regions. This matches the linescans where larger regions had higher wavenumbers (more compressive residual stress).

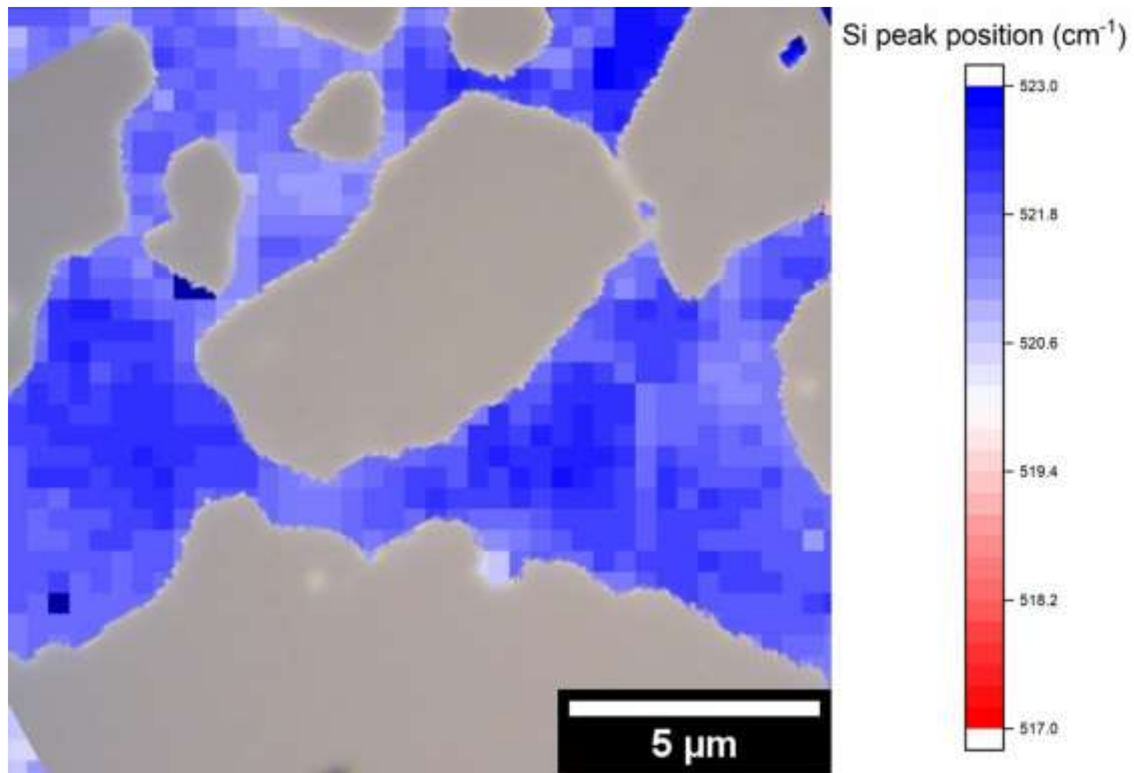

Figure 5-16: Area map of Raman peak position in residual silicon regions of in-house RB-SiC (overlaid with a 100x optical image)

Due to the three-dimensional microstructure of silicon regions, and the proposed origin of these stresses being crystallisation expansion of silicon, it could be assumed that within the interaction volume of each pixel the stress is approximately hydrostatic, so the piezospectroscopic coefficient of -533 MPa/cm could be used giving maximum compressive stresses of ~639.6 MPa. With the free surface, the σ_{33} stress could relax to zero, so the biaxial piezospectroscopic coefficient may be more appropriate. This gives a measured biaxial compressive stress of ~781.2 MPa.

5.1.5 Unirradiated nanoindentation cracking

5.1.5.1 Single crystal 6H-SiC

Single crystals of diamond cubic silicon and hexagonal 6H-SiC act as model reference materials for the deformation of polycrystalline RB-SiC. Their fracture response to nano-indentation deformation appears to be relatively simple.

Typically, the surface shows radial cracks emanating from the indenter corners shown in Figure 5-17. For single crystal silicon, in the cases where 1000 nm Berkovich indentation didn't cause large chipping fracture, cracks were 7.07 µm long, corresponding to a fracture toughness of 1.41 (1.94) MPa√m. 1000 nm Berkovich indents in 6H-SiC showed radial cracks 4.24 µm long on the surface, corresponding to a fracture toughness of 1.97 (2.71) MPa√m.

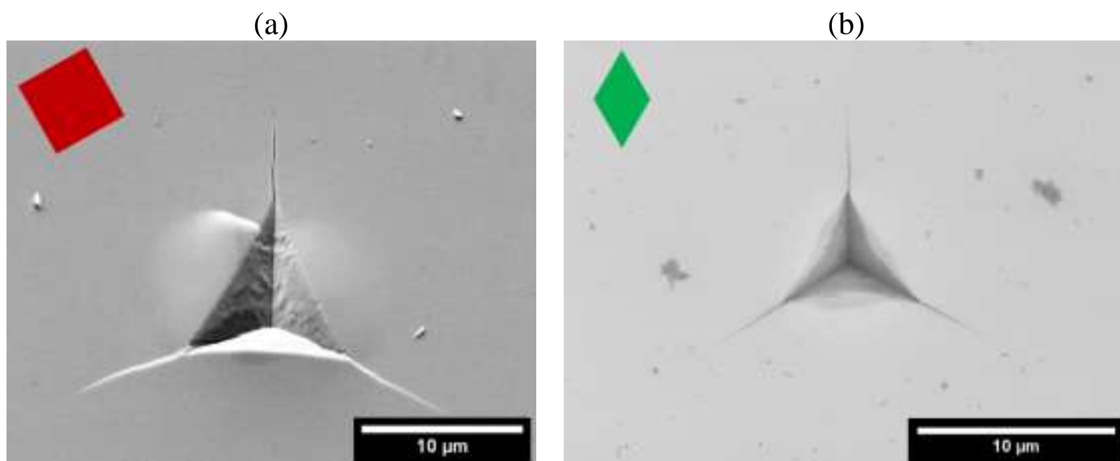

Figure 5-17: Berkovich nanoindents in (a) unirradiated single crystal silicon (001) and (b) unirradiated single crystal 6H-SiC (0001). The respective in-plane unit cell orientations are shown (SEM SE)

Elastic stress HR-EBSD maps were made of the 6H-SiC indent shown in Figure 5-17 (b). The tensor stress matrix is shown in Figure 5-18. The faces of the indent impression have residual compressive stresses extending at least 6 µm from the indent face (unfortunately just outside the scan area). Stresses are relieved by corner radial cracks, and there is a tensile stress ahead of the crack tip, seen in the σ_{11} map, and magnified in Figure 5-19. This horizontal tensile stress peaks around 600 MPa at the crack tip.

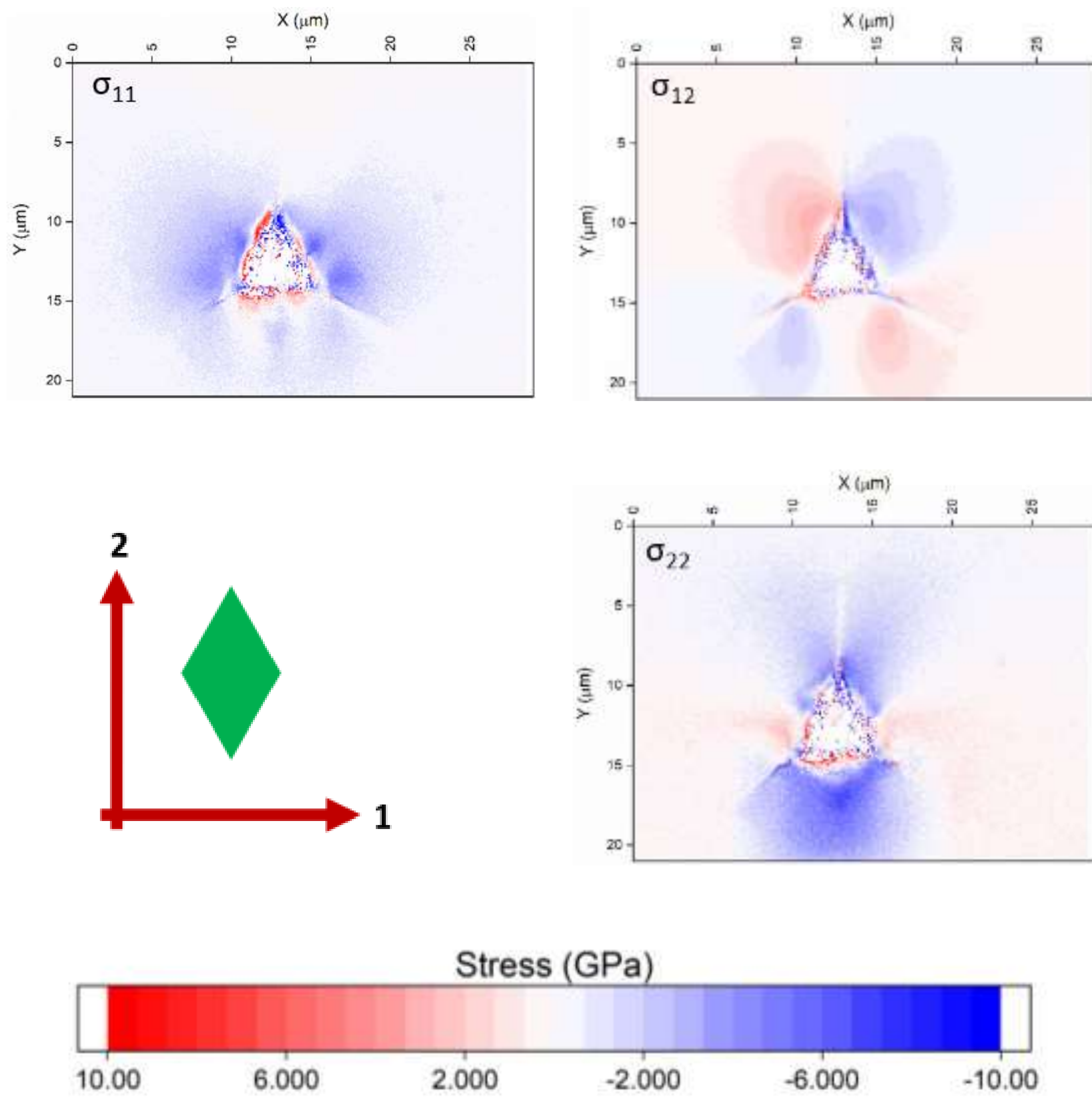

Figure 5-18: HR-EBSD Plane stress tensor of a 1000 nm Berkovich indent in unirradiated 6H-SiC with axes and the crystal unit cell orientation shown.

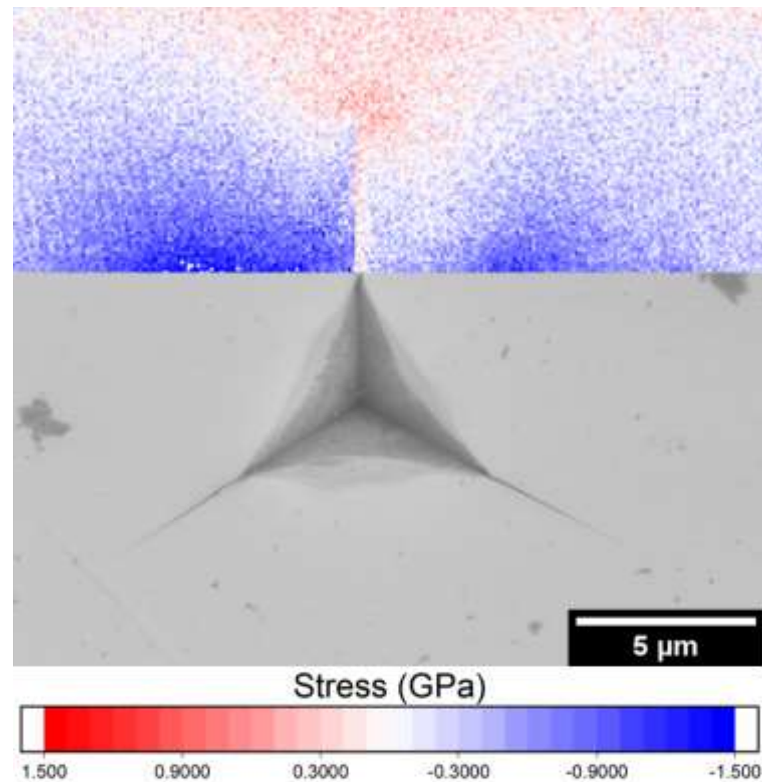

Figure 5-19: σ_{11} stress map from HR-EBSD showing the crack tip tensile stress in 6H-SiC

The planar von Mises stress and mean normal (biaxial) stress $((\sigma_{11} + \sigma_{22}) \div 2)$ is plotted for this unirradiated 6H-SiC indent in Figure 5-20 showing the extent of elastic deformation. The peak von Mises stresses are around 6-7 GPa. Near the lower indenter face there is a low stress corresponding to lower elastic stress, either by sub-surface fracture, or by plastic deformation. The biaxial stress component reaches a peak compressive stress of ~-4 GPa.

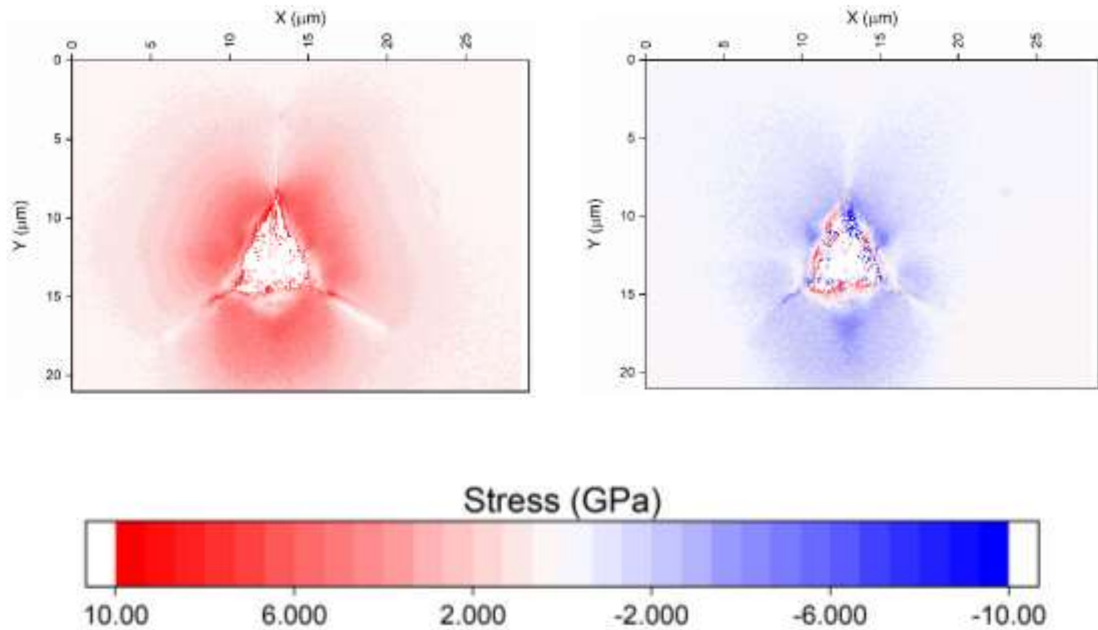

Figure 5-20: Planar von Mises stress and mean normal stress from HR-EBSD for a 1000 nm Berkovich indent in unirradiated 6H-SiC

Figure 5-21 shows a map of the 789 cm^{-1} 6H-SiC Raman peak position as it varies spatially around a 1000 nm Berkovich indent. Similar to the HR-EBSD stress maps, stress relief is seen along the crack paths, and a tensile stress can be seen at the crack tips. There is also a smaller peak position shift close to the indent faces, as seen in Figure 5-20, possibly caused by plastic deformation, pile-up, or fracture which don't contribute to Raman peak shifts. The peak shift at the crack tips is -1.3 cm^{-1} corresponding to a uniaxial tensile stress of 368 MPa based on the uniaxial constant in Table 4-3. The maximum peak shift in the compressive regions is +1.8 cm^{-1}. Assuming a hydrostatic stress state, σ = -510 MPa. If DiGregorio and Furtak are correct in claiming their piezospectroscopic coefficient is valid in non-hydrostatic conditions, an assumed biaxial stress would be -765 MPa and a uniaxial (σ_{22}) stress of 1.53 GPa [217]. The assumption of biaxial and uniaxial stress with this Raman shift and stress coefficient makes a better comparison to the HR-EBSD maps above. However, the Raman measured stresses are considerably lower than measured by HR-EBSD. This is probably due to the larger interaction volume in this transparent single

crystal incorporating some less strained material beneath the surface, despite the confocal aperture.

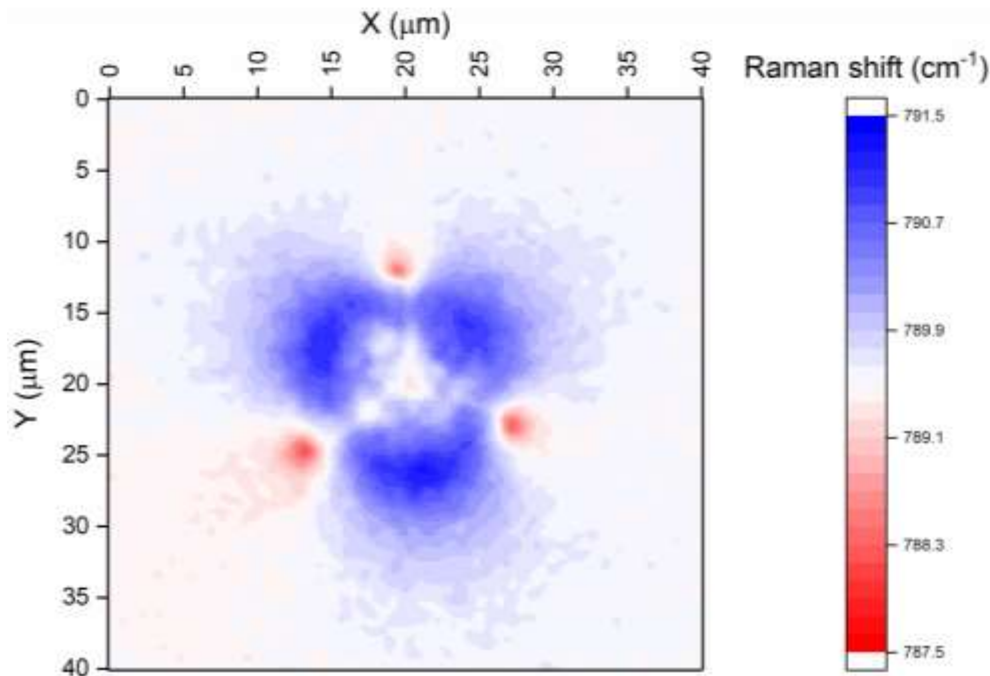

Figure 5-21: Raman shift map of the 789 cm^{-1} peak around a 1000nm Berkovich indent in unirradiated (0001) 6H-SiC

5.1.5.2 Nanoindentation cracking in unirradiated single crystal silicon

There was some variability in the fracture around nano-indents in silicon. The indent shown in Figure 5-17 (a) was taken as representative of most, however some indents such as the ones arrowed in Figure 5-27 show lateral cracks reaching the surface and chips being lifted up from the material surface.

HR-EBSD maps of these indents show the residual stresses. The tensor stresses for 1000nm Berkovich silicon indents are shown in Figure 5-22. Since this is plane stress, the stresses in the z direction out of the sample surface are 0 and not shown here.

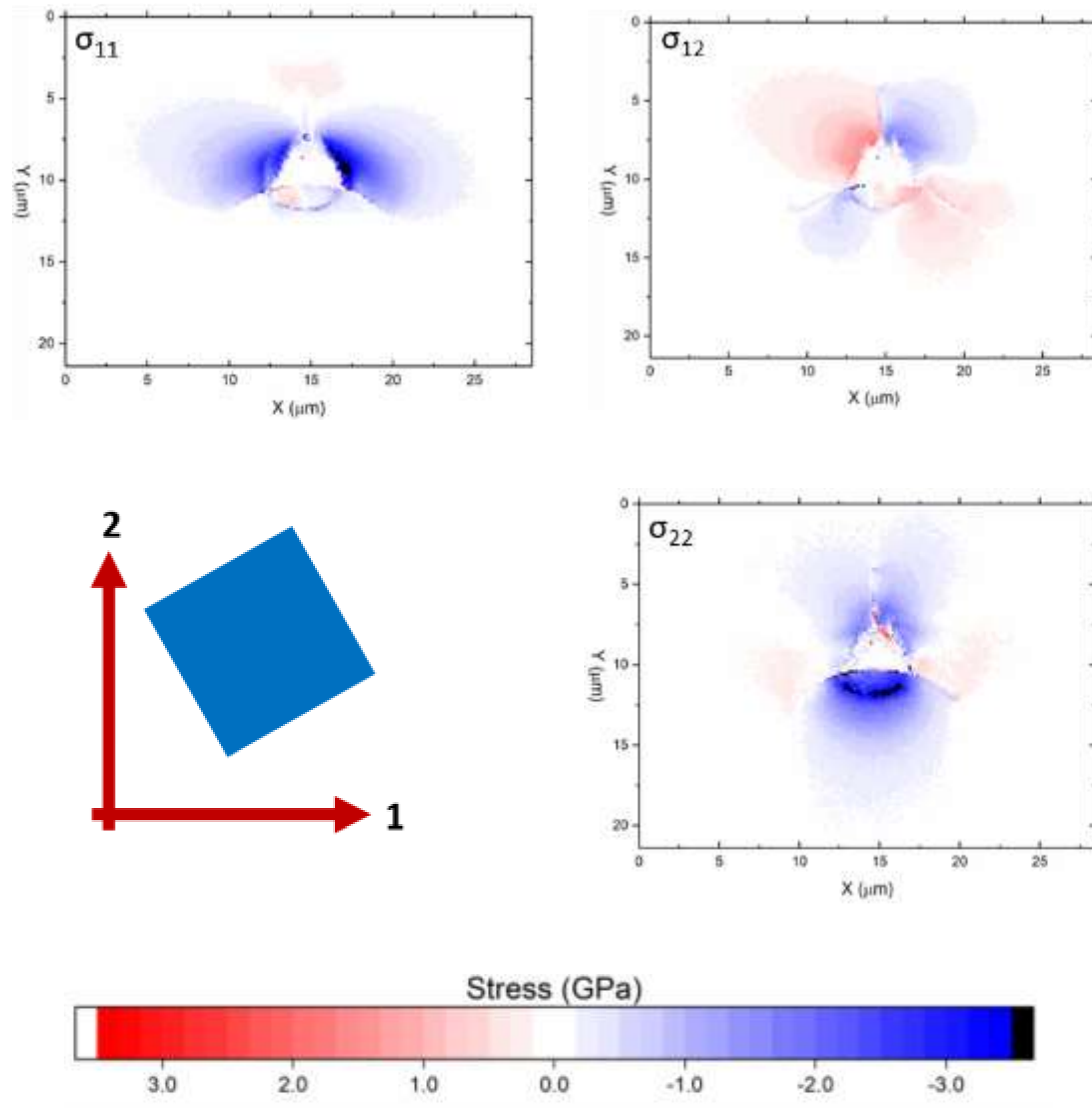

Figure 5-22: Residual stress maps from HR-EBSD for a 1000nm Berkovich indent into (001) single crystal silicon with the planar orientation indicated. Plane stress condition.

The σ_{11} map in Figure 5-22 shows a tensile residual stress at the crack tip, which decays with distance away from the crack tip (Figure 5-23). After around 4 µm the residual stress becomes negative (compressive) due to the indenter face compressing material, then tends to 0 after 10 µm.

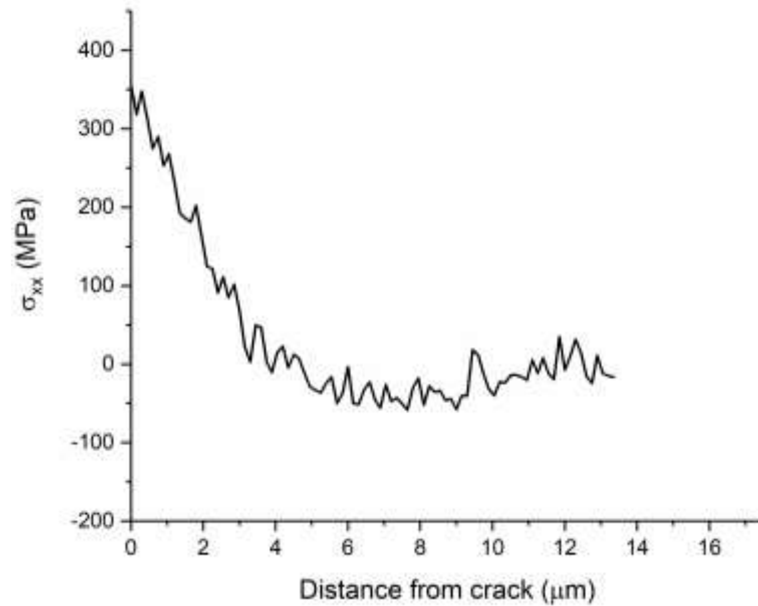

Figure 5-23: Horizontal residual stress with distance away from the crack tip.

The σ_{22} map in Figure 5-22 most clearly shows the compressive stress from the indenter face extending down 12 µm from the edge of the indenter impression to the bottom of the EBSD scan. There is a line of darker contrast which appears to correspond to a sub-surface crack changing the diffraction conditions. This is also visible in the map of geometrically necessary dislocations (GNDs) with the same contrast as the radial corner cracks (Figure 5-24). It appears that the discontinuity in the lattice caused by the cracks is being calculated into a high GND density.

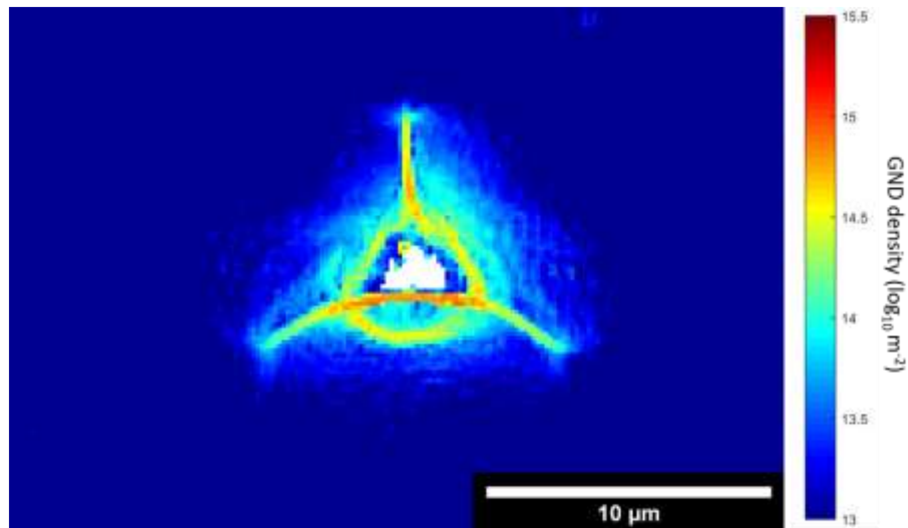

Figure 5-24: GND density map around a 1000 nm Berkovich indent into silicon (001). The green arrows indicate brighter contrast due to cracks, including the sub-surface/near surface lateral crack below the lower edge of the indent impression

The GND density map in Figure 5-24 shows plastic deformation is predominantly in a near circle connecting the indentation corners and tails off in density towards the crack tips. The elastic residual deformation extends considerably further from the indent impression, most clearly shown in the map of mean normal stresses (Figure 5-25). Elastic residual stresses appear to be relieved by the radial cracks while GND density remains high up to the cracks.

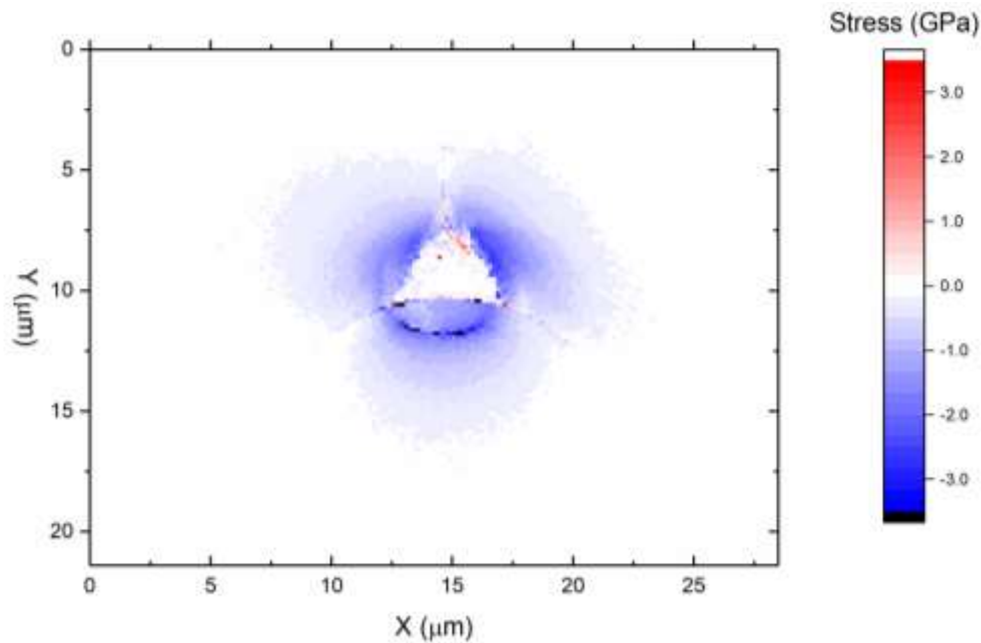

Figure 5-25: Mean normal (biaxial)l elastic stresses from HR-EBSD around a 1000nm Berkovich indent into (001) silicon.

As the spatial resolution of optical stress mapping is not as good as for an electron microscope, Raman peak position maps were made on a 2000 nm Berkovich indent in (001) single crystal silicon (Figure 5-26) rather than 1000 nm. No information is obtained for the direction of these stresses in the form of a stress tensor as no polariser and analyser were used; the peak shift corresponds to a mean stress on the interatomic covalent bonds in the Raman interaction volume. Determining the magnitude of these stresses is discussed in the methods, section 4.4.2. Assuming plane stress, as in the surface measurements using HR-EBSD, and a piezospectroscopic coefficient of -434 MPa/cm the peak stress is ~1.25 GPa in compression, similar to the measurements using HR-EBSD. The closer comparison for Raman piezospectroscopy mapping and HR-EBSD in silicon compared to 6H-SiC is probably due to the opacity of silicon to the 633 nm wavelength laser used in this experiment.

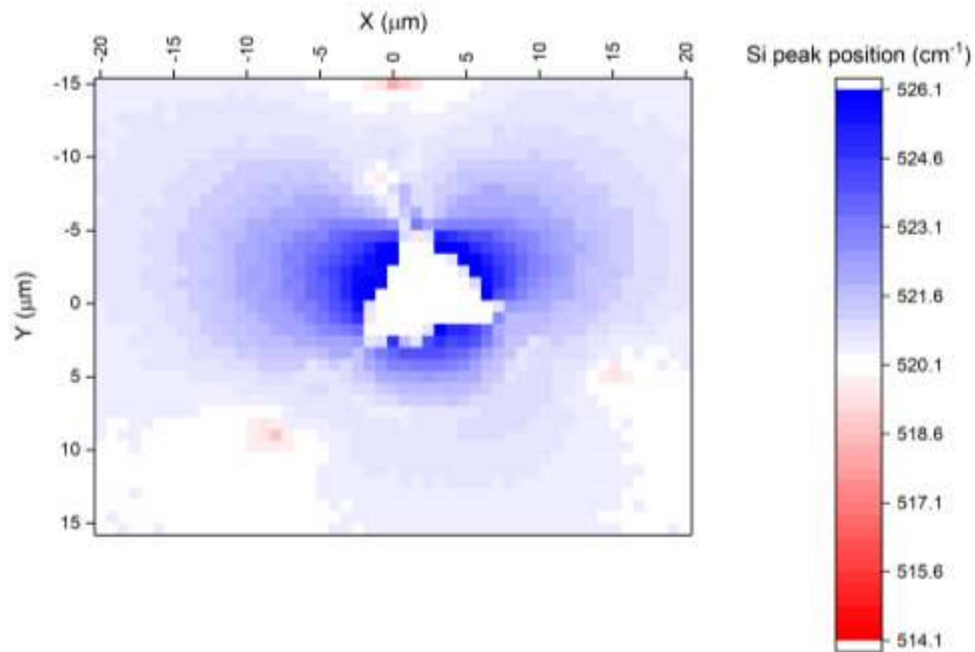

Figure 5-26: Raman peak position map of a 2000 nm Berkovich indent into single crystal silicon.

Figure 5-25 and Figure 5-26 are qualitatively similar, showing the compressive stress from indenter faces, and the tensile stress ahead of the crack tips. As the Raman peak position is not affected by cracks and crystal lattice rotations, cracks cannot be directly seen in this map, only the mean stress in that region, which is reduced near the radial cracks.

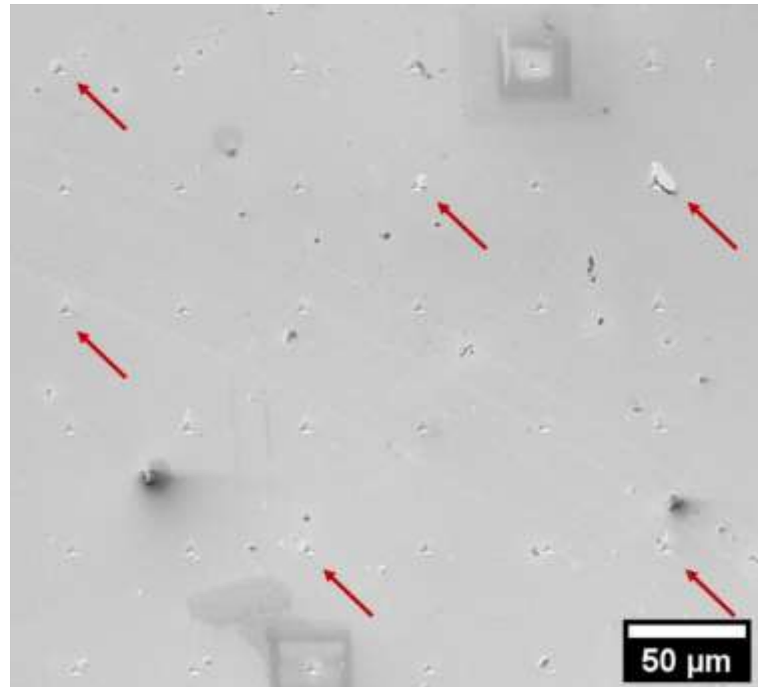

Figure 5-27: 1000 nm Berkovich indent array in (001) silicon. Arrowed indents show indents where lateral cracks reached the surface and material was chipped out. Contamination around indents 3 and 32 is due to carbon deposition during EBSD scans. (SEM SE)

Figure 5-17 (a) shows signs of sub-surface lateral fracture in silicon from the left-hand indenter face. Other indents in a 1000 nm array showed abnormal fracture with chips, or large lateral fracture (Figure 5-27). In deeper indents, chips of silicon were fractured from the indenter faces. Some shallower indents fractured more severely than deeper indents (Figure 5-28).

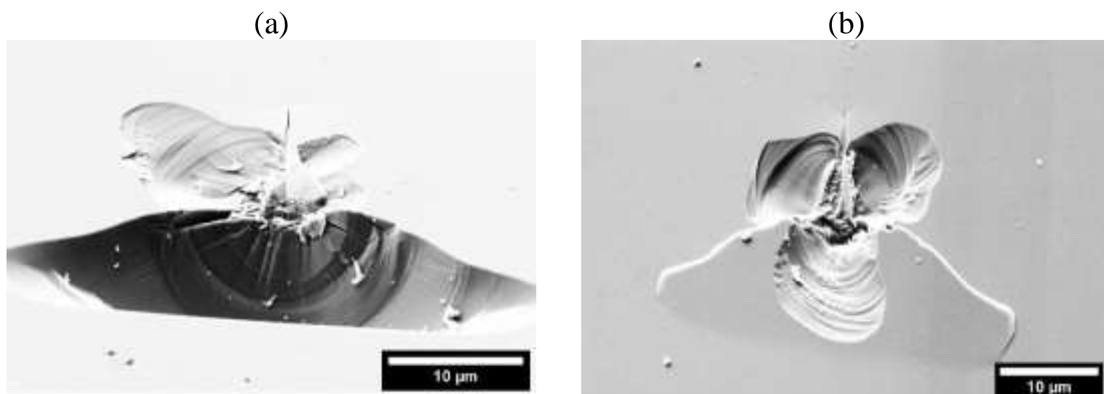

Figure 5-28: Fractured Berkovich indents in silicon (001) (a) 1750 nm. (b) 2000 nm. Sub-surface cracks are visible. (SEM SE)

5.1.5.3 Sub-surface crack morphology

To reveal the 3D crack morphology, FIB slice and view was used. Animated videos of these are available online (a link is in the appendix, section 8.1). At a critical point, the cracks jump forward in both single crystal silicon (Figure 5-29) and single crystal 6H-SiC (Figure 5-30), remaining stable at that length during the following slices. In silicon, the cracks grew up to the edge of the FIB milled trench and can be seen below the surface in the cross-section. In 6H-SiC, the cracks do not extend to the edge of the trench, and nothing can be seen below the surface.

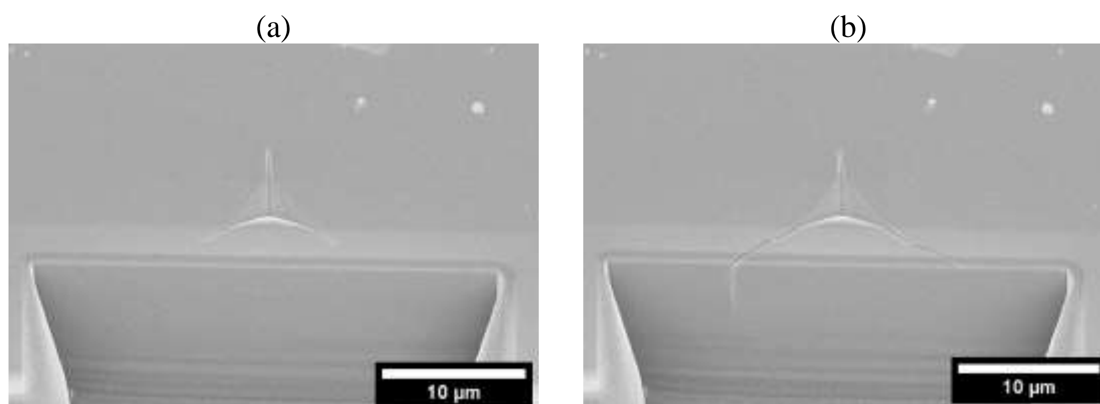

Figure 5-29: FIB slice and view (SEM in-lens) of 1000 nm Berkovich indent in silicon single crystal. (a) is the slice before crack extension. (b) is the slice immediately after crack extension

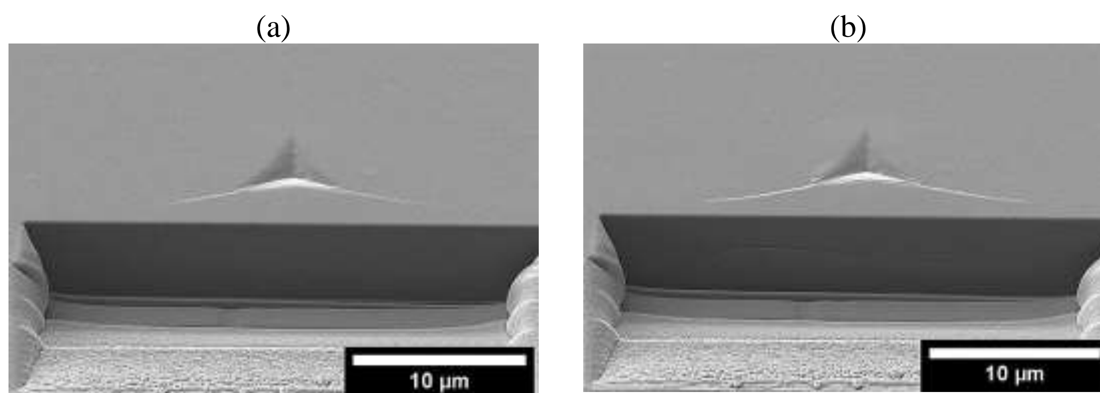

Figure 5-30: FIB slice and view (SEM SE) of 1000 nm Berkovich indent in 6H-SiC single crystal. (a) is the slice before crack extension. (b) is the slice immediately after crack extension

FIB slice and view from a corner into the indent impression rather than from an indenter face still shows cracks growing as material is removed (Figure 5-31). The radial

crack was 4.25 µm long before growing to the edge of the milled trench at a length of 5.66 µm.

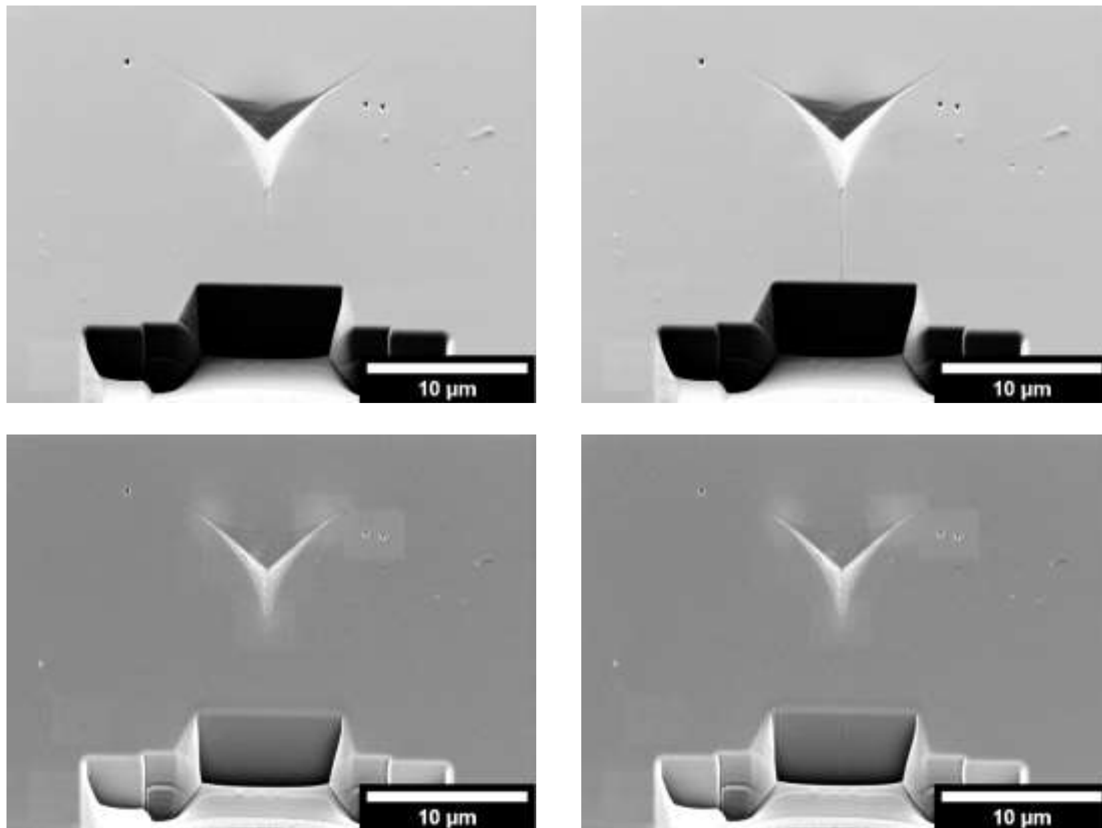

Figure 5-31: Subsequent FIB slice and view from a corner of an unirradiated 6H-SiC indent inwards, showing radial cracks growing on the surface and appearing below the surface. Top is the secondary electron image, below is from the in-lens detector and shows the sub-surface cracks more clearly because of the sample tilt geometry.

With further slices a lateral crack appears to the right of the radial crack and connects to the radial crack from the upper right corner of the indent impression (Figure 5-32). This lateral crack only appeared during FIB slicing. It is not a result of indentation, but of stress relief.

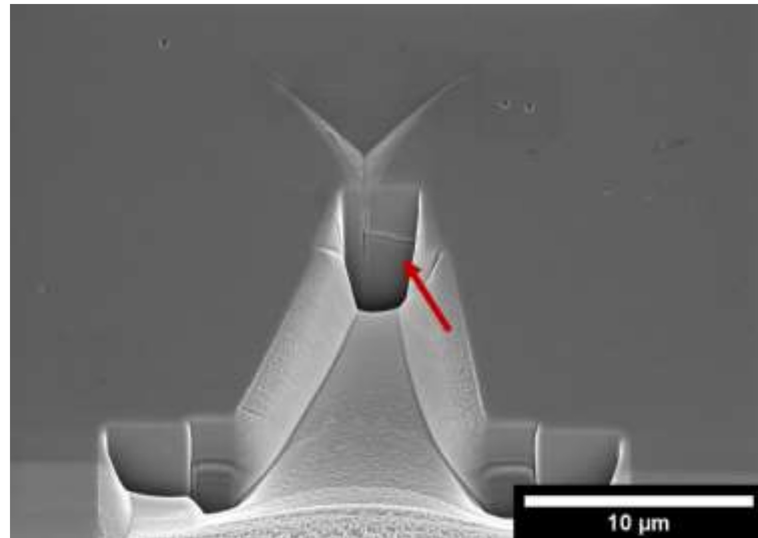

Figure 5-32: Appearance of a lateral crack under a 1000 nm Berkovich indent in 6H-SiC (SEM in-lens)

The left-hand lateral crack appears at the same time as the upper left radial crack extends (Figure 5-33). Further FIB slices seen in the video show that the lateral cracks connect radial cracks.

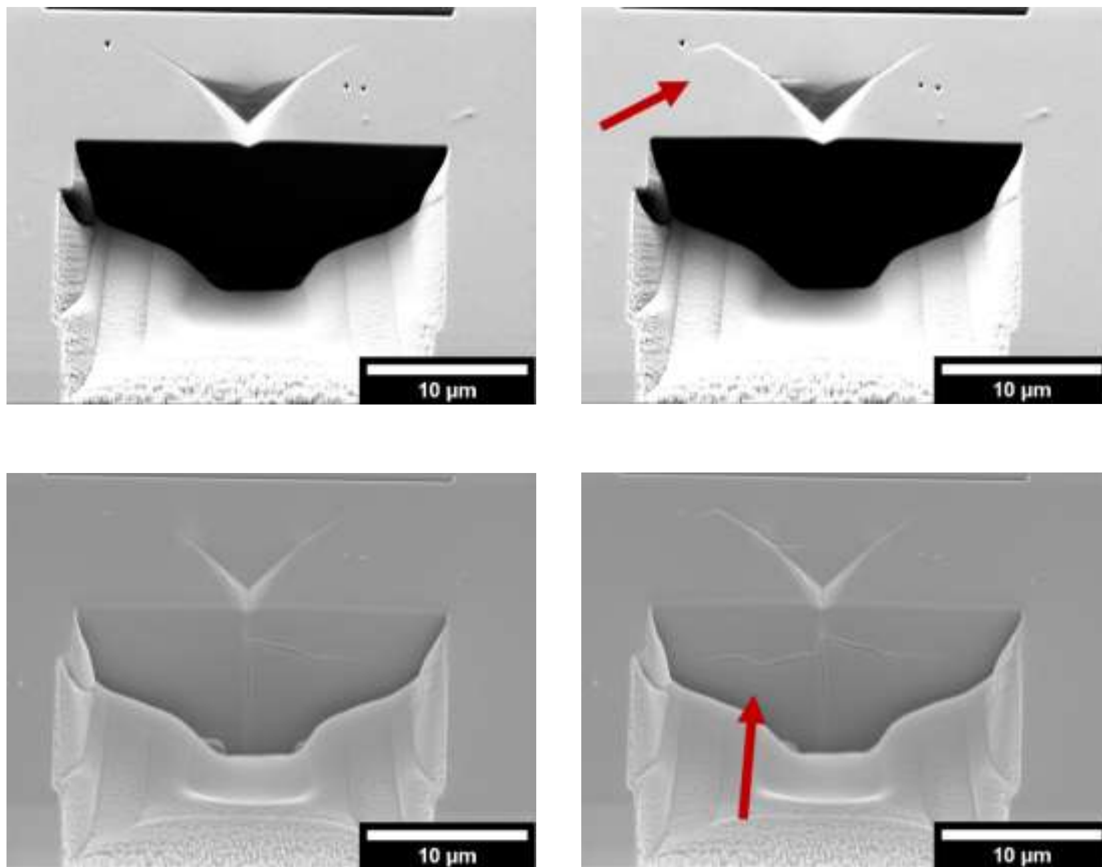

Figure 5-33: Lateral cracks grew during FIB silicing in the same frame as the radial crack grew. Further slices showed that these are connected. Top row are SEM SE images, bottom row are SEM in-lens detector images

Since the sub-surface cracks are changing during this crack extension, it appears impossible to know the sub-surface crack morphology without altering it using this measurement technique.

For one of the silicon indents, cross-sectional milling was stopped as soon as the cracks grew, then the indent was mapped using Raman piezo-spectroscopy (Figure 5-34). HR-EBSD could not be used as even a single FIB imaging scan damaged the surface preventing a suitable EBSD pattern being formed. After the crack growth, no compressive stress is found below the bottom face of the indent impression, showing that the compressive residual stress has been relieved by milling the trench. With no compressive residual stress acting to close the cracks from the bottom indent corners, they have grown.

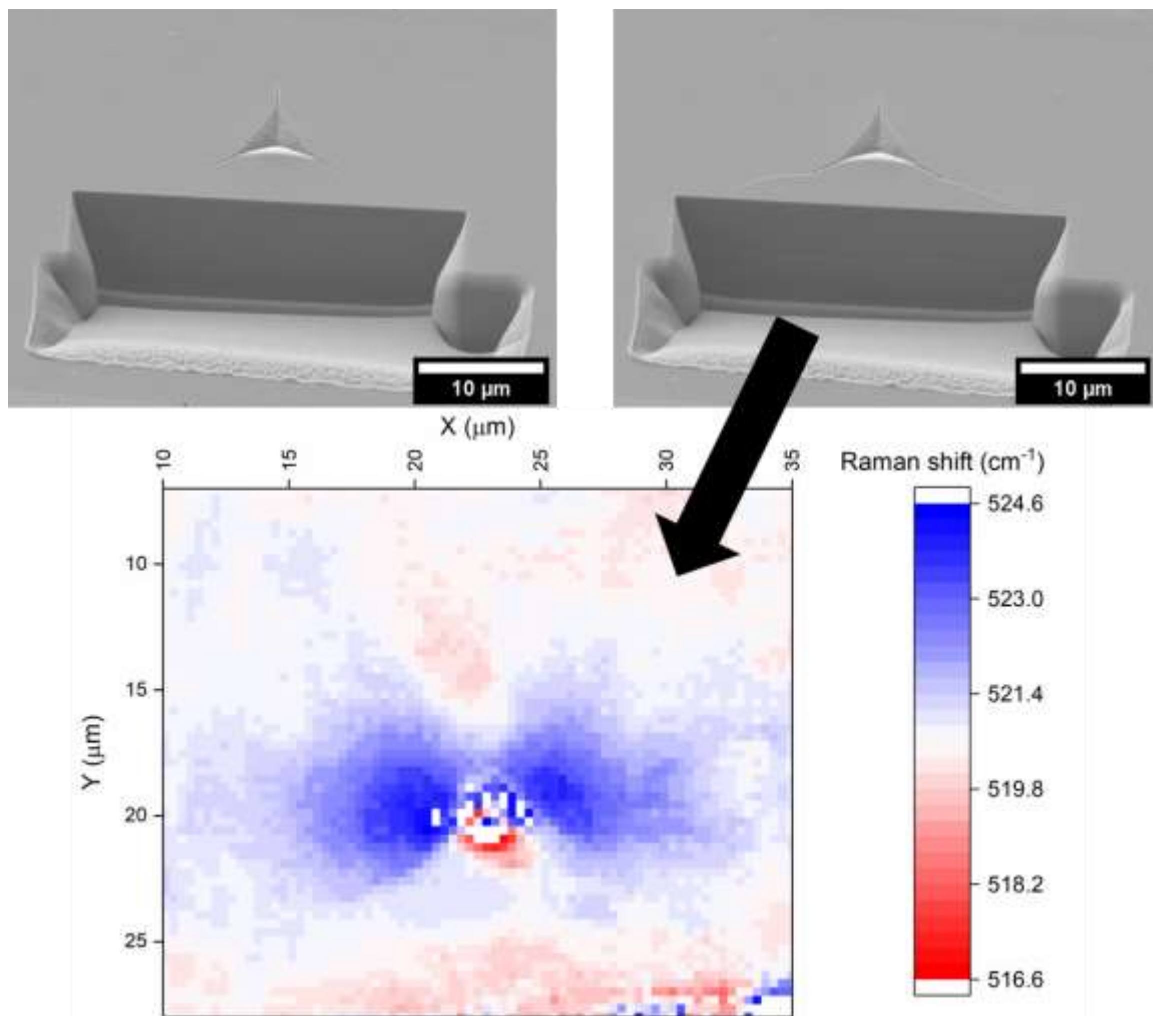

Figure 5-34: 1000 nm Berkovich indent in single crystal silicon (SEM SE) (a) is the slice before cracks grew, (b) is the slice after crack growth at which point the slicing was stopped. (c) is the Raman silicon peak position map of this

indent showing the blue compressive lobes at the side faces of the indent impression and the red tensile stress at the crack tip. The edge of the milled trench can be seen at the bottom of this image.

Another interesting feature is the rotation of radial corner cracks in 6H-SiC relative to the indenter orientation, as shown in Figure 5-35. The cracks are approximately 13° away from the angle of the indenter corners. This is expected to be due to the triangular indenter deforming a hexagonal crystal. There was no systematic investigation of crystallographic orientation relative to the indenter orientation here, but an investigation in the literature showed no effect of indenter orientation on mechanical properties in the c-plane [209]. However, their indentations in the {01-10} plane cracked preferentially along cleavage planes rather than emanating radially from the corners, and these indents had lower fracture toughness, hardness and modulus.

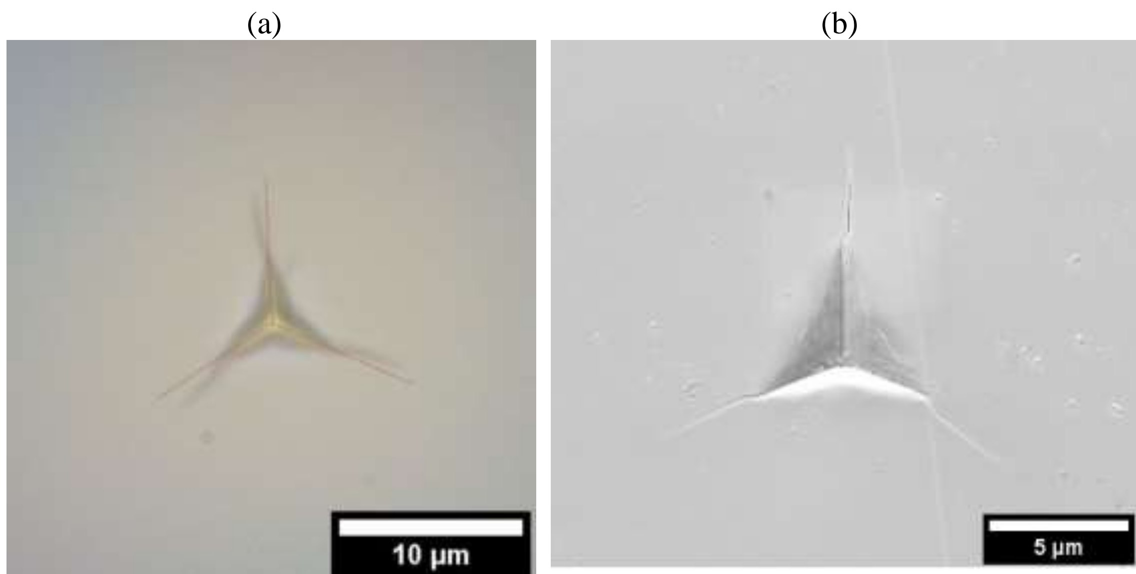

Figure 5-35: (a) 100x Optical and (b) SEM SE micrographs of selected 1000nm Berkovich nanoindents in 6H-SiC. The radial cracks are rotated relative to the indenter orientation, as highlighted by the red lines in the optical image

5.1.5.4 Nanoindents in polycrystalline RB-SiC

As a brittle ceramic, silicon carbide fractures to accommodate deformation during nanoindentation. In RB-SiC this fracture is particularly complicated due to the two-phase microstructure and the spatial variation of residual stresses in these phases (see section 5.1.4). The silicon regions appear resistant to indentation fracture, even when the indenter

corner is in the silicon region (Figure 5-36 (a)). SiC grains fracture transgranularly from the indenter corners in Figure 5-36 (a) and (b), while in (c) the crack from the top indent corner is deflected along the grain boundary, which also fractures inside the indent impression. Figure 5-36 (b) has a crack through the right indenter face extending transgranularly until stopping at the next grain boundary. This crack also extends inside the indent impression. The crack from the bottom right corner of Figure 5-36 (c) crosses through the boundary between reaction formed SiC layers (brighter contrast) and the darker starting SiC grain without deflection reiterating the strong coherent epitaxial interface.

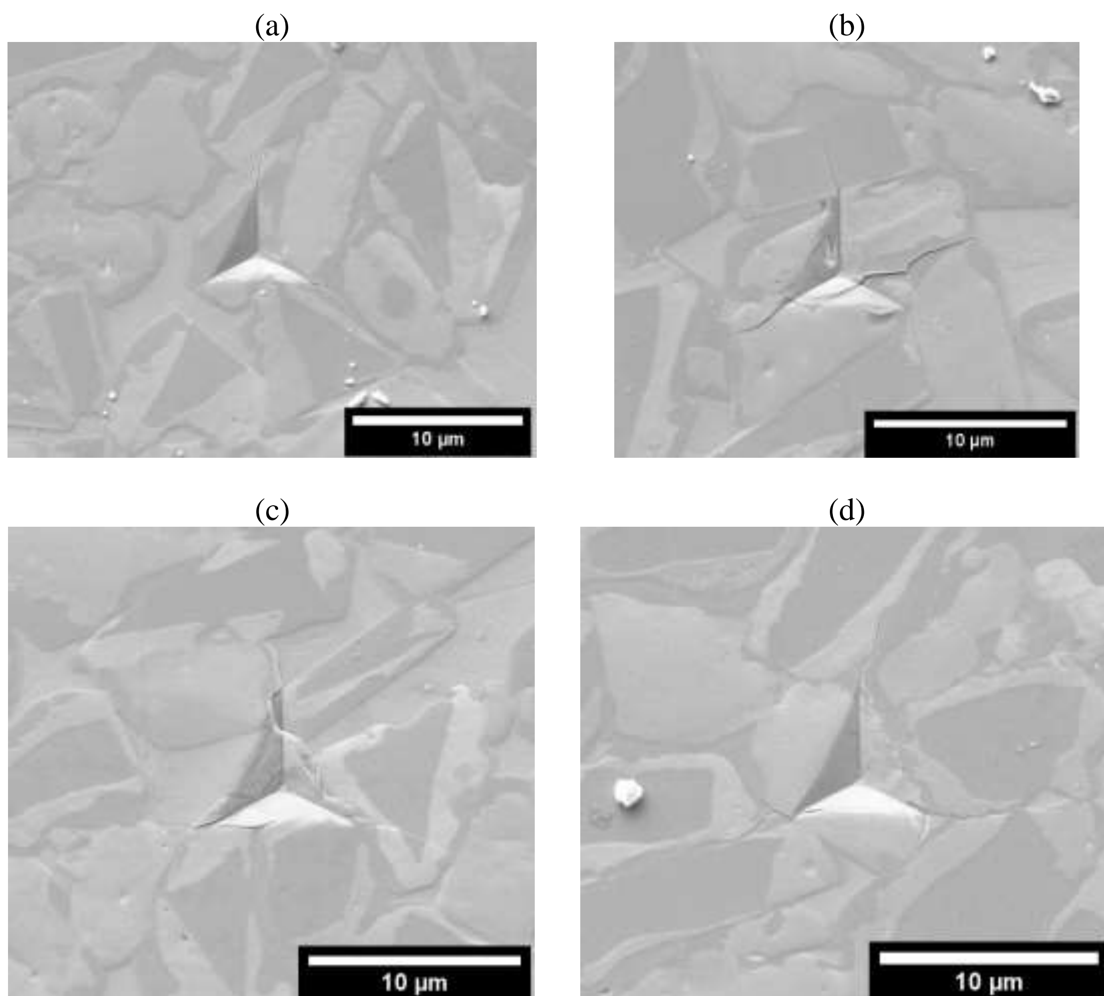

Figure 5-36: 1000 nm Berkovich indents in unirradiated REFEL (SEM SE). (a) shows radial cracks into SiC grains, but not into silicon. (b) shows non-uniform fracture in SiC grains. (c) shows intergranular fracture in the top corner of the indent impression. (d) has a lateral crack on the right edge of the indent impression and the bottom left radial crack is deflected along a Si-SiC boundary before continuing through SiC. The bottom right radial crack passes through SiC, then stops at the silicon region.

1000 nm indents in unirradiated in-house RB-SiC fracture the silicon regions as well as the SiC grains (Figure 5-37 (a)). Based on the cracks in Figure 5-37 (a) and the nanoindentation load for that indent, the apparent fracture toughness of silicon in RB-SiC was estimated as 2.3 MPa√m. This is not necessarily correct as part of the indentation is into SiC and it is unclear what is below the surface.

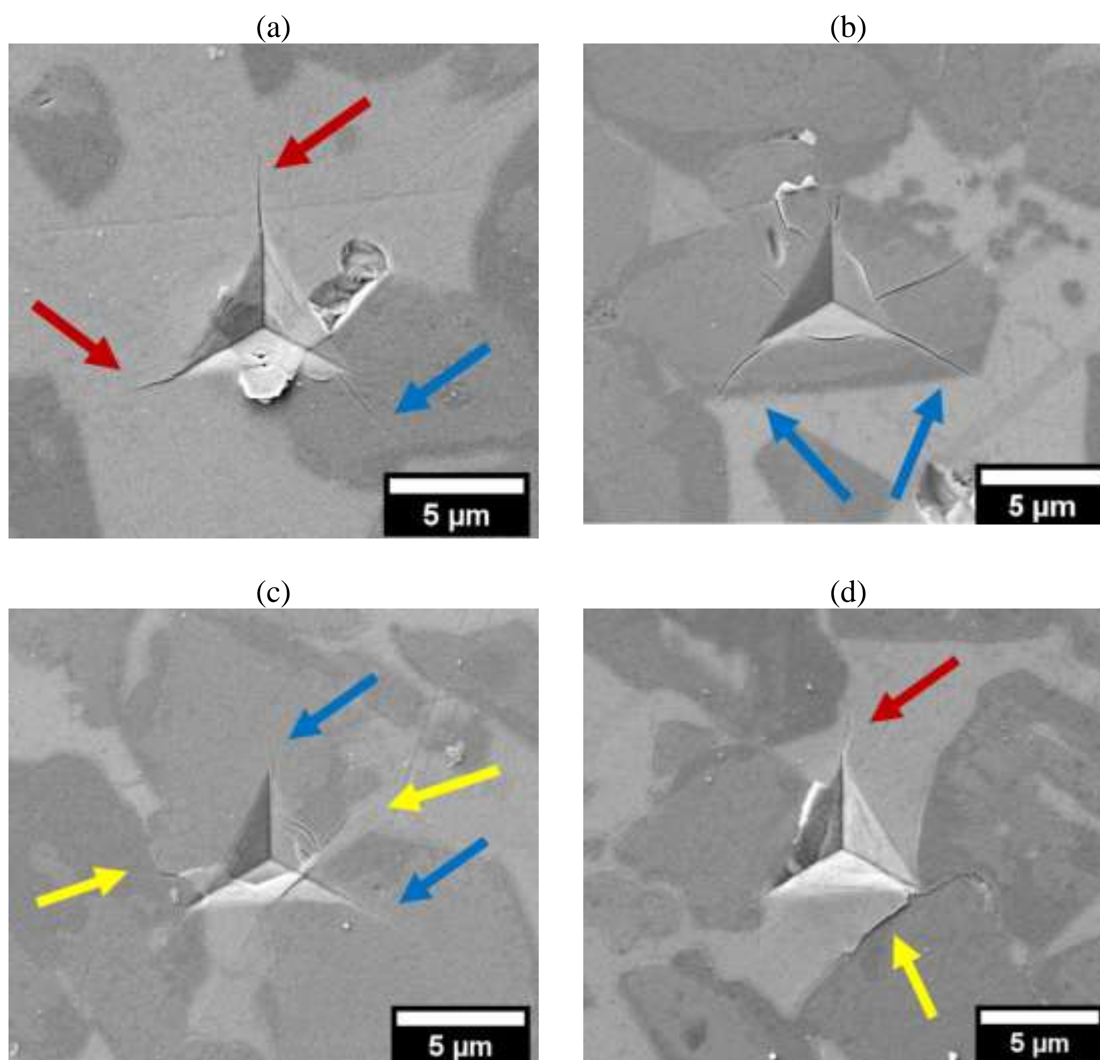

Figure 5-37: 1000 nm Berkovich indents in unirradiated in-house RB-SiC (SEM SE). Red arrows indicate radial cracks in silicon, blue arrows radial cracks in SiC, yellow arrows cracks along Si-SiC interfaces.

In RB-SiC, nanoindentation typically results in enhanced cracking in SiC grains compared to the single crystals, and subdued cracking in silicon regions due to residual compressive stress.

5.2 Radiation damage

5.2.1 Radiation-induced changes to hardness and modulus of single crystals

Mechanical properties were investigated using nanoindentation, as the technique is applicable to the small volume of ion implantation damaged material as well as the unirradiated material. The first ~200 nm are dominated by tip calibration and surface effects from polishing, so the region of interest is taken at depths deeper than this. Noisy tip calibrations and surface effects are filtered out, particularly in the case of the 2.5 dpa 300 °C Si ion implanted SiC in Figure 5-38. 500 nm indent arrays are used to reduce overlap of the indenter with multiple phase regions in RB-SiC, and to minimise the effect of the unirradiated substrate on mechanical property measurements.

Single crystal 6H-SiC results show significant hardening due to 2.5 dpa ion irradiation at 300 °C, (~5 GPa). This appears to be independent of whether the implanted ion was neon or silicon. The reduction in modulus is also similar for both silicon and neon 2.5 dpa implantation. At deeper depths, the elastic modulus tends towards the unirradiated value. The 0.25 dpa 750 °C sample shows far less hardening, (0.5-1.5 GPa), but a similar reduction in stiffness as the high dose irradiations.

These datasets show the importance of using the same tip calibration for measuring irradiated and unirradiated regions and comparing *changes* in properties rather than directly comparing values. In SiC which is extremely hard and stiff, different tip calibrations are exaggerated.

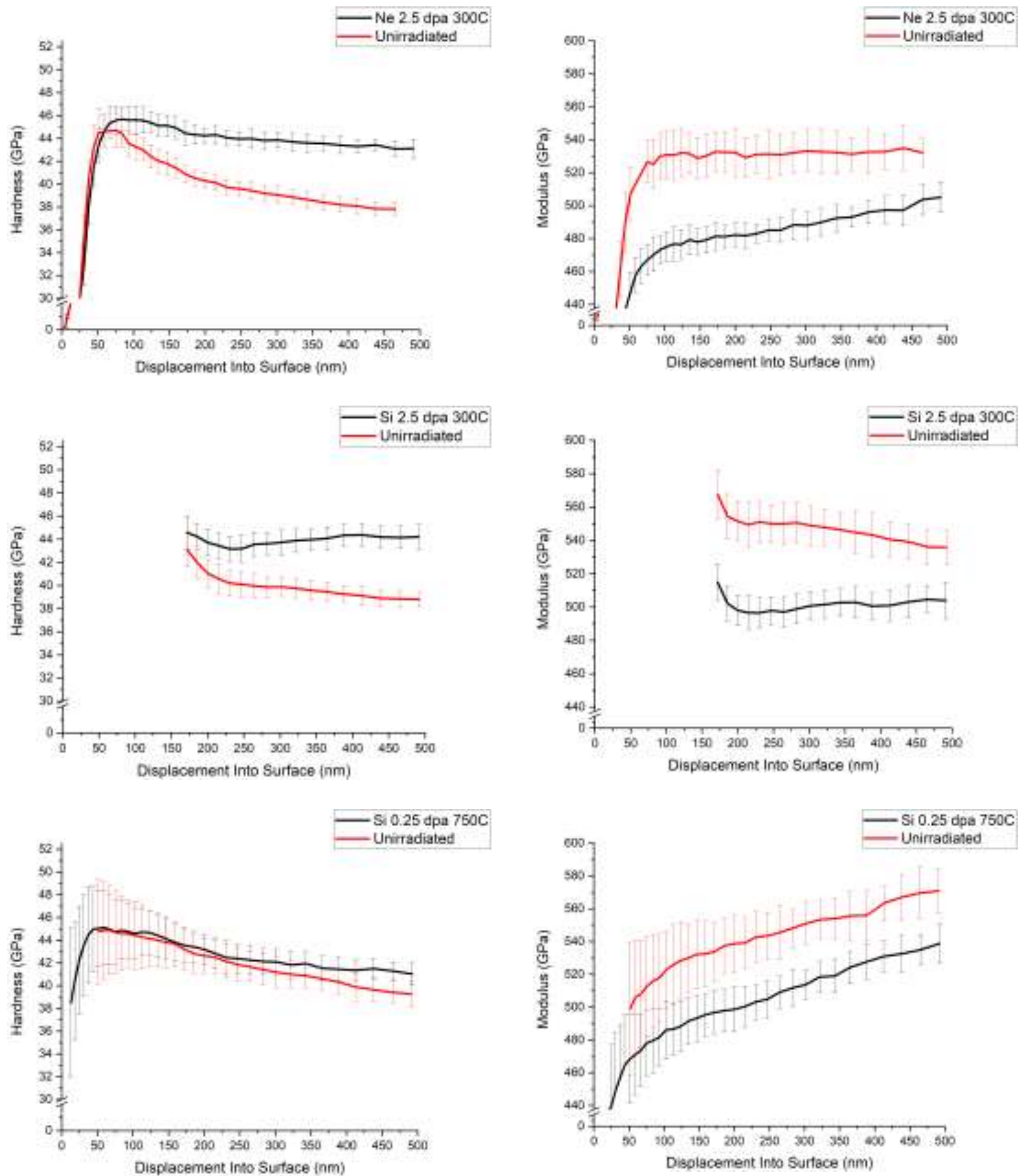

Figure 5-38: Ion implantation induced hardness and elastic modulus in 6H-SiC single crystals

Figure 5-39 compares the changes in hardness and modulus caused by the different irradiation conditions. These graphs are plotted for depths greater than 200 nm to avoid the surface effects. While modulus change reduces with depth and tends towards the unirradiated value, hardness change increases with depth through the irradiated layer. The hardening with depths appears to level out from around 400 nm, approximately coinciding with the flat-ish peak damage profile predicted from SRIM.

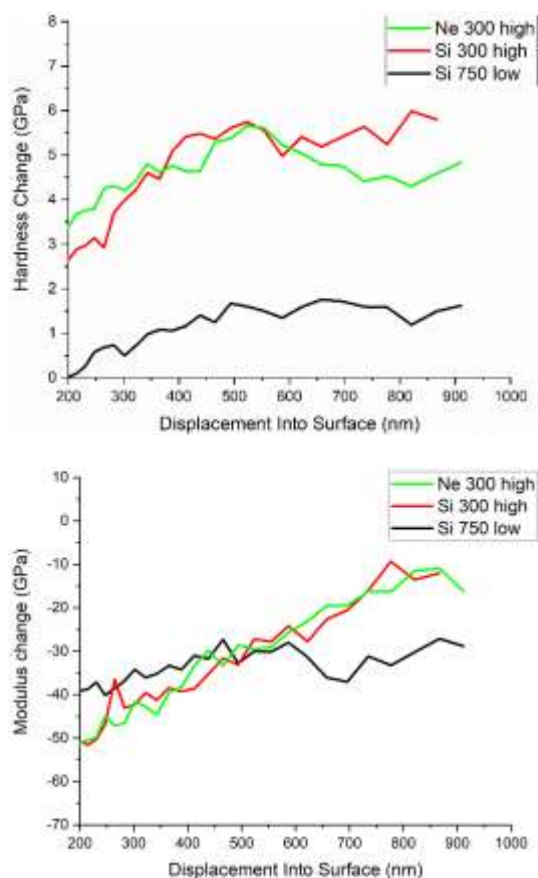

Figure 5-39: Changes in hardness and elastic modulus for the three irradiation conditions of 6H-SiC single crystals.

Ion irradiated single crystal silicon samples showed no change in hardness or modulus compared to unirradiated regions of the same samples, however there seems to be a larger standard deviation error after irradiation (Figure 5-40).

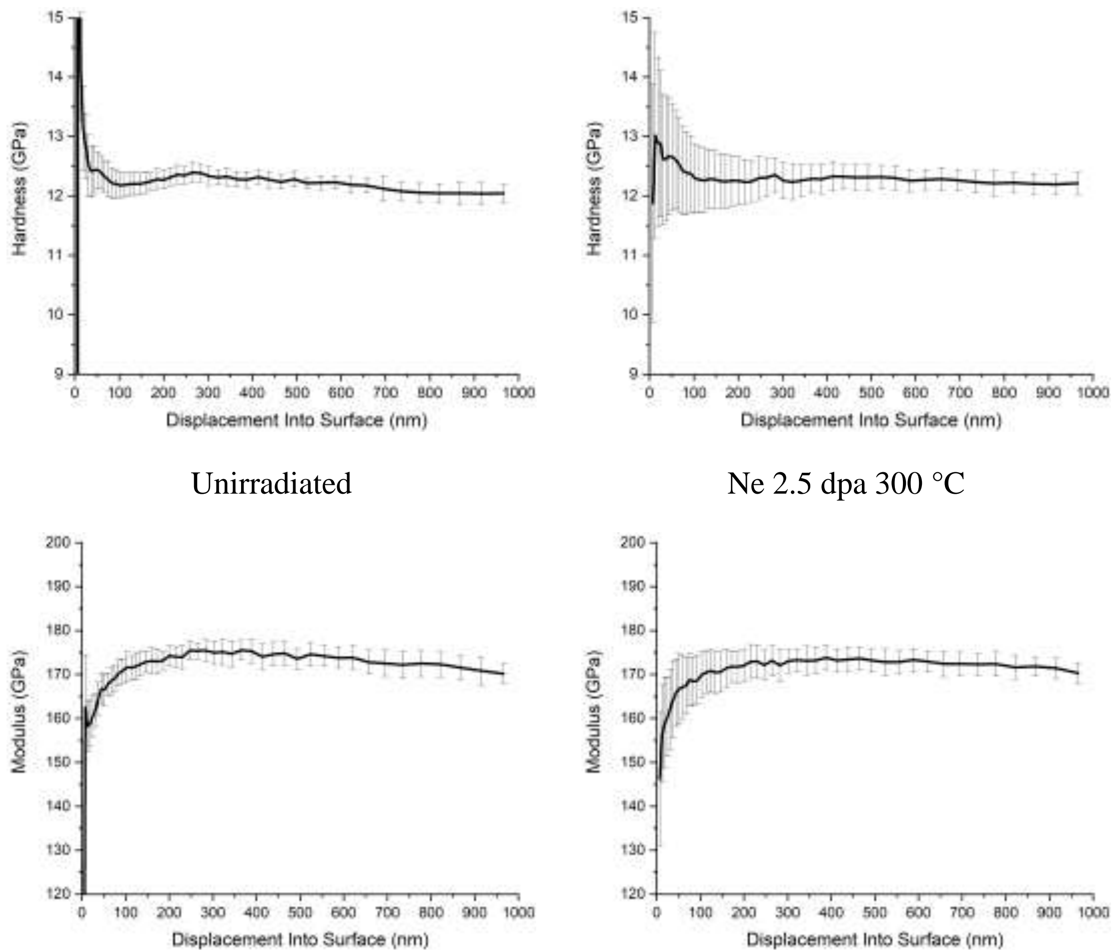

Figure 5-40: Nanoindentation hardness and modulus for single crystal silicon. Hardness and modulus are the same after irradiation, however standard deviation error bars have increased after irradiation

5.2.2 Radiation-induced changes to hardness and modulus of RB-SiC

Nanoindents in RB-SiC are difficult to analyse as each indent will be measuring the properties of a mixture of phases with very different properties. This gives a spectrum of mechanical responses across the indent array, ranging from soft silicon to hard SiC. A typical array of nanoindents in reaction-bonded SiC is shown in Figure 5-41 for neon irradiated in-house SiC. Sometimes the hardness curve will begin hard where the indenter tip initially interacts with SiC, then drops off as the sampling volume includes more silicon. The inverse is also observed in some indents. Elastic modulus is a longer-range effect, so an indent which appears hard and is attributed to SiC, may have a low elastic modulus if there is a large proportion of silicon in the elastic deformation region. Additionally, elastic measurements will include a contribution from the undamaged substrate, apart from the

shallowest depths where surface and tip calibration effects may be dominant. For this reason, hardness is considered the more useful property to measure.

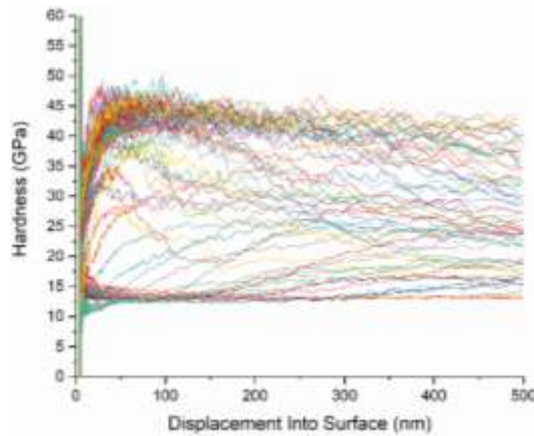

Figure 5-41: Typical nanoindentation hardness curves for reaction-bonded SiC showing a range of mechanical responses

Figure 5-42 show the response of conventional RB-SiC to neon ion irradiation. Curves where the indentation has included both phases are filtered out to show the response of SiC and silicon regions alone for easier comparison of the radiation effects. There is still some spread in the properties of SiC (~40 GPa), and silicon (~14 GPa) due to the microstructural environment of the indentations. The hardness of silicon in RB-SiC appears higher than in the single crystal. This may be caused by the processing-induced compressive residual stress. The other irradiation conditions produce similar graphs to those in Figure 5-42, and the changes are summarised in Table 5-1 & Table 5-2 with bar charts to more easily visualise the effects of samples and radiation conditions.

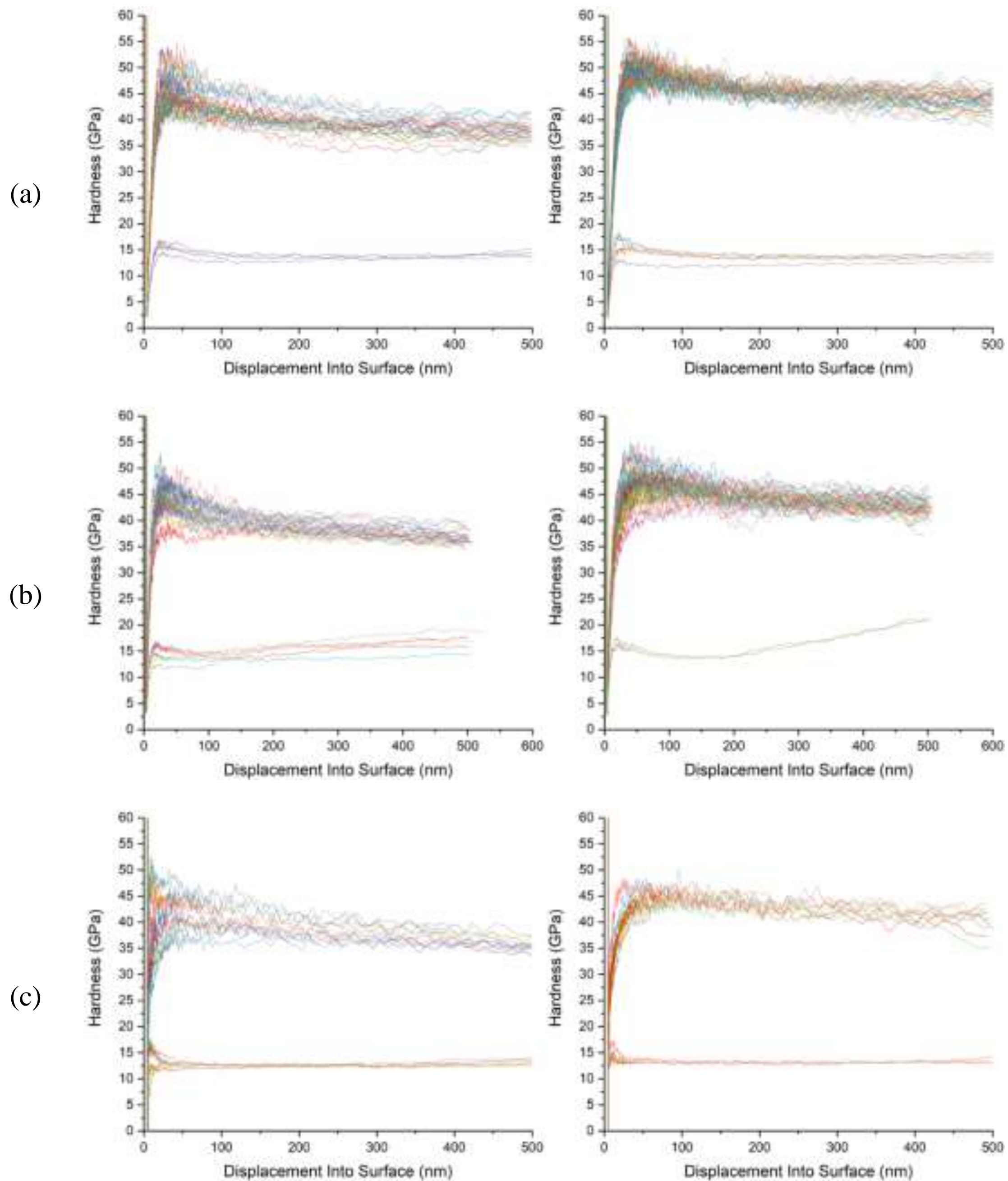

Figure 5-42: Nanoindentation hardness of neon ion irradiated samples of conventional RB-SiC. Left hand graph is unirradiated, right hand is irradiated. (a) is Starceram, (b) is REFEL, (c) is in-house RB-SiC.

As shown in Figure 5-42 no significant change is caused to the hardness of silicon regions in Starceram or in-house RB-SiC. The silicon regions in REFEL are too small to accurately indent. The resistance of silicon to measurable changes in mechanical properties agrees with indents in single crystal silicon (Figure 5-40).

The general trend for microstructural effects on hardness is that reducing grain size decreases radiation-induced hardening. In-house RB-SiC and REFEL have similar grain

sizes, but REFEL SiC is highly connected, while in-house RB-SiC is mostly isolated with more SiC-Si boundaries. In-house RB-SiC is hardened less by radiation than REFEL. The Si-Cr sample has the smallest SiC grains, and shows the least hardening, while Starceram has the largest SiC grains and the most hardening.

At 2.5 dpa, the effect of temperature seems insignificant – samples harden by approximately the same amount whether irradiated at 300 °C or 750 °C. At 0.25 dpa samples irradiated at 300 °C harden more than irradiated at 750 °C. Neon ion implantation appears to cause less hardening than the corresponding silicon ion implantation.

Table 5-1: Summary of radiation-induced changes to hardness of SiC regions in RB-SiC. Standard deviation is ~2%

Material	Ne 300 °C 2.5 dpa	Si 300 °C 2.5 dpa	Si 750 °C 2.5 dpa	Si 300 °C 0.25 dpa	Si 750 °C 0.25 dpa
Starceram	+15.2%	+18%	+17.2%	+17.4%	+14.6%
REFEL	+14.5%	+16.2%	+16.7%	+16.7%	+14.9%
In-house	+12.5%	+13.0%	+11.2%	+14.4%	+14.3%
Si-W	+13.7%				
Si-Cr	+10.72%				

Table 5-2: Radiation changes to elastic modulus of SiC regions in RB-SiC. Standard deviation is ~2%

Material	Ne 300 °C 2.5 dpa	Si 300 °C 2.5 dpa	Si 750 °C 2.5 dpa	Si 300 °C 0.25 dpa	Si 750 °C 0.25 dpa
Starceram	-8.02%	-9.54%	-2.04%	-4.65%	-2.03%
REFEL	-6.80%	-3.84%	-3.43%	-4.16%	-2.34%
In-house	-5.52%	-7.37%	-4.06%	-9.14%	-8.24%
Si-W	-9.35%				
Si-Cr	-9.90%				

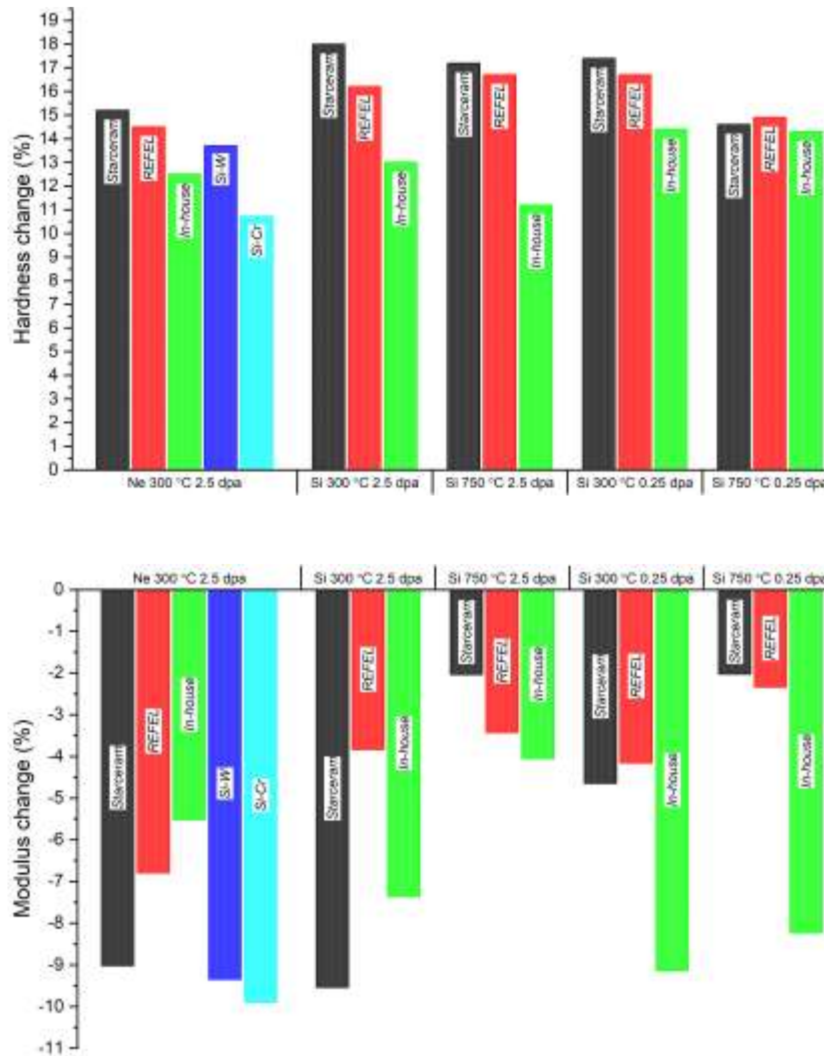

Figure 5-43: Bar charts of hardness and modulus change in ion irradiated RB-SiC.

5.2.3 Radiation changes to nanoindentation deformation

5.2.3.1 Single crystal

Compared to unirradiated single crystal 6H-SiC (Figure 5-17 (b)), irradiated 6H-SiC has a significant visual difference in the absence of radial cracks from the corners of the indent impression (Figure 5-44). The two high dose irradiated single crystal samples have no observable cracks, while the low dose, high temperature sample (Figure 5-44 (c)) has short cracks ~560 nm long.

Using equation (4-1) with the indentation cracks in Figure 5-44 (c) , the apparent fracture toughness of 6H-SiC after 0.25 dpa Si implantation at 750 °C is 14.1 (19.4) MPa√m, or 7.2 times larger than the unirradiated single crystal 6H- SiC. This equation can't be used with the indents in high dose irradiated single crystal SiC as there are no cracks to measure.

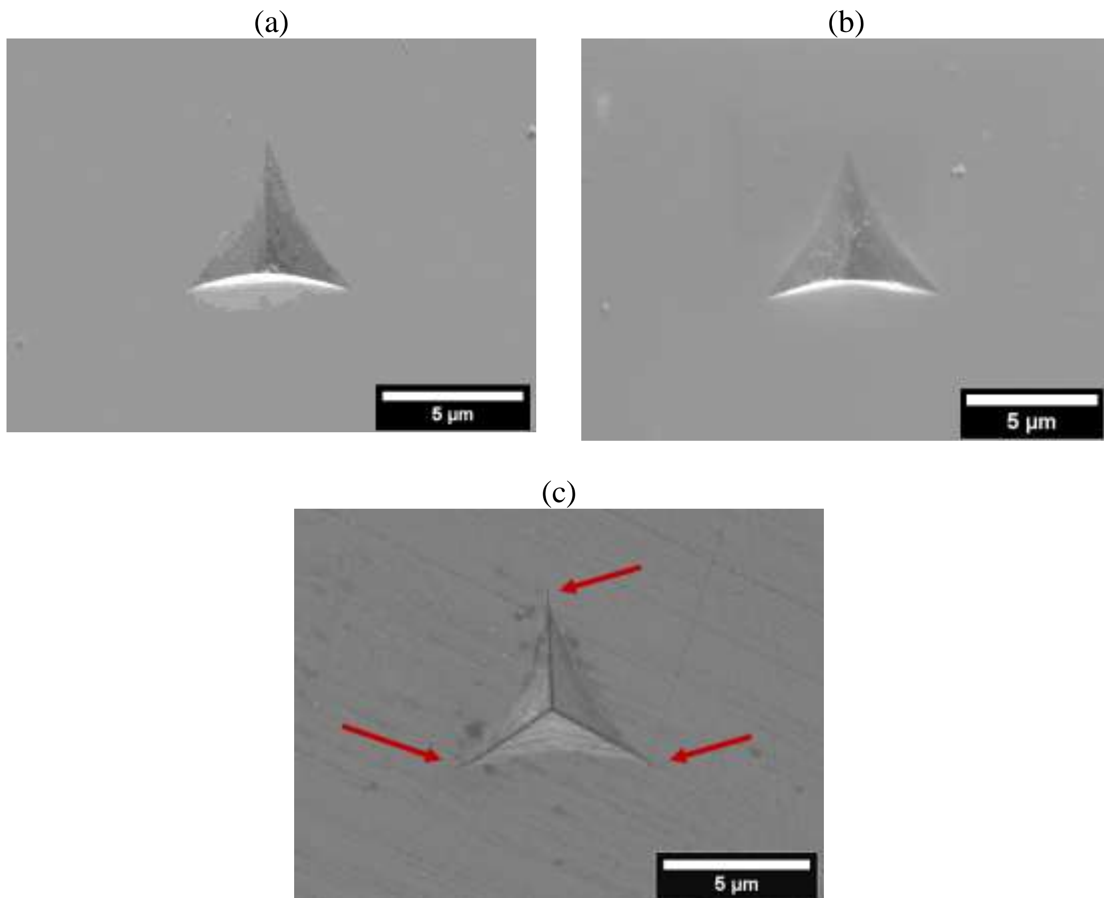

Figure 5-44: 1000 nm Berkovich indents in 6H-SiC single crystal after ion irradiation (SEM SE). (a) Si ions, 300 °C, 2.5 peak dpa. (b) Ne ions, 300 °C, 2.5 peak dpa. (c) Si ions, 750 °C, 0.25 peak dpa with radial corner cracks marked with arrows

One indent in the 300 °C 2.5 dpa neon irradiated 6H-SiC was cross-sectioned using FIB slice and view (Figure 5-45). During the slicing, radial cracks grew stably from the bottom corners of the indent impression before jumping forward after a critical amount of material was removed, similar to the unirradiated SiC indent (Figure 5-30). Further slices through the indent impression show these radial cracks link together laterally and join under the indent impression tip. Two short cracks grow from the top indent corner as the

indent impression is FIBed away (Figure 5-45 (d)). This can be seen dynamically in the video online.

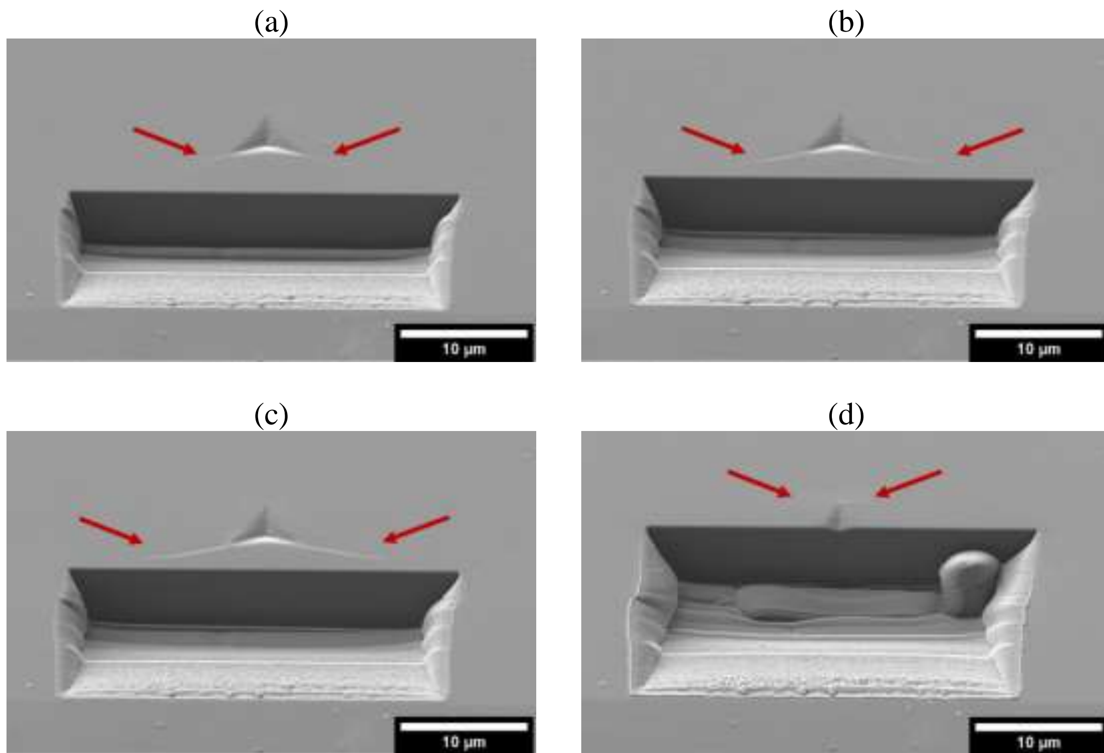

Figure 5-45: Cross-sectional slicing of a 1000 nm Berkovich nanoindent in Ne irradiated 6H SiC (SEM SE). (a) shows radial cracks growing from the lower corners of the indent impression as material is FIBed away. (c) is the slice after cracks jump forward, and (b) is the slice immediately before. (d) shows two cracks from the top corner of the indent.

Before the crack jump, the radial cracks which had been growing stably were ~4 µm long. Using equation (4-1) with this crack length, the fracture toughness K_c is 1.9 (2.6) MPa√m, very close to the unirradiated fracture toughness of 2.0 (2.7) MPa√m. As the top corner cracks have not grown at this point the bottom corner radial cracks are not necessarily the "correct" lengths to use equation (4-1) which is derived for three radial cracks. Using this equation here underestimates the fracture toughness. It may be a coincidence that the cracks have grown to a similar length to the unirradiated case as the stress and fracture state are significantly different to the unirradiated case.

Elastic deformation around 6H-SiC indents after irradiation is noticeably different, with more residual elastic deformation near the indent after irradiation. The plotted stresses are relative to a position in the upper left of the maps. This is *not* a stress-free position, as

discussed in section 5.2.6. The maps in Figure 5-47 show the planar von Mises and mean normal stresses of indents in the 6H-SiC sample irradiated with neon ions at 300 °C to 2.5 peak dpa. The top images are taken from the unirradiated side of the boundary, and bottom images are on the irradiated side. Both indents have the same crystallographic orientation. The absence of cracks is clearly visible in the irradiated indents as there is no stress release from the indent corners.

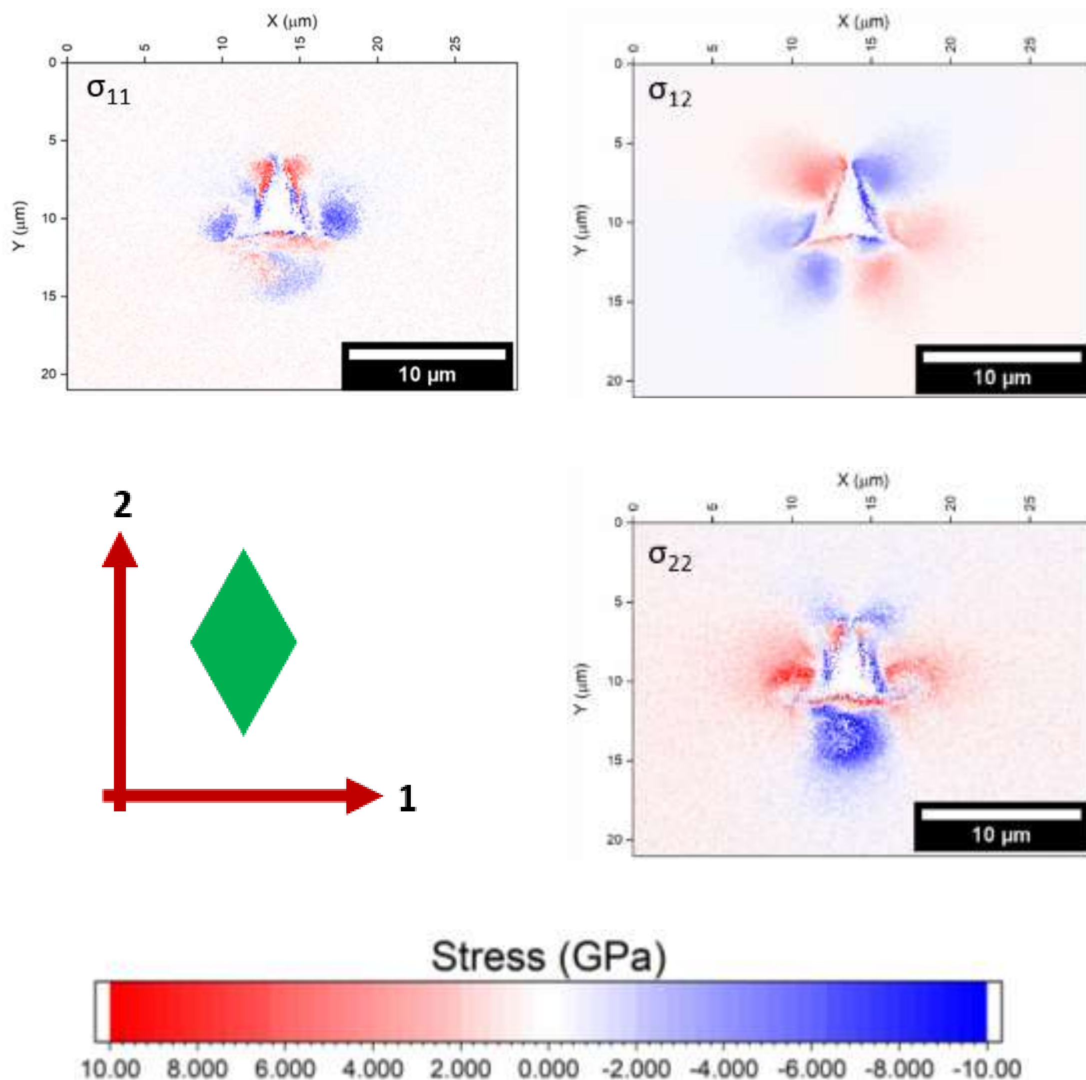

Figure 5-46: HR-EBSD plane stress tensor for a 1000 nm Berkovich indent in Neon irradiated 6H-SiC. Crystal orientation and stress axes are given in the lower left box. The reference position is taken in the upper left of the map. This is not *a stress-free position, so the mapped stresses are relative to this point.*

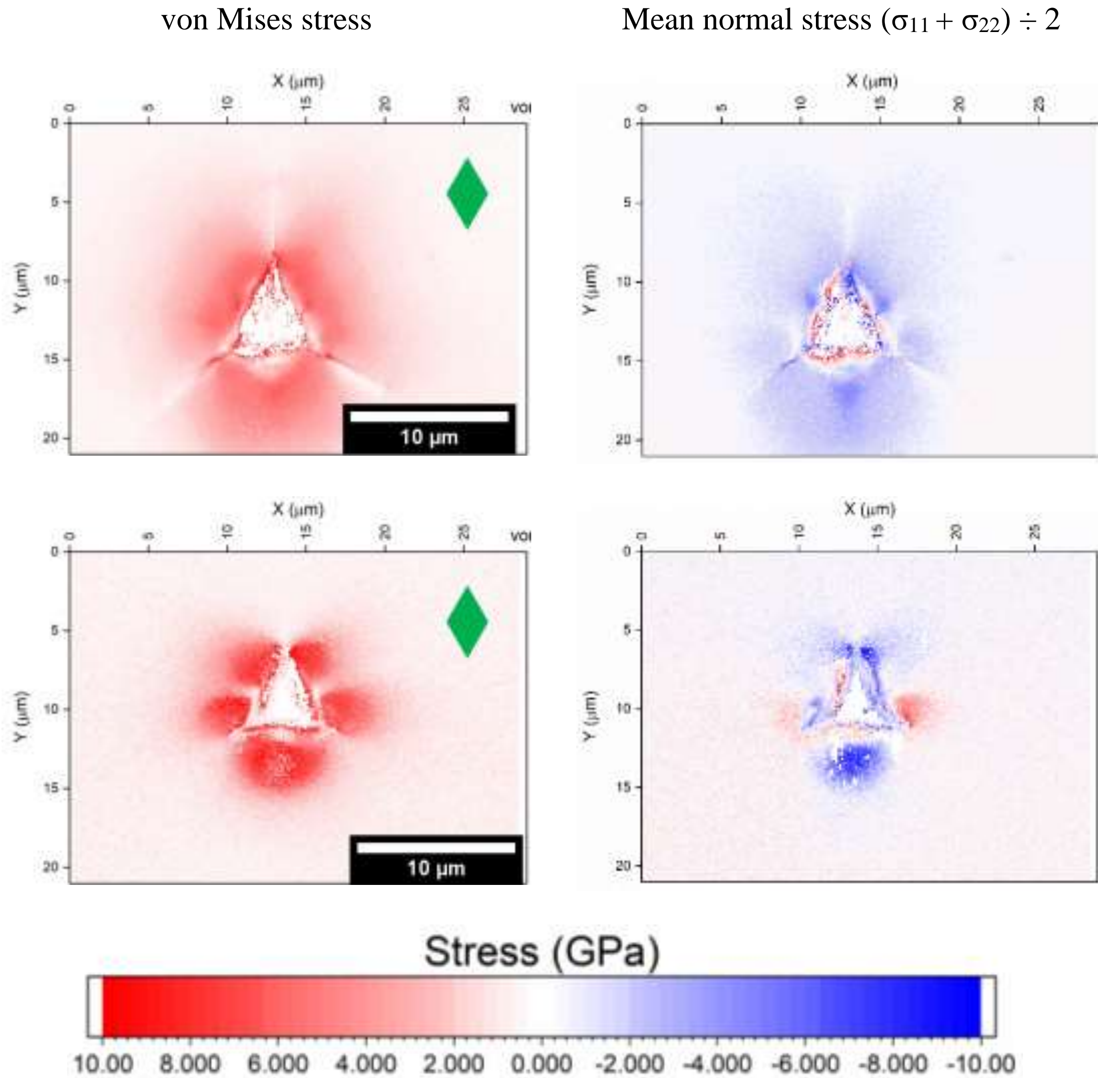

Figure 5-47: Comparison of planar von Mises and mean normal biaxial stress HR-EBSD maps of unirradiated (top) and irradiated (bottom) indents in 6H-SiC after irradiation with neon ions at 300 °C to 2.5 peak dpa.. Green hexagonal unit cell represents the crystal orientation in the (0001) plane. Scale bar is the same for both representations of stress

The residual compressive stress from the indenter face is higher in magnitude in the irradiated material and is more localised. σ_{22} for the irradiated indent is shown in Figure 5-46, highlighting the localisation of compressive stress from the bottom indenter face. Its magnitude peaks around 10 GPa. The unirradiated maximum compressive elastic stress in the lobe below the bottom indenter face was 6.5 GPa.

Geometrically necessary dislocation (GND) density was also calculated for 6H-SiC indents with a neon irradiated sample shown in Figure 5-48 in comparison with an unirradiated indent. Most obvious is the lack of radial cracks from the corners of the

irradiated indent. Regions of high GND density extend further from the indent impression after irradiation, but peak at similar GND densities. The spatial extent of GND deformation is similar to elastic deformation shown in Figure 5-47 for irradiated SiC, whereas plastic deformation is limited to very short distances from the unirradiated SiC indent impression compared to the extent of elastic deformation.

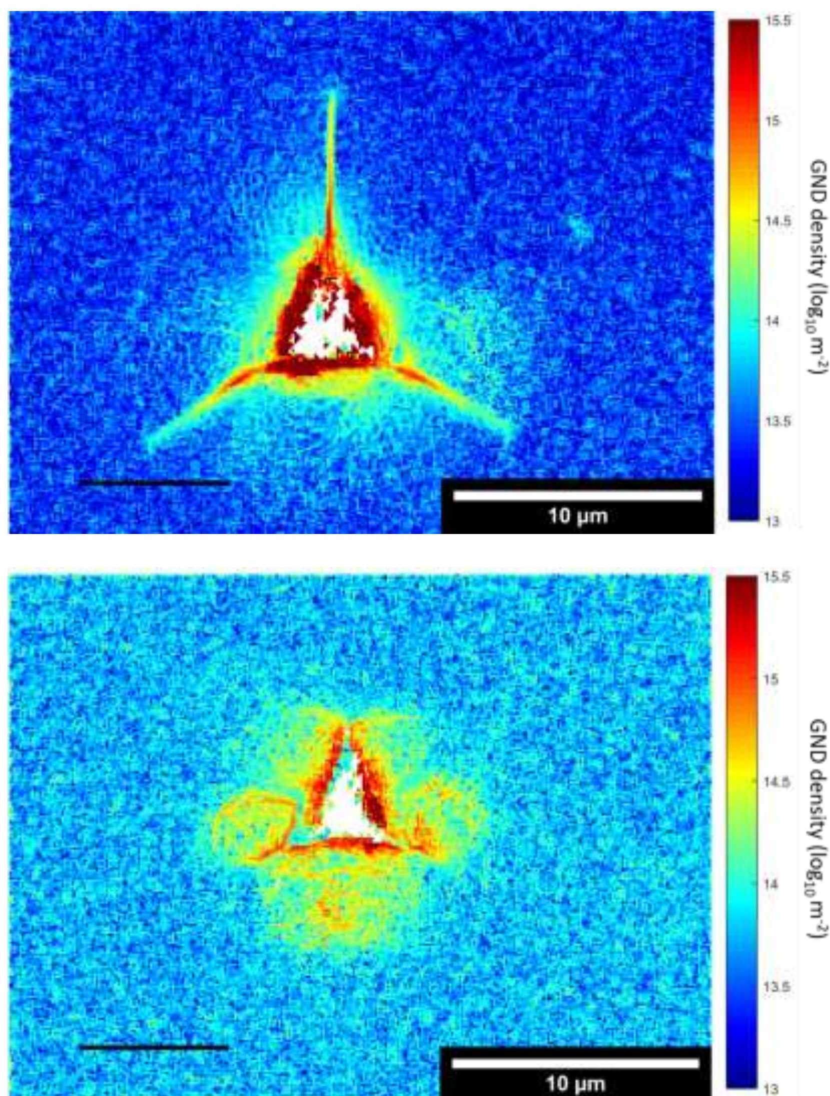

Figure 5-48: GND density around 1000 nm Berkovich indents in unirradiated 6H-SiC (top) and neon irradiated 6H-SiC (bottom)

The two HR-EBSD GND density maps in Figure 5-48 were acquired with the same SEM conditions, using a step size of 100 nm. The background away from the indent in the irradiated map has an average GND density of 6.28×10^{13} m^{-2}, and the unirradiated background has an average GND density of 2.57×10^{13} m^{-2}. GNDs are calculated by lattice

curvature caused by the extra planes of atoms in dislocations – there is no need for a reference position for this calculation. Lattice curvature caused by radiation-induced dislocations contribute to the calculated GND density in addition to “mechanical” dislocations. A radiation-induced increase in dislocation density is measurable using HR-EBSD. Quantifying this increase is uncertain due to the dislocation types and directions. Radiation dislocation loops can be created with a distribution of Burgers vectors, whether they are interstitial or vacancy type and the planes they lie on. The lattice curvature associated with them will also be different so there will be a cancelling effect on curvature measured by EBSD. This would give a lower estimate of GNDs rather than the true number of dislocations in the diffraction volume. Mechanical dislocations should be biased in particular slip systems due to plastic deformation rather than pseudo-uniformly created by radiation defects. Figure 5-49 shows schematically an example of this underestimation with Burgers vectors of opposite directions, but similar could be true for vacancy type, relative to interstitial type dislocation loops.

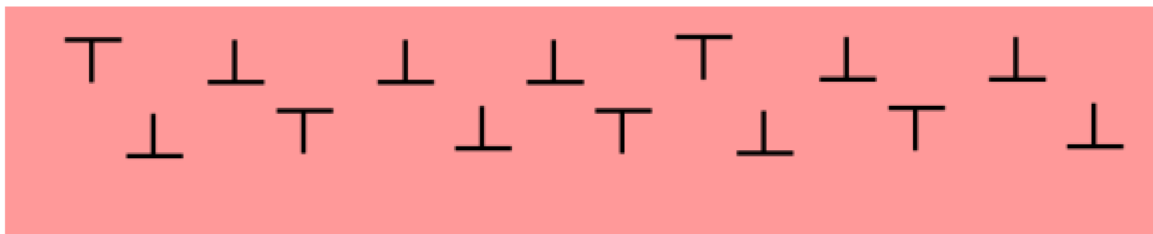

Figure 5-49: Schematic of radiation-induced dislocations in an EBSD interaction volume. In this example there are 14 dislocations, 5 of which have an opposite Burgers vector. The net lattice curvature is of 9 dislocations, so only 9 would contribute to the calculated GND density, underestimating the number of dislocations.

5.2.3.2 Polycrystalline RB-SiC

After irradiation, indentations in polycrystalline RB-SiC samples also showed a change in surface cracking. Silicon regions (as in the unirradiated cases) did not show cracking from indentation. Indentation into SiC grains also did not cause radial cracks from indent corners, in contrast to the unirradiated samples. When indent corners were near grain boundaries, cracks tended to propagate along them, stopping if they reached a silicon

region. It is unclear whether these cracks were caused by the indentation, radiation damage alone, or a combination of both where indentation grain boundary cracking was enhanced by radiation damage, or the radiation-induced cracking was triggered by the extra tensile stress from the indentation. Inside the indent impression, lateral cracks are visible (marked with red arrows in Figure 5-50 (c)) which were not there before irradiation. These are only apparent in the SiC grains within the indent impression.

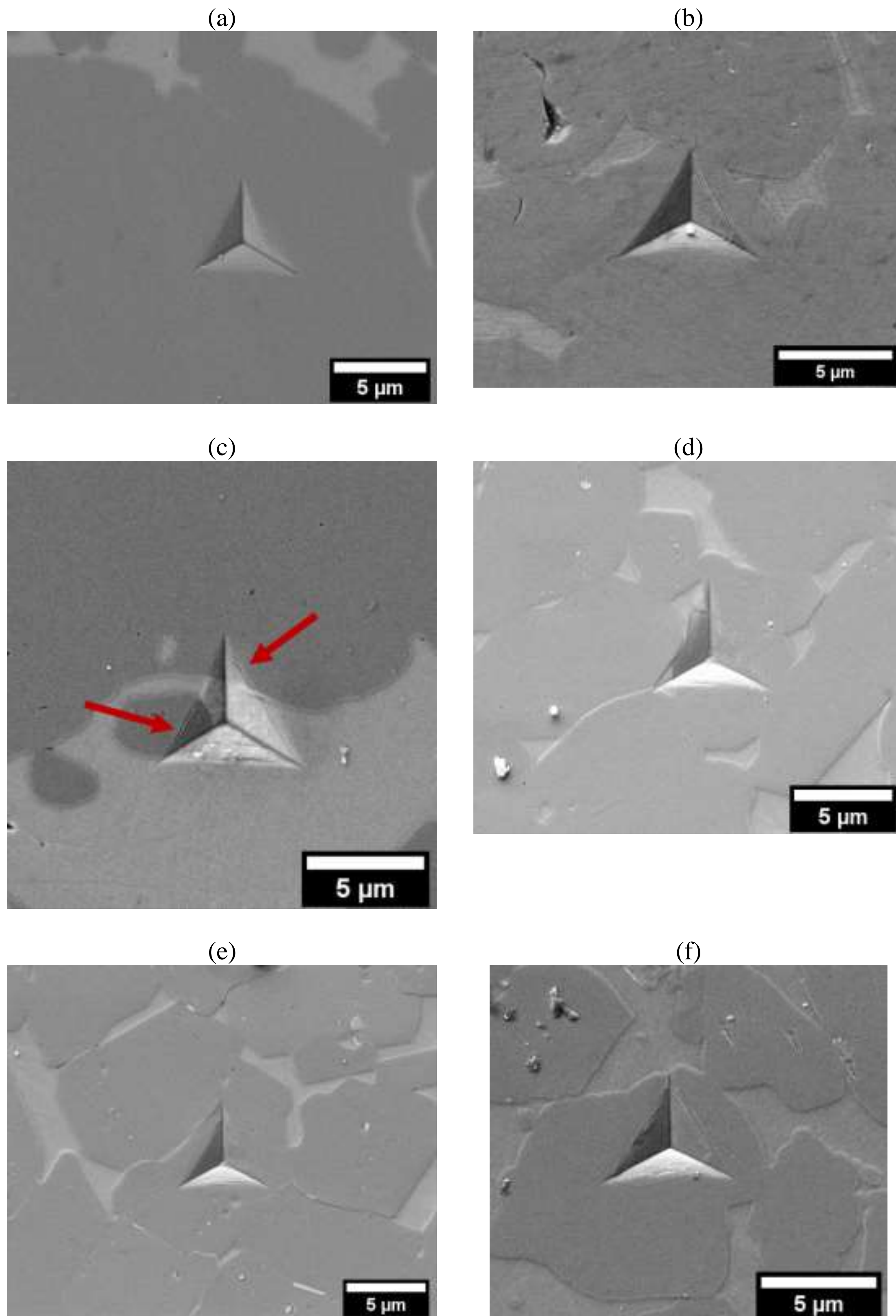

Figure 5-50: (a) Starceram Ne 300 high large SiC grain showing no radial corner cracks. (b) SiC region of REFEL Si 750 high showing short radial corner cracks. (c) Starceram Ne 300 high showing no radial corner cracks in the silicon region, nor the SiC. (d) REFEL Si 300 high showing a SiC grain boundary crack emanating from the left indent corner to a sharp silicon cusp. (e) REFEL Si 300 high showing SiC grain boundary cracks near indent corners, but not radially from them. Other SiC grain boundary cracks can be seen emanating from silicon cusps. (f) In-house RB-SiC, no indentation crack in SiC grain. All images are SEM SE.

Ion irradiation appears to make SiC grains in RB-SiC resistant to indentation fracture, and silicon regions remain resistant to fracture. Grain boundaries appear to remain weak (possibly weaker) and fracture near corners of nanoindents.

5.2.4 Microstructural changes

5.2.4.1 Microscope contrast

After ion implantation, silicon carbide specimens were visibly different. Single crystal 6H-SiC turns from translucent green to opaque grey (Figure 5-51). The 6H-SiC sample irradiated with silicon ions at 750 °C, 0.25 dpa peak retained some translucency and a green tinge when the sample was held up to a light, qualitatively suggesting less radiation damage.

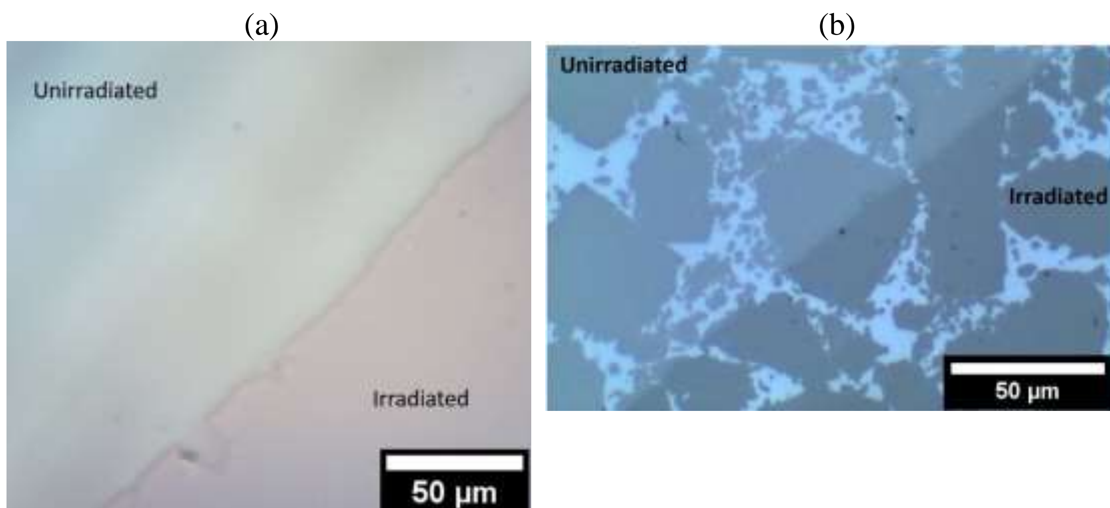

Figure 5-51: Optical image of the unirradiated/irradiated boundary in (a) single crystal 6H-SiC and (b) Starceram

Polycrystalline RB-SiC samples (Figure 5-51 (b)) also showed an optical colour change where the irradiated material is darker. Silicon regions in RB-SiC do not change colour, nor does the single crystal silicon.

The irradiated-unirradiated boundary is also apparent in the SEM, most visibly in REFEL using secondary electron imaging mode (Figure 5-52). The characteristic dark core

SiC grains and reaction formed layer seen in unirradiated REFEL is lost after ion implantation (Figure 5-52).

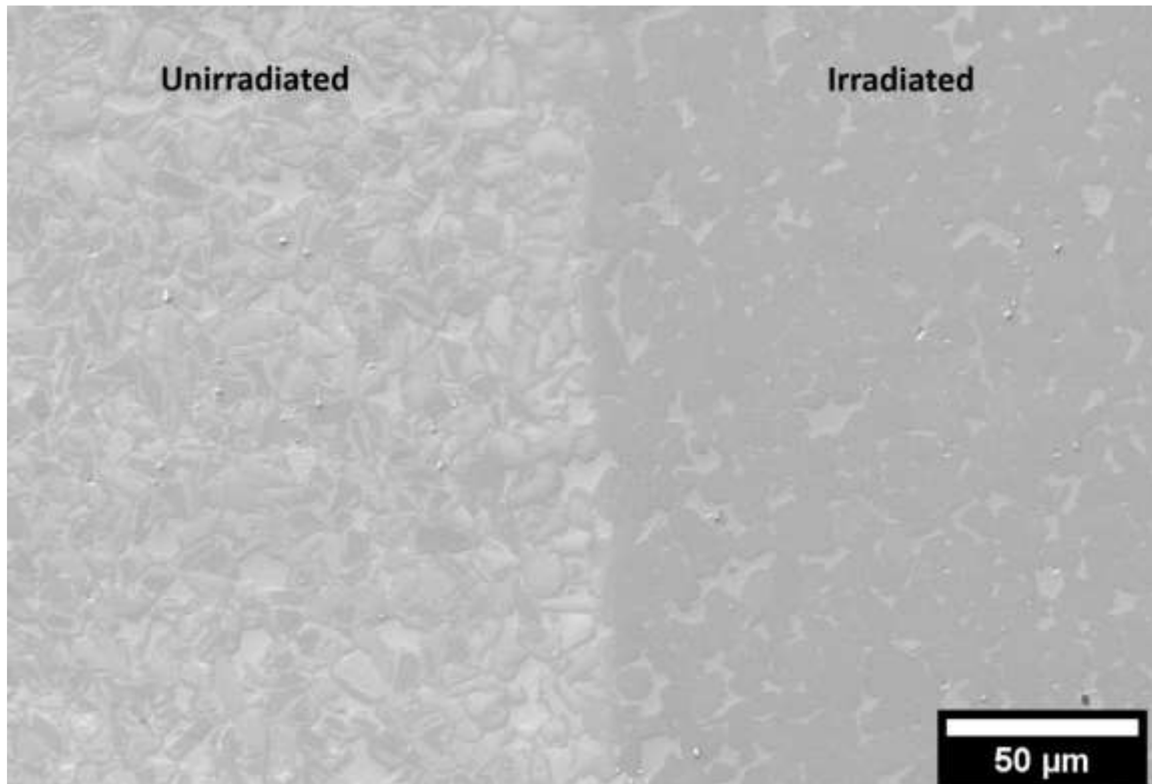

Figure 5-52: Boundary between unirradiated and irradiated (Si 300 °C, 2.5 peak dpa) in REFEL (SEM SE)

The optical change in single crystal 6H-SiC is also apparent in the SEM, using both secondary electron imaging and in the "Argus" image on the forescattered electron detectors (Figure 5-53). The "Argus" image is particularly sensitive to surface topology due to the geometry of the sample and detector and shows a step at this boundary. This will be investigated further in section 5.2.5.

(a) (b)

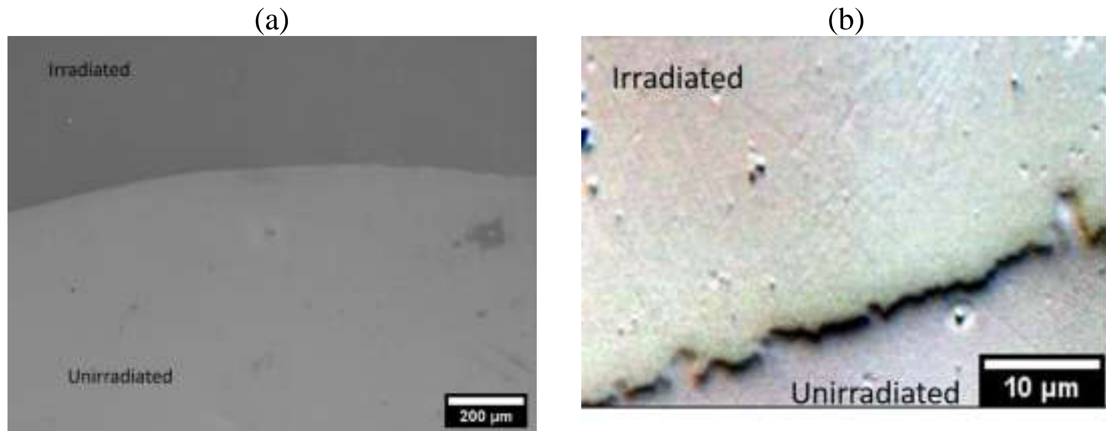

Figure 5-53: Irradiation boundaries in 6H-SiC single crystal. (a) is secondary electron image, (b) is "Argus" image

Although silicon does not optically show a change in contrast due to ion irradiation, the effect of irradiation is apparent in the SEM using secondary electrons (Figure 5-54).

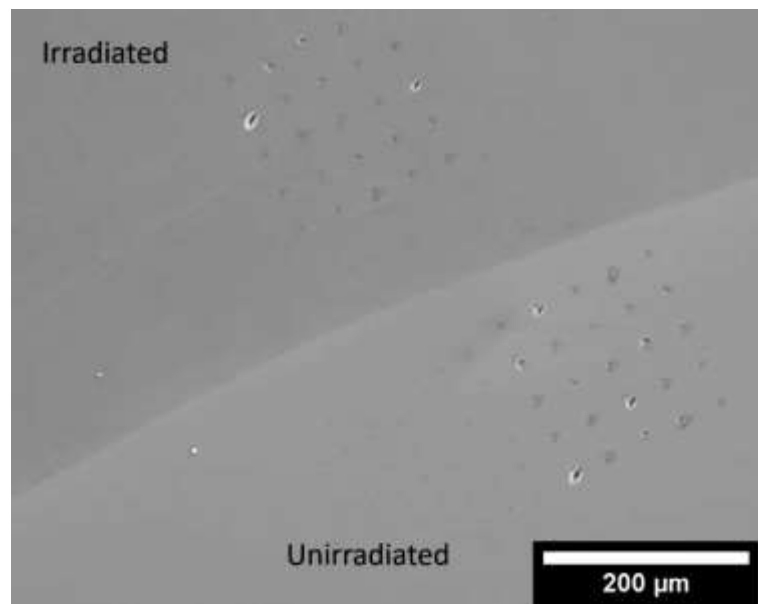

Figure 5-54: SEM SE image of the Irradiation boundary in single crystal silicon (001) implanted with Si ions 300 °C, 2.5 dpa peak. 1000 nm Berkovich indent arrays can be seen on both side of the boundary

Although it was not investigated quantitatively, electron and optical contrast is clearly affected by radiation damage. This may be due to changes in band gap which could be quantified experimentally.

5.2.4.2 Raman spectra

Raman spectroscopy is sensitive to interatomic bonding vibrational frequencies. These frequencies are affected by radiation damage making it useful for investigating

radiation-induced defects, however it can be somewhat difficult to quantify and interpret. Most attempts at quantification compare peak areas of unirradiated and irradiated samples to estimate the relative fractions of Si-Si, Si-C, and C-C bonding [125,129,147,155,158,159,164,165,243–246]. This is unreliable as different laser wavelengths excite different bond types more than others, potentially influencing the measured relative peak intensities [162]. For example, the shorter wavelength green laser excites C-C bonds more intensely than a red laser, but a red laser differentiates the triple Si-C Transverse Optic peaks better.

Figure 5-55 shows Raman spectra of 6H-SiC single crystals before and after ion irradiation. The peaks are identified based on ref [159]. The spectra were collected with the same laser and spectrometer settings and special care was taken in focussing the laser to optimise for intensity. The unirradiated spectrum is scaled by ×0.25. All the spectra show significant damage; reduction in intensity, peak asymmetry and broadening, and the appearance of extra peaks for Si-Si and C-C bonding. This makes exact peak positions and integrated areas difficult to identify.

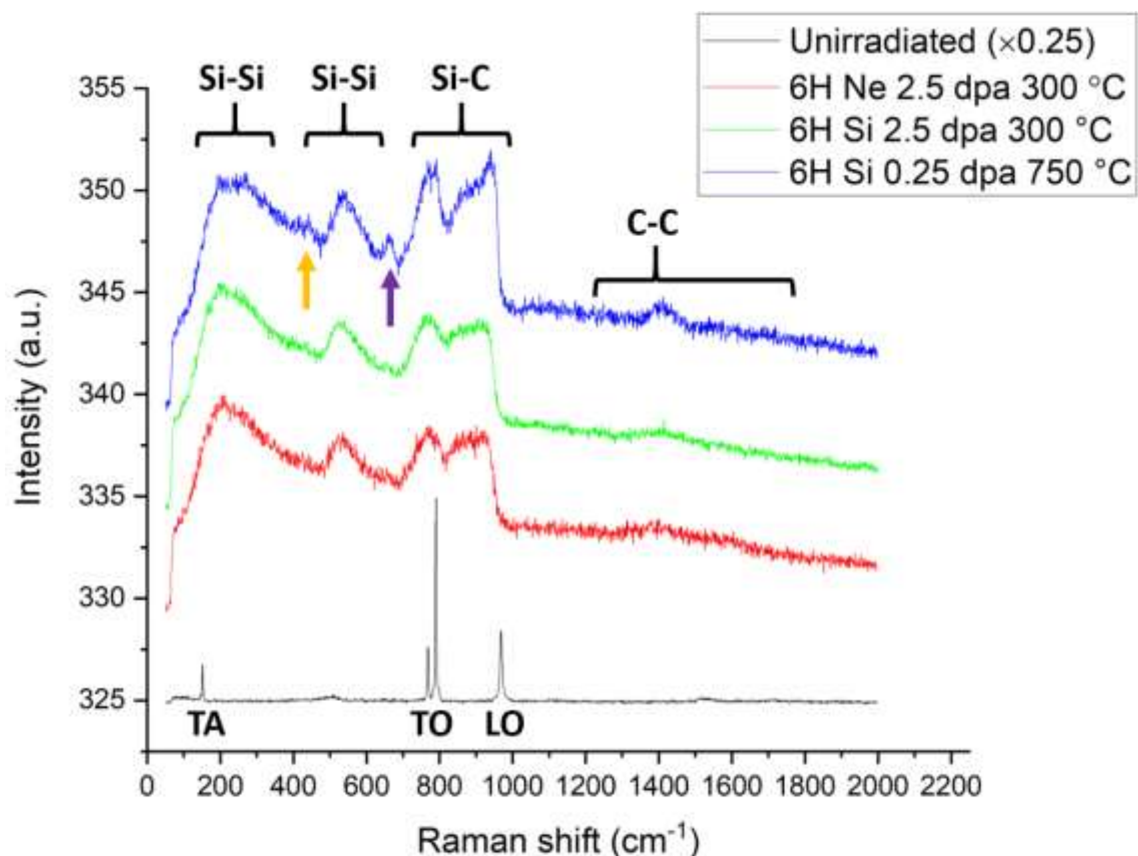

Figure 5-55: Raman spectra of unirradiated and ion implanted single crystal 6H-SiC. The unirradiated spectrum is multiplied by ×0.25 in the y axis and is from the unirradiated region of the 750 °C irradiated specimen. Orange arrow points at a peak for Si-O bonding. Purple arrow points at a peak for C-O bonding. Same spectroscopy conditions, 10 mW green laser, ×100 objective

The peak at ~530 cm^{-1} corresponds to Si-Si bonding. This peak is shifted right relative to the position of unstressed Si-Si bonds in silicon which is at 520 cm^{-1}. This shift to higher wavenumbers corresponds to a compressive stress on these bonds – they are shorter than they want to be in unstressed Si-Si_4 tetrahedra. The Si-Si peak in 0.25 dpa 750 °C spectrum is 1.4× taller relative to the background than the 2.5 dpa 300 °C spectra. The broad signal at lower frequencies, < 400 cm^{-1} is also attributed to silicon but is not used for analysis.

The small shoulder at ~430 cm^{-1} (marked with an orange arrow in Figure 5-55) in the sample irradiated at 750 °C is from frequencies associated with Si-O-Si bonding, and the peak at ~660 cm^{-1} (purple arrow) is associate with C-O-C bonding. This is not clearly visible in the samples irradiated at 300 °C, suggesting some oxidation occurred during the

higher temperature irradiation, although no surface oxidation was observed microscopically. The unirradiated spectrum is obtained from the blanked unirradiated regions of 6H-SiC irradiated at 750 °C and shows no signals corresponding to Si-O and C-O bonds suggesting the oxidation is enhanced by radiation damage.

The peaks associated with Si-C bonding remain sharper and with higher intensity after 0.25 dpa 750 °C Si ion implantation than the 300 °C high dose implantations. They are also not shifted as far left as the more damaged spectra, corresponding to less tensile stretching of the bonds in the distorted lattice.

All three irradiation conditions show signals corresponding to C-C bonding, but in different ways (Figure 5-56). The silicon irradiated samples have a single peak at ~1410 cm^{-1} corresponding to sp^2 type C-C bonding, most likely in isolated pairs or chains [164]. The higher temperature lower dose sample (green line in Figure 5-56) has a taller peak than the high dose low temperature (red line). The neon irradiated sample has a merged double peak with contributing signals from both the D and G bands of sp^2 carbon at ~1400 cm^{-1} and ~1580 cm^{-1}. This is associated with graphitic clusters rather than isolated pairs or chains of carbon atoms in the network [164].

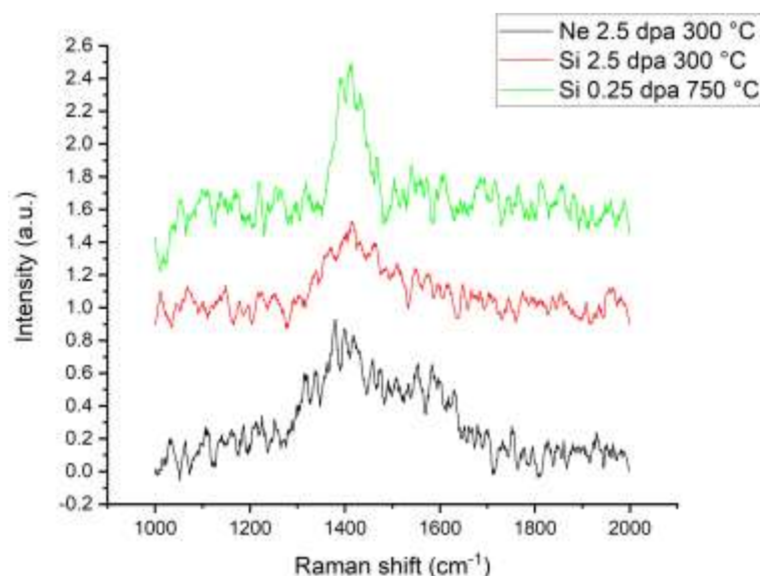

Figure 5-56: Spectra from the C-C bonding region of irradiated 6H-SiC with a straight baseline subtraction. The silicon irradiated samples have a single peak at ~1410 cm^{-1} while the neon irradiated sample has a double peak at 1400 $cm^{-1}$and 1580 cm^{-1}

As single crystal 6H-SiC samples were not irradiated in all conditions, spectra from the large grains of Starceram are taken to fill in the other ion irradiation conditions (Figure 5-57). Broadly they show the same features as the irradiated 6H-SiC specimens discussed above. No differences are observed between 2.5 dpa and 0.25 dpa, although significant differences are noticeable between 300 °C and 750 °C irradiations. Samples irradiated at 750 °C have sharper Si-Si and Si-C peaks, and more significant Si-O and C-O peaks. D-band carbon signals appear to increase in intensity with higher temperature.

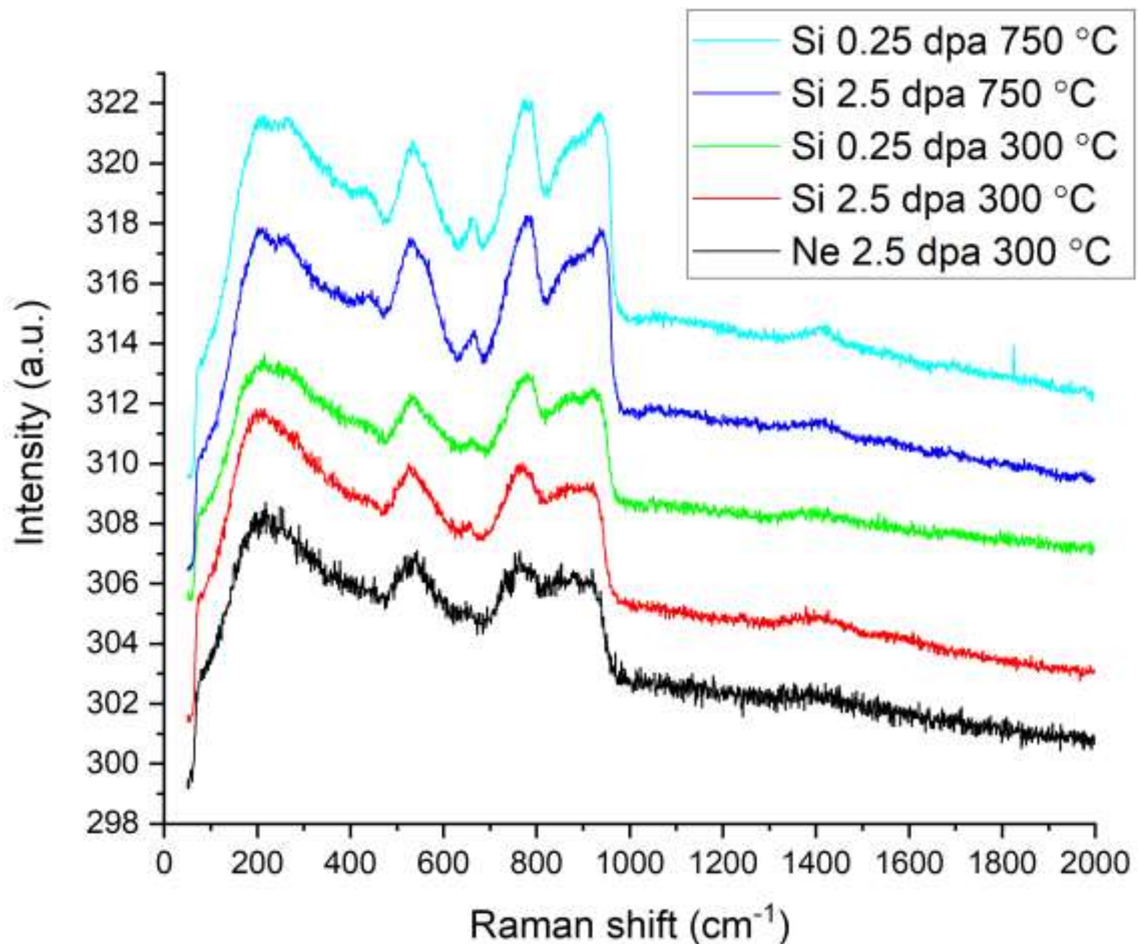

Figure 5-57: Raman spectra from large SiC grains of irradiated Starceram. No observable difference between 0.25 and 2.5 dpa ion implantations. Noticeable differences between 300 °C and 750 °C irradiations as discussed for single crystals.

Microstructure had no observable difference on Raman spectra for any of the irradiation conditions. Representative spectra from neon irradiated large (>50 µm) and small (~1 µm) SiC grains in Starceram are shown along with representative REFEL (~10 µm) and single crystal 6H-SiC spectra in Figure 5-58.

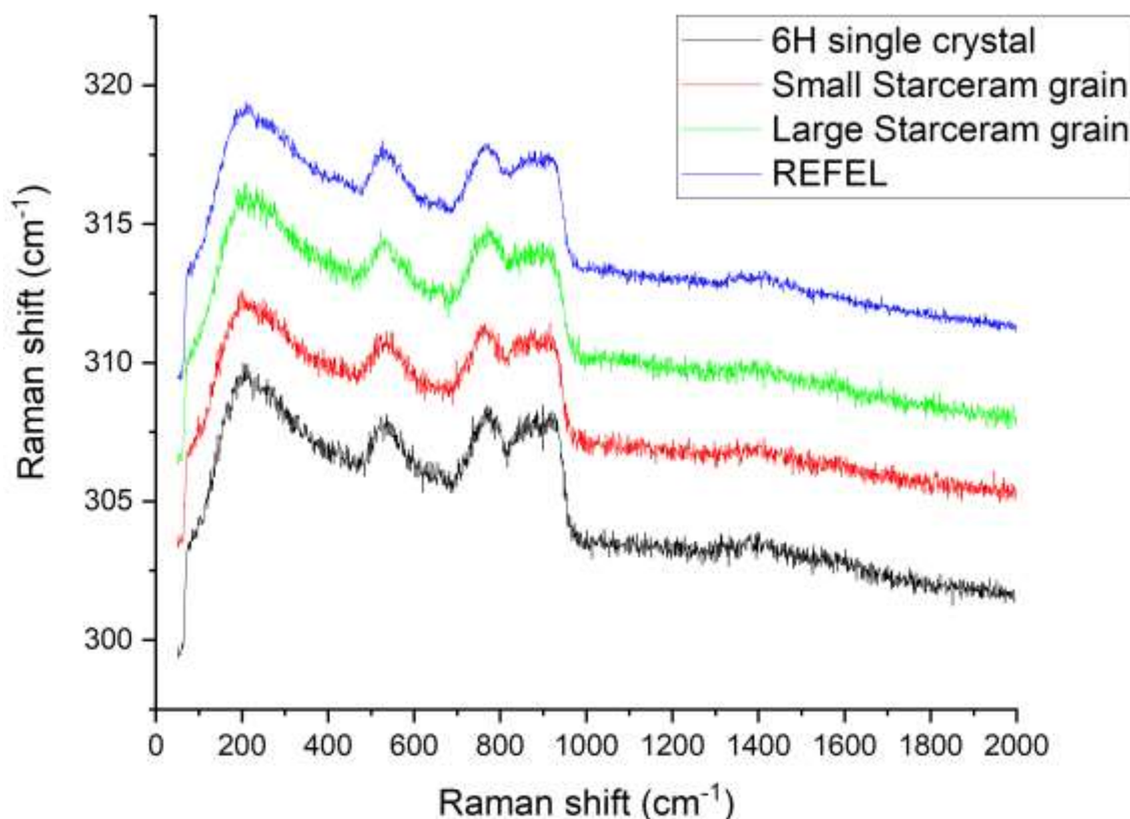

Figure 5-58: Comparison of Raman spectra from small and large SiC grains in Neon irradiated Starceram, REFEL, and single crystal 6H-SiC. No observable difference in measured spectra with microstructure

Optically, some of the irradiated regions displayed different contrast, lighter grey than most of the sample (Figure 5-59). These regions don't look like dirt or dust particles (some are visible in the photos), and they remained on the samples after cleaning. The Raman spectrum for these lighter coloured regions is significantly different with the broad, relatively high intensity signal between 1300 cm^{-1} and 1600 cm^{-1}. This signal is from amorphous C-C bonding, mixed with signals from sp^3 and sp^2 crystalline C-C bonding [153]. The Si-C and Si-Si peaks are less intense and broader in these regions, suggesting more structural disorder than in the dark regions. These features could not be identified in the SEM using secondary not backscattered electrons. Although these peaks are broad and low intensity, they are not characteristic of amorphous SiC or silicon [126,153]. Amorphous SiC spectra have merged TO and LO peaks which are shifted to lower

wavenumbers due to the large volumetric expansion, as seen in Figure 2-20 and in ref. [153].

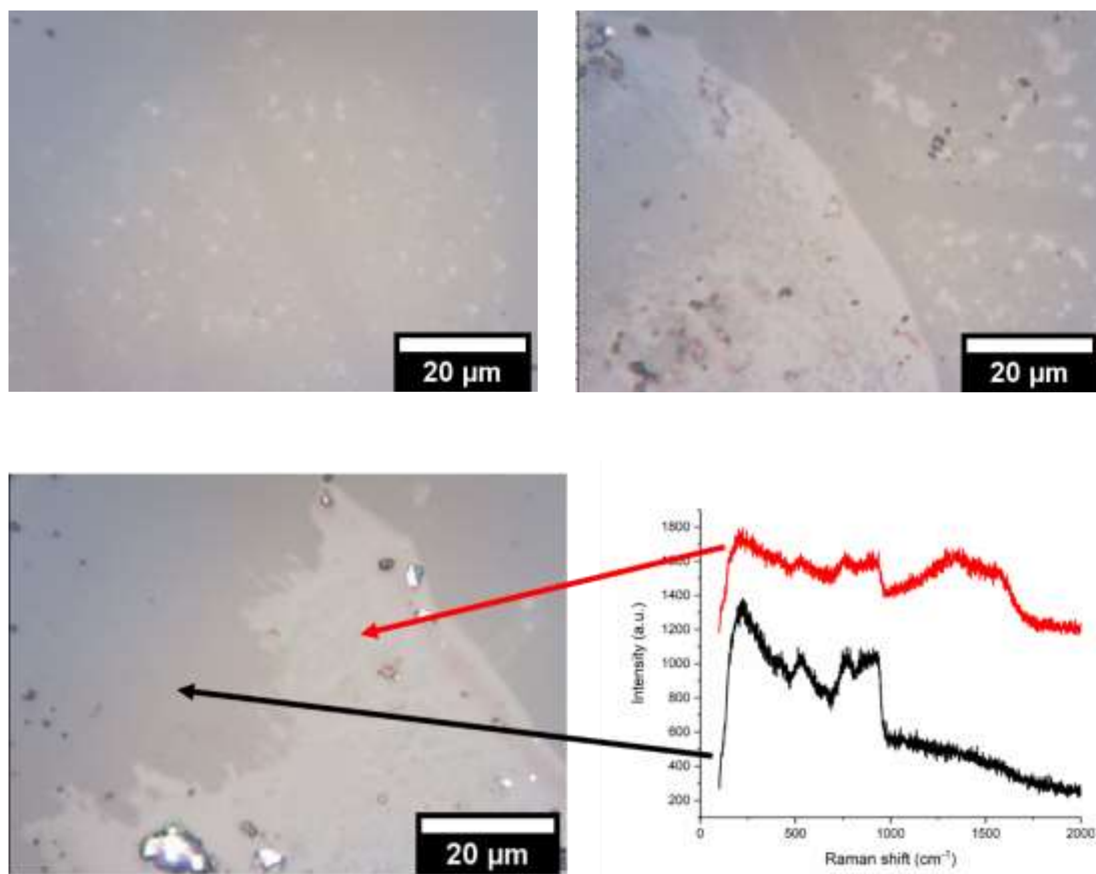

Figure 5-59: Optical micrographs of regions of lighter optical contrast in neon irradiated 6H-SiC and their Raman spectra. Red is from a lighter grey region. Both spectra are taken with the same spectrometer settings.

5.2.4.3 In situ Raman spectroscopy of post-irradiation annealed SiC

A sample of 6H-SiC irradiated with neon ions at 300 °C was annealed at 1000 °C in air on a heated stage in the Raman microscope, and spectra were acquired during this process, shown in Figure 5-60. After a very short time, characteristic SiC peaks begin to form, then sharpen with time. Initially the Si-Si peak increases in intensity and narrows, then begins to disappear with longer times. Initially there are two C-C peaks at ~1350 and 1480 cm^{-1} (line 2). The 1350 cm^{-1} peak disappears and the 1480 cm^{-1} peak increases in relative intensity (line 4). The spectra acquired at 1000 °C are shifted to lower wavenumbers than spectra acquired at room temperature, corresponding to thermal

expansion of the sample. Peaks are shifted by different amounts as different bonds are affected differently by temperature. The changes in peak position can be used for Raman thermometry [247,248]. Initially a C-O-C peak appears at ~650 cm^{-1} (lines 2, 3, and 4), then disappears by line 6. Unfortunately, the spectrometer grating did not allow collection of the low wavenumber end of the spectrum at the same time as the high wavenumber carbon end so the evolution of Si-O (~430 cm^{-1}) bonding cannot be seen.

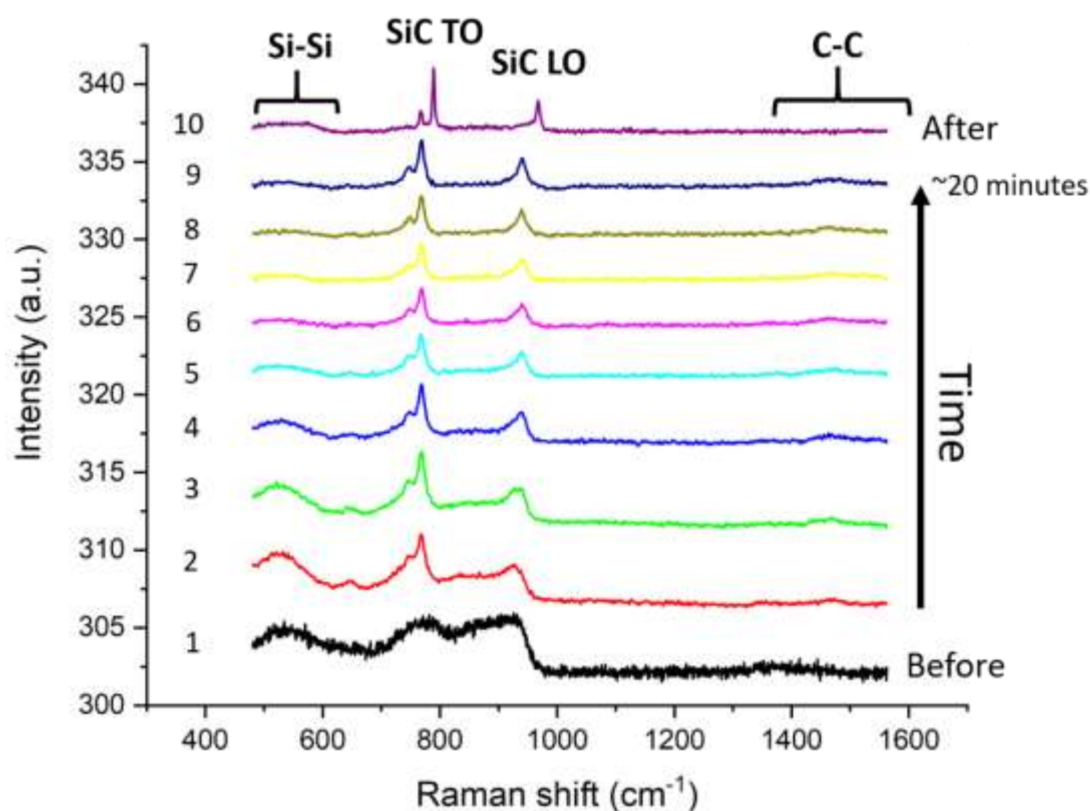

Figure 5-60: Raman spectra of 6H-SiC acquired during annealing at 1000 °C in air. "Before" and "After" lines were measured at room temperature using the same ×50 long focal length objective and heating stage window as the high temperature spectra

After annealing, the sample returned to translucent green, but not entirely to the pristine state. This is apparent in the "after" Raman spectrum (purple line in Figure 5-60) where there is still a small, broad Si-Si signal and asymmetry to the SiC LO signal. Optical micrographs showed what appeared to be sub-micron specks of dirt on the surface (Figure 5-61 (a)) with a denuded zone around some larger clusters of "dirt". Closer inspection with SEM-EDX (energy dispersive X-ray spectroscopy) (Figure 5-61 (b)) revealed that these

particles are silica and that the irradiated SiC had oxidised during annealing. The small oxygen peak in the "unoxidised" line in Figure 5-61 may be due to the thin native oxide layer on SiC, or oxygen possibly incorporated into the SiC bulk during irradiation which has not grown into oxide clusters. A sample of unirradiated 6H-SiC which had been annealed in air on the high temperature stage in the same Raman microscope to relieve residual stresses around nanoindents for FIB cross-sectioning showed no signs of surface oxidation.

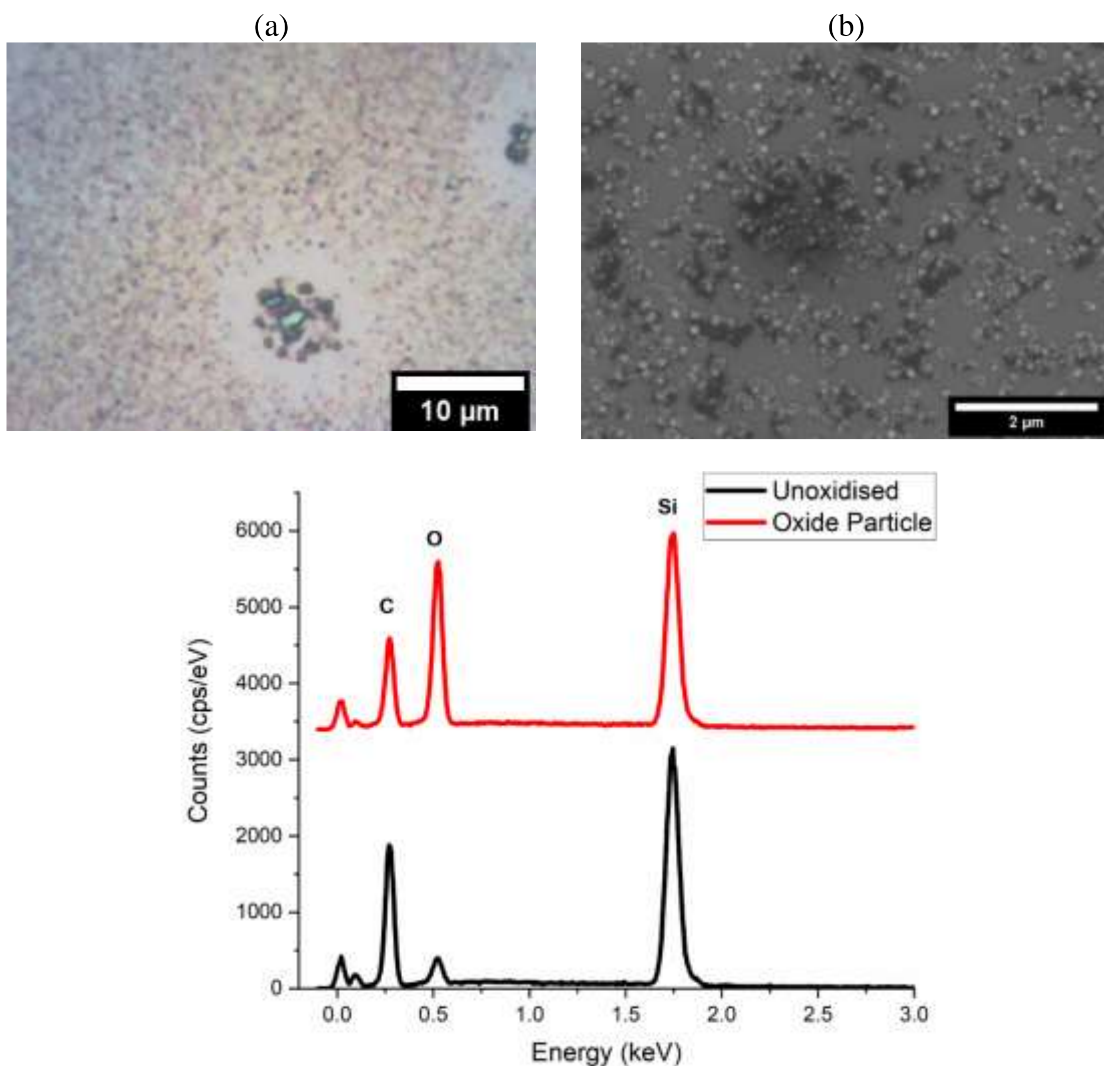

Figure 5-61: (a) Optical and (b) Secondary electron images of neon irradiated 6H-SiC after annealing at 1000 °C in air. Small sub-micron oxide particles are visible, some of which have clustered into larger particles. Below are EDX spectra of the background material and oxide particles.

A sample of 300 °C 2.5 dpa Si ion irradiated 6H-SiC was annealed in vacuum for 24 hours at 1200 °C. After this annealing the surface showed pitting near the sample edges, extending ~160 µm into the surface.

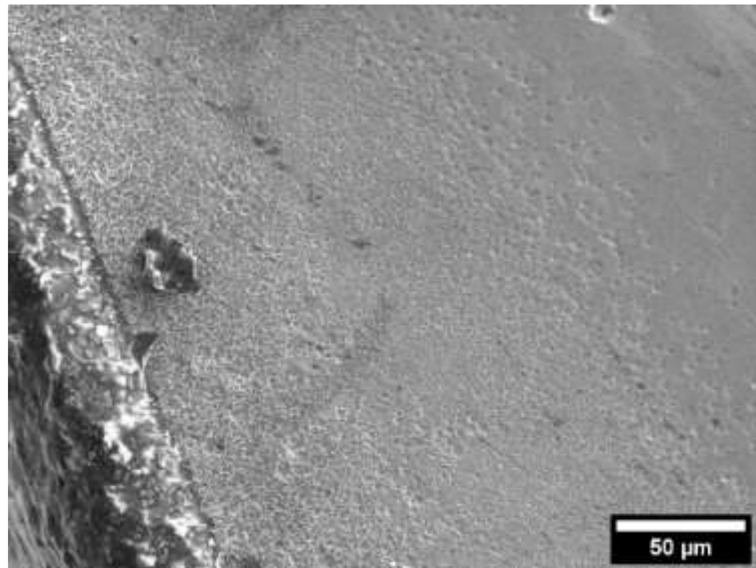

Figure 5-62: Surface of 300 °C 2.5 dpa Si ion irradiated 6H-SiC after annealing at 1200 °C for 24 hours in vacuum. The sample has pitted up to ~160 µm into the sample. (SEM SE)

Raman spectra for silicon single crystals (Figure 5-63) show no change in peak position, remaining at the unstressed position of 520 cm^{-1}. The reduction in intensity may be a true reflection of damage to the crystal lattice, or it may be due to the optical focus changing despite trying to optimise for intensity.

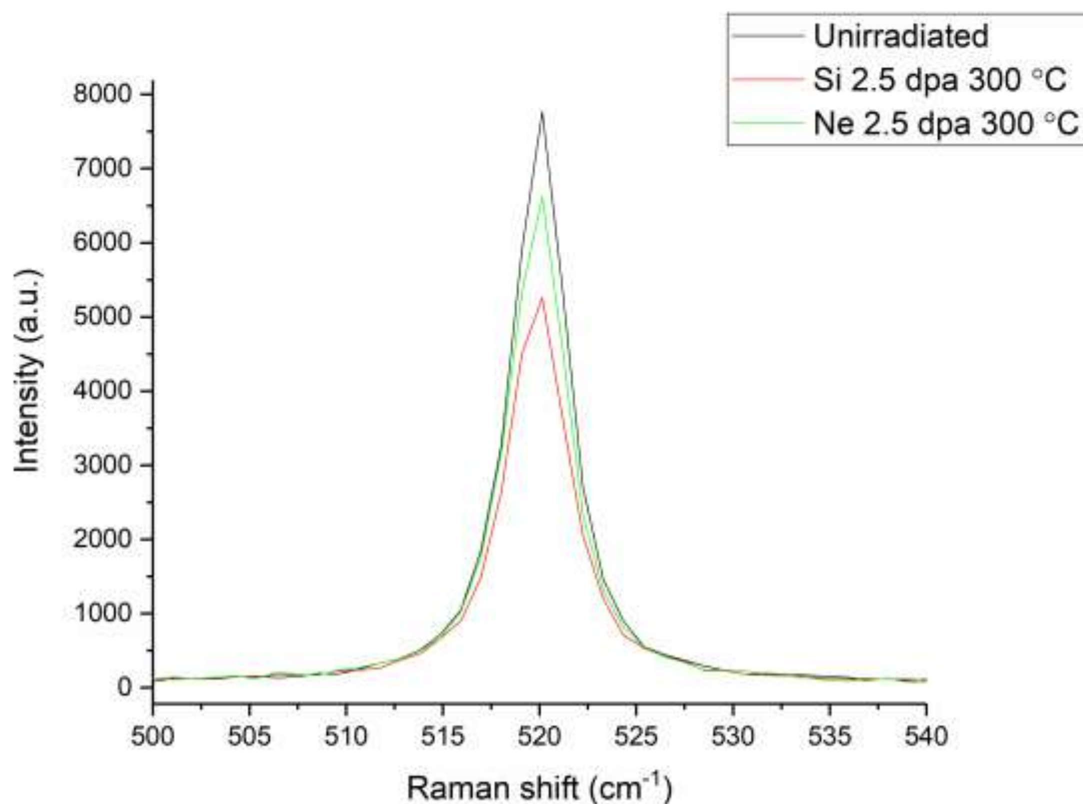

Figure 5-63: Raman spectra of irradiated silicon single crystals. Spectrometer and laser settings were kept constant; however, the optical focus may have changed while moving between samples

5.2.4.4 EBSD Kikuchi Patterns

Degradation of EBSD pattern quality caused by irradiation is apparent across the irradiation boundary when diffraction patterns are analysed using XEBSD. The standard Bruker Esprit software doesn't pick up this change; the higher sensitivity of the cross-correlation analysis in XEBSD is required. Figure 5-64 - Figure 5-67 (a) show peak height, which is a measure of pattern quality relative to the unirradiated reference pattern, across the boundary region in irradiated single crystals. EBSP degradation is caused by anything which contributes to diffuse electron scattering and changing the structure factor of the diffracting crystal. Diffuse electron scattering arises from crystalline defects including point defects , dislocations, or elastic strain, all of which change the structure factor of the crystal [249,250]. Typically degradation of pattern quality is considered in the context of

mechanical deformation where dislocations are generated and there is residual elastic strain, near indents for example [229]. The origin of the degradation is not explained in these papers. In this case degraded diffraction patterns are only caused by ion implantation defects and the knock-on effects of this, including residual stress from constrained swelling (see sections 5.2.5, 5.2.6, 5.2.7). EBSD patterns from either side of the boundary are shown in (b) and (c) for each condition. As reduction in pattern quality is caused by multiple mechanisms, it would be useful to deconvolute each contribution. A potential approach is discussed in section 6.2.2.

For single crystal silicon, there is little degradation in EBSD pattern quality after irradiation, as measured by peak height and subjectively by inspecting the Kikuchi diffraction patterns.

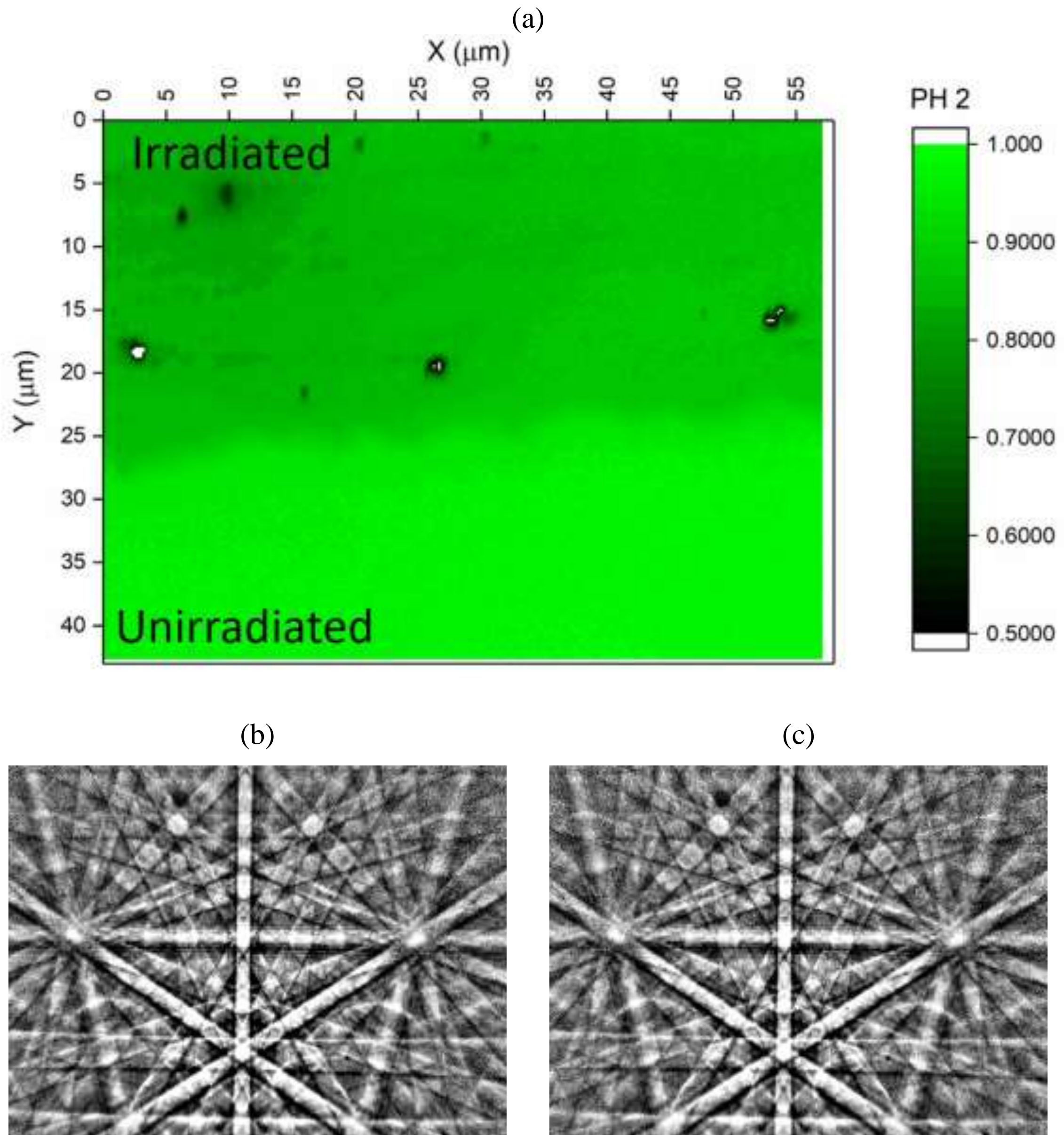

Figure 5-64: (a) EBSD peak height map of irradiation boundary in silicon crystal (001), Si ions 300 °C, 2.5 peak dpa. EBSD Kikuchi patterns from (b) unirradiated side and (c) irradiated side

For the high dose irradiations with both neon and silicon ions, the degradation in pattern quality is more pronounced across the irradiated boundary in 6H-SiC. The peak height change was similar whether silicon or neon ions were used. Different microscope conditions were used for Figure 5-65 and Figure 5-66 so the diffraction patterns in (b) and (c) are not comparable, but peak height is standardised against the unirradiated reference pattern. In both cases the diffraction patterns are clearly degraded.

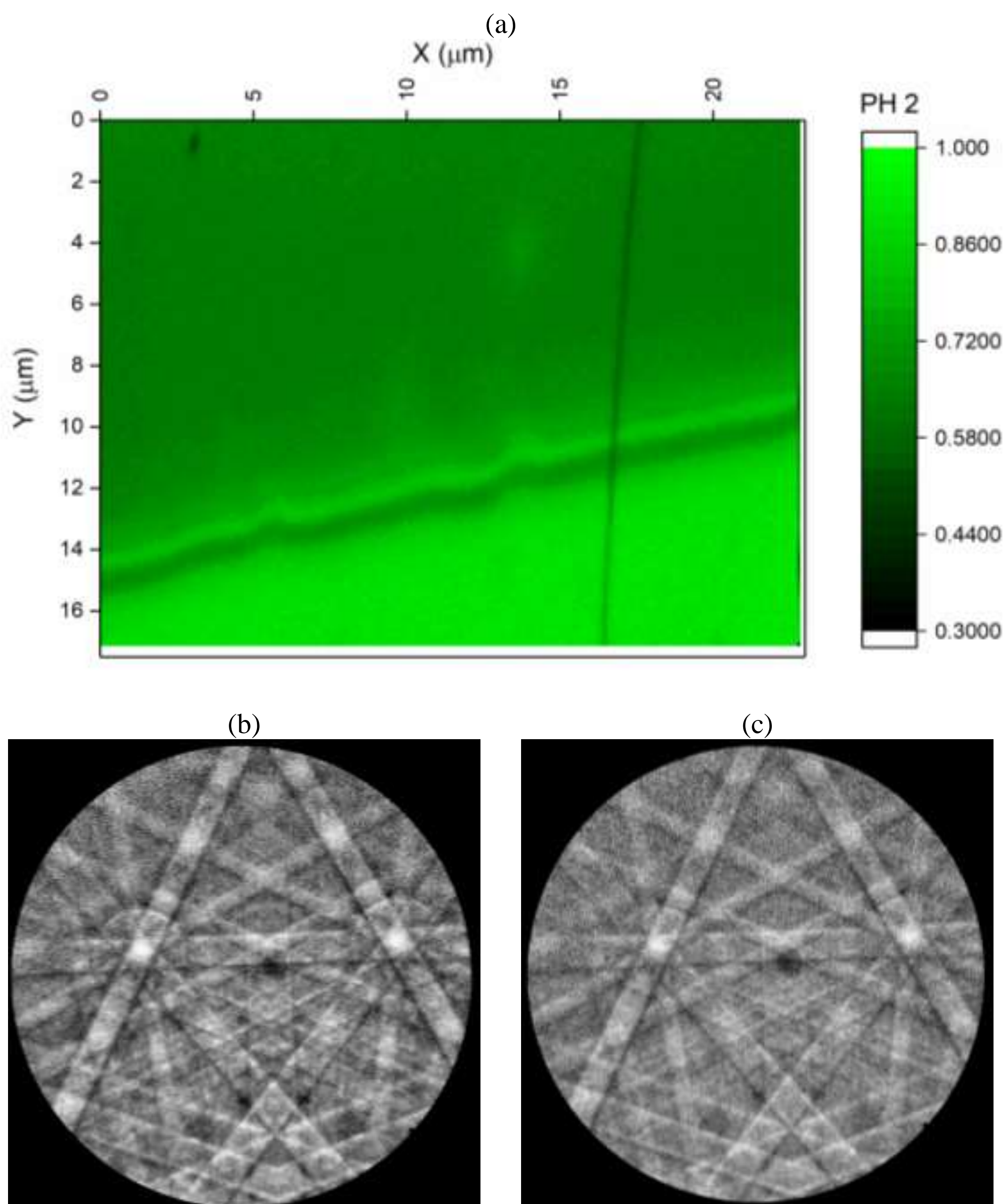

Figure 5-65: (a) EBSD peak height map of irradiation boundary in 6H-SiC crystal (0001), Ne ions 300 °C, 2.5 peak dpa. EBSD Kikuchi patterns from (b) unirradiated side and (c) irradiated side

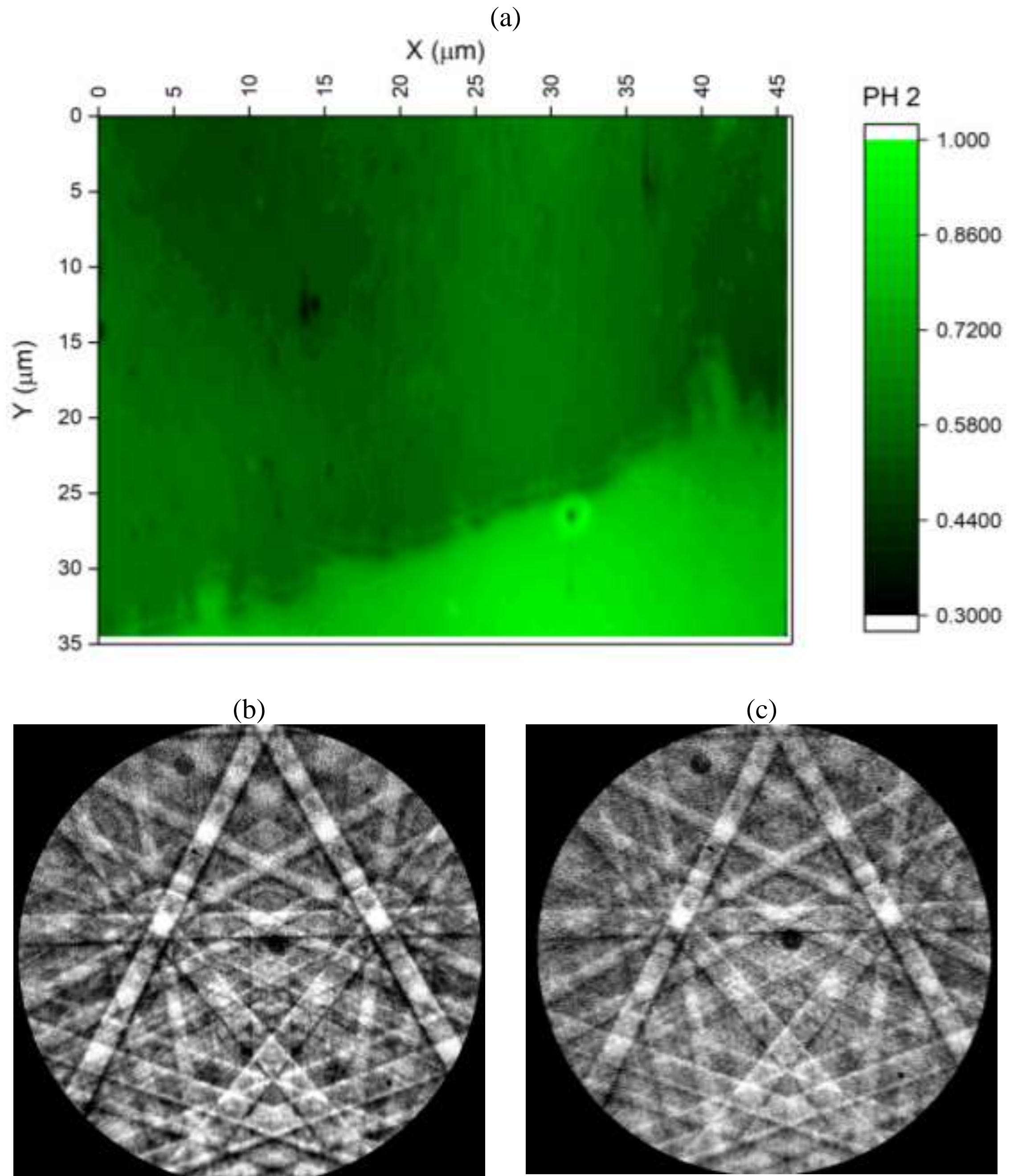

Figure 5-66: (a) EBSD peak height map of irradiation boundary in 6H-SiC crystal (0001), Si ions 300 °C, 2.5 peak dpa. EBSD Kikuchi patterns from (b) unirradiated side and (c) irradiated side

The single crystal 6H-SiC irradiated with a low dose of silicon ions at 750 °C has very little change in diffraction pattern peak height and pattern quality (Figure 5-67). Unfortunately, this sample was significantly more scratched than the others as obtained from the supplier, and this is very visible in the peak height map. The same imaging conditions were used as for the high dose silicon ion irradiated sample (Figure 5-66), although the sample was at a different orientation in the microscope, hence the diffraction

pattern is rotated. Comparing the irradiated patterns, it is clear that 2.5 dpa at 300 °C causes more measurable change to the diffraction patterns than 0.25 dpa at 750 °C.

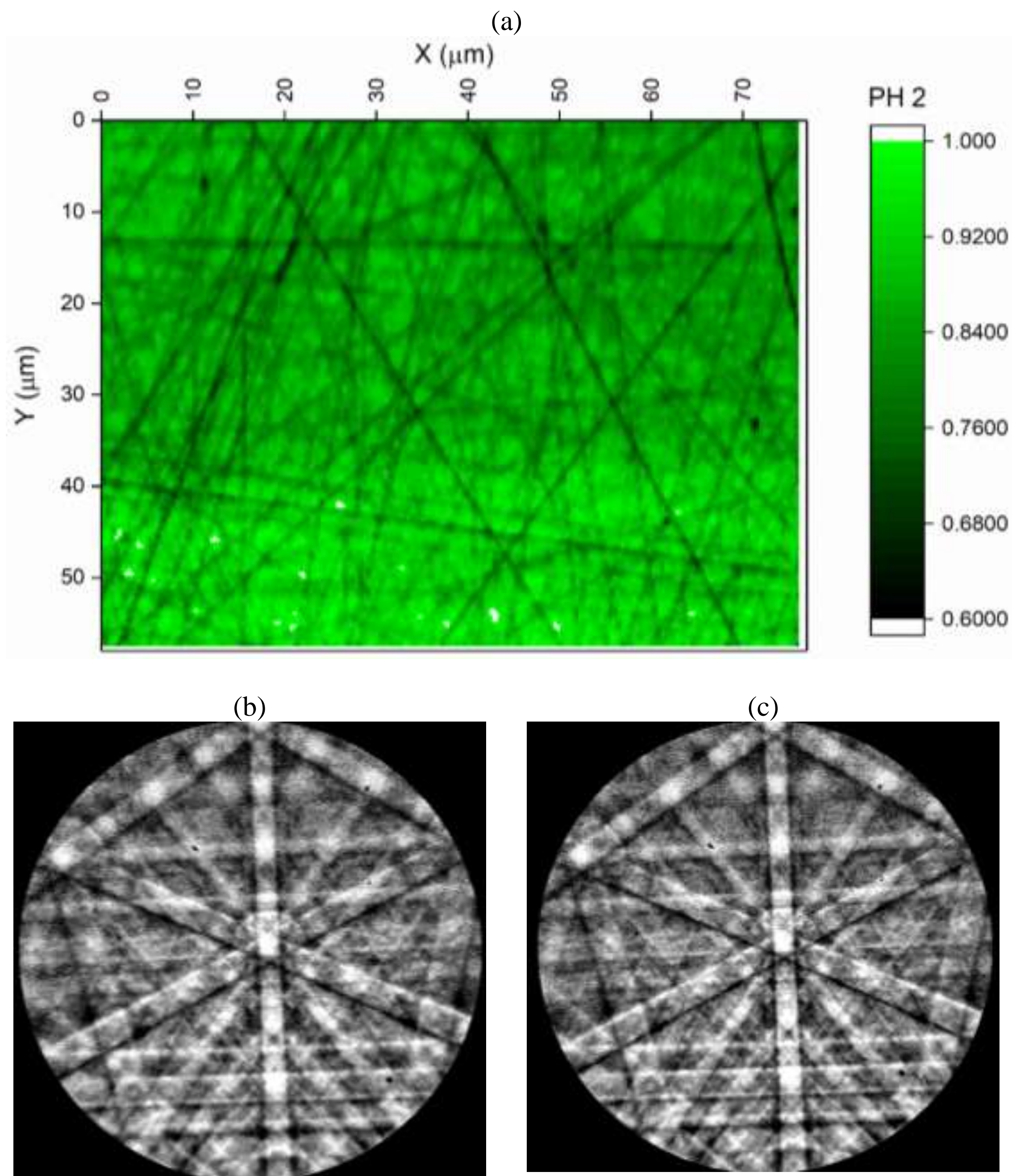

Figure 5-67: (a) EBSD peak height map of irradiation boundary in 6H-SiC crystal (0001), Si ions 750 °C, 0.25 peak dpa. EBSD Kikuchi patterns from (b) unirradiated side and (c) irradiated side

5.2.4.5 Grain boundary "cracks" or swelling steps

Closer inspection of surfaces of irradiated RB-SiC samples revealed what looked like microcracks emanating from silicon regions along SiC grain boundaries. Features like these were found in the irradiated regions of all types of RB-SiC, regardless of irradiation condition, but were not observed in the unirradiated regions of the same specimens. These cracks were found at sharp cusps in the silicon which pointed at a SiC grain boundary. Not all boundaries showed this kind of contrast in the SEM, many remained flat. The in-house RB-SiC had the fewest cracks as the microstructure rarely has SiC grain boundaries meeting silicon at a sharp cusp; SiC grains were mostly isolated in a silicon matrix. Crack-like features were regularly observed in both Starceram and REFEL samples.

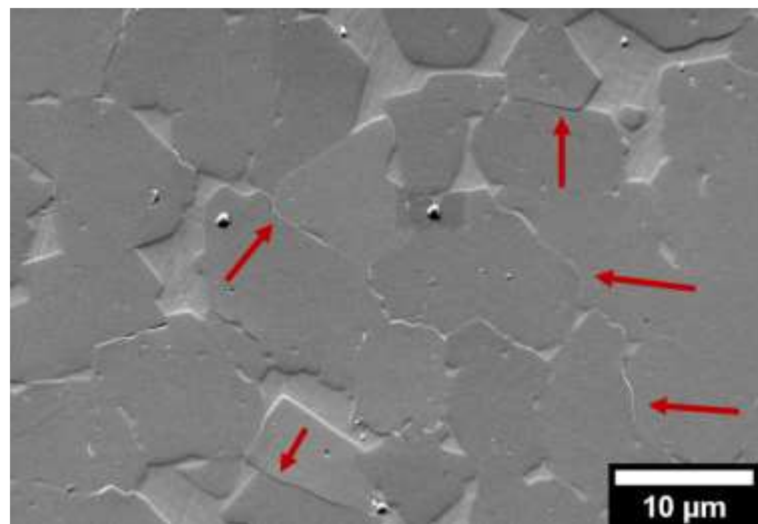

Figure 5-68: Irradiated REFEL microstructure. 2.5 dpa Si ions, 300 °C. Some crack-like features are marked. (SEM SE)

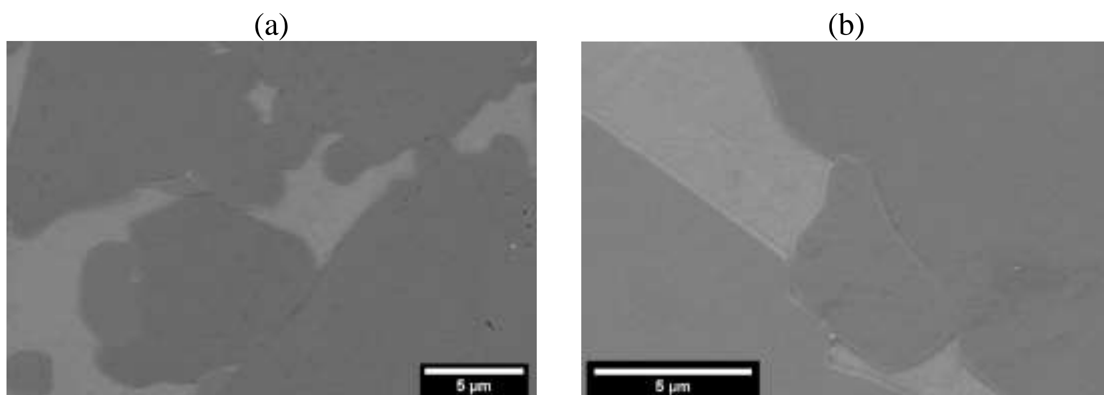

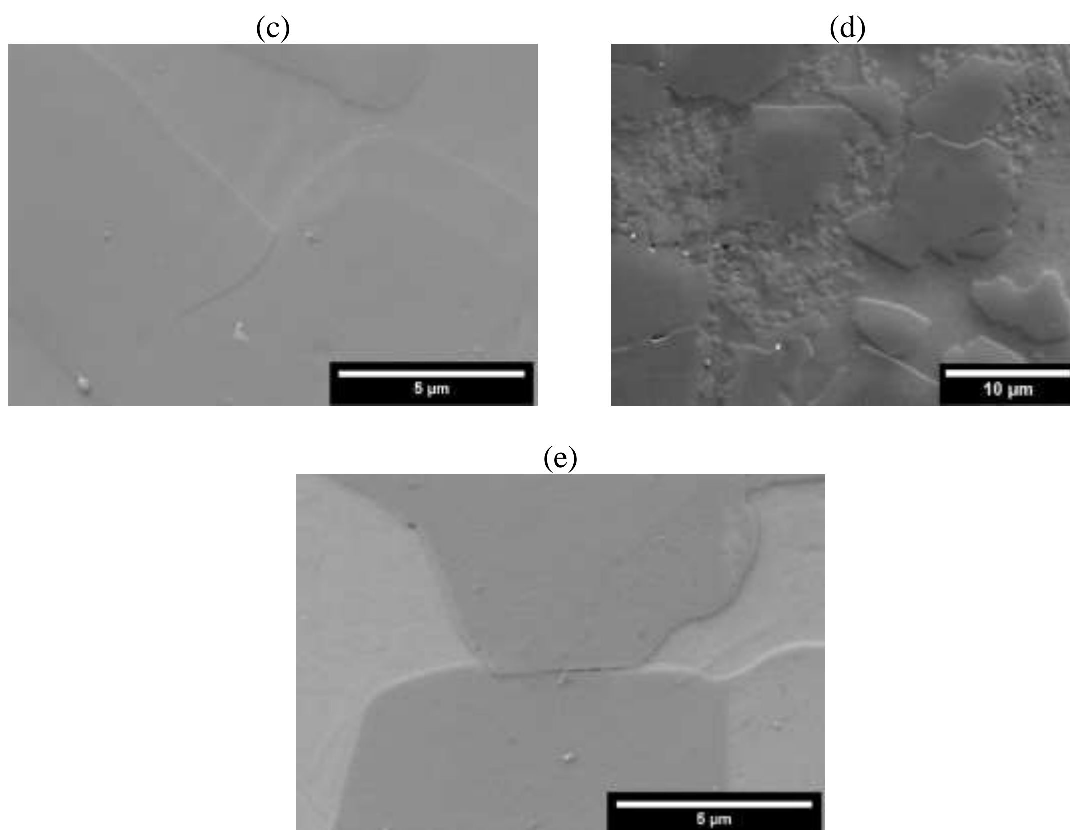

Figure 5-69: SEM SE images of interganular cracks in irradiated RB-SiC (a) Starceram Si 300 0.25 dpa. (b) Starceram Si 750 2.5 dpa. (c) REFEL Ne 300 2.5 dpa (d) 26A Ne 300 2.5 dpa (e) Starceram Ne 300 2.5 dpa.

Some of these features were cross-sectioned using FIB slice and view to see the sub-surface structure. In Figure 5-70 a line connecting two silicon regions is indicated with the red arrow. Further slices showed that the silicon regions are connected, and the line is a SiC-SiC grain boundary.

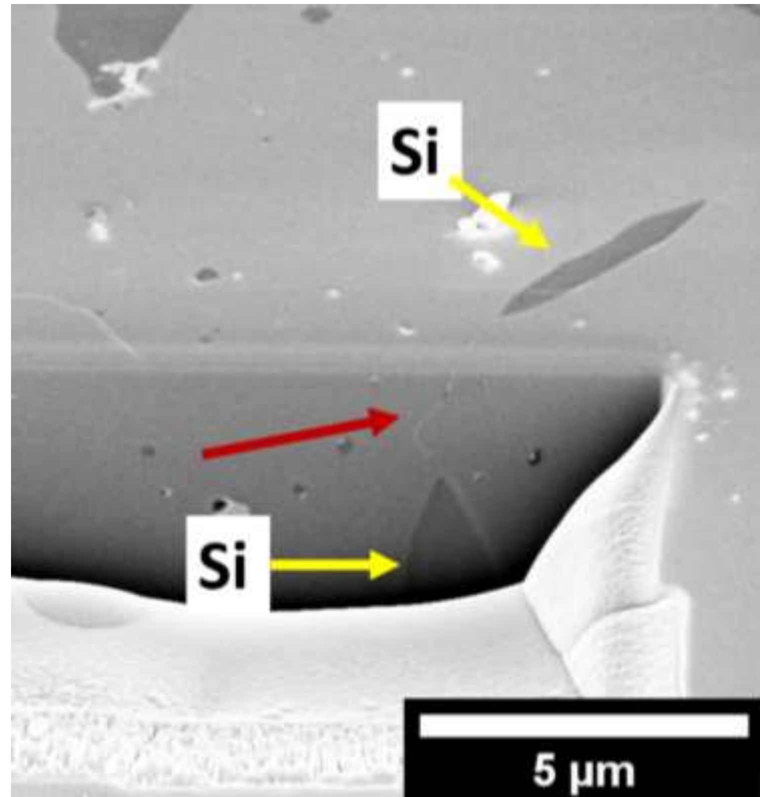

Figure 5-70: SEM in-lens image of a slice through a SiC "crack" in REFEL irradiated with Si ions to 2.5 dpa. The red arrow shows a contrast line connecting two silicon regions.

Slicing through another grain boundary "crack" showed bright regions on the grain boundary below the surface (Figure 5-71). TEM characterisation in the literature identified inclusions on REFEL grain boundaries consisting of impurity metal silicides, commonly Ca_2Si [59]. As silicon is consumed in the reaction-bonding process trace impurities insoluble in SiC are concentrated in the remaining silicon. Once the reaction is finished impurity-rich residual silicon can become trapped in closed regions of SiC leading to these grain boundary inclusions, possibly explaining what is seen here.

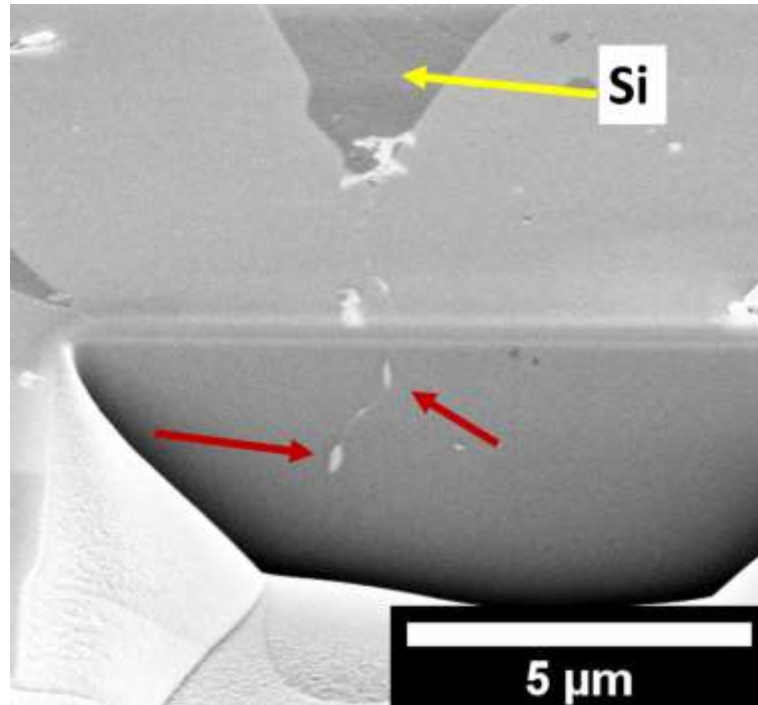

Figure 5-71: Bright spots along a SiC-SiC grain boundary below the surface. These could be impurity rich silicon, or a silicide phase. (SEM in-lens)

5.2.5 Radiation-induced swelling

5.2.5.1 Out of plane swelling

The SEM contrast change at the boundary (see section 5.2.4.1) showed a topology change in single crystal SiC, particularly in the ARGUS forescattered electron images. To quantify this, the boundary was mapped using atomic force microscopy (AFM). After levelling the measured data using a polynomial subtraction, the boundary step height was averaged along the mapped length of the boundary to make the curves in Figure 5-72. AFM data analysis for background subtraction is subjective and can influence the measured step height. The process used here followed the guide on the Gwyddion website designed to minimise user subjectivity in measuring step heights[2]. The same process was applied to all the measurements here for consistency. It was impossible to find a swelling step in silicon to measure using AFM.

[2] http://gwyddion.net/survey2/step3.php

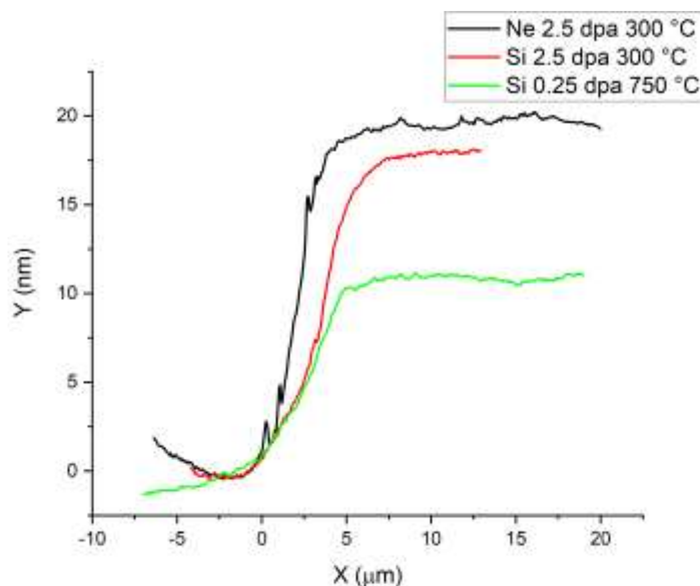

Figure 5-72: AFM measurements of swelling steps in ion irradiated single crystal SiC

The step heights were calculated from a "smooth bent step" fitting function in Gwyddion [237]. Swelling strain can be calculated as step height ÷ damaged layer depth (~1.2 μm) with these given in Table 5-3. These should be taken as an upper limit of strain as the damaged layer may be deeper due to ion channelling.

Table 5-3: AFM measured swelling step heights and estimated strain and the associated stress for ion implanted 6H-SiC

Condition	Step height (nm)	Swelling strain (%)
Ne 300 °C 2.5 dpa	18.6	1.55
Si 300 °C 2.5 dpa	16.5	1.38
Si 750 °C 0.25 dpa	10.0	0.83

HR-EBSD maps are assumed to be in plane stress as the signal comes from a thin layer, so σ_{33} is zero, but the ε_{33} lattice strain is *not* zero as it is free to expand and can be calculated within this thin layer. Figure 5-73 shows ε_{33} calculated from HR-EBSD across the boundaries of irradiated single crystal 6H-SiC. Assuming the EBSD signal is coming from less than the top 100 nm of the surface, the damage in this region is less than 1 dpa

(0.1 dpa), although damage varies quite steeply with depth in this region, so the damage at this depth is not clear, nor is the depth of the EBSD signal itself. This is only the elastic lattice strain with no contribution from any dislocations or voids.

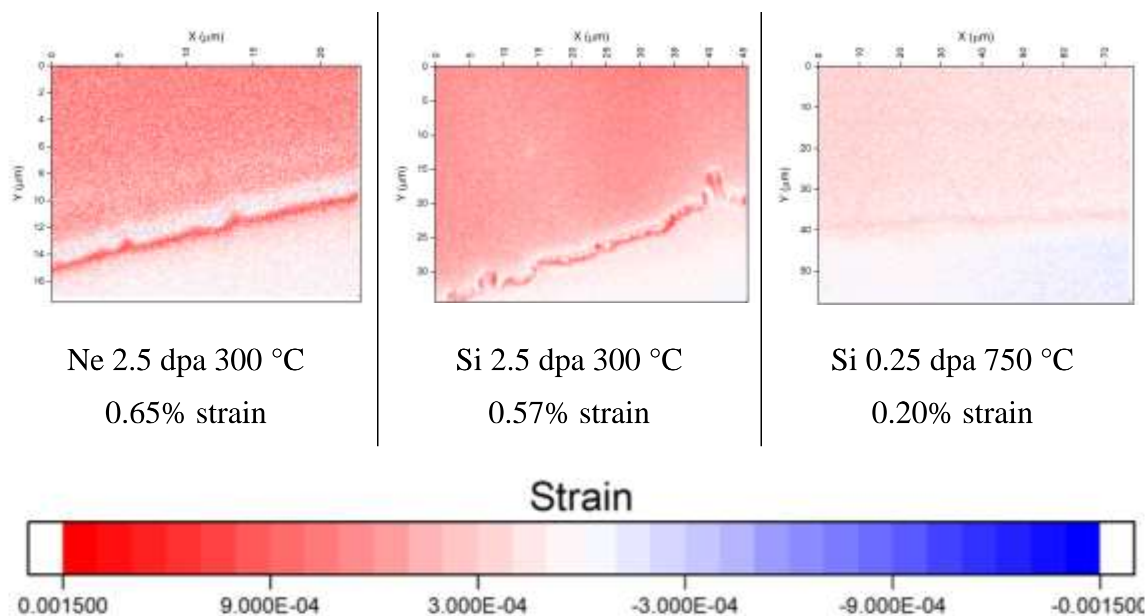

Figure 5-73: Out of plane (ε_{33}) elastic strain across boundaries in irradiated 6H-SiC from HR-EBSD

5.2.5.2 In-plane swelling

Figure 5-74 shows the strains of a micropillar measured by DIC in a single crystal of 6H-SiC irradiated with neon ions at 300 °C to a peak dose of 2.5 dpa. This is based on SEM-DIC between images taken before and after ion implantation. The observed strains are qualitatively similar to those predicted using this technique (Figure 4-13).

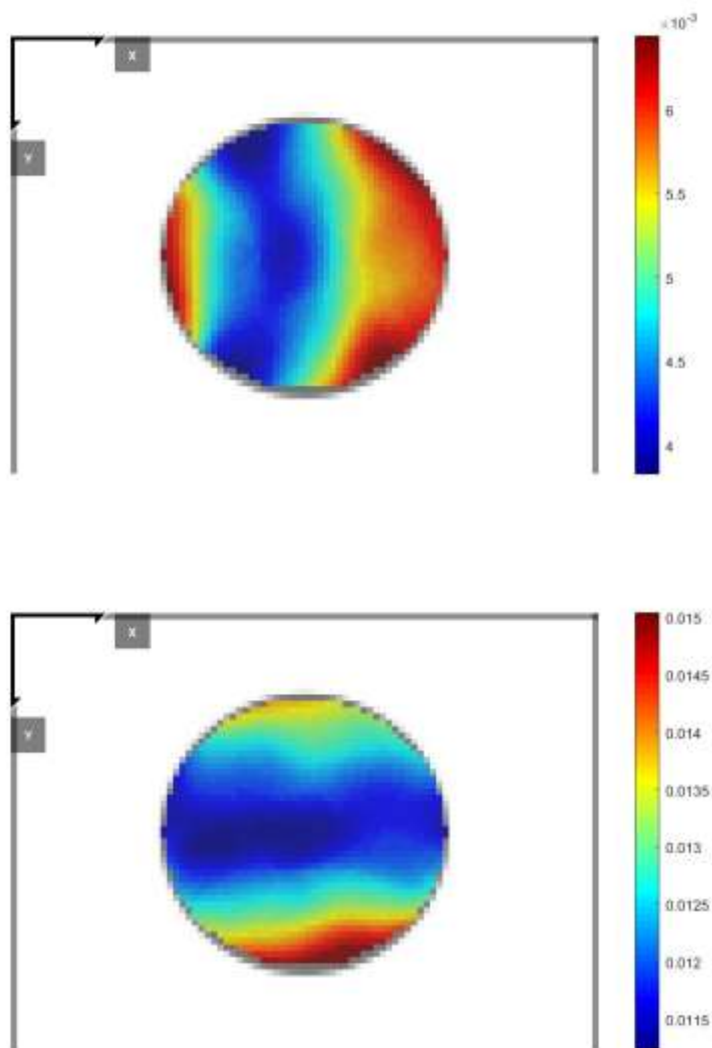

Figure 5-74: Strains measured by DIC in high dose neon irradiated 6H-SiC single crystal (a) xx (b) yy

The yy strains in Figure 5-74 are between 1.15% and 1.5%, however the xx strain between 0.4% and 0.7% seems low. This difference is likely to be due to different SEM imaging settings, despite best efforts to align the sample and correct astigmatism and focus for the images after irradiation.

In plane residual stresses calculated by HR-EBSD are shown in Figure 5-75 on the next page with their average stress and strains. These are derived from lattice elastic strains, but due to lateral constraints the lattice strain is compressive (planes are closer together). The compressive in-plane strains are smaller than the out of plane swelling strain.

5.2.6 Radiation-induced residual stresses/strains

5.2.6.1 Single crystals

Ion irradiation causes changes to the crystal lattice spacing in single crystals of 6H-SiC which are measurable using HR-EBSD. Using the elastic constants of 6H-SiC, these strains can be converted to elastic stresses (Figure 5-75). The detected diffraction pattern is formed from electrons backscattered from the top <50 nm of the sample, corresponding to ~1 dpa of damage (0.1 dpa for the low dose condition). The radiation-induced residual stresses are found to be compressive, with a larger magnitude for more damage. The sample irradiated with neon ions has a slightly larger compressive stress (-1.88 GPa) than the sample irradiated to the same nominal dpa with silicon ions (-1.74 GPa). The boundary swelling step caused rotations of the diffraction patterns causing the light/dark stripe of low/high stress.

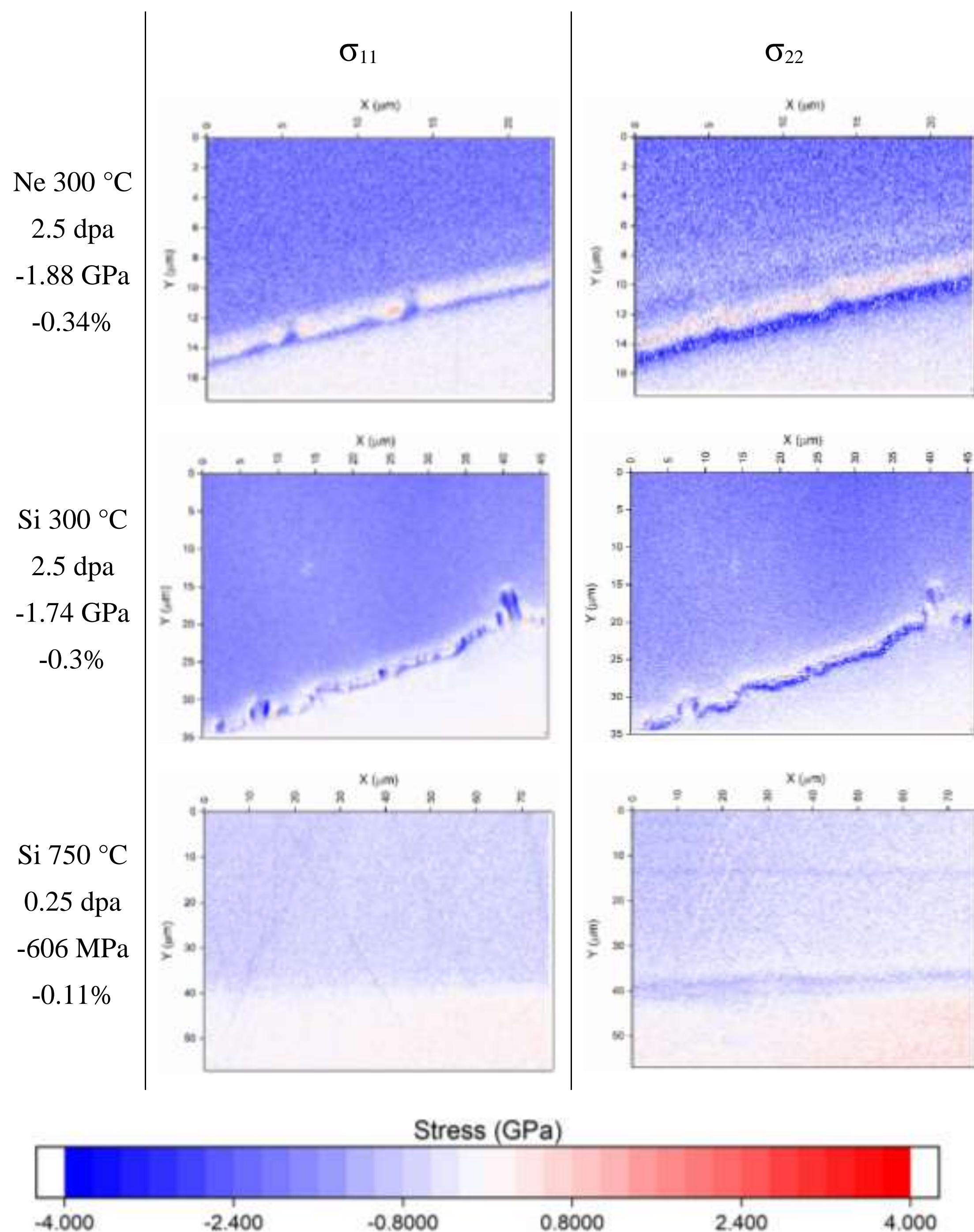

Figure 5-75: HR-EBSD in-plane stress maps of boundaries in ion irradiated single crystal 6H-SiC. All figures use the same scale. Upper part of the maps is the irradiated side. $\sigma_{33} = 0$ as plane stress. Reference pattern is taken on the unirradiated side.

Strains in silicon ion irradiated single crystal silicon are near the limit of sensitivity of HR-EBSD (~10^{-4}). Some sample drift appears to have affected the measurement of these very low strains and appears to be significant relative to the radiation-induced strain,

especially in the σ_{22} map in Figure 5-76. Raman spectra showed no change in peak position across the unirradiated-irradiated boundary, so no detectable change in atomic spacing.

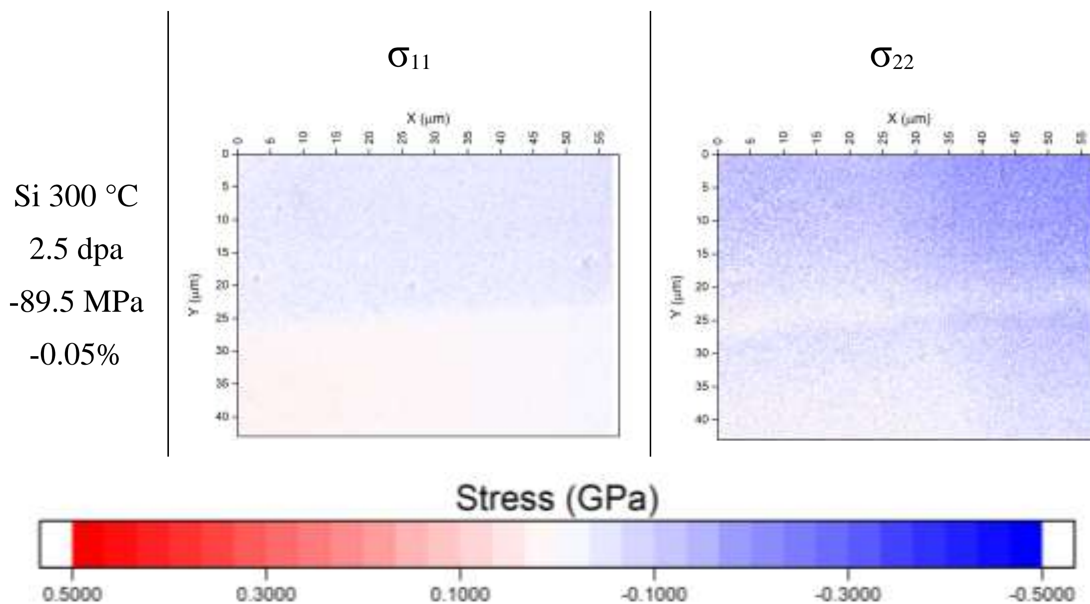

Figure 5-76: In-plane stress for 2.5 dpa 300 °C silicon ion irradiated silicon. Note the different colour scale bar to the SiC irradiations above. The result appears to have been affected by horizontal stage drift. The observed strains are close to the limit of strain sensitivity in HR-EBSD.

5.2.6.2 Radiation-induced stresses in reaction-bonded SiC

Residual stresses in the silicon regions of RB-SiC were investigated in a similar way as for the unirradiated case in section 5.1.4 using Raman spectroscopy mapping and HR-EBSD. After irradiation the Raman spectrum of silicon maintained a sharp peak suitable for peak fitting and finding its spectral position. Interestingly the "Fano" profile found in silicon regions for REFEL and Starceram was lost and the peak became sharp and symmetrical.

As in the unirradiated case, residual stresses in silicon regions are found to be compressive, however the spatial variation in stress has been reversed. The silicon region is now more compressed at the edge of the region than in the centre as shown by the Raman silicon peak position linescans in Figure 5-77.

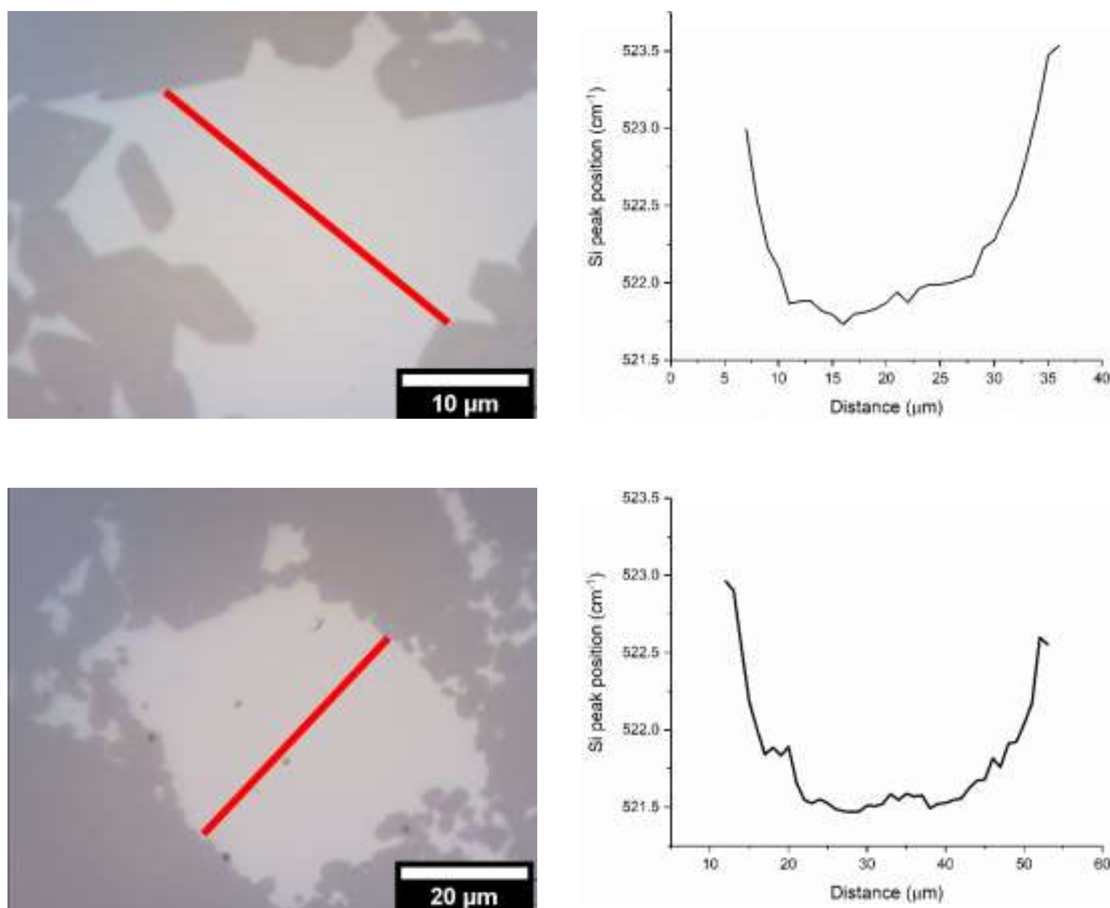

Figure 5-77: (top) Si Raman peak position linescan in REFEL after 2.5 dpa 300 C Ne irradiation. (bottom) Si Raman peak position linescan in Starceram after 0.25 dpa 300 C Si irradiation. Linescans are from left to right.

Two dimensional maps reveal further spatial variations in compressive stress based on geometry of the silicon regions. Figure 5-78 and Figure 5-79 show Raman silicon peak position maps of silicon regions in 2.5 dpa 300 °C neon ion irradiated Starceram and REFEL. As in the linescans shown above, the edges of silicon regions are more compressed than their centres. Higher compressive stresses are found in sharp cusps of silicon regions, as highlighted with a red arrow in Figure 5-79. However, some locations with similar geometry where a higher compressive stress might be expected (such as the one indicated by a green arrow) do not show a higher compressive stress. The white “halo” around silicon regions in Figure 5-79 is an artefact of the laser spot being larger than the pixel size, so the acquired spectrum is sampling some of the SiC grain as well as silicon. In Figure 5-78 the pixel size was matched to the laser spot size, so this halo effect isn’t seen to such an extent,

although some of the pixels have been filtered out where the laser overlapped with a SiC grain.

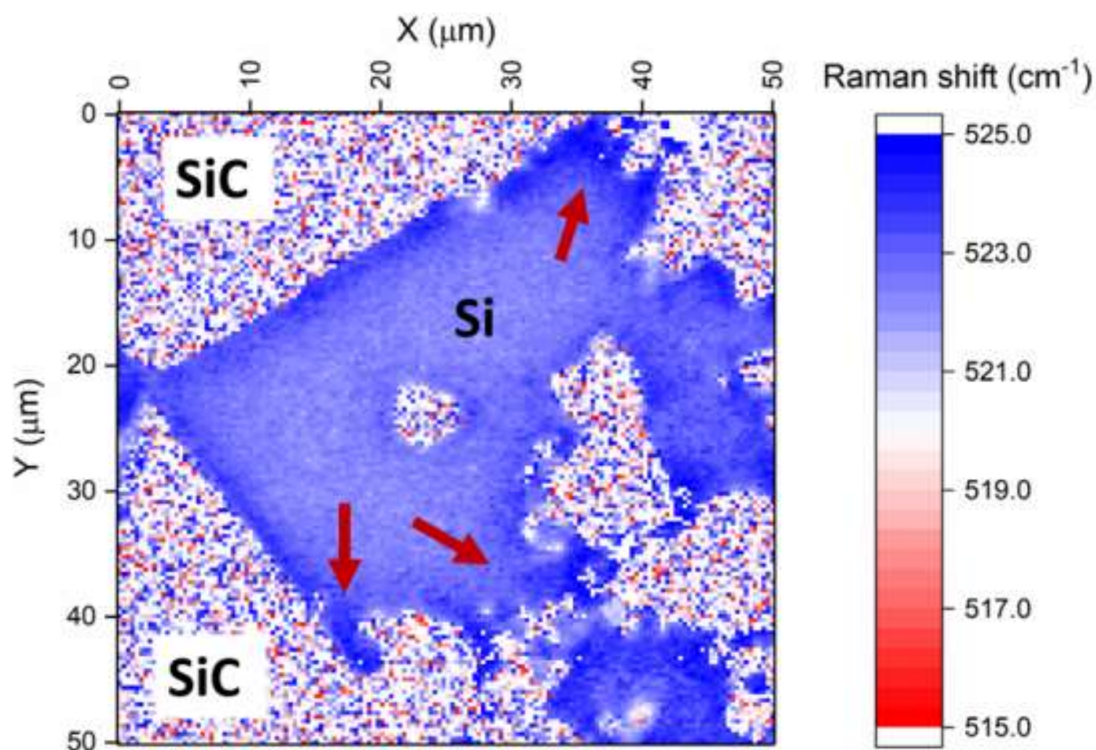

Figure 5-78: Silicon region in Starceram after irradiation with neon ions at 300 °C, 2.5 peak dpa. Edges of the silicon region close to SiC grains have a higher Raman shift peak position indicating a more compressive stress.

The silicon peak position moves to higher wavenumbers (more compressive stress) after irradiation in the Starceram sample shown in Figure 5-78 than the REFEL sample shown in Figure 5-79 after the same irradiation condition. The only difference is their microstructure with Starceram having larger SiC grains and silicon regions than REFEL.

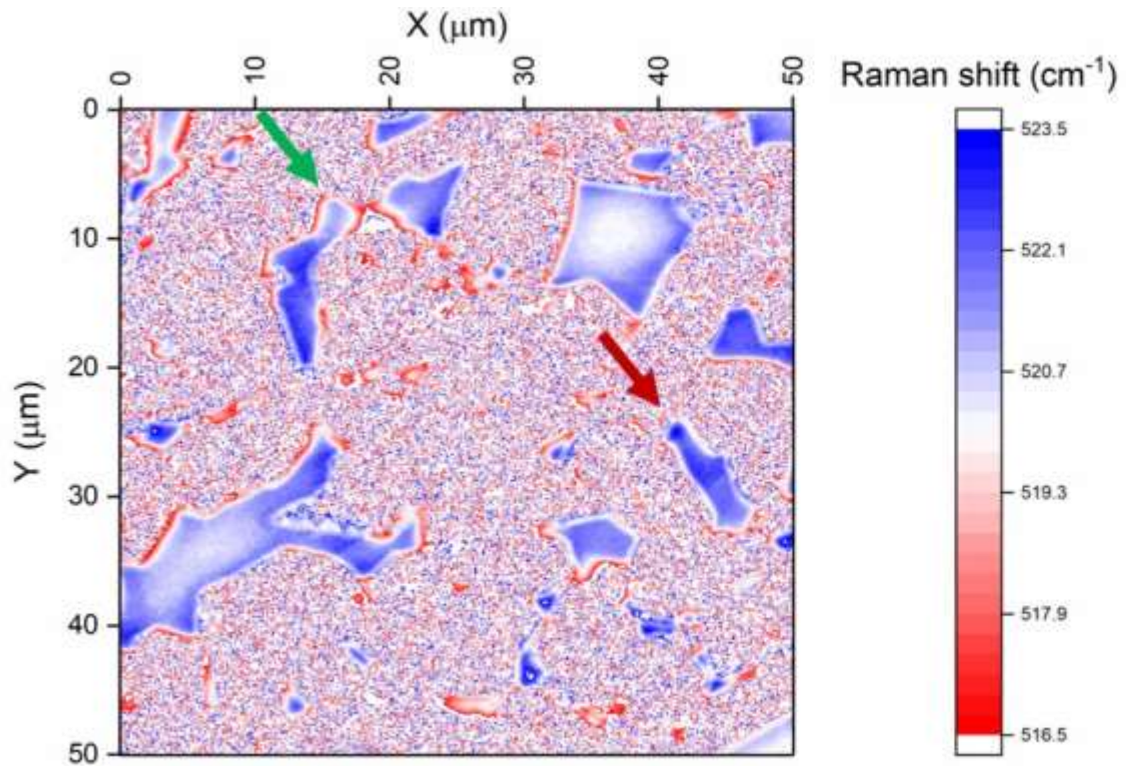

Figure 5-79: Raman peak shift map of silicon regions in REFEL after irradiation with neon ions at 300 °C, 2.5 peak dpa.

Higher spatial resolution is achieved using the SEM rather than an optical microscope, and strain/stress measurements are made using HR-EBSD. As this technique is not absolute, all the stress values in Figure 5-80 are relative to a reference diffraction pattern which was taken in the centre of the silicon region. Based on the Raman measurements which are absolute relative to an external unstressed reference sample, the centre of the silicon region which is the “zero” stress reference in EBSD, is actually at a compressive stress, so this compressive stress should be added to the calculated HR-EBSD stresses.

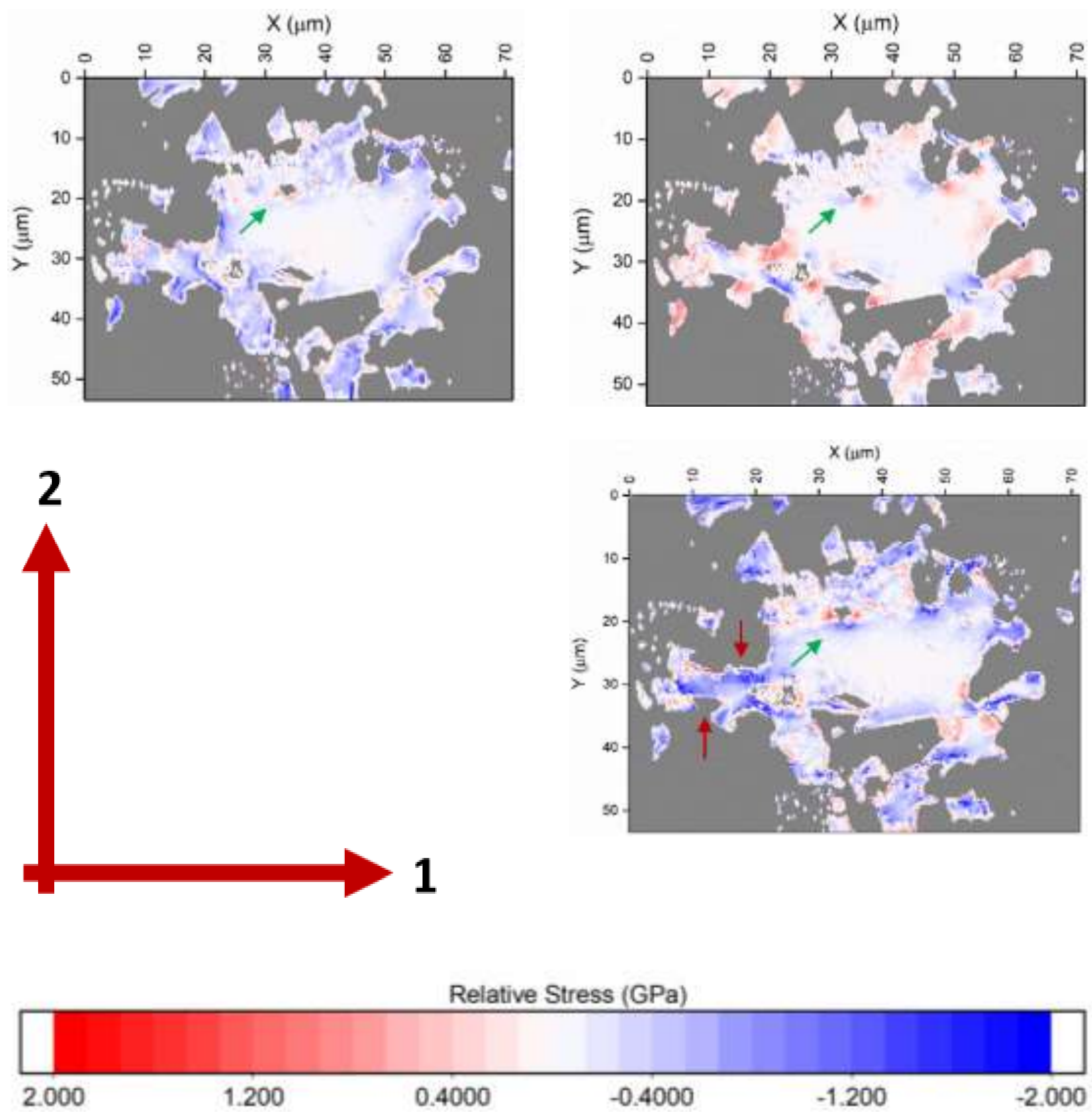

Figure 5-80: HR-EBSD plane stress maps of residual silicon in in-house RB-SiC irradiated with neon ions at 300 °C, 2.5 peak dpa. Stresses are relative to a point in the centre of the silicon region. Tensile stresses in silicon are seen near sharp points of SiC grains and compressive stresses in the concave cusps. The red arrows in the σ_{22} map show a region of higher compressive stress where the narrow region of silicon has been compressed by swelling SiC.

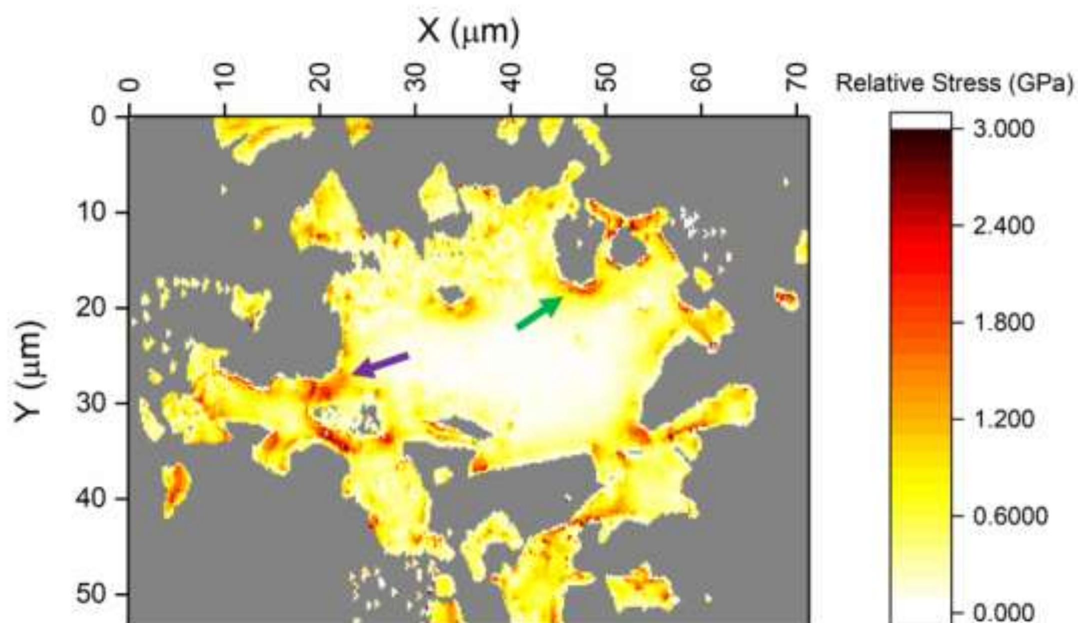

Figure 5-81: Plane stress von Mises stress map of neon irradiated in-house SiC

As well as calculating elastic strains/stresses, geometrically necessary dislocations (GND) were calculated in silicon. Figure 5-82 shows that this density increases towards the edges of the silicon region, and at the SiC boundaries, similar to the variation in elastic deformation. Generally, where there are large elastic stresses, there are also higher calculated GND densities. Some regions of high elastic stress, such as marked with the purple arrow in Figure 5-81, have low GND density whereas at the area marked with a green arrow there is both an increased GND density and a high elastic stress, but lower than at the purple arrow.

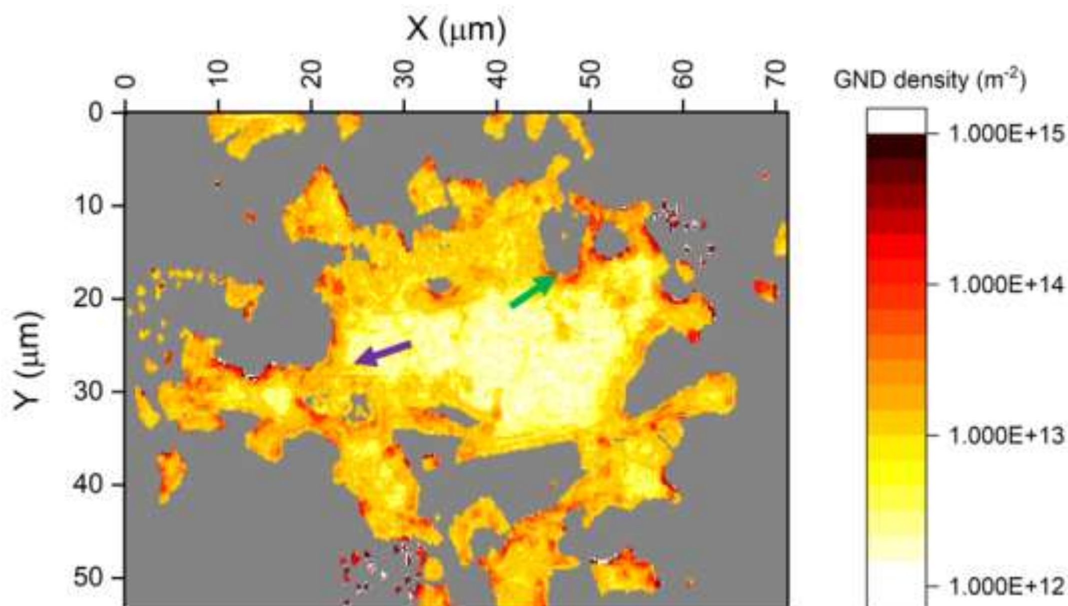

Figure 5-82: GND density of a silicon region of in-house RB-SiC irradiated with neon ions at 300 °C, 2.5 peak dpa.

Radiation changes to residual stress distribution in RB-SiC is very complicated and appears to be dependent on microstructure where large SiC grains result in larger compressive stresses in silicon regions. Smaller silicon regions appear to have larger compressive stresses.

5.2.7 Stress release in microcantilevers

Microcantilevers were fabricated in various irradiated samples to investigate swelling stresses in the irradiated layer. These cantilevers were made following the steps outlined in methods section 4.5.4. A link to animated videos of these experiments can be found in section 8.1.

As a reference, similar cantilevers were made in unirradiated regions of single crystal 6H-SiC. Figure 5-83 shows a microcantilever made in unirradiated 6H-SiC, oriented along $[10\bar{1}0]$ showing no deflection between the SEM frames taken just before and just after the final FIB milling operation. This shows that there is no influence of the FIB milling procedure on the deflection of cantilevers.

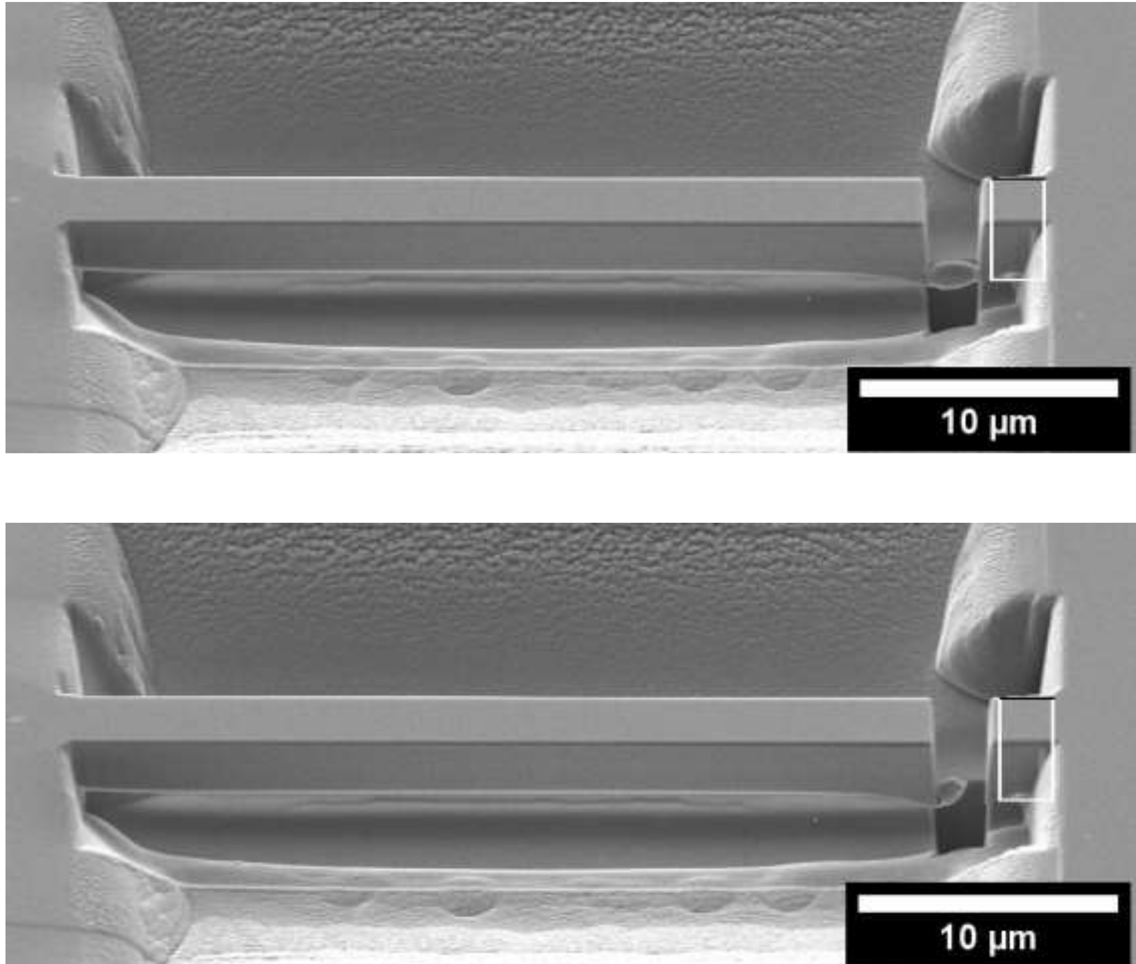

Figure 5-83: Cantilever in unirradiated 6H-SiC showing no deflection when the cantilever is released from the bulk. Top is the frame before the final layer of material is removed, below is the next frame. (SEM SE)

Cantilevers made in ion irradiated SiC single crystals showed significant bending downwards during FIB cutting. Selected SEM frames of one of the experiments are shown in Figure 5-84.

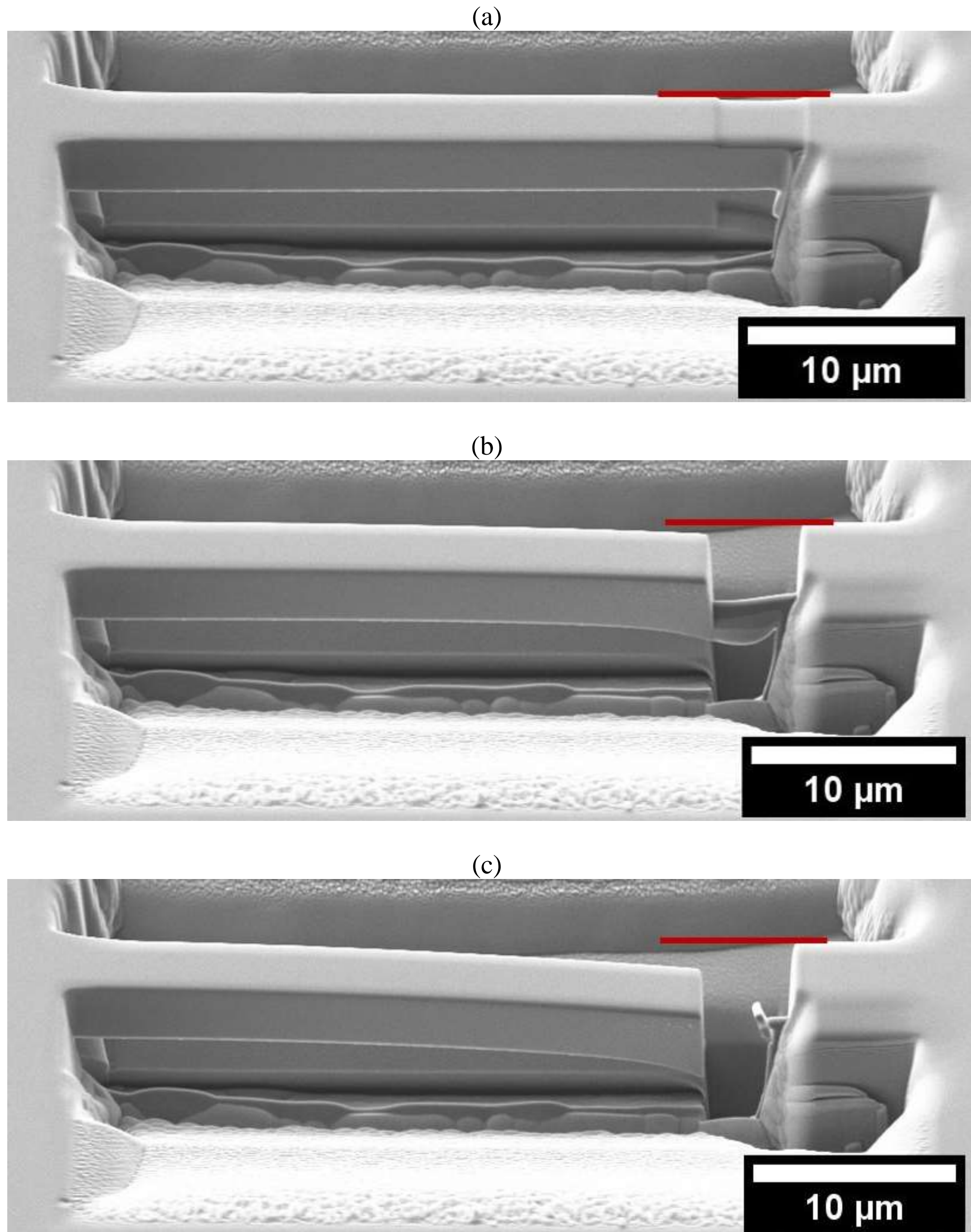

Figure 5-84: Example of cantilever bending in 6H-SiC after neon ion implantation at 300 °C, 2.5 peak dpa. (a) is the first stage of FIB, (b) is the frame before final cut-off, and (c) is immediately after final cut-off. The red line is a guide from the initial starting position of the beam. (SEM SE)

Two cantilevers were successfully made in neon ion irradiated 6H-SiC single crystal, with their deflections shown in Figure 5-85.

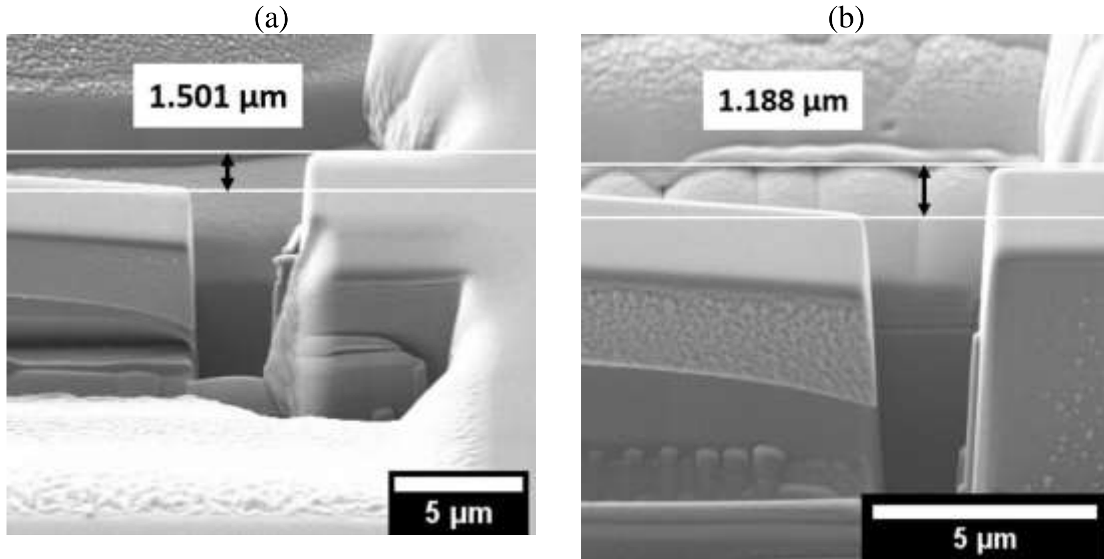

Figure 5-85: Deflection of two cantilevers made in neon ion irradiated 6H-SiC. Both images were acquired at 54 ° specimen tilt with tilt correction off. (a) is the same cantilever shown in Figure 5-84. (b) is the cantilever used for thinning and the "rebound" measurement. (SEM SE)

The dimensions and deflections (corrected for specimen tilt) of each cantilever are given in Table 5-4. The damaged layer is ~1.2 µm thick based on SRIM calculations.

Table 5-4: Dimensions, and deflection (corrected for specimen tilt), of irradiated 6H-SiC cantilevers

	Cantilever A	**Cantilever B**
Length (µm)	33.00	24.00
Width (µm)	3.93	2.74
Height (µm)	3.40	2.37
Uncorrected deflection	1.501	1.188
Tilt corrected deflection (µm)	1.85	1.47

The second cantilever, shown in Figure 5-85 (b) was used for a "rebound" experiment, where part of the cantilever was thinned, removing the ion irradiated layer. As shown in Figure 5-86, the cantilever partially moved back upwards, however it did not return to the horizontal position. This is probably due to the residual bending in the un-thinned section.

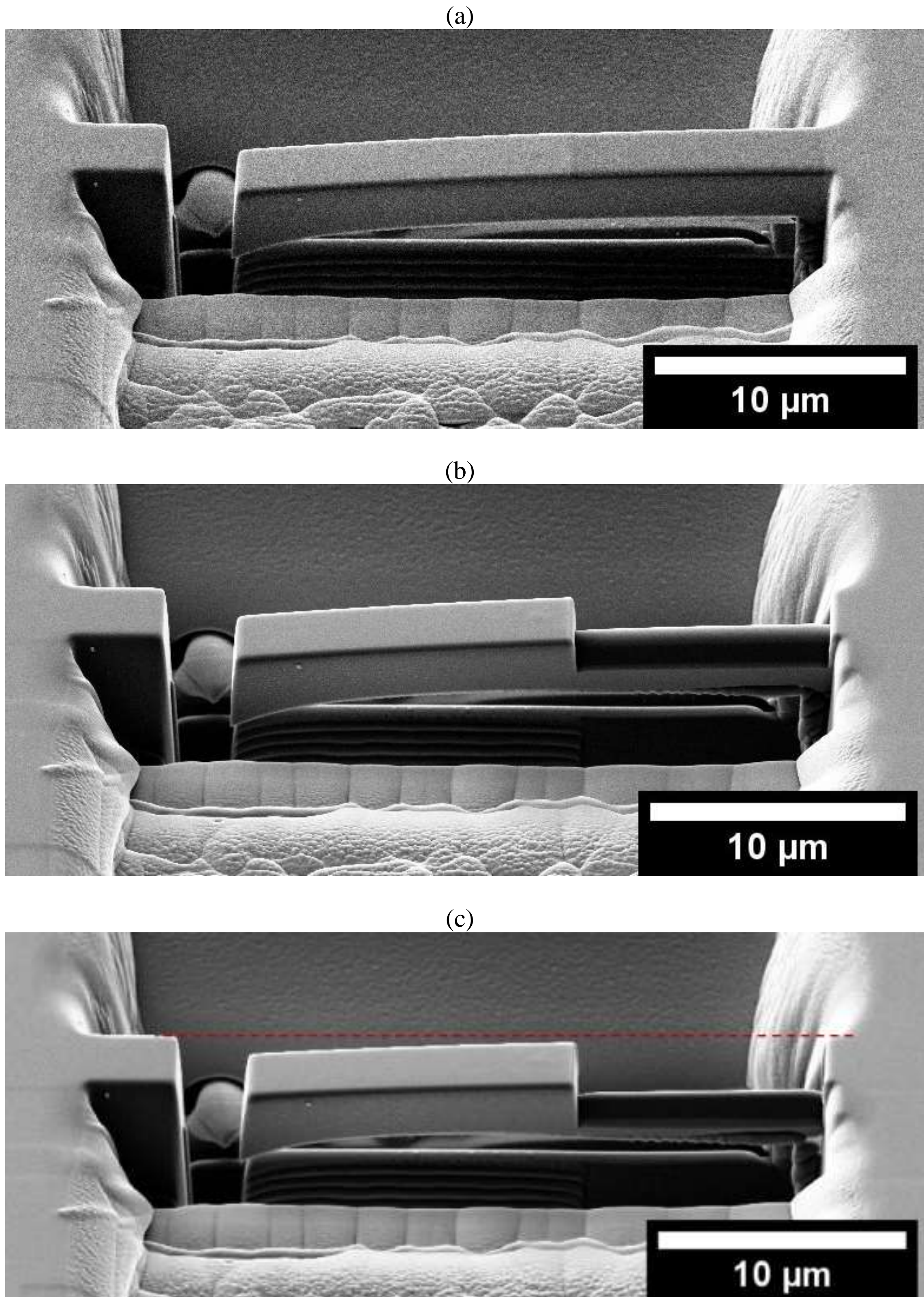

Figure 5-86: A bent 6H-SiC cantilever being thinned at one end and rebounding towards being straight again. (a) is the first step of thinning. (b) is the first detected movement. (c) is after the final thinning step. SEM images taken at 54 ° tilt, no tilt correction. (SEM SE)

Another 6H-SiC cantilever was made in neon irradiated 6H-SiC and was oriented along $[10\bar{1}0]$. During the cutting procedure, the cantilever arched upwards, then snapped off spontaneously before the cutting was completed (Figure 5-87).

(a)

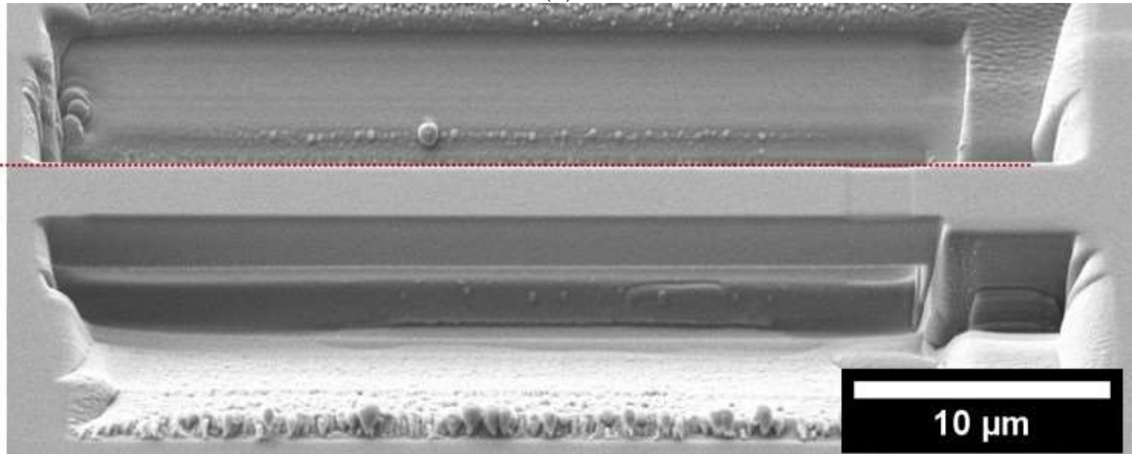

(b)

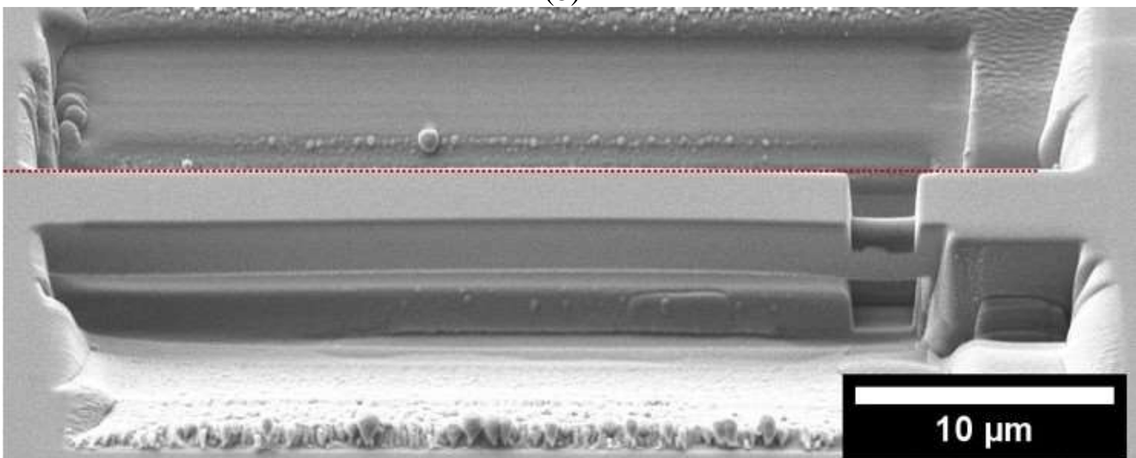

(c)

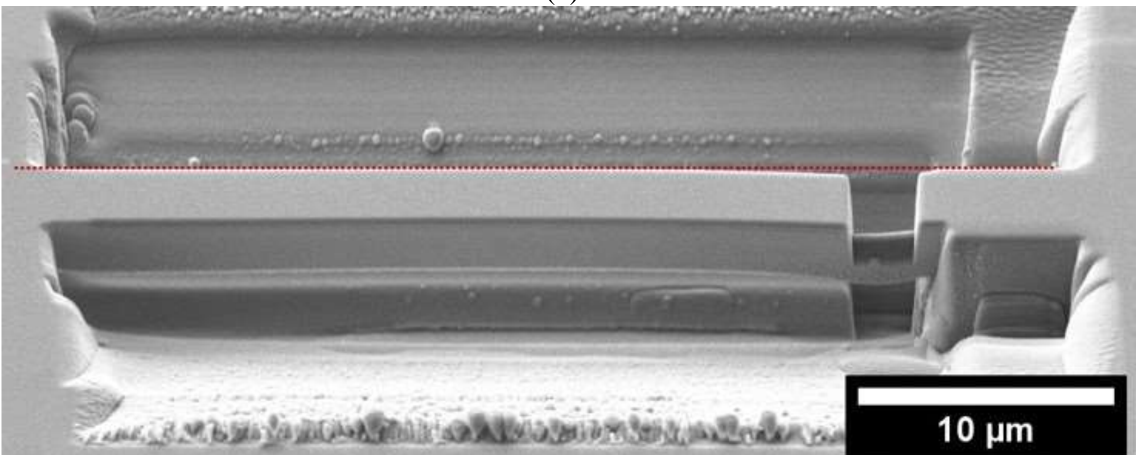

(d)

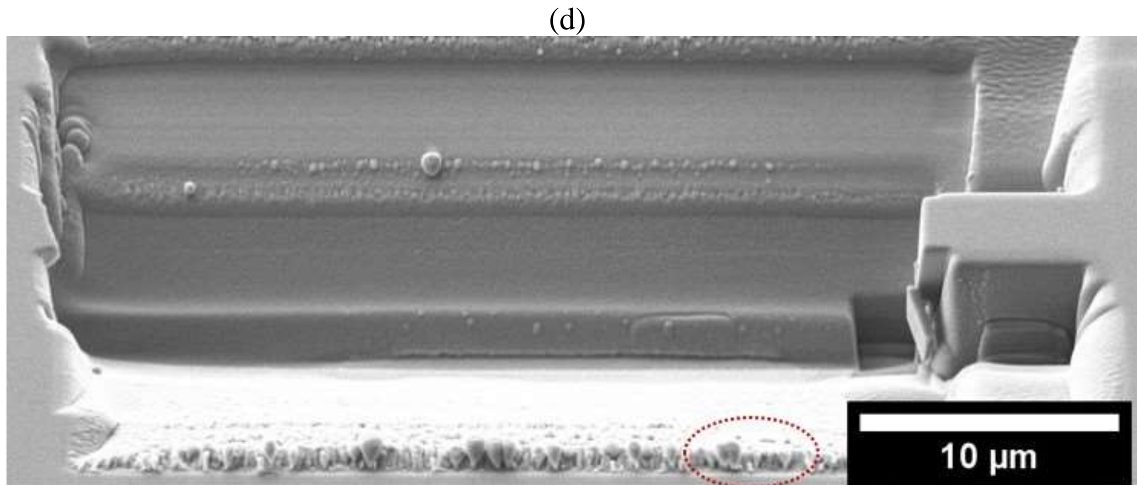

Figure 5-87: Neon ion-irradiated 6H-SiC cantilever oriented along [001] during end cut-off. (a) shows the first cutting stage, (b) the cantilever starts to arch upwards, (c) the cantilever begins bending down like the other irradiated 6H-SiC cantilevers. (d) after the cantilever has snapped off. The red circle shows where a piece of redeposited SiC was knocked off by the cantilever flying away. (SEM SE)

Similar cantilever release experiments were done in neon irradiated single crystal silicon. The results were less dramatic than the SiC cantilevers; nevertheless, a very small deflection was observed (Figure 5-88, but most clearly seen in the video). As ions are implanted deeper into silicon than silicon carbide, the triangular cross-section cantilever is made taller to ensure that both irradiated and unirradiated material is included, otherwise it would be impossible for the cantilever to bend.

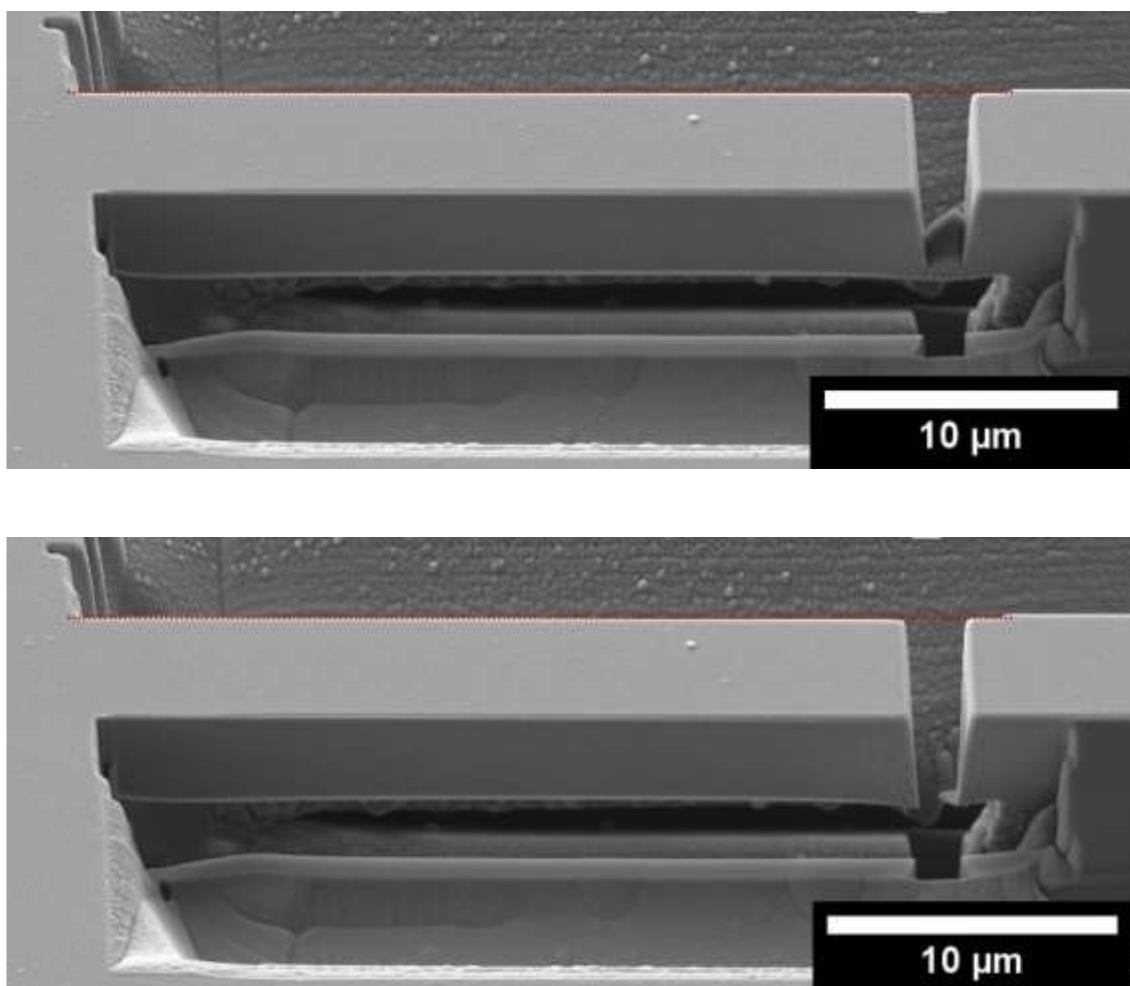

Figure 5-88: Cantilever deflection in neon irradiated single crystal silicon (SEM SE)

Cantilevers were also made in SiC grains of irradiated Starceram and REFEL. The Starceram cantilever shown in Figure 5-89 was made entirely in one of the large SiC grains, although this was shorter than the cantilevers made in single crystal 6H-SiC. The cantilever arches upwards in the initial stages of slicing the end off, then bends downwards. There is no sudden "snapping" as the final part of the cantilever is cut off – it looks like the cantilever tip is resting on redeposited material at the bottom of the trench.

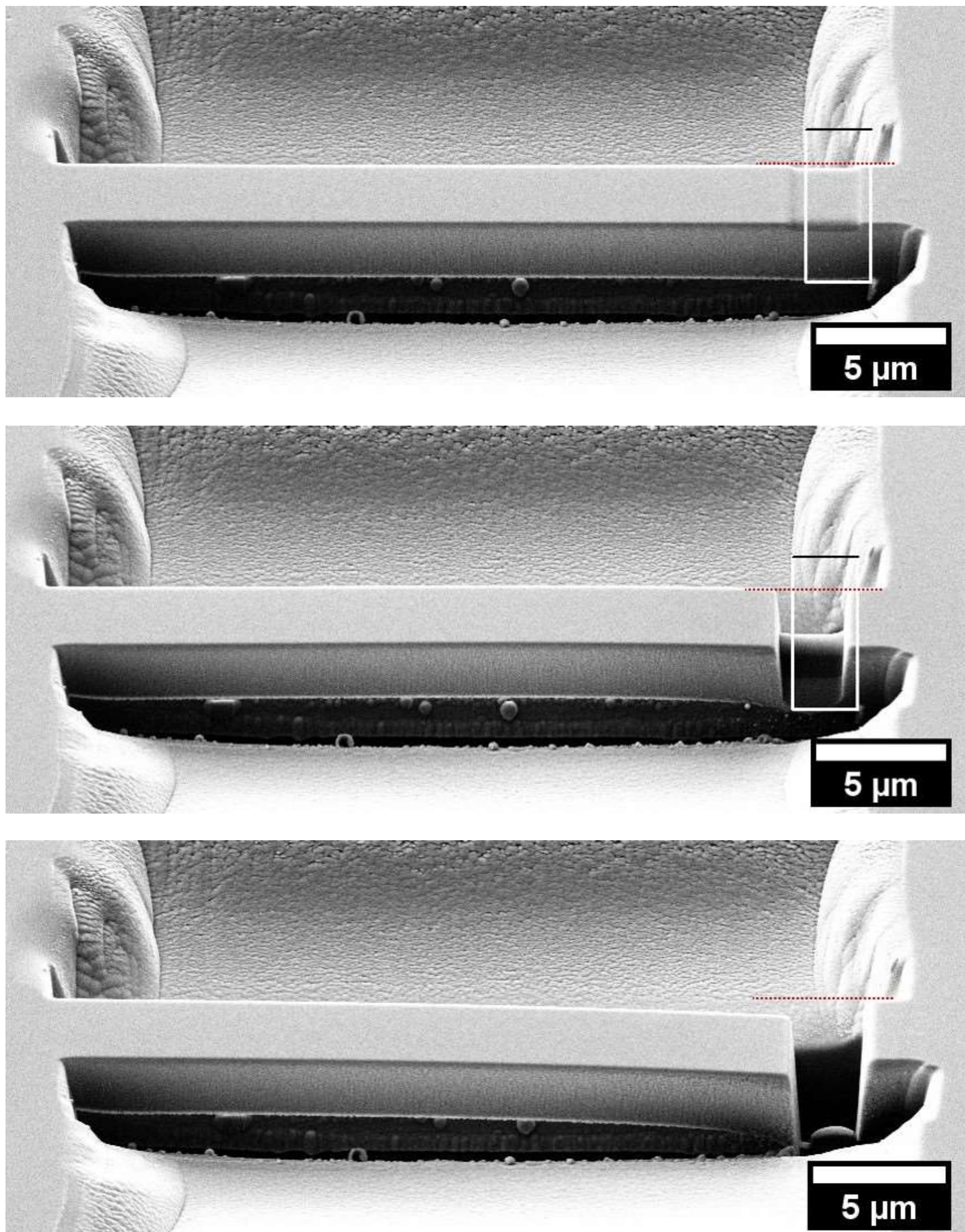

Figure 5-89: Cantilever deflection in neon ion irradiated Starceram. The cantilever was made entirely in one of the large SiC grains. The second frame shows the cantilever arching upwards, and the final frame shows the final position, possibly resting on some redeposited material in the trench. (SEM SE)

The REFEL cantilever is more complicated as it contains a few SiC grains and silicon regions. Again, the cantilever initially arches upwards, then bends down as the cut gets deeper. Once the cantilever is completely free, it moves right (into the picture). As well as the stress acting on the cantilever from radiation defects and swelling, there are

compressive stresses initially in the silicon regions from processing, plus the changes caused to these stresses by irradiation. Looking closely at the final frames when the cantilever shifts right (into the page), it appears that the silicon region near the base is expanding. This is most clear in the video played in slow motion, or quickly switching between these frames.

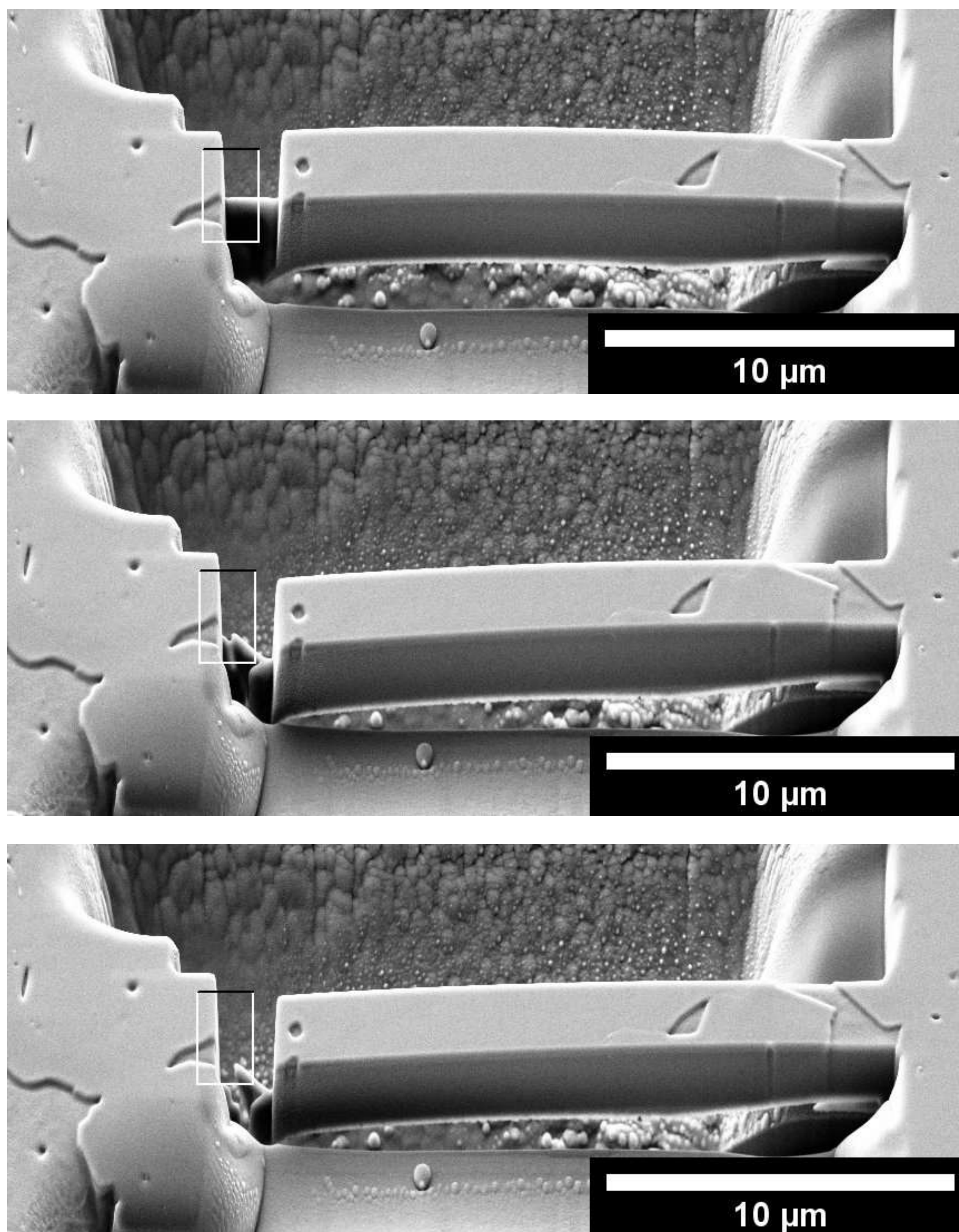

Figure 5-90: Microcantilever in a SiC grain of neon irradiated REFEL. Initially the cantilever arches upwards, then moves down directly, before moving right (into the screen) when it is fully released. (SEM SE)

These experiments are a stark demonstration of the large compressive residual stress in ion irradiated layers in SiC and the effect this may have on other properties. Analytical calculations based on Euler-Bernoulli [200] and Timoshenko beam theory struggled to reach a satisfactory solution due to uncertainty in the neutral axis relative to

the irradiated layer thickness, and the elastic response of the cantilever base, as discussed in ref. [201]. This led to using finite element modelling (FEM) to calculate the required strain to cause bending and the associated residual stress.

5.2.7.1 FEM simulations of bending cantilevers

To investigate the strain necessary to bend these cantilevers a finite element model was made by Dr Edmund Tarleton using ABAQUS. By applying a thermal expansion to a 1.2 μm layer of material to simulate radiation swelling, the cantilevers can be bent to the same displacement as measured experimentally (Figure 5-91). The magnitude of this thermal strain is related to the radiation-induced swelling strain and residual elastic stress can be calculated from the base of the cantilever. Since this is not a complete stress release, just a force and moment balance in the cantilever, the thermal swelling strain is *not* equivalent to the unconstrained radiation swelling strain. The lateral stress in the base of the cantilever is the relevant measurement corresponding to the constrained swelling stress.

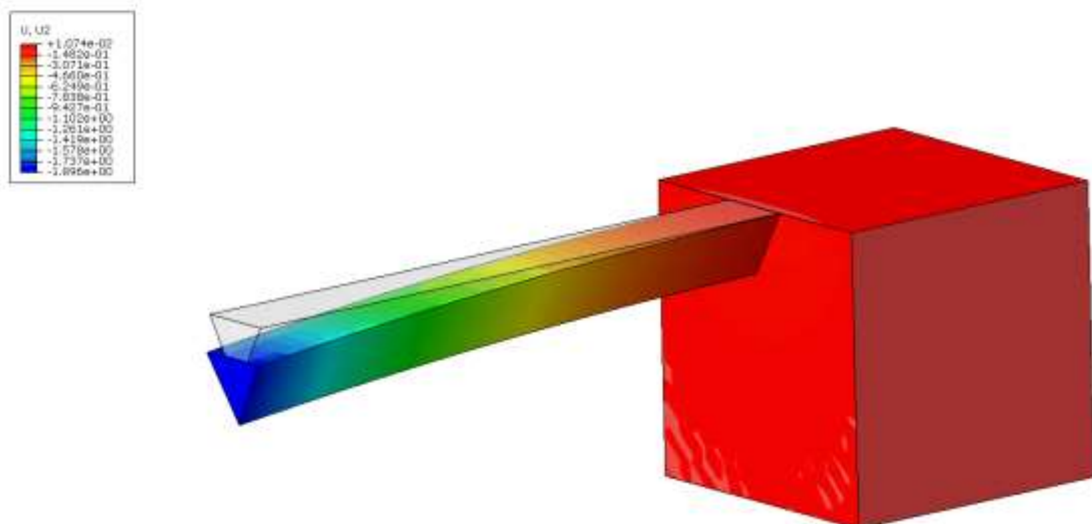

Figure 5-91: Vertical displacement of the FEM model of cantilever A which matches the measured displacement

The longitudinal residual stress distribution (S33) within the beam is shown in Figure 5-92, showing the compressed bottom layer, as expected in cantilever bending, but

also a tensile internal stress on the top surface of the unirradiated substrate material due to the "thermal" (radiation) swelling, and a compressive stress on the irradiated side.

The base of the cantilever has a residual compressive stress in the irradiated layer which is relaxed near the cantilever at the front face. The other faces of the base are constrained with fixed boundary conditions, but it is allowed to extend vertically as in the experiment. The base below the thermally expanding layer has a relatively small tensile stress to balance the large residual compressive stress. The biaxial compressive stress in the base in cantilever A is -5.94 GPa, and in cantilever B is -4.92 GPa. The difference is probably related to errors in measuring dimensions in the SEM images and in microcantilever fabrication. The process could be optimised to use rectangular cross-section cantilevers at specimen edges as the group at Leoben use in refs [198–200].

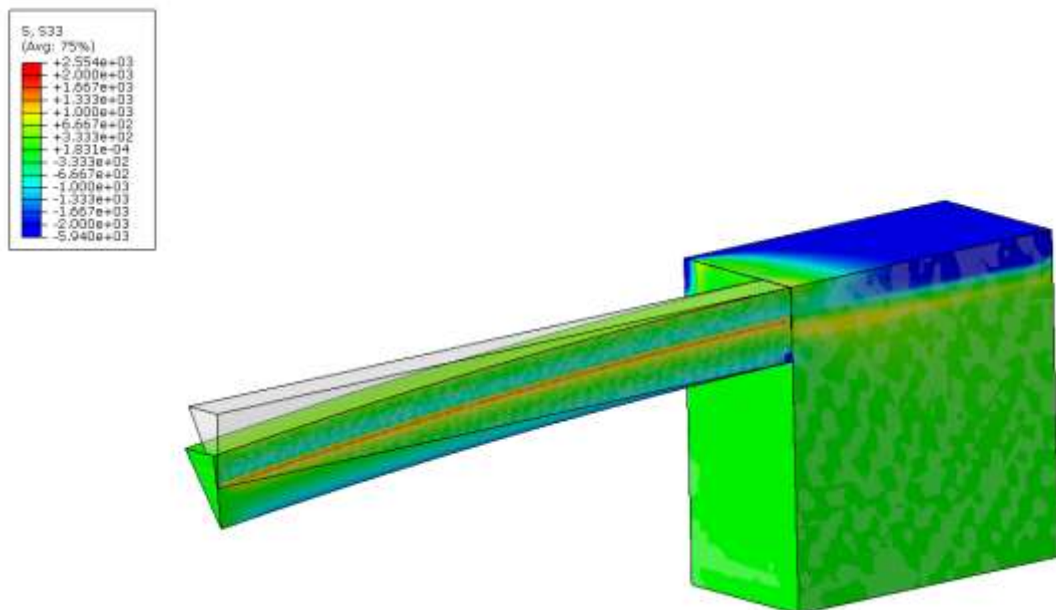

Figure 5-92: S33 (along the length of the beam) for cantilever A.

The experimental techniques used here demonstrate significant out of plane swelling (~1.5%) and in plane compressive residual stresses (~5 GPa) caused by constrained

swelling. These observations are critical to interpreting the other experimental measurements in this work.

6 Discussion

6.1 Processing RB-SiC

As discussed in the literature review, the mechanism of producing reaction-bonded SiC has been disputed, mainly around the formation mechanism of new SiC and the phase it takes. Optimising and understanding processing conditions was not the purpose of this work, but some comments can be made in the context of the results here.

Based on the observations in these experiments, reaction-formed SiC grows from carbon particles (Figure 5-9) and takes the crystal structure and orientation of the SiC substrate, based on the orientation-dependent ARGUS forescattered electron images. The reaction-formed layer of REFEL can been seen very clearly from impurities changing the secondary electron contrast. It is less apparent in Starceram and in-house RB-SiC which has a thinner reaction-formed layer, and/or purer silicon than REFEL. Micron- and sub-micron scale SiC particles appear to form directly from carbon agglomerates with a 3C-SiC structure without seeding on a 6H-SiC grain, consistent with the higher stability of the cubic phase at temperatures below 2100 °C, in particular if excess cubic silicon or carbon phases remain [134].

Somehow the REFEL recipe enables a very high connectivity with a high proportion of reaction-formed SiC without reactive blockages which other manufacturers have been unable to reproduce. Toshiba's NT-SiC appears exceptional but has not been independently studied despite being manufactured for large space mirrors with excellent properties [103]. Informal comments from collaborators at Tokyo Institute of Technology suggest there is a clever pre-sintering step before silicon melt infiltration which may allow the fine grain structure and small size of residual silicon regions. Reactive blockages were regularly observed when attempts were made to refine the grain structure in this work.

The microstructures produced by silicon alloy infiltration are inconsistent with literature where eutectic lamellae were found [14,18]. This may be due to the higher carbon content in these samples consuming silicon leaving tungsten silicide and chromium silicide to precipitate locally during the reaction rather than during cooling. The difficulty in melt infiltrating alloys appears related to their different surface tensions compared to pure silicon. Si-19%Cr alloy could only infiltrate a fine-grained sample due to higher capillary forces from small pores, but this resulted in reactive blockages with excess alloy solidified on the surface. Si-4.4%W infiltrated through the thickness in a larger-grained microstructure due to the higher silicon content and consequently a closer surface tension to pure silicon. A systematic study would measure contact angles of these alloys on dense SiC to develop a suitable alloy composition [75].

The research effort required to develop these materials specifically for fusion would be challenging, and probably not worth pursuing. The research on melt-infiltrated SiC_f/metal silicide composites for aerospace may advance research on these materials to a point where it could be worth revisiting them for a nuclear application [14,18].

6.2 Radiation-induced defects

Silicon and silicon carbide are covalently bonded ceramics with well-defined bond lengths determined by local chemistry, in contrast to close-packed metals. This is particularly important for silicon carbide where four types of bond are possible with different covalent bond lengths: Si-C (1.89 Å), Si-Si (2.35 Å), C-C (sp^3 1.54 Å, sp^2 1.47 Å). Both silicon and silicon carbide are connected as {4,4} tetrahedra, and structurally, 3C-SiC is identical to silicon, but with shorter lattice parameters (Figure 2-11). 6H-SiC has a twist in the atomic stacking, so stacking faults in 3C-SiC or silicon are identical to the crystal structure of 6H-SiC. This structural similarity made identifying phases using EBSD

very difficult. Additionally, as discussed in section 2.2.1, 6H-SiC and 3C-SiC are structurally more similar than crystallographic representations may suggest. The fundamental defect structures, if identified non-crystallographically, would be similar for different SiC polytypes.

Raman spectra for ion irradiated silicon carbide showed similar features to literature measurements. The appearance of a broad peak at ~530 cm^{-1} corresponds to a range of Si-Si bond lengths and environments. The range of bond lengths is due to Si-Si bonds being distorted to fit into the defected SiC lattice while “wanting” to be 2.35 Å long. The Raman interaction volume encompasses a range of atomic environments giving rise to the broad low intensity peak. This peak position at 530 cm^{-1} shows that the Si-Si bonds are compressed to shorter lengths than they would be in crystalline silicon. Considering the simplest case of a single Si_C anti-site, the four Si-Si bonds this creates would not be able to relax fully due to the surrounding Si-C bonds of the lattice, resulting in compressed Si-Si bonds and a corresponding Raman peak position greater than 520 cm^{-1}. Clearly the real situation is more complicated than single anti-sites; dumb-bell interstitials, vacancies and single interstitials all give rise to Si-Si bonds and the broad peak in the Raman spectrum corresponding to a range of atomic environments constraining Si-Si bonds.

Si-C peaks are broadened and shifted to lower Raman wavenumbers after irradiation, but the shift is not as far as in neutron irradiated SiC [55]. Similarly to the Si-Si peak, the broadening is attributed to a range of atomic environments and Si-C bond lengths. The shift to a lower wavenumber corresponds to a tensile stress on the bonds, related to the lattice expansion observed in the point defect swelling regime [143]. The constrained peak shift matches that seen in other ion implantations, which is not replicating the effect seen in neutron irradiated SiC. While the lattice can extend vertically out of the free surface, it

is constrained laterally. Since the signal is from a range of environments, it includes bonds constrained laterally, and those which have been free to extend out of the plane.

Raman spectra of neon ion irradiated SiC samples include a broad signal around 1400 – 1600 cm^{-1}, while in silicon ion irradiated single crystal SiC there is a single peak at ~1400 cm^{-1}. The broad signal comes from the D and G bands of C-C bonding showing the presence of both C-C pairs and short deformed chains, as well as longer ordered chains/rings of carbon atoms, similar to graphite. The presence of only a D band signal with Si ion irradiation may be due to implanted silicon ions bonding to carbon defects preventing formation of longer carbon chains/rings which would contribute to a G band signal. DFT simulations of defects in highly damaged SiC have shown the presence of sp^2 bonded carbon chains which contribute to the G band signal [114,153,251]. Silicon ion irradiated SiC in the literature shows only a D band signal whereas their He ion implantation produced both D and G band signals, although their irradiations were at room temperature [147]. Higher intensity and sharpness of the D band at 750 °C compared to 300 °C matches the higher temperature irradiations in the literature with enhanced recovery of the Si-C bonds by silicon being able to diffuse as well as carbon interstitials. Remaining defects are the more energetically stable C-C interstitial dumbbells rather than long C-C chains/rings which are broken by diffusing silicon atoms during dynamic recovery.

The lighter contrast regions of neon irradiated single crystal SiC shown in Figure 5-59 have very intense C-C signals from both D and G bands, and is similar to the C-C region of high dose high temperature neutron irradiated SiC [161] and helium implanted SiC [147]. Although there appears to be “amorphous” carbon clusters in these regions, the Si-Si and Si-C peaks remain crystalline but with lower relative intensity. These regions appear to have more residual damage possibly containing small amorphous clusters or a high density of black spot defects.

Atomic displacements in silicon would simply result in Si-Si bonding, so no chemical changes, only structural defects. These could be point defects like vacancies and interstitials, or possibly extended defects in the form of dislocations or amorphous zones. No sign of amorphisation was found in EBSD or Raman measurements, the crystal lattice was changed very little by radiation damage. Raman spectroscopy showed a sharp peak after irradiation, with a narrow range of vibrational frequencies corresponding to a narrow range of bond lengths, like the unirradiated state. There was also no change in peak position in the single crystal reference sample, so no detectable change in average bond length within the interaction volume of the Raman signal. Amorphisation of silicon results in a broad, low intensity Raman signal shifted to ~470 cm^{-1} corresponding to the longer bond lengths [252]. Radiation defects should also contribute to a shift to lower wavenumbers due to bond stretching. Point defects are difficult to detect as they are still Si-Si bonds so contribute to the same Raman signal. Radiation induced defects in silicon are mobile even at room temperature, and by 300 °C most defects will be thermally annihilated [253]. The slight damage observed in reduced EBSD pattern quality and the small bending of microcantilevers may be due to the excess volume of injected interstitials forming interstitial dislocation loops, although this did not contribute to an observable swelling step.

Diamond has the same crystal structure as crystalline silicon except with carbon atoms and does not show any change in Raman peak position after lithium ion implantation, only a reduction in intensity (Figure 6-1). According to nanoindentation by Dr Bo-Shiuan Li there is also no change in nanoindentation hardness and modulus, although indenting diamond with a diamond tip may be unreliable. This data is from a legacy sample where exact details of the irradiation are unknown, and no further analysis has been made at this stage. The explanation applied to silicon above could also be applied

to diamond where the only defects are C-C and these reform sp^3 bonds to fit into the lattice. Graphite is the thermodynamically stable phase of carbon, but point defects in a diamond lattice are likely to favour recombination into metastable diamond. This may depend on radiation temperature and type. Monatomic crystals appear to be quite resistant to radiation defects.

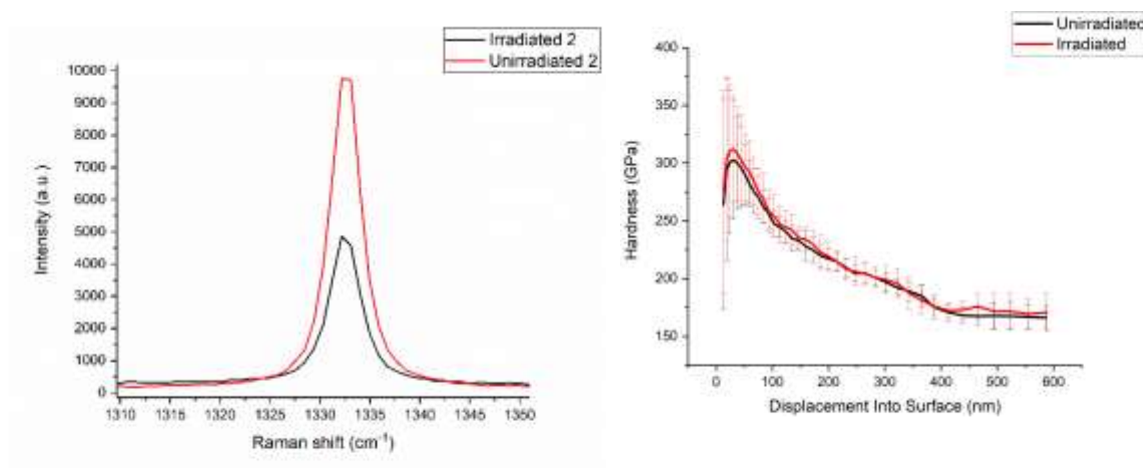

Figure 6-1: Raman spectra and nanoindentation hardness of unirradiated and lithium ion irradiated natural diamond. Radiation conditions are unknown. There is a reduction in intensity, but no change in position of the crystal sp^3 peak. No significant change in hardness is measurable. Nanoindentation by Dr Bo-Shiuan Li

Silicon and diamond are structurally very similar to SiC consisting of a {4,4} tetrahedral network (3C cubic SiC is identical apart from occupation of lattice sites (Figure 2-11 (b) and (d)). The significantly enhanced damage seen in SiC compared to silicon and diamond is likely to be caused by the chemical effects of having both carbon and silicon atoms in the structure rather than one or the other. A displacement in diamond or silicon will simply reproduce the same types of bond as the rest of the crystal network – displacements in SiC change the local chemistry which contributes to local strain.

Figure 6-2 shows a slightly damaged SiC lattice containing anti-site defects corresponding to a chemical disorder of χ=0.17 [114]. This is a simplified case to demonstrate the importance of chemical defects in SiC. Two Si-Si bonds caused by anti-sites are labelled with red arrows in Figure 6-2. Green arrows indicate the direction that

silicon atoms have been displaced to try to accommodate the longer Si-Si bond length. This is the origin of the Si-Si signal in Raman spectra. The two Si-Si bonds which have been marked have lengths of 2.23 Å and 2.25 Å rather than the crystalline silicon bond length of 2.35 Å, corresponding to ~4.5% compressive strain. The constraints of the surrounding SiC lattice have prevented the Si-Si bond reaching its crystalline length. This demonstrates why the Si-Si Raman peak in ion irradiated SiC is at a higher (compressive) wavenumber. Three C-C homonuclear bonds are indicated with orange arrows and have bond lengths of 1.68 Å, 1.70 Å, and 1.78 Å, a tensile strain relative to the 1.54 Å bond length of sp^3 diamond.

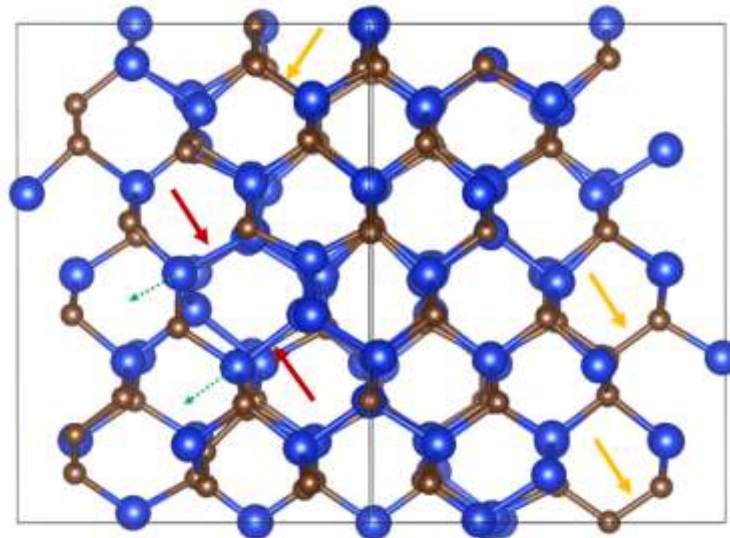

Figure 6-2: Relaxed SiC lattice containing χ=0.17 chemical disorder. Si atoms are blue, carbon atoms are brown. Si-C bonds are blue/brown. Homonuclear Si-Si bonds are blue, and C-C bonds are brown. Two Si-Si homonuclear bonds are marked with red arrows, and the atoms at the end of these bonds have been displaced in the direction of the green arrows. Orange arrows indicate three of the C-C homonuclear bonds

Diffraction is related to a material by the structure factor equation. This is sensitive to lattice site occupancy through the different atomic scattering factors for each atom, and also to strain due to the local atomic displacements. The change in local electron density due to defects changes electron and X-ray scattering conditions, contributing to diffuse scattering. This has historically been quantified as short range order (disorder) parameters from conventional Bragg diffraction experiments [254,255]. This diffuse scattering

contains additional short-range structural information which is typically ignored in diffraction experiments in favour of average crystallographic structures. Although not quantified here, nor from literature on EBSD patterns, it should be possible to extract short range structural information from diffraction experiments, correlate to chemical spectroscopy, and compare to molecular dynamics structural models to create a reliable, detailed picture of defects.

Silicon carbide shows more damage to the lattice than silicon based on Raman spectroscopy and EBSD pattern quality, but it is still crystalline despite the broad, low intensity Raman peaks. The low dose, high temperature silicon ion irradiation caused less degradation of the EBSPs than the high dose, low temperature irradiations, thus a less damaged crystal lattice which agrees with the Raman spectra of high temperature irradiations maintaining taller, sharper peaks.

6.2.1 Optical and SEM contrast

The change in optical appearance of irradiated SiC has previously been investigated by Wendler *et al.* using optical absorption experiments on neutron irradiated and boron ion implanted SiC [163]. The optical absorption coefficient increased linearly with defect concentration as measured by Rutherford backscattering experiments, with the same dependence for neutrons and boron ions. This suggests changes to the optical properties of single crystal SiC are related to radiation defects rather than chemical dopants, agreeing with the qualitative observation in this work.

In the SEM, secondary electron emission is affected by changes to the band gap [256]. This could result from doping as seen in unirradiated REFEL with its core-shell contrast, or by radiation defects as in the boundaries between blanked and un-blanked regions of ion implanted samples, or by strain [257]. The band gap of SiC has been

predicted to change with radiation damage, and in the extreme case, fully chemically disordered amorphous SiC is predicted to become metallic, although the conditions for this cannot be created experimentally [258]. Secondary electron contrast and changes to the band gap could be a measure of defect accumulation. Secondary electron contrast is not measured here, but could be quantified in a similar way to ref. [256] where 4H- and 6H-SiC were differentiated based on their SE contrast. The band gap of the ion implanted layer could be quantified using cathodoluminescence, and band gap as a function of dose could be a measure of relative radiation damage in SiC and could be related to microstructural features. In ref. [256] 6H-SiC with a band gap of 3.03 eV has brighter secondary electron contrast than 4H-SiC which has a wider band gap of 3.26 eV. The darker contrast seen on the irradiated side of the boundaries in Figure 5-52 and Figure 5-53 may suggest that ion implantation has widened the band gap of ion implanted SiC, however there is likely to be a strain contribution to the band gap change as well.

6.2.2 GND density and EBSD pattern quality

In the maps of geometrically necessary dislocation density in Figure 5-48, the irradiated sample has a higher background GND density. This was initially thought to be noise in the experiment, however increased GND density has recently been observed in our group in ion irradiated tungsten. Radiation-induced dislocation loops will cause a lattice curvature which will be detected as GNDs. As this was not initially considered as a "real" effect, it was not systematically investigated further in this work. The measurement is sensitive to step size, with smaller step sizes being able to detect lattice curvature caused by dislocations. If the step size is too large it can miss net lattice curvature and GNDs are not calculated. If the step size is too small, experimental and computational time is inefficient. The maps of boundaries were acquired with too large a step size to detect local lattice curvature and GNDs. Work in our group is ongoing to optimise this technique.

Quantifying the quality of Kikuchi patterns, and relating this to the cause of their degradation is difficult because several structural effects can affect diffraction [250]. Cross-correlation "peak height" was used as the measure of Kikuchi pattern quality relative to the reference pattern. The peak height is reduced by diffuse diffraction from a less perfect crystal volume. Crystal point defects and mechanical defects such as elastic strain and dislocations all contribute to reduced pattern quality [249]. Analogous to electron diffraction, X-ray diffraction peak broadening in neutron irradiated SiC has previously used as a measure of radiation-induced defects and was taken as an indication of the presence of small dislocation loop formation [137]. An initial simple attempt to correlate EBSD pattern quality to radiation damage is outlined below.

The peak height reduction caused by mechanical deformation around nanoindents is less than the peak height reduction across the irradiated-unirradiated boundary. The degradation across the irradiated-unirradiated boundary ($\Phi_{boundary}$) could consist of a contribution from mechanical residual stresses (Φ_{mech}) and radiation-induced defects (Φ_{irr}) (equation (6-1).

$$\Phi_{irr} = \Phi_{boundary} - \Phi_{mech} \quad (6\text{-}1)$$

Stresses in the irradiated material can be correlated to stresses around nanoindents and the corresponding peak heights at those locations in the indent map. If this is taken as the degradation in pattern quality due to mechanical effects, the remainder of the pattern quality degradation could be attributed to defects caused by ion implantation.

Since peak height is relative to the reference pattern in that particular map, the peak height value should be independent of instrument settings. Optimally the indent mapping would have been done with the same settings as the boundary mapping, however this was

not done during the experimental phase of the project as this analysis was not considered at the time. This technique needs refining and could be the subject of further work.

Residual stress on the irradiated side of the boundary of neon irradiated 6H-SiC is approximately -1.88 GPa (Figure 5-75). Pixels with mean stresses of -1.88±0.03 GPa were filtered from the nanoindent map in unirradiated 6H-SiC which was acquired with similar microscope settings and found to have a modal peak height between 0.9-0.93. The average peak height in neon irradiated SiC is 0.644. The difference between this and the mechanically stressed 6H-SiC could be attributed to radiation defects. Although there is a trend in peak height reducing with increasing stress, as seen in Figure 6-3 (a), there is a large spread of values which contributes to large errors.

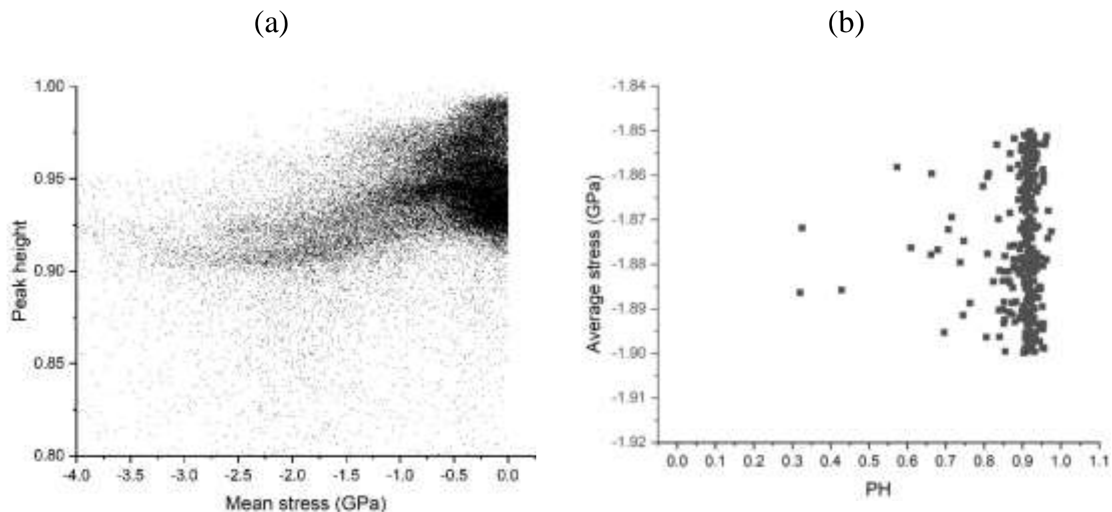

Figure 6-3: Variation of peak height caused by mechanical stress around a nanoinndent in 6H-SiC. (a) is all pixels in the map with compressive stresses, (b) is filtered to the pixels with mechanical stress equivalent to the stress in irradiated 6H-SiC.

A measure of damage to a crystal structure which can be measured spatially in a SEM may allow identification of microstructural features where there is less radiation damage based on their EBSD pattern quality, similar to variations in band gap or secondary electron contrast discussed above. This is tentative based on the analysis here but may be usefully developed in the future.

6.3 Radiation swelling and residual stresses

The measurements of vertical out of plane swelling across the irradiated-unirradiated boundary in single crystal SiC show that there is a volumetric expansion caused by ion implantation. It is difficult to compare to literature results as no previous work on swelling has been done using similar irradiation conditions. Most ion implantations with swelling measurements are high dose at low temperatures with heavy ions to study amorphisation [259], or low dose low energy to study ion implantations for doping semiconductor devices.

Typical strain values measured here from AFM step height measurements and micropillar DIC are ~1.4% which matches closely to XRD measurements of elastic lattice strain in ion implanted materials in a similar damage temperature regime (Figure 6-4) [188,260]. The HR-EBSD measurement of out of plane swelling is lower than the literature XRD and total swelling measured by AFM, probably because the signal is coming from near the surface which received a lower dpa than the plateau region of the damaged layer. AFM measures the total height change caused by the full thickness of the damaged layer, and literature XRD comes from the full thickness of the damaged layer, plus a contribution from the substrate. The XRD measured strains in these papers are from planes parallel to (0001) in single crystals, so is the strain out of the free surface, analogous to the step measured here. Xenon, argon, and neon follow a similar trend suggesting choice of inert gas is not important for strain with dose as these heavier inert gases sit substitutionally. Helium is different as it sits interstitially and contributes to linearly increasing elastic strain with dose beyond saturation of point defect swelling. Additionally, more helium is required for a given dpa than heavier implanted elements. As silicon and neon both substitute into the lattice, there should not be a significant effect from different swelling mechanisms between neon and silicon – the chemical effect of self-ion vs an inert gas should be isolated.

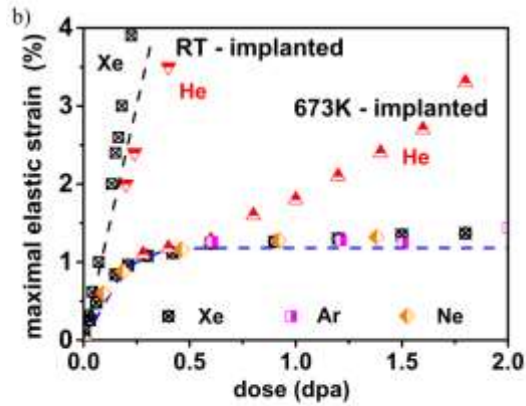

Figure 6-4: XRD lattice strain in ion implanted 4H-SiC [188]

From Hooke's law using a Poisson ratio of 0.16 and Young's modulus of 500 GPa, the stress out of the plane associated with ~1.5% swelling strain would be ~6.7 GPa. This is slightly larger than the lateral expansion stress required to bend the micro-cantilevers in section 5.2.7, and could be related to inaccuracies in the measurement of the microcantilevers, or AFM analysis. HR-EBSD measurements of ~1.9 GPa lateral stress in the near surface region (<100 nm at ~<1 dpa) gives one of the surface boundary conditions of lateral residual stress. The "irradiated" layer in the FEM model was created with uniform properties and a sharp transition from irradiated to unirradiated material but will in fact have a smooth transition. These assumptions could be considered in a more complex model but are not too unreasonable as a first approximation as the triple-energy ion implantation damage profile is relatively uniform.

Lateral stresses have been observed after ion implantation of other materials susceptible to radiation swelling. A previous study in the literature investigated residual stresses in ion implanted austenitic stainless steel by macroscopic curvature using an optical profilometer [261]. The residual stress caused by ion implantation in this ductile metal increased with dose up to ~250 MPa at $1x10^{17}$ ions/cm^2 and varied with ion species. Their context was surface modification to improve fracture toughness and investigation of phase transformations rather than in the context of a structural nuclear component. That an

optically measurable curvature resulted from ion irradiation of a ductile metal suggests that constrained swelling is an important effect in ion implantations, however austenitic stainless steels are particularly susceptible to radiation swelling compared to most nuclear-relevant materials. In their subsequent work, Wang *et al.* developed a technique to measure residual stress in an ion irradiated layer of austenitic stainless steel using nanoindentation coupled with FEM, finding a compressive stress of -631 MPa - higher than in the thin film due to the thicker substrate which prevented bending [262]. This result will be discussed more in the next section.

As well as affecting measurements of mechanical properties (see below), residual stresses may affect the fundamental defects which form, and their evolution. Raman spectra in this work did not recreate the shift to lower wavenumbers for Si-C bonding seen in neutron irradiations in the literature [55] and also showed a preference for D band C-C defects over G band. The preference for D band C-C defects may be due to their smaller size than G band C-C defects which requires a larger C-C network closer in structure to graphite rings. Conrad *et al.* go so far as to suggest that residual compressive stresses on covalent bonds may encourage amorphisation to relax the volume and the excess energy of the constrained bonds [154]. Li has shown that large interatomic strains due to constrained homonuclear bonds are relieved by amorphisation and geometric relaxation [258]. This may contribute to the higher critical amorphisation temperature for ion implantations than neutron irradiations [263]. It should be unsurprising that a crystalline substrate can hinder amorphisation if the amorphisation comes with a considerable volume expansion.

Calculations of threshold displacement energies in iron found 2% hydrostatic expansion reduced the threshold displacement energy by ~25%, thus a tensile stress would result in more atomic displacements than an unstressed material [264]. Conversely

hydrostatic compression may reduce atomic displacements. Another mechanism where stress influences radiation damage microstructure is stress-induced preferential absorption (SIPA). This is a mechanism of radiation creep where applied stress preferentially favours absorption of point defects into certain orientations of dislocation loops, giving anisotropic Burgers vector distribution in a specimen stressed during irradiation [265]. The typical stresses involved in radiation-creep experiments in metals are very low (normally less than a couple of hundred MPa) compared to the residual stresses generated by constrained swelling measured in these irradiated SiC specimens, yet still show a significant (measurable) effect on microstructural defects. The measured residual stress caused by ion irradiation of austenitic stainless steel (631 MPa [262]) would be sufficient to affect dislocation structures by the SIPA mechanism.

In the context of SiC, a hot press has been used to anneal neutron irradiated SiC specimens followed by measuring macroscopic length changes and TEM microstructure observation [128]. They found external uniaxial stress of 560 MPa had no effect on annealing below ~1300 °C – the same mechanism of interstitial migration and recombination occurred as in pressureless annealing. Above 1300 °C in the “void swelling” regime, length reduction was enhanced in the direction of applied pressure while the lateral swelling increased. The applied stress changed vacancy migration so that grain boundary helium bubbles and voids were anisotropic. Although no geometrical ordering of defects was observed in annealed, hot pressed, SiC, producing the TEM lamellae after pressing would have relieved any stress and possibly rearranged defects.

XRD measurements allow measurement of strain in the surface normal [0001] direction. Strain gradients in the [0001] direction in helium ion irradiated α-SiC show that interstitials created near the surface are driven to clustering in a buried, highly strained layer near the damage peak [266,267]. This is shown to have an effect on extended defects

with helium bubbles in less strained materials becoming helium platelets aligned to the basal plane in He implanted 6H-SiC after a higher dose [267]. Additionally, annealing of Xe ion implanted SiC showed that the activation energy for defect migration was lower than modelling suggested due to enhanced interstitial migration towards higher strained regions at the damage peak [268]. The clustering of interstitials and helium bubbles/platelets at the region of peak strain is an effect of ion implantation rather than an effect of the irradiation temperature or dose which could be applied to neutron irradiation. These literature experiments used single ion energies so there is a more significant damage and strain gradient than is produced in this work where we used three ion energies to create a flat damage profile. This may be a better way to induce uniform damage, despite the injected ions.

As fundamental studies of defects and swelling tend to use ion implantation of single crystals aligned to the basal plane, the correct geometry cannot be achieved for measuring elastic lattice strain in directions other than normal to the basal plane using x-ray diffraction. Debelle & Declémy attempt to resolve this by deriving equations for evaluating the in-plane stress from the normal strain measured by XRD, taking into account the unperturbed substrate [269]. They used Cs ion implanted cubic yttria stabilised zirconia (YSZ) and measured (400) and (311) reflections. (311) reflections are at a shallow glancing angle leading to large errors in their measurement by XRD, and they have a component of out of plane strain, as well as in-plane strain so are not an accurate measure of lateral strains. As equation (6-2) was derived for a cubic crystal, the anisotropic form (right side of equation 6-2) was used with a Poisson ratio of 0.16 and Young's modulus of 450 GPa for 6H-SiC. With the total out of plane strain measured by AFM for the neon ion irradiation (1.55 %) equation (6-2) gives an integrated in-plane biaxial stress in the implanted layer of -6.01 GPa. Using the out of plane elastic strain (ε_{zz} = 0.65%) in the near surface as

measured by HR-EBSD gives -2.52 GPa. The calculated lateral stress using AFM strain gives a similar value of in-plane stress as evaluated by microcantilever bending. Using the near-surface HR-EBSD strain with this equation gives a larger value of lateral stress than evaluated directly from HR-EBSD. These discrepancies have several possible origins: 1. the derivation of Debelle & Declémy assumes no in-plane strain, contrasting the compressive strain observed by HR-EBSD in this work. 2. Strain estimated by AFM is based on SRIM estimates of the damaged layer thickness which may be inaccurate.

$$\sigma_{//}^{(fix)} = -\frac{C_{11}(C_{11} + C_{12}) - 2C_{12}^2}{C_{11} + 2C_{12}}\varepsilon_N^{(tot)} = -\frac{E}{1+v}\varepsilon_N^{(tot)} \quad (6\text{-}2)$$

Lateral stress in the ion implanted layer could have an impact in preferential ordering of vacancy dislocations in planes perpendicular to the lateral stress to minimise elastic strain, as sketched in Figure 6-5. Interstitial loops may align parallel to the surface and contribute to out of plane swelling which is larger than the elastic contribution to vertical strain. Dudarev *et al.* calculated that strain fields around defects leads to ordered dislocation loop structures as observed in TEM micrographs of ion irradiated iron and tungsten [270]. Strain fields around dislocations which contribute to this ordering are small compared to the constrained swelling stresses identified in this work. However, observing the effect of this stress on defect structures using a TEM is likely to be impossible as producing a TEM foil necessarily relieves these stresses and dislocations which may have been in ordered structures will not be observed in this way. Meng *et al.* conducted HR-TEM on Kr implanted 6H-SiC and found the interatomic spacing to be 3.05 Å rather than 2.74 Å as in pristine 6H-SiC at the same orientation [271]. This interatomic spacing expansion should result in a tensile lattice strain, however the results in this work on bulk samples show a compressive lattice strain. This suggests the expansion observed in HR-TEM is as a result of releasing compressive stress in manufacturing the thin film.

Electron channelling contrast imaging (ECCI) can be used to observe dislocation structures near the surface using a SEM, so potential dislocation ordering could be observed without having to relieve lateral stresses, but the signal will only be near the surface [272]. Similarly, using high spatial resolution HR-EBSD may allow variations in dislocation density to be observed based on local lattice curvatures. The step/pixel size is important for identifying dislocations using HR-EBSD as there needs to be a net lattice curvature. Too large a step size may miss the curvature if it is cancelled out. Ongoing work in our group is aiming to optimise this technique.

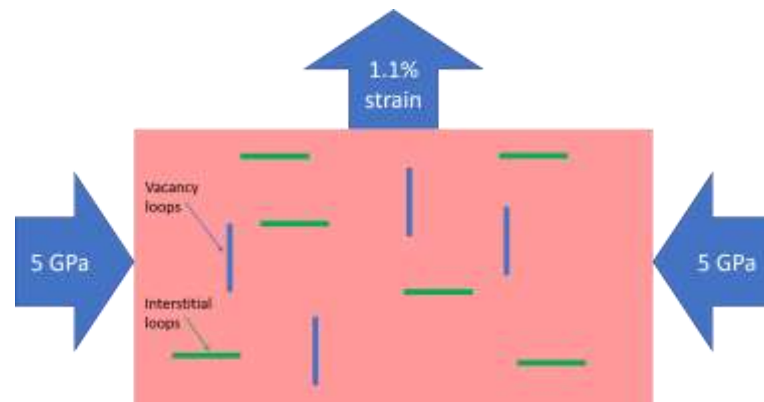

Figure 6-5: Sketch of interstitial and vacancy loop ordering in a stressed material

With stress being able to affect defect formation [264] and migration/recombination [128,265,266,268] the lateral residual stresses in ion implanted thin films may have a more fundamental effect than just the mechanical effect on micromechanical properties. This certainly needs more investigation. It also opens possibilities in engineering design of radiation defect resistance, similar to nano-engineered features to enhance radiation resistance [273,274].

6.4 Radiation effects on mechanical properties

Mechanical properties are difficult to extract from ion implanted samples as micromechanical testing must be used. The measurements made here using

nanoindentation show significant changes caused by ion irradiation of SiC, which hardens by at least 12% in these irradiation conditions as shown in sections 5.2.1 and 5.2.2. This agrees with nanoindentation measurements of ion implanted SiC in the literature [188] and other work done in our group on large grain sintered monolithic SiC (Helen Pratt). It is also consistent with the general response of materials to irradiation defects whereby dislocation mediated plasticity is hindered by point defects and extended radiation-induced defects [4].

In ceramics hardness and elastic modulus are related to the density and strength of covalent bonds [134,275]. These bonds in the crystal lattice network are broken and damaged by radiation defects which reduces hardness in addition to the observed reduction in elastic modulus. Hardness change in irradiated ceramics is an interplay between more difficult dislocation motion and easier deformation as the covalent bond density and strength is reduced by defects. The extreme case of changes to mechanical properties is full amorphisation where deformation is by viscous flow, and hardness is reduced to around 40% of unirradiated values due to reduction in covalent bond density [259,276]. The significant hardening observed in this work would initially suggest that hindered dislocation motion is dominant over crystal network damage. The work by Chen *et al.* is the only literature with a systematic comparison of neutron and ion irradiated SiC samples to the same nominal dpa and measurement procedures, and shows a discrepancy in that neutron irradiated SiC (2×10^{17} n/cm^2) does *not* show hardening as measured by nanoindentation while silicon ion implantation does, as summarised in Table 6-1 [166]. Radiation-induced defects appear similar whether they are caused by ions or neutrons based on TEM observations of “black spot defects” and dislocation loops in the literature (see section 2.2.2). Therefore they attribute this difference in hardness to lateral stresses caused by swelling of ion irradiated SiC on an unirradiated substrate, which are inferred

from HR-XRD measurements [165,166]. Their explanation of the large increase in hardness with low dose ion irradiation based on lateral stresses agrees with the observation of lateral stresses in this work (see section 6.3).

Table 6-1: Summary of measured mechanical property changes from Chen et al. compared with this work [166].

Radiation conditions	Hardness change (%)	Modulus change (%)	
n 0.1 dpa ~50 °C	*0*	*-10.1*	*Chen, 2018*
Si 0.1 dpa ~50 °C	*+14.3*	*-0.7*	*Chen, 2018*
C 0.1 dpa ~50 °C	*+12.5*	*-3*	*Chen, 2018*
n 0.2 dpa ~50 °C	*0*	*-15.9*	*Chen, 2018*
Si 0.2 dpa ~50 °C	*+11.8*	*-6.9*	*Chen, 2018*
C 0.2 dpa ~50 °C	*+9*	*-10.4*	*Chen, 2018*
Ne 2.5 dpa 300 °C	+14.2	-7.92	This work
Si 2.5 dpa 300 °C	+12.2	-7.45	This work
Si 0.25 dpa 750 °C	+3.3	-5.95	This work

Figure 6-6 shows the data for hardening of ion implanted 6H-SiC from this work plotted alongside all literature nanoindentation data for ion and neutron irradiations of SiC. The hardening here is similar to literature ion irradiations, apart from the 2.5 dpa 750 °C silicon irradiation which shows very low hardening compared to other ion and neutron irradiations. This is probably due to the comparably low dose at high temperature leading to comparably little residual damage, as shown in the EBSD and Raman data.

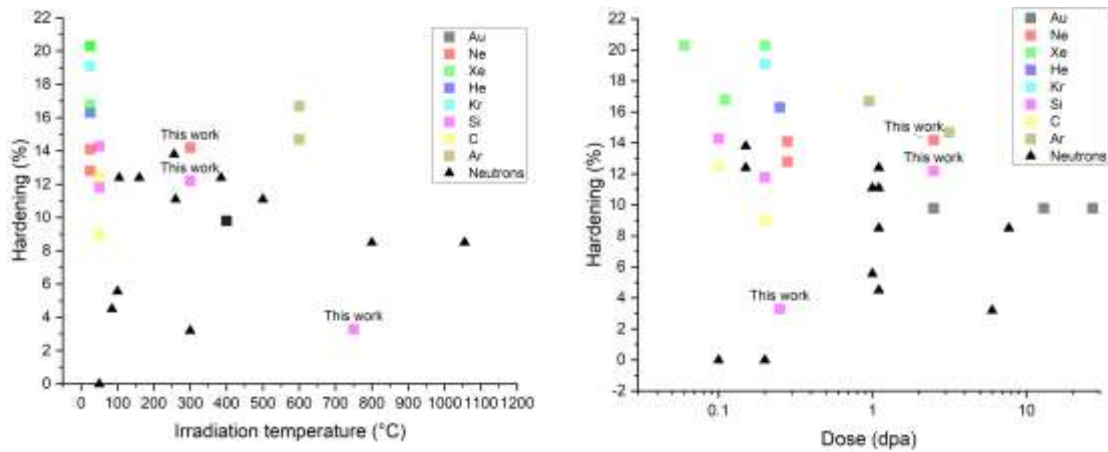

Figure 6-6: Comparison of literature ion and neutron irradiations with the 6H-SiC ion irradiations in this work

Osborne *et al.* measure more hardening with neutron irradiation at 500-550 °C than at 100-150 °C, which they explain by increased size of dislocation loops and defect clusters [277]. Ion implantation is the opposite, where higher temperature irradiation shows less hardening which correlates to less volumetric swelling with increasing temperature. Dislocation loops and defect clusters grow with temperature, while lattice swelling due to point defects decreases. This supports the analysis that a significant proportion of measured hardness in ion irradiated samples is related to the constrained swelling, which dominates over impeded dislocation motion from radiation defects.

0.25 dpa Si ion implantation of single crystal 6H-SiC at 750 °C showed a small hardening of 3.3%, while reaction-bonded SiC irradiated in the same condition showed hardening of 14.9% for REFEL and 14.6% for Starceram, similar to hardening for the 300 °C irradiations. The low hardening at 750 °C for 6H-SiC may be attributed to silicon diffusion in addition to carbon diffusion allowing enhanced defect recovery, annealing radiation-induced point defects. Unirradiated SiC grains in RB-SiC contain a high density of stacking faults and dislocations introduced during processing [87]. During irradiation and subsequent annealing, these original defects pin radiation-induced dislocation loops so that they do not annihilate at grain boundaries [177]. In the same work, dislocations generated in sintered SiC annihilated with grain boundaries during annealing [177]. Based

on this, the high hardening at high temperature ion irradiation observed in RB-SiC may be due to defects not being able to dynamically anneal. As dislocations are unable to anneal, swelling will also remain high in these SiC grains compared to single crystal SiC.

While hardness is related to both plastic and elastic properties of the material, elastic modulus is controlled by bond density and stiffness (interatomic potential energy function). After irradiation, elastic modulus is reduced as interatomic bonds in the crystalline network are broken by radiation defects. A direct experimental measurement of crystal network defects is impossible, only a measure of average bond types by spectroscopy, or of long-range structure by diffraction is experimentally possible, so the structure of defects can only be inferred indirectly from measurements of a different property [111,114,115]. Chen *et al.* measure a smaller decrease in elastic modulus for ion implantation than for neutrons which may be related to implanted ions sitting in the sites of point defects. Silicon atoms can substitute more successfully into the SiC crystal network than carbon atoms due to their longer covalent bond length and preference for tetrahedral bonding resulting in a less damaged network. Although less structurally damaged, it may have more strain associated with it, hence the bigger change in hardness compared to carbon in Chen *et al.*'s work [166]. Since there are no implanted interstitials from neutron irradiation this effect does not occur.

High temperature Si ion implantation causes less reduction in modulus than the low temperature ion implantations, suggesting dynamic annealing of point defects. The Raman spectra for these irradiated samples shows sharper crystalline peaks after silicon ion implantation than after neutron irradiation to the same nominal dose again suggesting that silicon ions cause less structural damage [165]. Although Chen *et al.* attribute the difference in elastic properties between neutron and ion irradiations to the effect of lateral residual stresses, it would appear that it is also an effect of the fundamental difference in

defect structures as their FEM model modifications to nanoindentation does not fully match the experimental data. There appears to be a complex interplay between lateral residual stresses and fundamental damage differences affecting measurement of reliable mechanical properties from ion implanted samples.

In unirradiated SiC, indent impressions show radial fracture and residual elastic deformation extending far from the indent impression, with a small amount of plastic deformation close to the indent impression as measured by GND density from HR-EBSD. Raman spectroscopy mapping and HR-EBSD agree on the spatial variation of residual elastic deformation, however the values from Raman piezospectroscopy are lower, probably due to the larger interaction volume than EBSD. Guo & Todd showed the effect of depth resolution on observed residual stress around indents in alumina [212]. Errors of greater than 40% could arise when non-confocal (~14 µm depth resolution) fluorescence mapping was used compared to confocal (~3 µm depth resolution) [212]. There is ~1 µm of lower magnitude elastic stress close to the indent impression which corresponds to the region of calculated high GND density. Dislocations are difficult to nucleate and move in covalent ceramics so plastic deformation is limited to the highest stressed region close to the indent, only relieving elastic stresses in these regions. The yield stress of 6H-SiC evaluated from micropillar compression is 12~16 GPa [278], and had previously been reported as high as 21 GPa [279] – plasticity around indents in 6H-SiC should be quite low.

After ion implantation, radial cracks are unable to grow due to the biaxial compressive lateral stresses generated by constrained swelling. Being unable to crack, indentation deformation is accommodated by plastic deformation, as seen by the extended region of high GND density in Figure 5-48. As crack nucleation is hindered, indentation stress can be high enough to nucleate dislocations during deformation without fracture.

Additionally, radiation defects include small dislocation loops which can flow plastically to accommodate indentation deformation [135]. It is unclear how much of an effect radiation induced dislocation loops have on enhancing plasticity in this case due to the large lateral residual stresses. Elastic deformation reaches a higher relative stress after irradiation and is more localised near the indent impression due to the opposing lateral swelling stress.

In addition to large hardening in ion implanted samples, fracture toughness was apparently increased by ion irradiation based on subdued indentation cracking. This has also been observed in the literature in ion irradiated samples and has recently been attributed to lateral residual strains [188]. Slight toughening by neutron irradiation has been observed in SiC [178,182] and was explained by crack deflection or enhanced crack tip plasticity caused by radiation-induced dislocation loops as it is difficult to nucleate dislocations mechanically in unirradiated pristine SiC. The slight toughening based on crack-tip plasticity is insufficient to explain the subdued cracking in this work and by Jiang *et al* [188]; the best explanation is the observed compressive lateral residual stresses caused by the thin irradiated layer on a thick substrate, although there could be a contribution from radiation-enhanced plasticity or crack deflection from defects. Once the radiation-induced lateral residual stress is removed and the crack has grown stably before jumping, the crack length and estimated fracture toughness based on equation (4-1) is close to what one might expect from a brittle ceramic. As only two cracks have grown rather than three, equation (4-1) for fracture toughness is not necessarily appropriate. The return of estimated fracture toughness to close to the unirradiated value demonstrates the significance of lateral residual stress on the mechanical properties measured by nanoindentation of ion implanted samples.

Observing crack paths underneath and around nanoindents is complicated in both unirradiated and irradiated samples. As shown by HR-EBSD and Raman maps, high

residual stresses exist around indent impressions which are relieved as the constraining material is removed. When this stress is removed cracks grow, as shown in the FIB cross-section experiments in section 5.1.5. In ion irradiated samples there is the addition of the lateral constrained swelling stress to complicate matters further. Crack growth during FIB slicing of unirradiated indents is sudden – the mechanical residual stress around the indent impression is relieved in one step. This jump in crack length occurs approximately when FIB slicing reaches the edge of the region of high elastic stress in the Raman and HR-EBSD maps. Crack growth during FIB slicing of irradiated indents is initially gradual as the origin of radiation-induced lateral stress is from the substrate rather than surrounding material so reduces linearly as material is removed. After linear stable crack growth with relief of radiation-induced lateral stress there is the same sudden jump as the mechanical residual stress from the indent impression is relieved. The similarity in crack length at the point of this jump suggests there is little real change in fracture toughness of SiC caused by radiation damage. As stress has only been relieved on one side, and only two of the three cracks have grown, fracture toughness equations are invalid for this condition, and the crack lengths in the stress-relieved irradiated indent are unlikely to be the length of cracks if the indent had been in unconstrained irradiated material.

The previous cross-sectional study of indentation cracks in Si ion implanted SiC shows crack deflection along the interface between damaged layer and substrate [280]. They do not discuss any surface crack growth or any changes to crack morphology during slicing, however they used a much larger 1 kg Vickers indenter than the nanoindents in this work. They attribute their observed 25% toughening to crack branching and deflection in the irradiated layer with no mention of lateral constrained swelling stresses. Yang *et al.* observed shortened surface cracks, and crack deflection and branching from nanoindents in room temperature Kr ion implanted SiC which they explain as being deflected by defect

clusters [281]. Their 60-80% toughening cannot wholly be attributed to radiation defect clusters as it would also be observed in neutron irradiated SiC, whereas low temperature neutron irradiation reduced fracture toughness of CVD SiC [182].

Even in ductile metals such as iron-chromium alloys, anomalous micromechanical results have tentatively been attributed to lateral residual stresses in ion implanted layers [282]. The effect of residual stress is perhaps not as obvious in metals as in SiC as indents in neither the unirradiated, nor irradiated metal crack; there is not an obvious change in deformation response which would spark further investigation. It may not be the dominant mechanism of property changes in metals – radiation defects are clearly influencing deformation in neutron irradiated samples; however, the microstructural origin of these changes may be different. The residual stress effect should not be ignored as measurable influences of residual stress on micromechanical properties of ion irradiated layers have been observed by Wang *et al.* [262]. Similar results have been observed when external stress is applied to a sample during indentation, and from this Lu *et al.* developed a model for estimating surface biaxial residual stresses using instrumented indentation (equation (6-3)) [283]. In equation (6-3) σ^R is residual stress, σ_y is yield stress, n is the strain hardening exponent, ε_y is the yield strain, F and F_0 are the maximum indentation load with and without residual stress respectively. Using this model with the results of the indentations in Wang *et al.*'s study of ion implanted austenitic steel [262] but with the unirradiated mechanical properties of the steel, they estimate the residual stress caused by ion implantation is -612 MPa, compared to the calculated value of -631 MPa directly from experiments. The 19 MPa difference between the calculation using unirradiated material properties, and the ion implantation experiment could be due to the change in mechanical properties caused by radiation defects, but there is no way of measuring the changed properties in the absence of residual stress. It could also be due to assumptions in the

model. Thus, the change to the measured indentation response in this steel which undergoes radiation swelling is dominated by compressive lateral stresses. Based on the premise that the residual stress is introduced to this sample by swelling which is constrained by the unirradiated substrate, ion implantation does not seem an appropriate way to introduce damage for measuring mechanical properties.

$$\frac{\sigma^R}{\sigma_y} = \left[(-1.0515n^2 + 0.7815n - 0.25528)\log\varepsilon_y - 2.36329n^2 + 1.9639n - 0.79588\right]^{-1} \times \frac{F - F_0}{F_o} \quad (6\text{-}3)$$

The empirical equation from Lu *et al.* (equation (6-3)) [283] is developed for metals so does not explicitly take into account fracture, thus the residual stresses calculated using this equation with SiC are unlikely to be correct for the unirradiated case. However, a simple estimate of residual stress, σ^R can be made using the indentation curves from irradiated 6H-SiC in this work. The value for strain hardening exponent (n) is taken from Datye *et al.* as 0.379, and yield strain (ε_y) and yield stress (σ_y) as 0.015 and 12-16 GPa respectively from Kwon *et al.* [209,278]. Taking peak loads from 500 nm indents in the neon irradiated sample to minimise the effect of the substrate on the indentation, lateral residual stress is estimated between -3.77 and -5.02 GPa, depending on the choice of yield stress. The upper bound is of the same order of residual stress estimated from cantilever bending and AFM swelling steps. It is also close to the value estimated using equation (6-2) with total out of plane swelling. If the lower estimate is considered, it could be due to fracture of the unirradiated indents, but not the irradiated indents. Values of yield stress in 6H-SiC vary quite widely, but the micropillar compression technique from Kwon *et al.* is chosen as it is from micromechanics on the same scale as these nanoindents and the implanted layer.

Almost all the observed changes to micromechanical properties and deformation are attributable to the compressive lateral constrained swelling stress. Elastic modulus, which should be unaffected by residual stresses appears to be affected by implanted ions. It appears impossible to replicate the mechanical properties of neutron irradiated single crystal SiC using ion implantation. It is, however, a way to increase toughness and wear resistance of the surfaces of ceramics and other materials [284–287]. The substrate-induced lateral residual stresses which cause increased hardness and subdued cracking suggests that ion implantation is not a suitable way to replicate neutron irradiation damage in materials which swell.

6.4.1 Ion implantation effect on RB-SiC micromechanical properties

As discussed in the methods, nanoindentation of polycrystalline RB-SiC is difficult to quantify as the measured indentation response is related to the whole deformation volume including contributions from SiC and silicon grains with considerably different properties. While the plastic effects are measured near the indentation, elastic contributions are far-reaching. An indentation which may appear as hard SiC could have a low elastic stiffness if it is surrounded by silicon. For this reason, hardness and hardness changes are considered the most appropriate measure for observing changes to mechanical properties in RB-SiC. Adding effects of ion irradiation into the mix makes it even more complicated.

There appears to be a trend with smaller grained RB-SiC having smaller changes to hardness and modulus with radiation damage. A larger area of SiC/Si interfaces also seems to reduce property changes for similar grain size – REFEL hardens more than in-house SiC with a similar grain size. However, based on Raman spectra there is no difference in radiation induced defects with grain size so there would be no reason to expect a difference in mechanical properties caused by radiation damage. Additionally, the grains are too large for grain boundaries to have any effect on annealing damage at the irradiation temperatures

in this work – only above ~1150 °C would long range vacancy mediated diffusion allow grain boundaries to act as effective defect sinks for the bulk of grains this large. Nanocrystalline SiC created during CVI of SiC_f/SiC composites appears to have a grain boundary density high enough to effectively anneal radiation defects, based on nanoindentation measurements by Dr Yevhen Zayachuk. As seen in the single crystal, hardening is dominated by the effects of constrained swelling. With decreasing grain size in RB-SiC, the lateral swelling stresses are reduced as silicon is less stiff than SiC and does not swell, so SiC grains are able to swell into the silicon regions, reducing the compressive stress in SiC. Additionally, a larger fraction of silicon would reduce lateral residual stresses in SiC. This swelling of SiC grains into silicon regions is apparent in the residual stress maps of silicon regions shown in section 5.2.6.2, and discussed more in section 6.6.2. Compressive stresses in both SiC and silicon phases hinders indentation cracking in ion implanted RB-SiC.

When extracting mechanical properties from nanoindentation data, the hard convergence was counted as the properties of SiC, and the soft convergence as silicon. Due to indentation overlap between SiC and Si, this precludes measuring mechanical properties at the edges of SiC grains where the boundary could be acting as a defect sink. The high concentration of processing defects near grain boundaries in RB-SiC, enhanced after radiation, may make SiC near grain boundaries harder than the bulk of the grain (if the constrained swelling effect could be ignored as in neutron irradiation).

6.5 Radiation-enhanced oxidation

Evidence of Si-O and C-O bonding is observed in the Raman spectra of all SiC specimens irradiated at 750 °C, despite surface oxidation being visible in optical microscopy or SEM; the Si-O and C-O signals are coming from within the Raman laser

interaction volume which corresponds to the ion implanted layer. The Raman peak at 660 cm^{-1} had previously been identified in the literature as distorted SiC, but the original reference for this does not include this peak. Iota *et al.* pressurised CO_2 into a solid and identified C-O-C bonding at 660 cm^{-1} and solid CO_2 with a {4,2} tetrahedral structure, is similar to silica SiO_2 [160]. Tetrahedral C-O-C or Si-O-Si bonds should substitute satisfactorily into a damaged tetrahedral SiC {4,4} network [111]. Although the ion implantation stage was held in a good vacuum ($\sim 1\times10^{-6}$ mbar) some oxygen inevitably remained in the chamber. Unirradiated regions of the same specimens did not have Si-O or C-O signals which suggests the oxidation is enhanced or caused by radiation defects. This is supported by the annealing experiments whereby samples irradiated at 300 °C annealed at high temperatures oxidised and unirradiated annealed samples did not. These oxide particles were large and visible on the specimen surface suggesting a different mechanism. Oxide formed during ion implantation could have been mixed into the bulk below the surface by ion beam mixing and the directionality of displacement damage during ion implantation. Si-O-Si bonds formed during annealing post irradiation are not mixed into the damaged ion implanted layer allowing them to develop into microscopic particles rather than being incorporated into the damaged SiC structure. C-O bonds would be expected to evaporate as CO_2 molecules, possibly leading to the pitting observed in some annealed samples. A molecular dynamics study could enlighten the mechanism of oxygen incorporation into the SiC structure during ion implantation.

Enhanced oxidation of defected SiC is not unreasonable. Molecular dynamics simulations have shown that incoherent grain boundaries oxidise faster than coherent grain boundaries and perfect crystal SiC surfaces [288]. This is due to undercoordinated bonds on the incoherent grain boundaries which enhanced their reactivity with oxygen. Radiation damage also produces undercoordinated bonds in SiC which will enhance oxidation.

McHargue and Williams found that ion beam amorphised SiC etched 2.5-4 times faster than un-irradiated samples in a boiling solution of potassium ferricyanide and potassium hydroxide, and had an oxide layer 1.67 – 3 times as thick after 1 hour in flowing oxygen at 1300 °C [276]. This enhanced oxidation or corrosion would be expected to occur in both ion implanted and neutron irradiated SiC and is likely to be an issue if oxygen concentrations are not carefully controlled. Experiments with different steam chemistries and pressure have shown that SiC can form a passive oxide layer resistant to erosion in flowing coolants, however this may be affected by radiation degradation [289,290]. It is more concerning for SiC_f/SiC composites where the interphase layer is especially susceptible to oxidation degradation [289].

The 2.5 dpa 300 °C Si ion implanted 6H-SiC sample annealed at 1200 °C in vacuum which pitted was not studied beyond surface SEM images. Two possible tentative explanations of the pitting are: 1. there was insufficient oxygen to form a passivating SiO_2 surface layer and volatile C-O and Si-O evaporated leaving these pits behind. or 2. vacancies which are mobile at 1200 °C may have diffused into voids in the near-surface region, possibly due to strain gradient effects, leaving undercoordinated atoms which evaporated. Without further experiments nothing more can be made of these results, but the different surface effect compared to air annealing is interesting.

The presence of undercoordinated atoms at (or near) irradiated surfaces is likely to enhance corrosion which may be important for the application of SiC in other corrosive media including fusion-relevant lithium-containing tritium breeding materials. This does not appear to have been investigated significantly with all relevant corrosion tests being conducted on unirradiated specimens. Grain boundaries and pores respond poorly to corrosion in Pb-Li, but a dense CVD SiC coating provided much improved protection supporting the enhanced corrosion due to undercoordinated atoms [39,40]. Ion

implantation may be a suitable surface modification mechanism for creating radiation damage relevant for studying radiation-enhanced corrosion of SiC without the issues of sample activation from neutron irradiation.

6.6 Residual stress in RB-SiC

6.6.1 As processed

The measurements of compressive residual stress in the silicon phase of reaction-bonded SiC agree with the work of Wing *et al*. and the values measured here are similar to their measurements [190,191]. The compressive stress arises from 11% crystallisation expansion of silicon during solidification, so qualitatively the compressive residual stress makes sense. Wing *et al.* don't map Raman peak shift variation with position, as in this work. Figure 5-15 and Figure 5-16 show that the compressive stress in silicon regions is higher in the centre than the edges. Considering a heterogeneous solidification of silicon, where the solid nucleates on the surface of SiC grains and grows inwards, the last silicon to solidify would be constrained by surrounding solid silicon, so is compressed relative to the volume it would like to occupy. Jannotti *et al.* map peak shifts in RB-SiC and find a tensile stress, but their analysis of peak position appears incorrect. Although a residual tensile stress in silicon can arise during cooling due to thermal expansion mismatch, they ignore the crystallisation expansion in their discussion which gives a much larger compressive stress before cooling and thermal expansion stresses arise [189–191].

These residual stresses impact the mechanical properties. Silicon is brittle and fractures during nanoindentation (Figure 5-17), but when incorporated in RB-SiC, it appears tough as it does not fracture from indent corners (Figure 5-36). The residual compressive stresses in silicon will act against the crack opening stresses from the indentation. The maximum residual tensile uniaxial stress just ahead of crack tips in single

crystal silicon is ~350 MPa measured by HR-EBSD, while the residual biaxial compressive stresses measured in the silicon regions of RB-SiC are higher than this, up to ~1 GPa.

SiC grains still fracture from indent corners as expected as there is no significant toughening mechanism introduced by processing. Cracks deflect to weak Si-SiC grain boundaries, but are not deflected in SiC grains, nor along SiC-SiC grain boundaries. Based on crystallisation expansion of silicon, there will be interfacial shear stress at Si-SiC boundaries. These Si-SiC boundaries appear to be the weakest defect which leads to failure. Microtensile measurements of interfaces in RB-SiC found SiC-Si interfaces had a tensile strength of 4.3 ± 1.9 GPa, much lower than the microtensile strengths of SiC (24-111 GPa) and silicon (23 GPa) [291]. The values referenced for microtensile strengths of SiC and silicon are from classical molecular dynamics models rather than experiments so are not likely to be comparable to the experimental value of RB-SiC interfaces. Hsu *et al.* say that microtensile measurements of SiC and silicon are underway in their group [291].

6.6.2 After ion implantation

Raman and HR-EBSD stress maps show a complex change to residual stress in reaction-bonded SiC after ion irradiation. The single crystal silicon reference sample showed very little change after ion irradiation, both structurally and mechanically, so it would be expected that silicon in RB-SiC is also not significantly changed directly by ion irradiation. Nanoindentation shows no significant change in hardness and modulus of silicon regions of RB-SiC, although the small size of these regions made measurement difficult. Meanwhile, SiC is very considerably changed structurally and mechanically by ion irradiation. It would therefore follow that the changes to residual stress in RB-SiC are caused by changes to SiC grains caused by ion irradiation damage.

Radiation induced defects in SiC have a positive volume, and this manifests as swelling of SiC grains in RB-SiC [127]. The microstructural geometry of RB-SiC is rather complicated, but some cases will be discussed in more detail here.

Taking the simple case of the small isolated SiC particle marked with a green arrow in Figure 5-80, the silicon around it has tensile stresses perpendicular to the components of the stress tensor, and compressive parallel to the component of the stress tensor. These stresses are consistent with the SiC grain swelling into the silicon region.

Where SiC grains form a corner, or a sharp cusp with silicon, the swelling SiC grains are compressing the silicon in these regions. Examples of these situations are marked with red arrows in Figure 5-78, and similar regions can be seen in other stress maps of irradiated RB-SiC.

Initially the features in Figure 5-68 and Figure 5-69 were thought to be microcracks emanating from silicon regions caused by the high local compressive stress in silicon pushing out, causing a localised tensile stress on a SiC grain boundary. In the case of a sharp cusp the resolved stress could act to open a crack along a weak grain boundary. The topology changes in secondary electron SEM images appeared to be cracks, however FIB cross-sections of these do not show any crack opening below the surface. The bright contrast below the surface suggests grain boundary inclusions of heavier element impurities (Figure 5-71). The surface topology change may be the result of anisotropic swelling for the different grain orientations of hexagonal SiC, possibly caused by different defect structures caused by lateral compressive stresses. Alternatively, different height changes could arise from one grain being SiC throughout the implanted layer while the lower grain has some silicon in the irradiated layer, shown schematically in Figure 6-7. Both mechanisms would be expected to cause misfit strains along the grain boundary contributing to grain boundary fracture. This would not appear as a mode I opening crack,

but a mode II shearing crack at the grain boundary which is unlikely to be resolvable with a SEM.

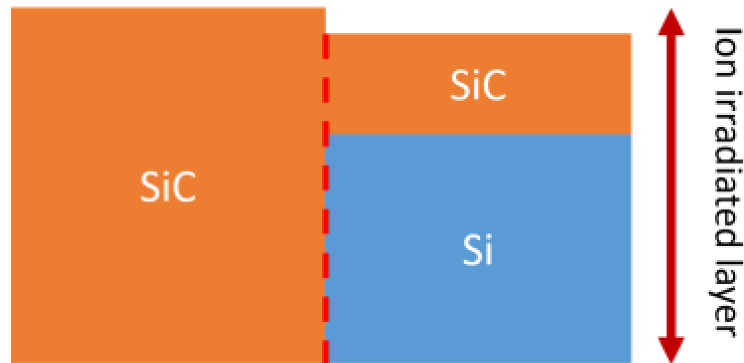

Figure 6-7: Intergranular swelling step schematic. 1.1% swelling in the left SiC grain would cause a higher surface swelling than 1.1% in the right SiC grain due to sub-surface silicon which does not swell.

With the observed large lateral stresses in the irradiated SiC layer, a mode I grain boundary crack would be unable to open from the pushing out of the compressed silicon. Figure 6-8 shows a preliminary finite element model of an initially unstressed silicon region in a silicon carbide matrix which was expanded by 1.1% with fixed boundary conditions. The vertical (yy) strain shows compression in the sharp cusps of the silicon region with a profile to be less compressed in the centre of the region and more compressed at the edges. This is consistent with the Raman mapping and HR-EBSD mapping of irradiated RB-SiC. No yy tensile strain is apparent in the SiC ahead of the compressed silicon, probably due to the compression caused by the 1.1% expansion in SiC.

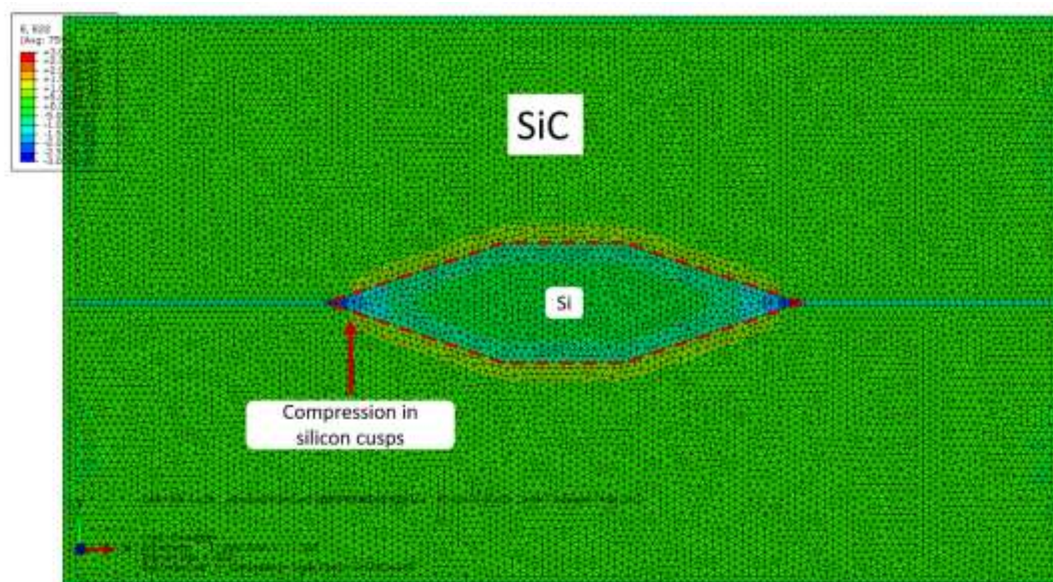

Figure 6-8: Preliminary FEM of a silicon region in expanding SiC, with compressive strain in the sharp corners of the silicon region. Red dashed line outlines the silicon region

The deflection of indentation cracks to grain boundaries in ion irradiated RB-SiC (Figure 5-50) suggests that grain boundaries are weakened after ion implantation. Even if the swelling-induced stresses are not the direct cause of failure, they are contributing to weakening the material. In an unconstrained neutron irradiated sample, it is possible that a grain boundary crack could open from the outward stress from compressed silicon as there is no lateral constraint to the swelling from an unirradiated substrate. Mismatch shear stresses could cause cracking along Si-SiC boundaries, similar to the original work on neutron irradiated RB-SiC by Matthews [171].

7 Conclusions and recommendations for further work

7.1 Radiation defects in SiC and Silicon

Hexagonal α-SiC undergoes significant detrimental radiation-induced changes. Si-Si and C-C homonuclear bonding is observed in addition to Si-C bonding after irradiation, and these chemical bonding defects indicate significant structural damage which results in macroscopic swelling. Chemical defects play an important role in the properties of silicon carbide. As well as chemical damage, the lattice structure of SiC is also significantly affected based on degraded EBSD patterns.

From the results of this research, it appears that silicon is remarkably resistant to ion implantation damage in the conditions studied here. There was no detectable change in mechanical properties, nor swelling and residual stresses. There was a small amount of structural damage as assessed by EBSD pattern quality and intensity of Raman spectra. The likely difference is due to chemical defects as diamond appears to show a similar resistance to radiation damage as silicon. Since these materials consist of only one atomic species, chemical defects are impossible, apart from different bond hybridisation in carbon (sp^2 to sp^3). It may be interesting to irradiate other tetrahedral silicon-based ceramics such as silicon nitride and silica which are more easily amorphisable due to lower connectivity ({4,3} and {4,2} networks respectively). This may help to explain the role of chemical defects in radiation damage of ceramics.

7.2 Identification of radiation induced changes

Raman spectroscopy is sensitive to short-range bonding defects in SiC and clearly shows defective Si-C bonds and the appearance of Si-Si and C-C bonds after irradiation. These appear to be important defects to identify and characterise but are invisible in

electron imaging or diffraction-based techniques. Structural defects can be characterised by diffraction and being able to do this in a SEM can be useful as TEM is inherently small-scale and difficult to use. In this work no progress was made in detailed analysis of defects using a SEM beyond qualitatively saying if one sample was more damaged than another. However, there are opportunities for quantifying defects using a SEM. SEM based techniques are easily implemented and can show spatial variations across a microstructure, possibly identifying defect sinks if these are on the scale of visibility in the SEM. The problem is separating changes caused by radiation from other potential causes of changes such as mechanical defects, sample preparation or microscope settings. As residual stress and strain gradients have an effect on radiation defects, it is important to identify radiation defects in bulk specimens as TEM sample preparation relieves this stress, possibly affecting the observation of defects.

Using the quality of EBSD patterns as a measure of radiation damage is only possible when there is a damage-free reference. This was easy in a single crystal where part of the specimen could be blanked and the orientation was constant. In a polycrystalline specimen only those grains along the irradiated/unirradiated boundary can be compared in this way. Future developments of the XEBSD code aim to improve its applicability to polycrystals, using multiple reference patterns from grains of the same orientation. This may be difficult to implement experimentally as different grain orientations or regions of the sample may polish to different qualities.

Investigating residual deformation around irradiated and unirradiated indents was obvious in SiC because the fracture had changed so significantly. In metals it is less obvious to want to investigate this. Recently elastic deformation around indents in irradiated tungsten has been investigated using HR-EBSD and X-ray microdiffraction, and

differences in pile-up and strain localisation were observed [292]. This should be investigated in more nuclear-relevant materials.

Grain boundaries are too small to observe in detail in a SEM, or in most TEMs. Aberration corrected STEM can enable observation of the chemistry and structure of grain boundaries in great detail [293]. Certain grain boundary complexions could be better than others for absorbing radiation defects. Identifying these and engineering a material to have more of these particular grain boundaries through controlling chemistry, heat treatments, or anisotropic processing could be an effective way of improving radiation properties, as has been done for improving mechanical properties of some ceramics [294–296].

Raman spectroscopy is useful for identifying radiation defects, while annealing experiments are helpful in observing the evolution of defects. The use of in-situ Raman spectroscopy during annealing and possibly during irradiation as Brunetto *et al.* have done [297] could be very powerful in identifying and measuring the thermodynamics and kinetics of defect formation and migration processes in silicon carbide, and possibly other Raman active materials. It is possible to simulate Raman spectra from atomic structures generated by molecular dynamics, so it may be a way of bench-marking models to experiments and developing a full picture of radiation defects. Combining experiments and modelling is important for accelerating material development and having predictive capabilities for the evolution of materials and components in an operating reactor.

In-situ annealing experiments in this work showed defects recover very quickly in SiC at high temperatures. This may make it difficult to measure radiation-induced changes to other properties at high temperatures without annealing defects out before the measurement is made. For example, it is important to know thermal conductivity as a function of temperature, and to know high temperature mechanical properties of irradiated materials. It may be necessary to design an experiment to measure these properties during

high temperature irradiation to avoid annealing effects. Microtensile tests could be conducted during ion irradiation if the sample is thin enough for uniform damage, as the specimen can be left exposed to an ion beam during the test, and micro-electronic devices could be used to measure microscopic thermal conductivity [298]. The apparatus for these measurements can easily be shielded from the ion beam, and target chambers for ion irradiations are large enough for this kind of equipment which can typically be put into a SEM chamber, or even into a TEM column.

Nanoindentation is a popular technique for measuring local micromechanical properties. One useful property for ceramics is the fracture toughness. Accurate measurement requires knowing the full crack morphology, but this appears impossible as cross-sectioning indents changes the crack structure significantly. Empirical equations based on measuring surface cracks are probably the best way for comparing fracture toughnesses, but the values are *not* fully quantitative as they assume crack morphology; they are only useful for comparisons. It is difficult to compare values of fracture toughness between this work and others as the calculations are inconsistent.

7.3 Effectiveness of ion implantation

The aim of ion implantation is to recreate, in a controlled manner, the effects of neutron irradiation in a nuclear reactor. The damage process is fundamentally different, but in certain circumstances it can replicate some properties, whether mechanical or structural defects. The changes to these properties can depend on the ion species one uses. Depending on the properties which one wants to study, different ions may be appropriate. For example, recreating neutron irradiation-induced chemical defects in SiC appears to require a non-self-ion. In contrast, the choice of silicon or neon appears not to have a significant effect on nanoindentation hardness. Light ions such as helium appear to cause

significant differences to heavy ions as such a high dose is required to cause significant displacements that bubbles form unnaturally. Dual ion implantation with a heavy ion plus helium appears to replicate the effects of helium transmutation well as helium can stabilise certain defect structures. The chemical effect of ion implantation may apply to other ceramics where the local chemical bonding is important.

This work has experimentally shown the presence of biaxial compressive stresses in the plane of ion irradiation damage. This is due to the unirradiated substrate constraining swelling in the damaged layer. This is a significant, unavoidable effect in ion irradiation of materials which swell under irradiation.

Micromechanical property measurements in this work appear to have been dominated by the residual compressive stress caused by the unirradiated substrate constraining lateral swelling of irradiated SiC. This effect needs to be decoupled from the measured values, whether by a mathematical correction, or by experimental design. In the case of experimental design, small micro-cantilevers made entirely within the irradiated layer could be used, or a thin film could be irradiated through its full thickness and allowed to swell unconstrained, similarly to neutron irradiations. With the small microcantilevers, damage gradients from heavy ion implantation could introduce internal stress gradients resulting in bending, although smaller than observed here.

The residual stress effect of an undamaged substrate must also be considered in other radiation-swelling materials, such as austenitic steels. Despite this significant effect being noticed over 15 years ago [261,262], it appears to have been ignored by the nuclear materials community while being developed in the residual stress and surface treatment community [283,299,300].

In the case of single crystal 6H-SiC, it appears impossible to recreate the effects of neutron irradiation using ion implantation. Constrained swelling stress appears to affect micromechanical properties, implanted ions affect chemical and structural defects, which are also affected by lateral compressive stresses. Having said this, without comparison to a neutron irradiation into a similar model material at similar nominal dpa and temperature it is impossible to make a conclusive remark on the effectiveness of ion implantation. Literature in this field is unsatisfactory due to variations in experimental conditions, and experimental conditions not being of relevance to nuclear material applications. If neutron irradiated samples in a model material are available, ion implantation can be tailored to recreate these properties and create guidelines for suitable conditions for effective ion implantation and microscopic experiments. Once suitable parameters are outlined it becomes possible to quickly and reliably investigate new materials and conditions using ion implantation.

A useful set of experiments would be neutron irradiation of model samples (single crystal and simple CVD SiC) at relevant temperatures, followed by ion irradiation at various conditions. As seen in this work and in the literature, temperature is dominant as damage saturates at a relatively low dose in SiC, which is accessible in operating fission reactors. These samples can be analysed by various techniques to explore which ion irradiation conditions most closely match the neutron irradiation. This can create guidelines for ion irradiation conditions for replicating certain neutron irradiation properties.

7.4 Replicating in-service environments

As fusion and advanced fission approach construction phases and commercial operation, engineers require more relevant information on the evolution of materials in

service. Current academic research irradiates materials in idealised laboratory conditions where specimens are nominally unstressed and are in an inert environment. Irradiations are commonly carried out at high temperatures to replicate operating temperatures. However, various other environmental conditions exist in reactors, including corrosion, and mechanical loadings (static and fatigue).

As suggested in this work, residual stress affects radiation defects, so mechanical stress may also be expected to have an effect which should be studied. This has somewhat been observed in terms of radiation creep in ex-service steels, however there is still opportunity to explore this fundamentally. Ion beams and miniaturisation of loading rigs could be used to quickly explore this. With laboratory scale low dose neutron irradiation facilities becoming available in the next few years (eg. Birmingham neutron source) specimens can be irradiated while under mechanical stress. Space in fission reactors is limited as experiments take the space of fuel, affecting neutronics and the economics of the power station, so moving larger experiments to labs is beneficial both for the experimentally and practically.

Most corrosion experiments are conducted on unirradiated specimens, however results of enhanced oxidation in this work and historic reports [276] suggest it is important to consider radiation damage coupled with corrosion. Pre ion irradiating a specimen could be a suitable way to controllably introduce some radiation damage for surface corrosion studies without problems of sample activation and contamination. This should be a simple modification to future corrosion experiments and would be valuable in understand the synergistic effects.

7.5 Future materials for fusion reactors

Currently the fusion research community is moving towards the construction of demonstration reactors and finalising design specifications. This is an engineering phase rather than scientific research so these demonstration reactors will aim to use currently available materials with well-known properties and supply chains.

Most of a fusion reactor could be designed conservatively using commonly available materials, or small variations on them. One key component without a material solution is the divertor. Most designs intend to use tungsten, mainly for its high melting point. The degradation of tungsten appears to be too great to work in a fusion power station, so work is moving towards assessing tungsten carbide or other ceramics including CVD SiC and polycrystalline diamond. These materials are relatively newly considered as plasma facing components and have not been considered sufficiently to be used in a demonstration reactor at this stage.

Academic research related to fusion materials could focus on predicting the changes to materials during their operating lifetime and recreating in-service conditions for more accurate prediction. Designing new materials should focus on improving the practicalities of using fusion reactors aiming for cost reductions. Lower costs could come from extending lifetimes of components by improving predictive modelling, or cheaper manufacturing and easier construction. Developing new materials from lab scale to manufacturing is unlikely to be viable except for critical components such as the divertor.

7.5.1 Suitability of reaction-bonded silicon carbide for a fusion reactor breeder blanket

It appears that radiation-induced degradation of reaction-bonded SiC would make it unsuitable for use in a nuclear environment. The differential swelling between SiC and

silicon and stresses which arise from this were previously identified as the cause of failure, in combination with degraded thermal properties. The results here support the original conclusions that differential swelling between SiC and silicon contribute to early failure. The properties of "nuclear grade" SiC still make it desirable, however using cheaper and more practical reaction-bonded SiC does not appear suitable, so SiC blanket research should focus on improving the practicalities of SiC_f/SiC.

7.5.2 Recommendations for material improvements

Fine-grained silicon carbide, such as made by chemical vapour deposition/infiltration is radiation resistant, likely due to the large area of grain boundaries and stacking faults acting as defect sinks rather than an inherent radiation resistance of SiC as is sometimes suggested in the literature. SiC incorporated in reaction-bonded SiC appears to be the cause of most property degradation. Nano-SiC grains isolated in a silicon matrix would likely be the most radiation-resistant form of RB-SiC, however the unirradiated properties would be inferior. Reducing the grain size in RB-SiC to a radiation resistant scale would be very difficult and would limit the size of components, removing the main benefit of RB-SiC in the first place.

8 Appendices

8.1 Videos

Indent cross section videos can be seen at: http://bit.ly/indent-cross-sections

Bendy cantilevers can be seen at: http://bit.ly/bendy-cantilevers

8.2 Phase diagrams

Silicon carbon phase diagram from [301]

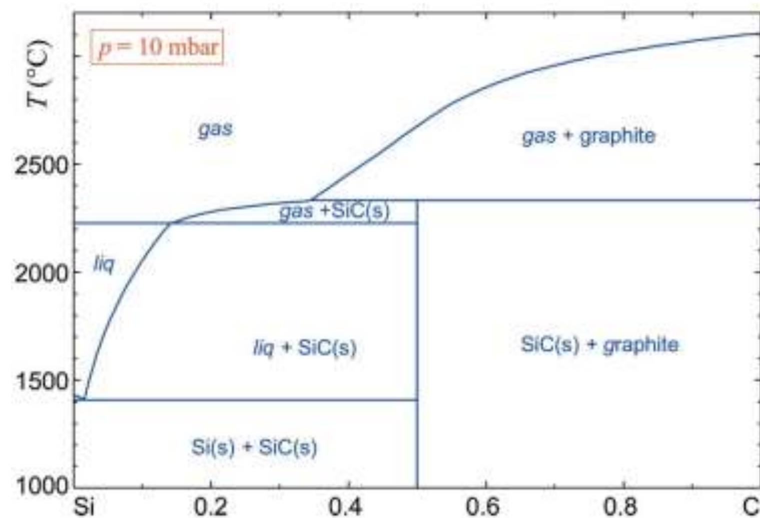

Silicon alloy phase diagrams for the alloy infiltration experiments from the FStel FactSage phase diagram database [302].

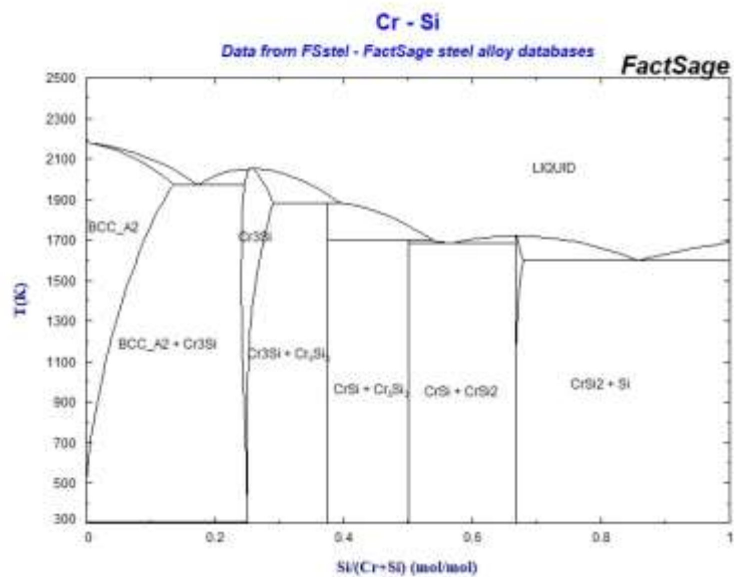
Cr - Si
Data from FSstel - FactSage steel alloy databases
FactSage
LIQUID
BCC_A2
Cr3Si
BCC_A2 + Cr3Si
Cr3Si + Cr5Si3
CrSi + Cr5Si3
CrSi + CrSi2
CrSi2 + Si
T(K)
Si/(Cr+Si) (mol/mol)

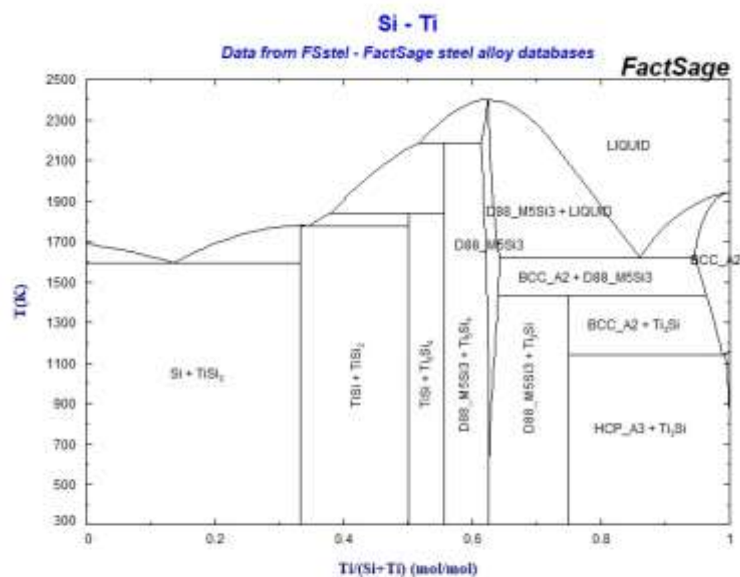
Si - Ti
Data from FSstel - FactSage steel alloy databases
FactSage
LIQUID
D88_M5Si3 + LIQUID
D88_M5Si3
BCC_A2
BCC_A2 + D88_M5Si3
BCC_A2 + Ti3Si
Si + TiSi2
TiSi + TiSi2
TiSi + Ti5Si4
D88_M5Si3 + Ti5Si4
D88_M5Si3 + Ti3Si
HCP_A3 + Ti3Si
T(K)
Ti/(Si+Ti) (mol/mol)

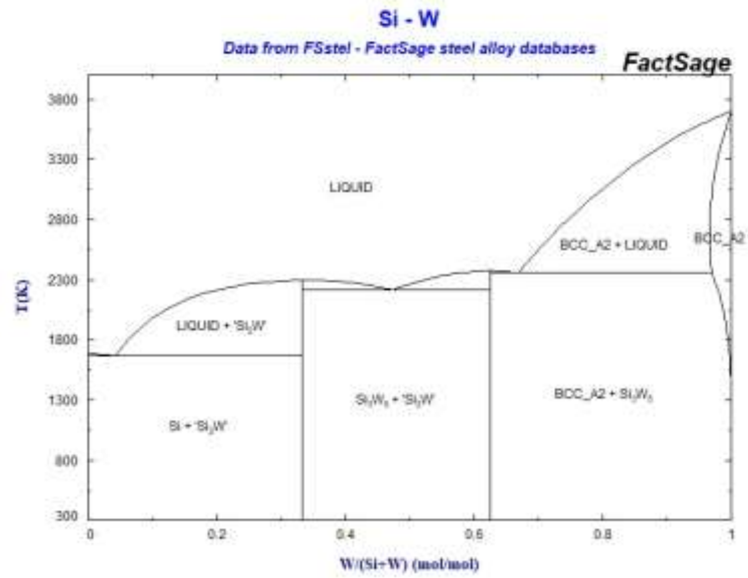
Si - W
Data from FSstel - FactSage steel alloy databases
FactSage
LIQUID
BCC_A2 + LIQUID
BCC_A2
LIQUID + 'Si_2W'
Si_3W_5 + 'Si_2W'
BCC_A2 + Si_3W_5
Si + 'Si_2W'
T(K)
3800
3300
2800
2300
1800
1300
800
300
0
0.2
0.4
0.6
0.8
1
W/(Si+W) (mol/mol)

References

[1] Iter organisation, Summary of the ITER final design report, ITER Doc. G A0 FDR. (2001). http://scholar.google.com/scholar?hl=en%7B&%7DbtnG=Search%7B&%7Dq=intitle:Summary+of+the+ITER+Final+Design+Report%7B#%7D2%5Cnhttp://scholar.google.com/scholar?hl=en&btnG=Search&q=intitle:Summary+of+the+ITER+Final+Design+Report#2.

[2] J. Knaster, A. Moeslang, T. Muroga, Materials research for fusion, Nat. Phys. (2016) 424–434. doi:10.1038/nphys3735.

[3] G.S. Was, Fundamentals of Radiation Materials Science: Metals and Alloys, Springer Science & Business Media, 2007. https://books.google.com/books?id=9JnzUljkAx8C&pgis=1 (accessed April 6, 2016).

[4] S.J. Zinkle, G.S. Was, Materials challenges in nuclear energy, Acta Mater. 61 (2013) 735–758. doi:10.1016/j.actamat.2012.11.004.

[5] R. Betti, P.Y. Chang, B.K. Spears, K.S. Anderson, J. Edwards, M. Fatenejad, J.D. Lindl, R.L. McCrory, R. Nora, D. Shvarts, Thermonuclear ignition in inertial confinement fusion and comparison with magnetic confinement, Phys. Plasmas. 17 (2010) 058102. doi:10.1063/1.3380857.

[6] J. Sanz, J.M. Perlado, A.S. Pérez, D. Guerra, Low activation structural materials for ICF reactors: differences with MCF environments, J. Nucl. Mater. 191–194 (1992) 1450–1454. doi:10.1016/0022-3115(92)90715-W.

[7] M.E. Sawan, N.M. Ghoniem, L. Snead, Y. Katoh, Damage production and accumulation in SiC structures in inertial and magnetic fusion systems, J. Nucl. Mater. 417 (2011) 445–450. doi:10.1016/j.jnucmat.2010.12.077.

[8] J.. Perlado, E. Domínguez, L. Malerba, J. Marian, D. Lodi, M. Salvador, E. Alonso, M.. Caturla, T. Díaz de la Rubia, Results from systematic modeling of neutron damage in inertial fusion energy reactors, Fusion Eng. Des. 60 (2002) 55–63. doi:10.1016/S0920-3796(01)00596-8.

[9] M.E. Sawan, Y. Katoh, L.L. Snead, Transmutation of silicon carbide in fusion nuclear environment, J. Nucl. Mater. 442 (2013) S370–S375. doi:10.1016/j.jnucmat.2012.11.018.

[10] Y. Katoh, L.L. Snead, I. Szlufarska, W.J. Weber, Radiation effects in SiC for nuclear structural applications, Curr. Opin. Solid State Mater. Sci. 16 (2012) 143–152. doi:10.1016/j.cossms.2012.03.005.

[11] C.W. Forrest, P. Kennedy, J. V. Shennan, The Fabrication and Properties of Self-Bonded Silicon Carbide Bodies, in: P. Popper (Ed.), Spec. Ceram. 5, The British Ceramic Research Association, Stoke-on-Trent, 1970: pp. 99–124.

[12] Y. Katoh, M. Kotani, H. Kishimoto, W. Yang, A. Kohyama, Properties and radiation effects in high-temperature pyrolyzed PIP-SiC/SiC, J. Nucl. Mater. 289 (2001) 42–47. doi:10.1016/S0022-3115(00)00681-4.

[13] C.P. Deck, H.E. Khalifa, B. Sammuli, T. Hilsabeck, C.A. Back, Fabrication of SiC–

SiC composites for fuel cladding in advanced reactor designs, Prog. Nucl. Energy. 57 (2012) 38–45. doi:10.1016/j.pnucene.2011.10.002.

[14] T. Aoki, T. Ogasawara, Tyranno ZMI fiber/TiSi2–Si matrix composites for high-temperature structural applications, Compos. Part A Appl. Sci. Manuf. 76 (2015) 102–109. doi:10.1016/j.compositesa.2015.05.018.

[15] K. Shimoda, A. Kohyama, T. Hinoki, High mechanical performance SiC/SiC composites by NITE process with tailoring of appropriate fabrication temperature to fiber volume fraction, Compos. Sci. Technol. 69 (2009) 1623–1628. doi:10.1016/j.compscitech.2009.03.011.

[16] A. Iveković, S. Novak, G. Dražić, D. Blagoeva, S.G. de Vicente, Current status and prospects of SiCf/SiC for fusion structural applications, J. Eur. Ceram. Soc. 33 (2013) 1577–1589. doi:10.1016/j.jeurceramsoc.2013.02.013.

[17] K. Shimoda, T. Hinoki, Y. Katoh, A. Kohyama, Development of the tailored SiC/SiC composites by the combined fabrication process of ICVI and NITE methods, J. Nucl. Mater. 384 (2009) 103–108. doi:10.1016/j.jnucmat.2008.10.025.

[18] T. Aoki, T. Ogasawara, Y. Okubo, K. Yoshida, T. Yano, Fabrication and properties of Si−Hf alloy melt-infiltrated Tyranno ZMI fiber/SiC-based matrix composites, Compos. Part A Appl. Sci. Manuf. 66 (2014) 155–162. doi:10.1016/j.compositesa.2014.07.009.

[19] T. Hinoki, Y. Katoh, L.L. Snead, H.-C. Jung, K. Ozawa, H. Katsui, Z.-H. Zhong, S. Kondo, Y.-H. Park, C. Shih, C.M. Parish, R.A. Meisner, A. Hasegawa, Silicon Carbide and Silicon Carbide Composites for Fusion Reactor Application, Mater. Trans. 54 (2013) 472–476. doi:10.2320/matertrans.MG201206.

[20] E.T. Cheng, Assessment of low activation materials, in: [Proceedings] 14th IEEE/NPSS Symp. Fusion Eng., IEEE, 1991: pp. 621–625. doi:10.1109/FUSION.1991.218844.

[21] F. Porz, G. Grathwohl, F. Thümmler, SiC as a structural material in the plasma chamber of nuclear fusion reactors, Mater. Sci. Eng. 71 (1985) 273–282. doi:10.1016/0025-5416(85)90237-X.

[22] G.P. Pells, Ceramic materials for fusion reactor applications, J. Nucl. Mater. 123 (1984) 1338–1351. doi:10.1016/0022-3115(84)90264-2.

[23] W. Dienst, Assessment of silicon carbide as a potential wall protection material for fusion reactors, Fusion Eng. Des. 16 (1991) 311–316. doi:10.1016/0920-3796(91)90203-3.

[24] S.A. Bringuier, T. Abrams, H. Khalifa, D.M. Thomas, L. Holland, D.L. Rudakov, A.R. Briesemeister, Erosion and Surface Morphology of Silicon Carbide Under Variable DIII-D Divertor Heat Fluxes, in: 59th Annu. Meet. APS Div. Plasma Phys., Milwaukee, 2017: pp. 1–18. https://www.researchgate.net/profile/Stefan_Bringuier/publication/324950394_Erosion_and_Surface_Morphology_of_Silicon_Carbide_Under_Variable_DIII-D_Divertor_Heat_Fluxes_Affiliations/links/5aec72ce458515f599828165/Erosion-and-Surface-Morphology-of-Silicon-.

[25] S.J. Zinkle, Advanced materials for fusion technology, Fusion Eng. Des. 74 (2005) 31–40. doi:10.1016/j.fusengdes.2005.08.008.

[26] L. Giancarli, H. Golfier, S. Nishio, R. Raffray, C. Wong, R. Yamada, Progress in blanket designs using SiCf/SiC composites, Fusion Eng. Des. 61–62 (2002) 307–318. doi:10.1016/S0920-3796(02)00213-2.

[27] B. Riccardi, L. Giancarli, A. Hasegawa, Y. Katoh, A. Kohyama, R.. Jones, L.. Snead, Issues and advances in SiCf/SiC composites development for fusion reactors, J. Nucl. Mater. 329 (2004) 56–65. doi:10.1016/j.jnucmat.2004.04.002.

[28] R.F. Mattas, M.C. Billone, Materials for breeding blankets, J. Nucl. Mater. 233–237 (1996) 72–81.

[29] M. Mahdavi, E. Asadi, Estimates of Tritium Produced Ratio in the Blanket of Fusion Reactors, 2013 (2013) 8–11. doi:10.4236/ojm.2013.31002.

[30] M.J. Pattison, S. Smolentsev, R. Munipalli, M.A. Abdou, Tritium transport in poloidal flows of a dcll blanket, Fusion Sci. Technol. 60 (2011) 809–813. doi:10.13182/FST10-309.

[31] Y. Wu, Conceptual design and testing strategy of a dual functional lithium–lead test blanket module in ITER and EAST, Nucl. Fusion. 47 (2007) 1533–1539. doi:10.1088/0029-5515/47/11/015.

[32] M.A. Abdou, N.B. Morley, A.Y. Ying, S. Smolentsev, P. Calderoni, Overview of Fusion Blanket R & D in the US Over the Last Decade, Nucl. Eng. Technol. 37 (2005) 401–422.

[33] C.P.C. Wong, S. Malang, M. Sawan, M. Dagher, S. Smolentsev, B. Merrill, M. Youssef, S. Reyes, D.K. Sze, N.B. Morley, S. Sharafat, P. Calderoni, G. Sviatoslavsky, R. Kurtz, P. Fogarty, S. Zinkle, M. Abdou, An overview of dual coolant Pb–17Li breeder first wall and blanket concept development for the US ITER-TBM design, Fusion Eng. Des. 81 (2006) 461–467. doi:10.1016/j.fusengdes.2005.05.012.

[34] L. Giancarli, V. Chuyanov, M. Abdou, M. Akiba, B.G. Hong, R. Lässer, C. Pan, Y. Strebkov, Breeding Blanket Modules testing in ITER: An international program on the way to DEMO, Fusion Eng. Des. 81 (2006) 393–405. doi:10.1016/j.fusengdes.2005.08.096.

[35] A. Ying, M. Abdou, C. Wong, S. Malang, N. Morley, M. Sawan, B. Merrill, D.K. Sze, R. Kurtz, S. Willms, M. Ulrickson, S. Zinkle, An overview of US ITER test blanket module program, Fusion Eng. Des. 81 (2006) 433–441. doi:10.1016/j.fusengdes.2005.06.379.

[36] Y. Poitevin, L.V. Boccaccini, M. Zmitko, I. Ricapito, J.-F. Salavy, E. Diegele, F. Gabriel, E. Magnani, H. Neuberger, R. Lässer, L. Guerrini, Tritium breeder blankets design and technologies in Europe: Development status of ITER Test Blanket Modules, test & qualification strategy and roadmap towards DEMO, Fusion Eng. Des. 85 (2010) 2340–2347. doi:10.1016/j.fusengdes.2010.09.027.

[37] M. Abdou, N.B. Morley, S. Smolentsev, A. Ying, S. Malang, A. Rowcliffe, M. Ulrickson, Blanket/first wall challenges and required R&D on the pathway to DEMO, Fusion Eng. Des. 100 (2015) 2–43. doi:10.1016/j.fusengdes.2015.07.021.

[38] C. Soto, J.M. Martínez-Esnaola, C. García-Rosales, Thermomechanical analysis of a Flow Channel Insert based on a SiC-sandwich material concept, Nucl. Mater. Energy. 7 (2016) 5–11. doi:10.1016/j.nme.2016.04.005.

[39] C. Soto, C. Garcia-Rosales, J. Echeberria, J.M. Martinez Esnaola, T. Hernandez, M. Malo, E. Platacis, F. Muktepavela, SiC-based sandwich material for Flow Channel Inserts in DCLL blankets : manufacturing , characterization, in: 29th Symp. Fusion Technol., 2016.

[40] A. Bereciartu, N. Ordás, C. García-Rosales, A. Moroño, M. Malo, E.R. Hodgson, J. Abellà, L. Sedano, Manufacturing and characterization of porous SiC for flow channel inserts in dual-coolant blanket designs, Fusion Eng. Des. 86 (2011) 2526–2529. doi:10.1016/j.fusengdes.2011.03.091.

[41] N. Ordás, A. Bereciartu, C. García-Rosales, A. Moroño, M. Malo, E.R. Hodgson, J. Abellà, S. Colominas, L. Sedano, Testing of porous SiC with dense coating under relevant conditions for Flow Channel Insert application, Fusion Eng. Des. 89 (2014) 1274–1279. doi:10.1016/j.fusengdes.2014.03.056.

[42] L.M. Giancarli, M.Y. Ahn, I. Bonnett, C. Boyer, P. Chaudhuri, W. Davis, G. Dell'Orco, M. Iseli, R. Michling, J.C. Neviere, R. Pascal, Y. Poitevin, I. Ricapito, I. Schneiderova, L. Sexton, H. Tanigawa, Y. Le Tonqueze, J.G. van der Laan, X. Wang, R. Yoshino, ITER TBM Program and associated system engineering, Fusion Eng. Des. (2018) 1–7. doi:10.1016/j.fusengdes.2018.04.014.

[43] D. Maisonnier, I. Cook, S. Pierre, B. Lorenzo, B. Edgar, B. Karin, D.P. Luigi, F. Robin, G. Luciano, H. Stephan, N. Claudio, N. Prachai, P. Aldo, T. Neill, W. David, The European power plant conceptual study, Fusion Eng. Des. 75–79 (2005) 1173–1179. doi:10.1016/j.fusengdes.2005.06.095.

[44] C.E. Kessel, M.S. Tillack, F. Najmabadi, F.M. Poli, K. Ghantous, N. Gorelenkov, X.R. Wang, D. Navaei, H.H. Toudeshki, C. Koehly, L. El-Guebaly, J.P. Blanchard, C.J. Martin, L. Mynsburge, P. Humrickhouse, M.E. Rensink, T.D. Rognlien, M. Yoda, S.I. Abdel-Khalik, M.D. Hageman, B.H. Mills, J.D. Rader, D.L. Sadowski, P.B. Snyder, H. St. John, A.D. Turnbull, L.M. Waganer, S. Malang, A.F. Rowcliffe, The ARIES advanced and conservative tokamak power plant study, Fusion Sci. Technol. 67 (2015) 1–21. doi:10.13182/FST14-794.

[45] A.. Raffray, L. El-Guebaly, S. Gordeev, S. Malang, E. Mogahed, F. Najmabadi, I. Sviatoslavsky, D.. Sze, M.. Tillack, X. Wang, High performance blanket for ARIES-AT power plant, Fusion Eng. Des. 58 (2001) 549–553. doi:10.1016/S0920-3796(01)00493-8.

[46] P. Norajitra, L. Bühler, U. Fischer, S. Gordeev, S. Malang, G. Reimann, Conceptual design of the dual-coolant blanket in the frame of the EU power plant conceptual study, Fusion Eng. Des. 69 (2003) 669–673. doi:10.1016/S0920-3796(03)00207-2.

[47] D.-K. Sze, M. Tillack, L. El-Guebaly, Blanket system selection for the ARIES-ST, Fusion Eng. Des. 48 (2000) 371–378. doi:http://dx.doi.org/10.1016/S0920-3796(00)00146-0.

[48] H. Golfier, G. Aiello, M. Futterer, L. Giancarli, A. Li-Puma, Y. Poitevin, J. Szczepanski, Progress on the TAURO blanket system, Fusion Eng. Des. 61–62 (2002) 461–470. doi:10.1016/S0920-3796(02)00235-1.

[49] B. Badger, E. Al., HIBALL-II - An Improved Conceptual Heavy Ion Beam Driven Fusion ReactorStudy, (n.d.).

[50] Y. Katoh, T. Koyanagi, J.L. McDuffee, L.L. Snead, K. Yueh, Dimensional stability and anisotropy of SiC and SiC-based composites in transition swelling regime, J.

Nucl. Mater. 499 (2018) 471–479. doi:10.1016/j.jnucmat.2017.12.009.

[51] Y. Katoh, L.L. Snead, T. Nozawa, S. Kondo, J.T. Busby, Thermophysical and mechanical properties of near-stoichiometric fiber CVI SiC/SiC composites after neutron irradiation at elevated temperatures, J. Nucl. Mater. 403 (2010) 48–61. doi:10.1016/j.jnucmat.2010.06.002.

[52] Y. Katoh, L.L. Snead, C.H. Henager, T. Nozawa, T. Hinoki, a. Iveković, S. Novak, S.M. Gonzalez de Vicente, Current status and recent research achievements in SiC/SiC composites, J. Nucl. Mater. 455 (2014) 387–397. doi:10.1016/j.jnucmat.2014.06.003.

[53] M. Ferraris, M. Salvo, V. Casalegno, S. Han, Y. Katoh, H.C. Jung, T. Hinoki, A. Kohyama, Joining of SiC-based materials for nuclear energy applications, J. Nucl. Mater. 417 (2011) 379–382. doi:10.1016/j.jnucmat.2010.12.160.

[54] Y. Katoh, L.L. Snead, T. Cheng, C. Shih, W.D. Lewis, T. Koyanagi, T. Hinoki, C.H. Henager, M. Ferraris, Radiation-tolerant joining technologies for silicon carbide ceramics and composites, J. Nucl. Mater. 448 (2014) 497–511. doi:10.1016/j.jnucmat.2013.10.002.

[55] T. Koyanagi, Y. Katoh, T. Nozawa, L.L. Snead, S. Kondo, C.H. Henager, M. Ferraris, T. Hinoki, Q. Huang, Recent progress in the development of SiC composites for nuclear fusion applications, J. Nucl. Mater. 511 (2018) 544–555. doi:10.1016/j.jnucmat.2018.06.017.

[56] R. Schleicher, A.R. Raffray, C.P. Wong, An Assessment of the Brayton Cycle for High Performance Power Plants, Fusion Technol. 39 (2001).

[57] P. Popper, The Preparation of Dense Self-Bonded Silicon Carbide, in: Spec. Ceram., 1960: pp. 209–219.

[58] H.C. Starck, H.C. Starck - About H.C. Starck, (n.d.). https://www.hcstarck.com/en/hc_starck_group/about_hc_starck.html (accessed September 24, 2019).

[59] J.N. Ness, T.F. Page, Microstructural evolution in reaction-bonded silicon carbide, J. Mater. Sci. 21 (1986) 1377–1397. doi:10.1007/BF00553278.

[60] A. Ciftja, Wettability of Silicon with Refractory Materials : A Review, (2008).

[61] O. Dezellus, S. Jacques, F. Hodaj, N. Eustathopoulos, Wetting and infiltration of carbon by liquid silicon, J. Mater. Sci. 40 (2005) 2307–2311. doi:10.1007/s10853-005-1950-7.

[62] Y. Tong, S. Bai, X. Liang, Q.H. Qin, J. Zhai, Reactive melt infiltration fabrication of C/C-SiC composite: Wetting and infiltration, Ceram. Int. 42 (2016) 17174–17178. doi:10.1016/j.ceramint.2016.08.007.

[63] J.-G. Li, H. Hausner, Reactive Wetting in the Liquid-Silicon/Solid-Carbon System, J. Am. Ceram. Soc. 79 (1996) 873–880. doi:10.1111/j.1151-2916.1996.tb08519.x.

[64] S. Meier, J.G. Heinrich, Processing–microstructure–properties relationships of MoSi2–SiC composites, J. Eur. Ceram. Soc. 22 (2002) 2357–2363. doi:10.1016/S0955-2219(02)00035-3.

[65] P. Sangsuwan, J.A. Orejas, J.E. Gatica, S.N. Tewari, M. Singh, Reaction-Bonded Silicon Carbide by Reactive Infiltration, Ind. Eng. Chem. Res. 40 (2001) 5191–5198. doi:10.1021/ie001029e.

[66] J.C. Margiotta, D. Zhang, D.C. Nagle, C.E. Feeser, Formation of dense silicon carbide by liquid silicon infiltration of carbon with engineered structure, J. Mater. Res. 23 (2011) 1237–1248. doi:10.1557/JMR.2008.0167.

[67] V.M. Samoilov, a. N. Vodovozov, V.K. Smirnov, G.G. Zaitsev, Physicomechanical and thermophysical properties of SiC-based ceramics, Inorg. Mater. 47 (2011) 911–915. doi:10.1134/S0020168511070193.

[68] Y.-M. Chiang, R.P. Messner, C.D. Terwilliger, D.R. Behrendt, Reaction-formed silicon carbide, Mater. Sci. Eng. A. 144 (1991) 63–74. doi:10.1016/0921-5093(91)90210-E.

[69] E.O. Einset, Analysis of reactive melt infiltration in the processing of ceramics and ceramic composites, Chem. Eng. Sci. 53 (1998) 1027–1039. doi:10.1016/S0009-2509(97)00379-5.

[70] F.H. Gern, R. Kochendörfer, Liquid silicon infiltration: description of infiltration dynamics and silicon carbide formation, Compos. Part A Appl. Sci. Manuf. 28 (1997) 355–364. doi:10.1016/S1359-835X(96)00135-2.

[71] R.P. Messner, Y.-M. Chiang, Liquid-Phase Reaction-Bonding of Silicon Carbide Using Alloyed Silicon-Molybdenum Melts, J. Am. Ceram. Soc. 73 (1990) 1193–1200. doi:10.1111/j.1151-2916.1990.tb05179.x.

[72] M. Esfehanian, J. Günster, F. Moztarzadeh, J.G. Heinrich, Development of a high temperature Cf/XSi2–SiC (X=Mo, Ti) composite via reactive melt infiltration, J. Eur. Ceram. Soc. 27 (2007) 1229–1235. doi:10.1016/j.jeurceramsoc.2006.05.058.

[73] C.B. Lim, T. Yano, T. Iseki, Microstructure and mechanical properties of RB-SiC / MoSi2 composite, J. Mater. Sci. 24 (1989) 4144–4151. http://link.springer.com/article/10.1007/BF01168987.

[74] M. Singh, D.R. Behrendt, Reactive melt infiltration of silicon-molybdenum alloys into microporous carbon preforms, Mater. Sci. Eng. A. 194 (1995) 193–200. doi:10.1016/0921-5093(94)09663-5.

[75] M. Singh, D.R. Behrendt, Studies on the Reactive Melt Infiltration of Silicon and Silicon-Molybdenum Alloys in Porous Carbon, (1992).

[76] W.-C. Wei, J.S. Lee, Formation and reaction kinetics of Mo and Mo silicides in the preparation of MoSi2/SiC composites, J. Eur. Ceram. Soc. 18 (1998) 509–520. doi:10.1016/S0955-2219(97)00156-8.

[77] L. Hozer, J.-R. Lee, Y.-M. Chiang, Reaction-infiltrated, net-shape SiC composites, Mater. Sci. Eng. A. 195 (1995) 131–143. doi:10.1016/0921-5093(94)06512-8.

[78] M. Singh, D.R. Behrendt, Reactive melt infiltration of silicon-niobium alloys in microporous carbons, J. Mater. Res. 9 (1994) 1701–1708. doi:10.1557/JMR.1994.1701.

[79] Y. Tong, Y. Ye, S. Bai, H. Zhang, Effects of zirconium addition on microstructure and ablation resistance of carbon fibre reinforced carbon and SiC ceramic matrix composite prepared by reactive melt infiltration, Adv. Appl. Ceram. (2014). http://www.tandfonline.com/doi/abs/10.1179/1743676114Y.0000000159 (accessed May 24, 2016).

[80] Y. Tong, S. Bai, H. Zhang, K. Chen, C/C–SiC composite prepared by Si–10Zr alloyed melt infiltration, Ceram. Int. 38 (2012) 3301–3307.

doi:10.1016/j.ceramint.2011.12.038.

[81] X. Cao, X. Yin, X. Ma, X. Fan, Y. Cai, J. Li, L. Cheng, L. Zhang, The microstructure and properties of SiC/SiC-based composites fabricated by low-temperature melt infiltration of Al-Si alloy, Ceram. Int. 42 (2016) 10144–10150. doi:10.1016/j.ceramint.2016.03.126.

[82] S.. Lee, J.. Jin, J.. Park, A. Kohyama, Y. Katoh, H.. Yoon, D.. Bae, I.. Kim, High temperature characterization of reaction sintered SiC based materials, J. Nucl. Mater. 329–333 (2004) 534–538. doi:10.1016/j.jnucmat.2004.04.283.

[83] S. V. Raj, Thermal expansion behavior of hot-pressed engineered matrices, Ceram. Int. 42 (2016) 2557–2569. doi:10.1016/j.ceramint.2015.10.058.

[84] M.R. Gilbert, J.-C. Sublet, R.A. Forrest, Handbook of activation, transmutation, and radiation damage properties of the elements simulated using FISPACT-II & TENDL-2014; Magnetic Fusion Plants, Ccfe-R(15)26. (2015). http://www.ccfe.ac.uk/assets/documents/easy/CCFE-R(15)26.pdf.

[85] R. Rosenkranz, G. Frommeyer, W. Smarsly, Microstructures and properties of high melting point intermetallic Ti5Si3 and TiSi2 compounds, Mater. Sci. Eng. A. 152 (1992) 288–294. doi:10.1016/0921-5093(92)90081-B.

[86] A.K. Vasudévan, J.J. Petrovic, A comparative overview of molybdenum disilicide composites, Mater. Sci. Eng. A. 155 (1992) 1–17. doi:10.1016/0921-5093(92)90308-N.

[87] G.R. Sawyer, T.F. Page, Microstructural characterization of “REFEL” (reaction-bonded) silicon carbides, J. Mater. Sci. 13 (1978) 885–904. doi:10.1007/BF00570528.

[88] R. Pampuch, E. Walasek, J. Bialoskórski, Reaction mechanism in carbon-liquid silicon systems at elevated temperatures, Ceram. Int. 12 (1986) 99–106. doi:10.1016/0272-8842(86)90023-4.

[89] R. Pampuch, J. Białoskórski, E. Walasek, Mechanism of reactions in the Sil + Cf system and the self-propagating high-temperature synthesis of silicon carbide, Ceram. Int. 13 (1987) 63–68. doi:10.1016/0272-8842(87)90039-3.

[90] O.. Chakrabarti, P.. Das, J. Mukerji, Growth of SiC particles in reaction sintered SiC, Mater. Chem. Phys. 67 (2001) 199–202. doi:10.1016/S0254-0584(00)00439-9.

[91] W.P. Minnear, Interfacial Energies in the Si/SiC System and the Si+C Reaction, J. Am. Ceram. Soc. 65 (1982) C-10-C–10. doi:10.1111/j.1151-2916.1982.tb09930.x.

[92] J.C. Margiotta, D. Zhang, D.C. Nagle, Microstructural evolution during silicon carbide (SiC) formation by liquid silicon infiltration using optical microscopy, Int. J. Refract. Met. Hard Mater. 28 (2010) 191–197. doi:10.1016/j.ijrmhm.2009.09.002.

[93] A. Favre, H. Fuzellier, J. Suptil, An original way to investigate the siliconizing of carbon materials, Ceram. Int. 29 (2003) 235–243. doi:10.1016/S0272-8842(02)00110-4.

[94] T. Hase, H. Suzuki, T. Iseki, Formation process of β-SiC during reaction-sintering, J. Nucl. Mater. 59 (1976) 42–48. doi:10.1016/0022-3115(76)90006-4.

[95] G.A.S. R.I. Scace, Solubility of Carbon in Silicon and Germanium, J. Chem. Phys.

30 (1959) 1551–1555. doi:10.1063/1.1730236.

[96] S. Li, Y. Zhang, J. Han, Y. Zhou, Fabrication and characterization of SiC whisker reinforced reaction bonded SiC composite, Ceram. Int. 38 (2012) 1261–1266. doi:10.1016/j.ceramint.2012.06.047.

[97] G.E.J. Beckmann, The Growth of Silicon Carbide from Molten Silicon, J. Electrochem. Soc. 110 (1963) 84. doi:10.1149/1.2425678.

[98] T. Hase, H. Suzuki, Rise in temperature of SiC pellet involving reaction sintering, Bull. Res. Lab. Nucl. React. (Tokyo Inst. Technol. 1 pp. 37–42 (1976). http://inis.iaea.org/Search/search.aspx?orig_q=RN:11517009 (accessed March 23, 2016).

[99] S. Li, Y. Zhang, J. Han, Y. Zhou, Effect of carbon particle and carbon fiber on the microstructure and mechanical properties of short fiber reinforced reaction bonded silicon carbide composite, J. Eur. Ceram. Soc. 33 (2013) 887–896. doi:10.1016/j.jeurceramsoc.2012.10.026.

[100] Y. Li, J. Lin, J. Gao, G. Qiao, H. Wang, Fabrication of reaction-bonded SiC ceramics by slip casting of SiC/C suspension, Mater. Sci. Eng. A. 483–484 (2008) 676–678. doi:10.1016/j.msea.2006.12.162.

[101] E. Phillips, Hutchings, The fabrication and burst testing of reaction bonded silicon carbide tubes, Manitoba, 1971. https://www.ipen.br/biblioteca/rel/R28856.pdf.

[102] S. Suyama, T. Kameda, Y. Itoh, Development of high-strength reaction-sintered silicon carbide, Diam. Relat. Mater. 12 (2003) 1201–1204. doi:10.1016/S0925-9635(03)00066-9.

[103] K. Tsuno, K. Ono, H. Irikado, S. Suyama, Y. Itoh, NTSIC(New Technology SiC): the progress of recent two years, Int. Conf. Sp. Opt. — ICSO 2006. (2017) 15. doi:10.1117/12.2308049.

[104] G.R. Hopkins, R.J. Price, Fusion reactor design with ceramics, Nucl. Eng. Des. 2 (1985) 111–143.

[105] L.W. Hobbs, F.W. Clinard, S.J. Zinkle, R.C. Ewing, Radiation effects in ceramics, J. Nucl. Mater. 216 (1994) 291–321. doi:10.1016/0022-3115(94)90017-5.

[106] R. Devanathan, Radiation damage evolution in ceramics, Nucl. Instruments Methods Phys. Res. Sect. B Beam Interact. with Mater. Atoms. 267 (2009) 3017–3021. doi:10.1016/j.nimb.2009.06.020.

[107] A. Debelle, A. Boulle, A. Chartier, F. Gao, W.J. Weber, Interplay between atomic disorder, lattice swelling, and defect energy in ion-irradiation-induced amorphization of SiC, Phys. Rev. B. 90 (2014) 174112. doi:10.1103/PhysRevB.90.174112.

[108] D. Simeone, J.M. Costantini, L. Luneville, L. Desgranges, P. Trocellier, P. Garcia, Characterization of radiation damage in ceramics: Old challenge new issues?, J. Mater. Res. 30 (2015) 1495–1515. doi:10.1557/jmr.2015.77.

[109] C.J. McHargue, Ion beam modification of ceramics, Mater. Sci. Eng. A. 253 (1998) 94–105.

[110] M. Ishimaru, I.T. Bae, Y. Hirotsu, Electron-beam-induced amorphization in SiC, Phys. Rev. B - Condens. Matter Mater. Phys. 68 (2003) 1–4. doi:10.1103/PhysRevB.68.144102.

[111] L.W. Hobbs, Topological Approaches to the Structure of Crystalline and Amorphous Atom Assemblies, in: J.J. Novoa, D. Braga, L. Addadi (Eds.), Eng. Cryst. Mater. Prop., Springer Netherlands, 2008: pp. 193–230.

[112] P.K. Gupta, A.R. Cooper, Topologically disordered networks of rigid polytopes, J. Non. Cryst. Solids. 123 (1990) 14–21. doi:10.1016/0022-3093(90)90768-H.

[113] J.C. Maxwell, XLV. On reciprocal figures and diagrams of forces , London, Edinburgh, Dublin Philos. Mag. J. Sci. 27 (1864) 250–261. doi:10.1080/14786446408643663.

[114] A.J. Leide, L.W. Hobbs, Z. Wang, D. Chen, L. Shao, J. Li, The role of chemical disorder and structural freedom in radiation-induced amorphization of silicon carbide deduced from electron spectroscopy and ab initio simulations, J. Nucl. Mater. 514 (2019) 299–310. doi:10.1016/j.jnucmat.2018.11.036.

[115] X. Yuan, L.W. Hobbs, Modeling chemical and topological disorder in irradiation-amorphized silicon carbide, Nucl. Instruments Methods Phys. Res. Sect. B Beam Interact. with Mater. Atoms. 191 (2002) 74–82. doi:10.1016/S0168-583X(02)00516-5.

[116] L.W. Hobbs, C.E. Jesurum, B. Bergert, Rigidity Constraints in Amorphization of Multiply-Polytopic Multiply-Connected Ceramic Structures, in: Symp. N / Microstruct. Process. Irradiat. Mater., 1999. doi:10.1557/PROC-540-717.

[117] C.S. Marians, L.W. Hobbs, Local structure of silica glasses, J. Non. Cryst. Solids. 119 (1990) 269–282. doi:10.1016/0022-3093(90)90299-2.

[118] C.E. Jesurum, V. Pulim, L.W. Hobbs, Topological modeling of amorphized tetrahedral ceramic network structures, J. Nucl. Mater. 253 (1998) 87–103.

[119] L.L. Snead, Y. Katoh, T. Koyanagi, K. Terrani, E.D. Specht, Dimensional isotropy of 6H and 3C SiC under neutron irradiation, J. Nucl. Mater. 471 (2016) 92–96. doi:10.1016/j.jnucmat.2016.01.010.

[120] X. Yuan, L.W. Hobbs, Influence of Interatomic Potentials in MD Investigation of Ordering in a -SiC, MRS Proc. 650 (2000) R3.18. doi:10.1557/PROC-650-R3.18.

[121] B.J. Cowen, M.S. El-Genk, Point defects production and energy thresholds for displacements in crystalline and amorphous SiC, Comput. Mater. Sci. 151 (2018) 73–83. doi:10.1016/j.commatsci.2018.04.063.

[122] R. Devanathan, W.J. Weber, Displacement energy surface in 3C and 6H SiC, J. Nucl. Mater. 278 (2000) 258–265. doi:10.1016/S0022-3115(99)00266-4.

[123] F. Gao, W.J. Weber, W. Jiang, Primary damage states produced by Si and Au recoils in SiC: A molecular dynamics and experimental investigation, Phys. Rev. B. 63 (2001) 214106. doi:10.1103/PhysRevB.63.214106.

[124] J. Tersoff, Chemical order in amorphous silicon carbide, Phys. Rev. B. 49 (1994) 16349.

[125] S. Sorieul, J.-M. Costantini, L. Gosmain, L. Thomé, J.-J. Grob, Raman spectroscopy study of heavy-ion-irradiated α-SiC, J. Phys. Condens. Matter. 18 (2006) 5235–5251. doi:10.1088/0953-8984/18/22/022.

[126] W. Bolse, Amorphization and recrystallization of covalent tetrahedral networks, Nucl. Instruments Methods Phys. Res. Sect. B Beam Interact. with Mater. Atoms. 148 (1999) 83–92. doi:10.1016/S0168-583X(98)00855-6.

[127] J. Li, L. Porter, S. Yip, Atomistic modeling of finite-temperature properties of crystalline β-SiC, J. Nucl. Mater. 255 (1998) 139–152. doi:10.1016/S0022-3115(98)00034-8.

[128] T. Suzuki, T. Yano, T. Iseki, T. Mori, Effects of External Stress on Defect Annihilation and Bubble Swelling During Annealing of Neutron-Irradiated Silicon Carbide, J. Am. Ceram. Soc. 73 (1990). doi:10.1111/j.1151-2916.1990.tb07609.x.

[129] H. Zang, T. Yang, D. Guo, J. Xi, C. He, Z. Wang, T. Shen, L. Pang, C. Yao, P. Zhang, Modifications of SiC under high fluence Kr-ion irradiation at different temperatures, Nucl. Instruments Methods Phys. Res. Sect. B Beam Interact. with Mater. Atoms. 307 (2013) 558–561. doi:10.1016/j.nimb.2012.11.089.

[130] T. Sawabe, M. Akiyoshi, K. Ichikawa, K. Yoshida, T. Yano, Microstructure of heavily neutron-irradiated SiC after annealing up to 1500°C, J. Nucl. Mater. 386–388 (2009) 333–337. doi:10.1016/j.jnucmat.2008.12.322.

[131] B. Tyburska-Püschel, Y. Zhai, L. He, C. Liu, A. Boulle, P.M. Voyles, I. Szlufarska, K. Sridharan, Size distribution of black spot defects and their contribution to swelling in irradiated SiC, J. Nucl. Mater. 476 (2016) 132–139. doi:10.1016/j.jnucmat.2016.04.044.

[132] R.. Harrison, S. Ebert, J.. Hinks, S.. Donnelly, Damage microstructure evolution of helium ion irradiated SiC under fusion relevant temperatures, J. Eur. Ceram. Soc. 38 (2018) 24. doi:10.1016/j.jeurceramsoc.2018.04.060.

[133] Y. Katoh, N. Hashimoto, S. Kondo, L.L. Snead, A. Kohyama, Microstructural development in cubic silicon carbide during irradiation at elevated temperatures, J. Nucl. Mater. 351 (2006) 228–240. doi:10.1016/j.jnucmat.2006.02.007.

[134] L.L. Snead, T. Nozawa, Y. Katoh, T.-S. Byun, S. Kondo, D.A. Petti, Handbook of SiC properties for fuel performance modeling, J. Nucl. Mater. 371 (2007) 329–377. doi:10.1016/j.jnucmat.2007.05.016.

[135] T. Yano, T. Iseki, High-resolution electron microscopy of neutron-irradiation-induced dislocations in SiC, Philos. Mag. A Phys. Condens. Matter, Struct. Defects Mech. Prop. 62 (1990) 421–430. doi:10.1080/01418619008244788.

[136] Y.R. Lin, L.G. Chen, C.Y. Hsieh, M.T. Chang, K.Y. Fung, A. Hu, S.C. Lo, F.R. Chen, J.J. Kai, Atomic Configuration of Point Defect Clusters in Ion-Irradiated Silicon Carbide, Sci. Rep. 7 (2017) 1–6. doi:10.1038/s41598-017-15037-w.

[137] T. Yano, M. Akiyoshi, K. Ichikawa, Y. Tachi, T. Iseki, Physical property change of heavily neutron-irradiated Si3N4 and SiC by thermal annealing, J. Nucl. Mater. 289 (2001) 102–109. doi:10.1016/S0022-3115(00)00688-7.

[138] T. Yano, H. Miyazaki, M. Akiyoshi, T. Iseki, X-ray diffractometry and high-resolution electron microscopy of neutron-irradiated SiC to a fluence of 1.9×1027 n/m2, J. Nucl. Mater. 253 (1998) 78–86. doi:10.1016/S0022-3115(97)00331-0.

[139] S. Yamazaki, K. Yoshida, T. Yano, Recovery behavior of point defects after low-dose neutron irradiation of sintered SiC by thermal diffusivity and swelling measurements, J. Nucl. Mater. 417 (2011) 425–429. doi:10.1016/j.jnucmat.2010.12.178.

[140] S. Yamazaki, M. Imai, T. Yano, Recovery of neutron-induced damage of SiC by thermal annealing up to 1400°C, Prog. Nucl. Energy. 50 (2008) 601–605.

doi:10.1016/j.pnucene.2007.11.046.

[141] W.J. Weber, W. Jiang, S. Thevuthasan, Defect annealing kinetics in irradiated 6H–SiC, Nucl. Instruments Methods Phys. Res. Sect. B Beam Interact. with Mater. Atoms. 166–167 (2000) 410–414. doi:10.1016/S0168-583X(99)00868-X.

[142] M.I. Idris, S. Yamazaki, K. Yoshida, T. Yano, Recovery behavior of high purity cubic SiC polycrystals by post-irradiation annealing up to 1673 K after low temperature neutron irradiation, J. Nucl. Mater. 465 (2015) 814–819. doi:10.1016/j.jnucmat.2015.07.046.

[143] L.L. Snead, Y. Katoh, S. Connery, Swelling of SiC at intermediate and high irradiation temperatures, J. Nucl. Mater. 367–370 (2007) 677–684. doi:10.1016/j.jnucmat.2007.03.097.

[144] F. Gao, W.J. Weber, Recovery of close Frenkel pairs produced by low energy recoils in SiC, J. Appl. Phys. 94 (2003) 4348–4356. doi:10.1063/1.1605254.

[145] W.J. Weber, W. Jiang, S. Thevuthasan, Accumulation, dynamic annealing and thermal recovery of ion-beam-induced disorder in silicon carbide, Nucl. Instruments Methods Phys. Res. Sect. B Beam Interact. with Mater. Atoms. 175–177 (2001) 26–30. doi:10.1016/S0168-583X(00)00542-5.

[146] W.J. Weber, F. Gao, R. Devanathan, W. Jiang, C.M. Wang, Ion-beam induced defects and nanoscale amorphous clusters in silicon carbide, Nucl. Instruments Methods Phys. Res. Sect. B Beam Interact. with Mater. Atoms. 216 (2004) 25–35. doi:10.1016/j.nimb.2003.11.016.

[147] X. Wang, Y. Zhang, D. Han, Y. Zhao, Z. Zhao, M. Zhang, Damage production in silicon carbide by dual ion beams irradiation, J. Nucl. Mater. 499 (2018) 326–333. doi:10.1016/j.jnucmat.2017.11.020.

[148] C.H. Chen, Y. Zhang, E. Fu, Y. Wang, M.L. Crespillo, C. Liu, S. Shannon, W.J. Weber, Irradiation-induced microstructural change in helium-implanted single crystal and nano-engineered SiC, J. Nucl. Mater. 453 (2014) 280–286. doi:10.1016/j.jnucmat.2014.07.020.

[149] I. De Wolf, Micro-Raman spectroscopy to study local mechanical stress in silicon integrated circuits, Semicond. Sci. Technol. 11 (1996) 139–154. doi:10.1088/0268-1242/11/2/001.

[150] C. V. Raman, A new radiation, Indian J. Phys. 2 (1928) 387–398. doi:10.1007/BF03052651.

[151] S. Nakashima, H. Harima, Raman Investigation of SiC Polytypes, Phys. Status Solidi A. 162 (1997) 39–64. doi:10.1002/1521-396X(199707)162:1<39::AID-PSSA39>3.0.CO;2-L.

[152] H. Okumura, E. Sakuma, J.H. Lee, H. Mukaida, S. Misawa, K. Endo, S. Yoshida, Raman scattering of SiC: Application to the identification of heteroepitaxy of SiC polytypes, J. Appl. Phys. 61 (1987) 1134. doi:10.1063/1.338157.

[153] W. Bolse, J. Conrad, T. Rödle, T. Weber, Ion-beam-induced amorphization of 6H-SiC, Surf. Coatings Technol. 74 (1995) 927–931. doi:10.1016/0257-8972(95)08288-3.

[154] J. Conrad, T. Rödle, T. Weber, W. Bolse, Irradiation effects in α-SiC studied via RBS-C, Raman-scattering and surface profiling, Nucl. Instruments Methods Phys.

Res. Sect. B Beam Interact. with Mater. Atoms. 118 (1996) 748–752. doi:10.1016/0168-583X(95)01113-7.

[155] A. Debelle, L. Thomé, D. Dompoint, A. Boulle, F. Garrido, J. Jagielski, D. Chaussende, Characterization and modelling of the ion-irradiation induced disorder in 6H-SiC and 3C-SiC single crystals, J. Phys. D. Appl. Phys. 43 (2010). doi:10.1088/0022-3727/43/45/455408.

[156] E. Viswanathan, Y.S. Katharria, S. Selvakumar, A. Arulchakkaravarthi, D. Kanjilal, K. Sivaji, Investigations on the structural and optical properties of the swift heavy ion irradiated 6HSiC, Nucl. Instruments Methods Phys. Res. Sect. B Beam Interact. with Mater. Atoms. 269 (2011) 1103–1107. doi:10.1016/j.nimb.2011.01.017.

[157] S. Nakashima, Y. Nakatake, Y. Ishida, T. Talkahashi, H. Okumura, Detection of defects in SiC crystalline films by Raman scattering, Phys. B Condens. Matter. 308–310 (2001) 684–686. doi:10.1016/S0921-4526(01)00795-5.

[158] T. Koyanagi, M.J. Lance, Y. Katoh, Quantification of irradiation defects in beta-silicon carbide using Raman spectroscopy, Scr. Mater. 125 (2016) 58–62. doi:10.1016/j.scriptamat.2016.08.004.

[159] N. Chaâbane, A. Debelle, G. Sattonnay, P. Trocellier, Y. Serruys, L. Thomé, Y. Zhang, W.J.J. Weber, C. Meis, L. Gosmain, A. Boulle, Investigation of irradiation effects induced by self-ion in 6H-SiC combining RBS/C, Raman and XRD, Nucl. Instruments Methods Phys. Res. Sect. B Beam Interact. with Mater. Atoms. 286 (2012) 108–113. doi:10.1016/j.nimb.2011.11.018.

[160] V. Iota, C.S. Yoo, H. Cynn, Quartzlike carbon dioxide: An optically nonlinear extended solid at high pressures and temperatures, Science (80-.). 283 (1999) 1510–1513. doi:10.1126/science.283.5407.1510.

[161] T. Koyanagi, Recent progress in the development of SiC composites at ORNL Presented by Takaaki Koyanagi SiC material development at ORNL, (2017).

[162] J. Filik, J. Hodkiewicz, T.F. Scientific, T.R. Society, P. Transactions, E. Sciences, I. Childres, L. Jauregui, W. Park, H. Cao, Y. Chen, J. B. Lambert, Raman spectroscopy : a the lightest touch, Spectrosc. Eur. 17 (2005) 10–16. doi:10.1088/0022-3727/46/12/122001.

[163] E. Wendler, T. Bierschenk, F. Felgenträger, J. Sommerfeld, W. Wesch, D. Alber, G. Bukalis, L.C. Prinsloo, N. Van Der Berg, E. Friedland, J.B. Malherbe, Damage formation and optical absorption in neutron irradiated SiC, Nucl. Instruments Methods Phys. Res. Sect. B Beam Interact. with Mater. Atoms. 286 (2012) 97–101. doi:10.1016/j.nimb.2012.01.010.

[164] P.F. Wang, L. Huang, W. Zhu, Y.F. Ruan, Raman scattering of neutron irradiated 6H-SiC, Solid State Commun. 152 (2012) 887–890. doi:10.1016/j.ssc.2012.02.010.

[165] X. Chen, W. Zhou, Q. Feng, J. Zheng, X. Liu, B. Tang, J. Li, J. Xue, S. Peng, Irradiation effects in 6H–SiC induced by neutron and heavy ions: Raman spectroscopy and high-resolution XRD analysis, J. Nucl. Mater. 478 (2016) 215–221. doi:10.1016/j.jnucmat.2016.06.020.

[166] X. Chen, W. Zhou, X. Zhang, Q. Feng, J. Zheng, X. Liu, B. Tang, J. Li, J. Xue, S. Peng, Mechanical properties of 6H-SiC irradiated by neutron and MeV heavy ions: A nanoindentation and finite element method study, J. Appl. Phys. 123 (2018) 025104. doi:10.1063/1.5006378.

[167] M.I. Idris, H. Konishi, M. Imai, K. Yoshida, T. Yano, Neutron Irradiation Swelling of SiC and SiCf/SiC for Advanced Nuclear Applications, Energy Procedia. 71 (2015) 328–336. doi:10.1016/j.egypro.2014.11.886.

[168] K. Yoshida, H. Akimoto, T. Yano, M. Kotani, T. Ogasawara, Mechanical properties of unidirectional and crossply SiCf/SiC composites using SiC fibers with carbon interphase formed by electrophoretic deposition process, Prog. Nucl. Energy. 82 (2015) 148–152. doi:10.1016/j.pnucene.2014.07.027.

[169] F.W. Clinard, G.F. Hurley, L.W. Hobbs, D.L. Rohr, R.A. Youngman, Structural performance of ceramics in a high-fluence fusion environment, J. Nucl. Mater. 123 (1984) 1386–1392. doi:10.1016/0022-3115(84)90272-1.

[170] P. Kennedy, J. V. Shennan, REFEL Silicon Carbide: The development of a ceramic for a nuclear engineering application, 1974.

[171] R.B. Matthews, Irradiation damage in reaction-bonded silicon carbide, J. Nucl. Mater. 51 (1974) 203–208. doi:10.1016/0022-3115(74)90003-8.

[172] R.A. Matheny, J.C. Corelli, G.G. Trantina, Radiation damage in silicon carbide and graphite for fusion reactor first wall applications, J. Nucl. Mater. 83 (1979) 313–321. doi:10.1016/0022-3115(79)90616-0.

[173] A.M. Carey, F.J. Pineau, C.W. Lee, J.C. Corelli, Radiation response of reaction-bonded and sintered SiC: Effects of boron isotopes, J. Nucl. Mater. 103 (1981) 789–793. doi:10.1016/0022-3115(82)90695-X.

[174] J.W. Malloy, J.M. McKenzie, J.C. Corelli, Effects of neutron irradiation on the fracture of silicon carbide, in: D. Francois (Ed.), Adv. Fract. Res. Proc. 5th Int. Conf. Fract., Cannes, 1981: pp. 2477–2484.

[175] R.J. Price, G.R. Hopkins, Flexural strength of proof-tested and neutron-irradiated silicon carbide, J. Nucl. Mater. 108 (1982) 732–738. doi:10.1016/0022-3115(82)90547-5.

[176] J.C. Corelli, J. Hoole, J. Lazarro, C.W. Lee, Mechanical, Thermal, and Microstructural Properties of Neutron-Irradiated SiC, J. Am. Ceram. Soc. 66 (1983) 529–538. doi:10.1111/j.1151-2916.1983.tb10596.x.

[177] S.D. Harrison, J.C. Corelli, Microstructure of neutron irradiation-induced defects in sintered and siliconized SiC, J. Nucl. Mater. 122 (1984) 833–839. doi:10.1016/0022-3115(84)90708-6.

[178] T. Iseki, T. Maruyama, T. Yano, T. Suzuki, T. Mori, Effects of neutron irradiation and subsequent annealing on strength and toughness of SiC ceramics, J. Nucl. Mater. 170 (1990) 95–100. doi:10.1016/0022-3115(90)90330-P.

[179] W. Liu, L. Cheng, Y. Wang, H. Ma, Investigation of the residual stress in reaction-bonded SiC under irradiation, J. Eur. Ceram. Soc. 36 (2016) 3901–3907. doi:10.1016/j.jeurceramsoc.2016.06.033.

[180] X. Kerbiriou, J.-M. Costantini, M. Sauzay, S. Sorieul, L. Thomé, J. Jagielski, J.-J. Grob, Amorphization and dynamic annealing of hexagonal SiC upon heavy-ion irradiation: Effects on swelling and mechanical properties, J. Appl. Phys. 105 (2009) 073513. doi:10.1063/1.3103771.

[181] M.C. Osborne, J.C. Hay, L.L. Snead, D. Steiner, Mechanical- and Physical-Property Changes of Neutron-Irradiated Chemical-Vapor-Deposited Silicon Carbide, J. Am.

Ceram. Soc. 82 (1999) 2490–2496. doi:10.1111/j.1151-2916.1999.tb02108.x.

[182] S. Nogami, A. Hasegawa, L.L. Snead, Indentation fracture toughness of neutron irradiated silicon carbide, J. Nucl. Mater. 307–311 (2002) 1163–1167. doi:10.1016/S0022-3115(02)01055-3.

[183] B. Su, H. Liang, G. Liu, Z. Huang, X. Liu, Z. Chen, D.Y.W. Yu, Damage development of sintered SiC ceramics with the depth variation in Ar ion-irradiation at 600 °C, J. Eur. Ceram. Soc. 38 (2018) 2289–2296. doi:10.1016/j.jeurceramsoc.2017.12.050.

[184] C.L. Xu, C.H. Zhang, J.J. Li, L.Q. Zhang, Y.T. Yang, Y. Song, X.J. Jia, J.Y. Li, K.Q. Chen, A HRXRD and nano-indentation study on Ne-implanted 6H–SiC, Nucl. Instruments Methods Phys. Res. Sect. B Beam Interact. with Mater. Atoms. 286 (2012) 129–133. doi:10.1016/j.nimb.2012.01.009.

[185] J. Li, H. Huang, G. Lei, Q. Huang, R. Liu, D. Li, L. Yan, Evolution of amorphization and nanohardness in SiC under Xe ion irradiation, J. Nucl. Mater. 454 (2014) 173–177. doi:10.1016/j.jnucmat.2014.07.036.

[186] Y. Yang, C. Zhang, C. Su, Z. Ding, Y. Song, Dose dependence of nano-hardness of 6H-SiC crystal under irradiation with inert gas ions, Nucl. Instruments Methods Phys. Res. Sect. B Beam Interact. with Mater. Atoms. 422 (2018) 50–53. doi:10.1016/j.nimb.2018.02.035.

[187] D.E.J. Armstrong, P.D. Edmondson, S.G. Roberts, Effects of sequential tungsten and helium ion implantation on nano-indentation hardness of tungsten, Appl. Phys. Lett. 102 (2013). doi:10.1063/1.4811825.

[188] C. Jiang, L. Dagault, V. Audurier, C. Tromas, A. Declémy, M.F. Beaufort, J.F. Barbot, Strain buildup in 4H-SiC implanted with noble gases at low dose, Mater. Today Proc. 5 (2018) 14722–14731. doi:10.1016/j.matpr.2018.03.062.

[189] P. Jannotti, G. Subhash, J. Zheng, V. Halls, Measurement of microscale residual stresses in multi-phase ceramic composites using Raman spectroscopy, Acta Mater. 129 (2017) 482–491. doi:10.1016/j.actamat.2017.03.015.

[190] B.L. Wing, F. Esmonde-White, J.W. Halloran, Microstress in Reaction-Bonded SiC from Crystallization Expansion of Silicon, J. Am. Ceram. Soc. 99 (2016) 3705–3711. doi:10.1111/jace.14398.

[191] B.L. Wing, J.W. Halloran, Microstress in the matrix of a melt-infiltrated SiC/SiC ceramic matrix composite, J. Am. Ceram. Soc. 100 (2017) 5286–5294. doi:10.1111/jace.15038.

[192] R. Gajic, D. Braun, F. Kuchar, A. Golubovi, R. Korntner, H. L schner, J. Butschke, R. Springer, F. Letzkus, Boron-content dependence of Fano resonances in p-type silicon, J. Phys. Condens. Matter. 15 (2003) 2923–2931. doi:10.1088/0953-8984/15/17/340.

[193] A.J.G. Lunt, A.M. Korsunsky, A review of micro-scale focused ion beam milling and digital image correlation analysis for residual stress evaluation and error estimation, Surf. Coatings Technol. 283 (2015) 373–388. doi:10.1016/j.surfcoat.2015.10.049.

[194] E. Salvati, A.M. Korsunsky, An analysis of macro- and micro-scale residual stresses of Type I, II and III using FIB-DIC micro-ring-core milling and crystal plasticity

FE modelling, Int. J. Plast. 98 (2017) 123–138. doi:10.1016/j.ijplas.2017.07.004.

[195] A.J.G. Lunt, E. Salvati, L. Ma, I.P. Dolbyna, T.K. Neo, A.M. Korsunsky, Full in-plane strain tensor analysis using the microscale ring-core FIB milling and DIC approach, J. Mech. Phys. Solids. 94 (2016) 47–67. doi:10.1016/j.jmps.2016.03.013.

[196] A.M. Korsunsky, M. Sebastiani, E. Bemporad, Focused ion beam ring drilling for residual stress evaluation, Mater. Lett. 63 (2009) 1961–1963. doi:10.1016/j.matlet.2009.06.020.

[197] A.W. Mello, T.A. Book, A. Nicolas, S.E. Otto, C.J. Gilpin, M.D. Sangid, Distortion Correction Protocol for Digital Image Correlation after Scanning Electron Microscopy: Emphasis on Long Duration and Ex-Situ Experiments, Exp. Mech. 57 (2017) 1395–1409. doi:10.1007/s11340-017-0303-1.

[198] S. Massl, H. Köstenbauer, J. Keckes, R. Pippan, Stress measurement in thin films with the ion beam layer removal method: Influence of experimental errors and parameters, Thin Solid Films. 516 (2008) 8655–8662. doi:10.1016/j.tsf.2008.06.091.

[199] S. Massl, J. Keckes, R. Pippan, A new cantilever technique reveals spatial distributions of residual stresses in near-surface structures, Scr. Mater. 59 (2008) 503–506. doi:10.1016/j.scriptamat.2008.04.037.

[200] S. Massl, J. Keckes, R. Pippan, A direct method of determining complex depth profiles of residual stresses in thin films on a nanoscale, Acta Mater. 55 (2007) 4835–4844. doi:10.1016/j.actamat.2007.05.002.

[201] R. Schöngrundner, R. Treml, T. Antretter, D. Kozic, W. Ecker, D. Kiener, R. Brunner, Critical assessment of the determination of residual stress profiles in thin films by means of the ion beam layer removal method, Thin Solid Films. 564 (2014) 321–330. doi:10.1016/j.tsf.2014.06.003.

[202] N. Katsikis, Private communication, (2016).

[203] M. Singh, T.A. Leonhardt, Microstructural characterization of reaction-formed silicon carbide ceramics, Mater. Charact. 35 (1995) 221–228. doi:10.1016/1044-5803(95)00152-2.

[204] A.J. Whitehead, T.F. Page, Fabrication and characterization of some novel reaction-bonded silicon carbide materials, J. Mater. Res. 27 (1992) 839–852. http://link.springer.com/article/10.1007/BF00554061.

[205] J.F. Ziegler, M.D. Ziegler, J.P. Biersack, SRIM - The stopping and range of ions in matter (2010), Nucl. Instruments Methods Phys. Res. Sect. B Beam Interact. with Mater. Atoms. 268 (2010) 1818–1823. doi:10.1016/j.nimb.2010.02.091.

[206] R.E. Stoller, M.B. Toloczko, G.S. Was, A.G. Certain, S. Dwaraknath, F.A. Garner, On the use of SRIM for computing radiation damage exposure, Nucl. Instruments Methods Phys. Res. Sect. B Beam Interact. with Mater. Atoms. 310 (2013) 75–80. doi:10.1016/j.nimb.2013.05.008.

[207] M.T. Laugier, Palmqvist indentation toughness in WC-Co composites, J. Mater. Sci. Lett. 6 (1987) 897–900. doi:10.1007/BF01729862.

[208] R.D. Dukino, M. V. Swain, Comparative Measurement of Indentation Fracture Toughness with Berkovich and Vickers Indenters, J. Am. Ceram. Soc. 75 (1992) 3299–3304. doi:10.1111/j.1151-2916.1992.tb04425.x.

[209] A. Datye, U. Schwarz, H.-T. Lin, Fracture Toughness Evaluation and Plastic Behavior Law of a Single Crystal Silicon Carbide by Nanoindentation, Ceramics. 1 (2018) 198–210. doi:10.3390/ceramics1010017.

[210] N. Cuadrado, D. Casellas, M. Anglada, E. Jiménez-Piqué, Evaluation of fracture toughness of small volumes by means of cube-corner nanoindentation, Scr. Mater. 66 (2012) 670–673. doi:10.1016/j.scriptamat.2012.01.033.

[211] H. Harima, Raman scattering characterization on SiC, Microelectron. Eng. 83 (2006) 126–129. doi:10.1016/j.mee.2005.10.037.

[212] S. Guo, A. Limpichaipanit, R.I. Todd, High resolution optical microprobe investigation of surface grinding stresses in Al2O3 and Al2O3/SiC nanocomposites, J. Eur. Ceram. Soc. 31 (2011) 97–109. doi:10.1016/j.jeurceramsoc.2010.08.021.

[213] E. Anastassakis, A. Pinczuk, E. Burstein, F.H. Pollak, M. Cardona, Effect of static uniaxial stress on the Raman spectrum of silicon, Solid State Commun. 88 (1993) 1053–1058. doi:10.1016/0038-1098(93)90294-W.

[214] E. Anastassakis, A. Cantarero, M. Cardona, Piezo-Raman measurements and anharmonic parameters in silicon and diamond, Phys. Rev. B. 41 (1990) 7529–7535. doi:10.1103/PhysRevB.41.7529.

[215] M.D. Vaudin, A. Gayle, L.H. Friedman, R.F. Cook, Strain Mapping Using EBSD Cross Correlation and Raman Methods, Microsc. Microanal. 24 (2018) 960–961. doi:10.1017/S1431927618005299.

[216] D. Olego, M. Cardona, Pressure dependence of Raman phonons of Ge and 3 C -SiC, Phys. Rev. B. 25 (1982) 1151–1160. doi:10.1103/PhysRevB.25.1151.

[217] J.F. DiGregorio, T.E. Furtak, Analysis of Residual Stress in 6H-SiC Particles within Al2O3/SiC Composites through Raman Spectroscopy, J. Am. Ceram. Soc. 75 (1992) 1854–1857. doi:10.1111/j.1151-2916.1992.tb07207.x.

[218] R. Stadelmann, B. Hughes, N. Orlovskaya, S. Grasso, M.J. Reece, 2D Raman mapping and thermal residual stresses in SiC grains of ZrB2-SiC ceramic composites, Ceram. Int. 41 (2015) 13630–13637. doi:10.1016/j.ceramint.2015.07.161.

[219] A.M. Gigler, A.J. Huber, M. Bauer, A. Ziegler, R. Hillenbrand, R.W. Stark, Nanoscale residual stress-field mapping around nanoindents in SiC by IR s-SNOM and confocal Raman microscopy, Opt. Express. 17 (2009) 22351. doi:10.1364/OE.17.022351.

[220] I. De Wolf, J. Vanhellemont, A. Romano-Rodríguez, H. Norström, H.E. Maes, Micro-Raman study of stress distribution in local isolation structures and correlation with transmission electron microscopy, J. Appl. Phys. 71 (1992) 898–906. doi:10.1063/1.351311.

[221] R.P. Koseski, W.A. Osborn, S.J. Stranick, F.W. Delrio, M.D. Vaudin, T. Dao, V.H. Adams, R.F. Cook, Micro-scale measurement and modeling of stress in silicon surrounding a tungsten-filled through-silicon via, J. Appl. Phys. 110 (2011). doi:10.1063/1.3644971.

[222] G.A. Myers, S.S. Hazra, M.P. De Boer, C.A. Michaels, S.J. Stranick, P. Ryan, R.F. Cook, F.W. Delrio, microscopy Stress mapping of micromachined polycrystalline silicon devices via confocal Raman microscopy, Appl. Phys. Lett. 104 (2014).

doi:http://dx.doi.org/10.1063/1.4878616.

[223] Y. Kang, Y. Qiu, Z. Lei, M. Hu, An application of Raman spectroscopy on the measurement of residual stress in porous silicon, Opt. Lasers Eng. 43 (2005) 847–855. doi:10.1016/j.optlaseng.2004.09.005.

[224] J. Liu, Y.K. Vohra, Raman Modes of <math display="inline"> <mn>6</mn> <mi>H</mi> </math> Polytype of Silicon Carbide to Ultrahigh Pressures: A Comparison with Silicon and Diamond, Phys. Rev. Lett. 72 (1994) 4105–4108. doi:10.1103/PhysRevLett.72.4105.

[225] D. Ghosh, G. Subhash, N. Orlovskaya, Measurement of scratch-induced residual stress within SiC grains in ZrB2-SiC composite using micro-Raman spectroscopy, Acta Mater. 56 (2008) 5345–5354. doi:10.1016/j.actamat.2008.07.031.

[226] B.J. Griffin, A comparison of conventional Everhart-Thornley style and in-lens secondary electron detectors-a further variable in scanning electron microscopy, Scanning. 33 (2011) 162–173. doi:10.1002/sca.20255.

[227] T. Ben Britton, J. Jiang, P.S. Karamched, A.J. Wilkinson, Probing Deformation and Revealing Microstructural Mechanisms with Cross-Correlation-Based, High-Resolution Electron Backscatter Diffraction, JOM. 65 (2013) 1245–1253. doi:10.1007/s11837-013-0680-6.

[228] T.B. Britton, J.L.R. Hickey, Understanding deformation with high angular resolution electron backscatter diffraction (HR-EBSD), IOP Conf. Ser. Mater. Sci. Eng. 304 (2018) 012003. doi:10.1088/1757-899X/304/1/012003.

[229] A.J. Wilkinson, D. Randman, Determination of elastic strain fields and geometrically necessary dislocation distributions near nanoindents using electron back scatter diffraction, Philos. Mag. 90 (2010) 1159–1177. doi:10.1080/14786430903304145.

[230] K. Persson, Materials Data on SiC (SG:186) by Materials Project, (2014). doi:10.17188/1293198.

[231] M. De Jong, W. Chen, T. Angsten, A. Jain, R. Notestine, A. Gamst, M. Sluiter, C. Krishna Ande, S. Van Der Zwaag, J.J. Plata, C. Toher, S. Curtarolo, G. Ceder, K.A. Persson, M. Asta, C.K. Ande, S. Van Der Zwaag, J.J. Plata, C. Toher, S. Curtarolo, G. Ceder, K.A. Persson, M. Asta, Charting the complete elastic properties of inorganic crystalline compounds, Sci. Data. 2 (2015) 1–13. doi:10.1038/sdata.2015.9.

[232] J.. Nye, Some geometrical relations in dislocated crystals, Acta Metall. 1 (1953) 153–162. doi:10.1016/0001-6160(53)90054-6.

[233] W. Wisniewski, C. Rüssel, An experimental viewpoint on the information depth of EBSD, Scanning. 38 (2016) 164–171. doi:10.1002/sca.21251.

[234] W. Wisniewski, S. Saager, A. Böbenroth, C. Rüssel, Experimental evidence concerning the significant information depth of electron backscatter diffraction (EBSD), Ultramicroscopy. 173 (2017) 1–9. doi:10.1016/j.ultramic.2016.11.004.

[235] D.E.J. Armstrong, A.J. Wilkinson, S.G. Roberts, Measuring anisotropy in Young's modulus of copper using microcantilever testing, J. Mater. Res. 24 (2009) 3268–3276. doi:10.1557/jmr.2009.0396.

[236] J. Blaber, B. Adair, A. Antoniou, Ncorr: Open-Source 2D Digital Image Correlation

Matlab Software, Exp. Mech. 55 (2015) 1105–1122. doi:10.1007/s11340-015-0009-1.

[237] D. Nečas, P. Klapetek, Gwyddion: An open-source software for SPM data analysis, Cent. Eur. J. Phys. 10 (2012) 181–188. doi:10.2478/s11534-011-0096-2.

[238] J.B. Renucci, R.N. Tyte, M. Cardona, Resonant Raman scattering in silicon, Phys. Rev. B. 11 (1975) 3885–3895. doi:10.1103/PhysRevB.11.3885.

[239] P. Hermet, M. Khalil, R. Viennois, M. Beaudhuin, D. Bourgogne, D. Ravot, Revisited phonon assignment and electro-mechanical properties of chromium disilicide, RSC Adv. 5 (2015) 19106–19116. doi:10.1039/C4RA15576A.

[240] I. Volotsenko, M. Molotskii, Z. Barkay, J. Marczewski, P. Grabiec, B. Jaroszewicz, G. Meshulam, E. Grunbaum, Y. Rosenwaks, Secondary electron doping contrast: Theory based on scanning electron microscope and Kelvin probe force microscopy measurements, J. Appl. Phys. 107 (2010). doi:10.1063/1.3276090.

[241] M. Shuaib, T.. Davies, Wear behaviour of a REFEL SiC containing fluorides up to 900°C, Wear. 249 (2001) 20–30. doi:10.1016/S0043-1648(00)00545-7.

[242] G.D. Watkins, W.B. Fowler, Resonant interactions of optical phonons with acceptor continuum states in silicon, Phys. Rev. B. 16 (1977) 4524–4529. doi:10.1103/PhysRevB.16.4524.

[243] X. Wang, Y. Zhang, S. Liu, Z. Zhao, Depth profiling by Raman spectroscopy of high-energy ion irradiated silicon carbide, Nucl. Instruments Methods Phys. Res. Sect. B Beam Interact. with Mater. Atoms. 319 (2014) 55–61. doi:10.1016/j.nimb.2013.10.017.

[244] X. Wang, Y.-W. Zhang, D. Han, Y.-B. Zhao, Z.-Q. Zhao, M. Zhang, Cross-sectional investigation of radiation damage of 2 MeV proton-irradiated silicon carbide, Nucl. Sci. Tech. 29 (2018) 57. doi:10.1007/s41365-018-0386-0.

[245] T. Koyanagi, Y. Katoh, M.J. Lance, Raman spectroscopy of neutron irradiated silicon carbide: Correlation among Raman spectra, swelling, and irradiation temperature, J. Raman Spectrosc. 49 (2018) 1686–1692. doi:10.1002/jrs.5425.

[246] L. Thomé, G. Velisa, S. Miro, A. Debelle, F. Garrido, G. Sattonnay, S. Mylonas, P. Trocellier, Y. Serruys, Recovery effects due to the interaction between nuclear and electronic energy losses in SiC irradiated with a dual-ion beam, J. Appl. Phys. 117 (2015). doi:10.1063/1.4914305.

[247] D. Tuschel, Raman thermometry, Spectrosc. (Santa Monica). 31 (2016) 8–13.

[248] J. Jaramillo-Fernandez, E. Chavez-Angel, C.M. Sotomayor-Torres, Raman thermometry analysis: Modelling assumptions revisited, Appl. Therm. Eng. 130 (2018) 1175–1181. doi:10.1016/j.applthermaleng.2017.11.033.

[249] R.A. Schwarzer, J. Sukkau, Automated Evaluation of Kikuchi Patterns by Means of Radon and Fast Fourier Transformation, and Verification by an Artificial Neural Network, Adv. Eng. Mater. 5 (2003) 601–606. doi:10.1002/adem.200300374.

[250] M. Schreck, C. Grunick, C. Haug, R. Brenn, B. Stritzker, Bias assisted growth on diamond single crystals: The defect formation due to ion bombardment studied by ion channelling, electron backscatter diffraction, and micro-Raman spectroscopy, Diam. Relat. Mater. 11 (2002) 487–492. doi:10.1016/S0925-9635(01)00546-5.

[251] F. Finocchi, G. Galli, M. Parrinello, C.M. Bertoni, Microscopic struture of

amorphous covalent alloys probed by ab initio molecular dynamics: SiC, 68 (1992). doi:10.1103/PhysRevLett.68.3044.

[252] M.M. Khayyat, G.K. Banini, D.G. Hasko, M.M. Chaudhri, Raman microscopy investigations of structural phase transformations in crystalline and amorphous silicon due to indentation with a Vickers diamond at room temperature and at 77 K, J. Phys. D. Appl. Phys. 36 (2003) 1300–1307. doi:10.1088/0022-3727/36/11/310.

[253] J. Schneider, K. Maier, Point defects in silicon carbide, Phys. B Condens. Matter. 185 (1993) 199–206. doi:10.1016/0921-4526(93)90237-Z.

[254] T.R. Welberry, T. Weber, One hundred years of diffuse scattering, Crystallogr. Rev. 22 (2016) 2–78. doi:10.1080/0889311X.2015.1046853.

[255] R.B. Neder, T. Proffen, Introduction, in: Diffus. Scatt. Defect Struct. Simulations, Oxford University Press, 2008: pp. 1–2. doi:10.1093/acprof:oso/9780199233694.003.0001.

[256] A.A. Suvorova, S. Samarin, Secondary electron imaging of SiC-based structures in secondary electron microscope, Surf. Sci. 601 (2007) 4428–4432. doi:10.1016/j.susc.2007.04.142.

[257] M.R. Castell, D.D. Perovic, H. Lafontaine, Electronic contribution to secondary electron compositional contrast in the scanning electron microscope, Ultramicroscopy. 69 (1997) 279–287. doi:10.1016/S0304-3991(97)00051-X.

[258] J. Li, Transformation strain by chemical disordering in silicon carbide, J. Appl. Phys. 95 (2004) 6466–6469. doi:10.1063/1.1690093.

[259] J.-M.M. Costantini, X. Kerbiriou, M. Sauzay, L. Thomé, Ion-beam modifications of mechanical and dimensional properties of silicon carbide, J. Phys. D. Appl. Phys. 45 (2012) 465301. doi:10.1088/0022-3727/45/46/465301.

[260] H. Zang, D. Guo, T. Shen, C. He, Z. Wang, L. Pang, C. Yao, T. Yang, Investigation of swelling induced by heavy ion and neutron irradiation in SiC, J. Nucl. Mater. 433 (2013) 378–381. doi:10.1016/j.jnucmat.2012.10.029.

[261] Q. Wang, H. Ishikawa, S. Nakano, H. Ogiso, J. Akedo, Curvature-based residual stress measurement for ion-implanted stainless-steel sheet, Vacuum. 75 (2004) 225–229. doi:10.1016/j.vacuum.2004.03.002.

[262] Q. Wang, K. Ozaki, H. Ishikawa, S. Nakano, H. Ogiso, Indentation method to measure the residual stress induced by ion implantation, Nucl. Instruments Methods Phys. Res. Sect. B Beam Interact. with Mater. Atoms. 242 (2006) 88–92. doi:10.1016/j.nimb.2005.08.008.

[263] L.L. Snead, S.J. Zinkle, Structural relaxation in amorphous silicon carbide, Nucl. Instruments Methods Phys. Res. Sect. B Beam Interact. with Mater. Atoms. 191 (2002) 497–503. doi:10.1016/S0168-583X(02)00599-2.

[264] B. Beeler, M. Asta, P. Hosemann, N. Grønbech-Jensen, Effect of strain and temperature on the threshold displacement energy in body-centered cubic iron, J. Nucl. Mater. 474 (2016) 113–119. doi:10.1016/j.jnucmat.2016.03.017.

[265] F.A. Garner, D.S. Gelles, Irradiation creep mechanisms: An experimental perspective, J. Nucl. Mater. 159 (1988) 286–309. doi:10.1016/0022-3115(88)90098-0.

[266] S. Leclerc, M.F. Beaufort, A. Declémy, J.F. Barbot, Strain-induced drift of

interstitial atoms in SiC implanted with helium ions at elevated temperature, J. Nucl. Mater. 397 (2010) 132–134. doi:10.1016/j.jnucmat.2009.12.011.

[267] N. Daghbouj, B.S. Li, M. Callisti, H.S. Sen, M. Karlik, T. Polcar, Microstructural evolution of helium-implanted 6H-SiC subjected to different irradiation conditions and annealing temperatures: a multiple characterization study, Acta Mater. (2019). doi:10.1016/j.actamat.2019.09.027.

[268] J.J. Li, C.H. Zhang, C.L. Xu, X.J. Jia, Y. Song, J.Y. Li, Y.F. Jin, Lattice damage and nanohardness in 6H-SiC implanted with multiple-energy Xe ions, Nucl. Instruments Methods Phys. Res. Sect. B Beam Interact. with Mater. Atoms. 286 (2012) 124–128. doi:10.1016/j.nimb.2011.11.034.

[269] A. Debelle, A. Declémy, XRD investigation of the strain/stress state of ion-irradiated crystals, Nucl. Instruments Methods Phys. Res. Sect. B Beam Interact. with Mater. Atoms. 268 (2010) 1460–1465. doi:10.1016/j.nimb.2010.01.009.

[270] S.L. Dudarev, K. Arakawa, X. Yi, Z. Yao, M.L. Jenkins, M.R. Gilbert, P.M. Derlet, Spatial ordering of nano-dislocation loops in ion-irradiated materials, J. Nucl. Mater. 455 (2014) 16–20. doi:10.1016/j.jnucmat.2014.02.032.

[271] Y. Meng, J. Li, C. Xu, Y. Song, X. Fu, T. Mac, C.H. Zhang, Production and annealing behavior of lattice damage in energetic Kr and Ne-ion implanted 6H-SiC, Nucl. Instruments Methods Phys. Res. Sect. B Beam Interact. with Mater. Atoms. 307 (2013) 552–557. doi:10.1016/j.nimb.2013.01.082.

[272] I. Gutierrez-Urrutia, S. Zaefferer, D. Raabe, Coupling of Electron Channeling with EBSD: Toward the Quantitative Characterization of Deformation Structures in the SEM, JOM. 65 (2013) 1229–1236. doi:10.1007/s11837-013-0678-0.

[273] K.P. So, D. Chen, A. Kushima, M. Li, S. Kim, Y. Yang, Z. Wang, J.G. Park, Y.H. Lee, R.I. Gonzalez, M. Kiwi, E.M. Bringa, S. Lin, J. Li, Dispersion of carbon nanotubes in aluminum improves radiation resistance, Nano Energy. (2016) 319–327. doi:10.1016/j.nanoen.2016.01.019.

[274] S.J. Zinkle, J.P. Blanchard, R.W. Callis, C.E. Kessel, R.J. Kurtz, P.J. Lee, K.A. McCarthy, N.B. Morley, F. Najmabadi, R.E. Nygren, G.R. Tynan, D.G. Whyte, R.S. Willms, B.D. Wirth, Fusion materials science and technology research opportunities now and during the ITER era, Fusion Eng. Des. 89 (2014) 1579–1585. doi:10.1016/j.fusengdes.2014.02.048.

[275] F. Gao, J. He, E. Wu, S. Liu, D. Yu, D. Li, S. Zhang, Y. Tian, Hardness of Covalent Crystals, Phys. Rev. Lett. 91 (2003) 1–4. doi:10.1103/PhysRevLett.91.015502.

[276] C.J. McHargue, J.M. Williams, Ion implantation effects in silicon carbide, Nucl. Instruments Methods Phys. Res. Sect. B Beam Interact. with Mater. Atoms. 80–81 (1993) 889–894. doi:10.1016/0168-583X(93)90703-9.

[277] M.. Osborne, C.. Hubbard, L.. Snead, D. Steiner, Neutron irradiation effects on the density, tensile properties and microstructural changes in Hi-Nicalon^{TM} and Sylramic^{TM} SiC fibers, J. Nucl. Mater. 253 (1998) 67–77. doi:10.1016/S0022-3115(97)00306-1.

[278] G. Kwon, H.H. Jo, S. Lim, C. Shin, H.H. Jin, J. Kwon, G.M. Sun, Room-temperature yield and fracture strength of single-crystalline 6H silicon carbide, J. Mater. Sci. 50 (2015) 8104–8110. doi:10.1007/s10853-015-9379-0.

[279] K.E. Petersen, Silicon as a mechanical material, Proc. IEEE. 70 (1982) 420–457. doi:10.1109/PROC.1982.12331.

[280] H.P. Kyeong, H. Kishimoto, A. Kohyama, 3D analysis of cracking behaviour under indentation in ion-irradiated β-SiC, J. Electron Microsc. (Tokyo). 53 (2004) 511–513. doi:10.1093/jmicro/dfh079.

[281] T. Yang, H. Zang, C. He, D. Guo, P. Zhang, J. Xi, L. Ma, Z. Wang, T. Shen, L. Pang, C. Yao, Evaluation of Mechanical Properties Variations for Kr Ion-Irradiated 6H-SiC by Nanoindentation Methods, Int. J. Appl. Ceram. Technol. 12 (2015) 390–398. doi:10.1111/ijac.12170.

[282] C.D. Hardie, S.G. Roberts, Nanoindentation of model Fe-Cr alloys with self-ion irradiation, J. Nucl. Mater. 433 (2013) 174–179. doi:10.1016/j.jnucmat.2012.09.003.

[283] Z. Lu, Y. Feng, G. Peng, R. Yang, Y. Huan, T. Zhang, Estimation of surface equi-biaxial residual stress by using instrumented sharp indentation, Mater. Sci. Eng. A. 614 (2014) 264–272. doi:10.1016/j.msea.2014.07.041.

[284] S.G. Roberts, T.F. Page, The effects of N2+ and B+ ion implantation on the hardness behaviour and near-surface structure of SiC, J. Mater. Sci. 21 (1986) 457–468. doi:10.1007/BF01145509.

[285] T. Hioki, A. Itoh, S. Noda, H. Doi, J. Kawamoto, O. Kamigaito, Modification of the mechanical properties of ceramics by ion implantation, Nucl. Instruments Methods Phys. Res. Sect. B Beam Interact. with Mater. Atoms. 39 (1989) 657–664. doi:10.1016/0168-583X(89)90869-0.

[286] C.E.J. Dancer, N.A. Yahya, T. Berndt, R.I. Todd, G. De Portu, Effect of residual compressive surface stress on severe wear of alumina-silicon carbide two-layered composites, Tribol. Int. 74 (2014) 87–92. doi:10.1016/j.triboint.2014.02.010.

[287] G. de Portu, L. Micele, D. Prandstraller, G. Palombarini, G. Pezzotti, Abrasive wear in ceramic laminated composites, Wear. 260 (2006) 1104–1111. doi:10.1016/j.wear.2005.07.009.

[288] C. Liu, J. Xi, I. Szlufarska, Sensitivity of SiC Grain Boundaries to Oxidation, J. Phys. Chem. C. 123 (2019) 11546–11554. doi:10.1021/acs.jpcc.9b00068.

[289] K. Fitzgerald, D. Shepherd, Review of SiCf/SiCmcorrosion, erosion and erosion-corrosion in high temperature helium relevant to GFR conditions, J. Nucl. Mater. 498 (2018) 476–494. doi:10.1016/j.jnucmat.2017.09.010.

[290] V.A. Avincola, M. Grosse, U. Stegmaier, M. Steinbrueck, H.J. Seifert, Oxidation at high temperatures in steam atmosphere and quench of silicon carbide composites for nuclear application, Nucl. Eng. Des. 295 (2015) 468–478. doi:10.1016/j.nucengdes.2015.10.002.

[291] C. yen Hsu, Y. Zhang, Y. Xie, F. Deng, P. Karandikar, J.Q. Xiao, C. Ni, In-situ measurement of SiC/Si interfacial tensile strength of reaction bonded SiC/Si composite, Compos. Part B Eng. 175 (2019) 107116. doi:10.1016/j.compositesb.2019.107116.

[292] S. Das, H. Yu, E. Tarleton, F. Hofmann, Hardening and Strain Localisation in Helium-Ion-Implanted Tungsten, (2018). http://arxiv.org/abs/1901.00745.

[293] P.R. Cantwell, M. Tang, S.J. Dillon, J. Luo, G.S. Rohrer, M.P. Harmer, Grain

boundary complexions, Acta Mater. 62 (2014) 1–48. doi:10.1016/j.actamat.2013.07.037.

[294] O. Schumacher, C.J. Marvel, M.N. Kelly, P.R. Cantwell, R.P. Vinci, J.M. Rickman, G.S. Rohrer, M.P. Harmer, Complexion time-temperature-transformation (TTT) diagrams: Opportunities and challenges, Curr. Opin. Solid State Mater. Sci. 20 (2016) 316–323. doi:10.1016/j.cossms.2016.05.004.

[295] S.J. Dillon, K. Tai, S. Chen, The importance of grain boundary complexions in affecting physical properties of polycrystals, Curr. Opin. Solid State Mater. Sci. 20 (2016) 324–335. doi:10.1016/j.cossms.2016.06.003.

[296] C. Carter, C. Opinions, S. State, M. Science, Grain boundary complexions – current status and future directions, Curr. Opin. Solid State Mater. Sci. 20 (2016) iv–v. doi:10.1016/S1359-0286(16)30168-1.

[297] R. Brunetto, G.A. Baratta, G. Strazzulla, Raman spectroscopy of ion irradiated diamond, J. Appl. Phys. 96 (2004) 380–386. doi:10.1063/1.1759080.

[298] S. Ganguli, A. Roy, R. Wheeler, L. Starman, A. Force, Steady State Thermal Conductivity, (2009).

[299] J. Jin, W. Wang, X. Chen, Microstructure and mechanical properties of Ti + N ion implanted Cronidur30 steel, Materials (Basel). 12 (2019) 1–13. doi:10.3390/ma12030427.

[300] D. Hoeft, B.A. Latella, K.T. Short, Residual stress and cracking in expanded austenite layers, J. Phys. Condens. Matter. 17 (2005) 3547–3558. doi:10.1088/0953-8984/17/23/007.

[301] D. Klimm, Electronic materials with a wide band gap: Recent developments, IUCrJ. 1 (2014) 281–290. doi:10.1107/S2052252514017229.

[302] C.W. Bale, E. Bélisle, P. Chartrand, S.A. Decterov, G. Eriksson, A.E. Gheribi, K. Hack, I.H. Jung, Y.B. Kang, J. Melançon, A.D. Pelton, S. Petersen, C. Robelin, J. Sangster, P. Spencer, M.A. Van Ende, Reprint of: FactSage thermochemical software and databases, 2010–2016, Calphad Comput. Coupling Phase Diagrams Thermochem. 55 (2016) 1–19. doi:10.1016/j.calphad.2016.07.004.

List of figures reproduced with permission

Figure 1-1: Schematic of Iter showing key components. Adult human for scale in bottom right (Credit © ITER Organization, http://www.iter.org/) [1]

The ITER Organization provides images and videos on its public website free of charge for educational and institutional use, www.iter.org

Figure 1-2: Simulated PKA energies for the Starfire (MCF) and KOYO (ICF) fusion reactor concepts. ICF has a lower average PKA energy in chamber walls [8].

Reprinted from Fusion Engineering and Design, Vol 60 Issue 1, J.M Perlado,E Domínguez,L Malerba,J Marian,D Lodi,M Salvador,E Alonso,Ma.J Caturla,T Díaz de la Rubia, Results from systematic modeling of neutron damage in inertial fusion energy reactors, 55-63, Copyright (2002), with permission from Elsevier

Figure 1-4: Typical microstructures of SiC/SiC composites fabricated by different techniques. a) PIP [16], b) CVI [17], c) RMI [18], d) NITE [17]

(a) Reprinted from Journal of the European Ceramics Society, Vol 33 Issue 10, Aljaž Iveković,Saša Novak,Goran Dražić,Darina Blagoeva,Sehila, Gonzalez de Vicente, Current status and prospects of SiCf/SiC for fusion structural applications, 1577-1589, Copyright (2013), with permission from Elsevier
(b) Reprinted from Journal of Nuclear Materials, Vol 384 Issue 2, Kazuya Shimoda,Tatsuya Hinoki,Yutai Katoh,Akira Kohyama, Development of the tailored SiC/SiC composites by the combined fabrication process of ICVI and NITE methods, 103-108, Copyright (2009), with permission from Elsevier
(c) Reprinted from Composites Part A: Applied Science and Manufacturing, Vol 66, Takuya Aoki,Toshio Ogasawara,Yosuke Okubo,Katsumi, Yoshida,Toyohiko Yano, Fabrication and properties of Si−Hf alloy melt-

infiltrated Tyranno ZMI fiber/SiC-based matrix composites, 155-162, Copyright (2014), with permission from Elsevier

(d) Reprinted from Journal of Nuclear Materials, Vol 384 Issue 2, Kazuya Shimoda,Tatsuya Hinoki,Yutai Katoh,Akira Kohyama, Development of the tailored SiC/SiC composites by the combined fabrication process of ICVI and NITE methods, 103-108, Copyright (2009), with permission from Elsevier

Figure 1-5: Structure of the Iter DFLL-TBM showing SiC as a flow channel insert [31]

Reprinted from Nuclear Fusion, Vol 47 Issue 11, Y. Wu and the FDS Team, Conceptual design and testing strategy of a dual functional lithium–lead test blanket module in ITER and EAST, © IAEA, 2007, pp.1533-1539.

Figure 1-6:Structure of the Iter DCLL-TBM with a SiC flow channel insert [35]

Reprinted from Fusion Engineering and Design, Vol 81 Issue 1-7, A. Ying,M. Abdou,C. Wong,S. Malang,N. Morley,M. Sawan,B. Merrill,D.K. Sze,R. Kurtz,S. Willms,M. Ulrickson,S. Zinkle, An overview of US ITER test blanket module program, 433-441, Copyright (2006), with permission from Elsevier

Table 1-1: Design parameters for two blanket types incorporating SiC structurally, along with typical measured values of SiC/SiC composites [26]

Reprinted from Fusion Engineering and Design, Vol 61, L Giancarli,H Golfier,S Nishio,R Raffray,C Wong,R Yamada, Progress in blanket designs using SiCf/SiC composites, 307-318, Copyright (2002), with permission from Elsevier

Table 1-2: Methods of joining SiC from Katoh et al.[54]

Reprinted from Journal of Nuclear Materials, Vol 448, Issue 1-3, Yutai Katoh, Lance L. Snead, Ting Cheng, Chunghao Shih, W. Daniel Lewis, Takaaki Koyanagi, Tatsuya Hinoki, Charles H. Henager, Monica Ferraris, Radiation-tolerant joining

technologies for silicon carbide ceramics and composites, 497-511, Copyright (2014), with permission from Elsevier

Figure 2-1: Infiltration heights into porous carbon based on wetting curve which includes Si + C reaction, and from Washburn equation based on viscosity of silicon [62]

Reprinted from Ceramics International, Vol 42, Issue 15, Yonggang Tong, Shuxin Bai, Xiubing Liang, Qing H. Qin, Jiangtao Zhai, Reactive melt infiltration fabrication of C/C-SiC composite: Wetting and infiltration, 17174-17178, Copyright (2016), with permission from Elsevier

Figure 2-2: 3-point bending strength of Si infiltrated composite and Si-Hf infiltrated composite at room and elevated temperatures (top) [18] 3-point bending strength of Si-infiltrated composite with crystalline fibres and BN interphase (bottom) [82].

(top) Reprinted from Composites Part A: Applied Science and Manufacturing, Vol 66, Takuya Aoki,Toshio Ogasawara,Yosuke Okubo,Katsumi, Yoshida,Toyohiko Yano, Fabrication and properties of Si−Hf alloy melt-infiltrated Tyranno ZMI fiber/SiC-based matrix composites, 155-162, Copyright (2014), with permission from Elsevier

(bottom) Reprinted from Journal of Nuclear Materials, Vol 329, S.P Lee, J.O Jin, J.S Park, A Kohyama, Y Katoh, H.K Yoon, D.S Bae, I.S Kim, High temperature characterization of reaction sintered SiC based materials, 534-538, Copyright (2004), with permission from Elsevier

Figure 2-3: Thermal expansion coefficients of SiC, Si, Si3N4 and various silicides [83]

Reprinted from Ceramics International, Vol 42, Issue 2, S.V. Raj, Thermal expansion behavior of hot-pressed engineered matrices, 2557-2569, Copyright (2016), with permission from Elsevier

Figure 2-4: 3-point bending strength of RB-SiC with residual Si, and RB-SiC where residual silicon is replaced with MoSi2 [73]

Reprinted by permission from Springer Nature, Journal of Materials Science, Vol. 24, 4144-4151, Microstructure and mechanical properties of RB-SiC/MoSi2 composite, C.B. Lim *et al.*, Copyright (1989)

Figure 2-5: Process for forming RB-SiC followed by melt infiltration of MoSi2 [73]

Reprinted by permission from Springer Nature, Journal of Materials Science, Vol. 24, 4144-4151, Microstructure and mechanical properties of RB-SiC/MoSi2 composite, C.B. Lim et al., Copyright (1989)

Figure 2-6: Eroded graphite crucible with SiC formed top and bottom. The centre region with eroded walls was at 2300°C while top and bottom were at 1800°C [97]

Reprinted from Journal of the Electrochemical Society, Vol 110, Issue 1, G. Beckmann, The Growth of Silicon Carbide from Molten Silicon, 84-86, Copyright (1963), © IOP Publishing. Reproduced with permission. All rights reserved

Figure 2-7: SiC layer I is formed heterogeneously on a glassy carbon surface within a few minutes of reaction. SiC layer II is formed by precipitation of dissolved carbon on the SiC layer during cooling [63].

Reprinted from Journal of the American Ceramic Society, Vol 79, Issue 4, Hans Hausner, Jian-Guo Li, Reactive Wetting in the Liquid-Silicon/Solid-Carbon System, 873-880, Copyright (2005), with permission from John Wiley and Sons

Figure 2-8: Glassy carbon in contact with molten Si for 24 hours at 1600C. 10 µm layer of SiC on the surface of carbon, and approximately 150 µm SiC layer on the surface of Silicon [93]

Reprinted from Ceramics International, Vol 29, Issue 3, A. Favre, H. Fuzellier, J. Suptil, An original way to investigate the siliconizing of carbon materials, 235-243, Copyright (2003), with permission from Elsevier

Figure 2-9: Impact of carbon content on strength and density [100]

Reprinted from Materials Science and Engineering: A, Vol 483, Yuan Li, Jing Lin, Jiqiang Gao, Guanjun Qiao, Hongjie Wang, Fabrication of reaction-bonded SiC ceramics by slip casting of SiC/C suspension, 676-678, Copyright (2008), with permission from Elsevier

Figure 2-10: Dependence of bending strength with residual silicon content and SiC particle size, and with size of residual silicon pools [102]

Reprinted from Diamond and Related Materials, Vol 12, Issue 3-7, S. Suyama, T. Kameda, Y. Itoh, Development of high-strength reaction-sintered silicon carbide, 1201-1204, Copyright (2003), with permission from Elsevier

Figure 2-13: (a) evolution of enthalpy per atom and chemical disorder with dose during MD simulated displacements. Dashed lines are the enthalpy and chemical disorder values of a melt-quenched amorphous structure (b) Proportions of different point defects up to the point of amorphisation at 0.15 MD.dpa. Reproduced from [106] (c) is experimental Raman measurements of chemical disorder showing the continued evolution of chemical disorder after room temperature amorphisation, while 400 °C irradiated SiC saturates in chemical disorder and does not amorphise [125].

(a) and (b) Reprinted from Nuclear Instruments and Methods in Physics Research Section B: Beam Interactions with Materials and Atoms, Vol 267, Issue 18, Ram

Devanathan, Radiation damage evolution in ceramics, 3017-3021, Copyright (2009), with permission from Elsevier.

(c) Reprinted from Journal of Physics: Condensed Matter, Vol 18, Sorieul, S., Costantini, J-M, Gosmain, L., Thomé, L., Grob, J-J, Raman spectroscopy study of heavy-ion-irradiated α-SiC, 5235-5251, Copyright (2006), IOP Publishing. Reproduced with permission. All rights reserved.

Figure 2-16: Raman spectra of neutron irradiated SiC showing dependence of dose on spectra. (a) is from irradiations of 6H-SiC at <50 °C from ref. [163], (b) is from irradiations of 6H-SiC at <100 °C from ref. [164]. (c) is from irradiations of 3C-SiC at ~600 °C from ref. [161] 1 dpa is ~1×1021n/cm2. The peak labelled "Disordered SiC" in (c) is incorrectly labelled by the authors, it is Si-Si

(a) Reprinted from Nuclear Instruments and Methods in Physics Research Section B: Beam Interactions with Materials and Atoms, Vol 286, E. Wendler, Th. Bierschenk, F. Felgenträger, J. Sommerfeld, W. Wesch, D. Alber, G. Bukalis, L.C. Prinsloo, N. van der Berg, E. Friedland, J.B. Malherbe, Damage formation and optical absorption in neutron irradiated SiC, 97-101, Copyright (2012), with permission from Elsevier.

(b) Reprinted from Solid State Communications, Vol 152, Issue 10, P.F. Wang, L. Huang, W. Zhu, Y.F. Ruan, Raman scattering of neutron irradiated 6H-SiC, 887-889, Copyright (2012), with permission from Elsevier.

(c) Reprinted with permission from Dr Takaaki Koyanagi from Recent progress in the development of SiC composites at ORNL, Presented by Takaaki Koyanagi at ICFRM 2017.

Figure 2-17: High temperature neutron irradiated 3C-SiC Raman spectra from ref. [158].

Reprinted from Scripta Materialia, Vol 125, T. Koyanagi, M.J. Lance, Y. Katoh, Raman scattering of neutron irradiated 6H-SiC, 58-62, Copyright (2016), with permission from Elsevier.

Figure 2-18: Comparison of Raman spectra produced by 50 °C neutron irradiations and room temperature (a) carbon ion and (b) silicon ion implantations in 6H-SiC. C-3 and C-4 approximately match the dpa of neutron-1, and Si-4 and Si-5 approximately match neutron-1 and neutron-2 respectively. From [165].

Reprinted from Journal of Nuclear Materials, Vol 478, Xiaofei Chen, Wei Zhou, Qijie Feng, Jian Zheng, Xiankun Liu, Bin Tang, Jiangbo Li, Jianming Xue, Shuming Peng, Irradiation effects in 6H–SiC induced by neutron and heavy ions: Raman spectroscopy and high-resolution XRD analysis, 215-221, Copyright (2016), with permission from Elsevier.

Figure 2-19: Comparison of Raman spectra of 6H-SiC irradiated with (a) C ions 1.6 dpa 400 °C (red line) [159], and (b) Au and Xe ions at comparable dpa also at 400 C [125]

(a) Reprinted from Nuclear Instruments and Methods in Physics Research Section B: Beam Interactions with Materials and Atoms, Vol 286, N. Chaâbane, A. Debelle, G. Sattonnay, P. Trocellier, Y. Serruys, L. Thomé, Y. Zhang, W.J. Weber, C. Meis, L. Gosmain, A. Boulle, Investigation of irradiation effects induced by self-ion in 6H-SiC combining RBS/C, Raman and XRD, 108-113, Copyright (2012), with permission from Elsevier.

(b) Reprinted from Journal of Physics: Condensed Matter, Vol 18, Sorieul, S., Costantini, J-M, Gosmain, L., Thomé, L., Grob, J-J, Raman spectroscopy

study of heavy-ion-irradiated α-SiC, 5235-5251, Copyright (2006), IOP Publishing. Reproduced with permission. All rights reserved.

Figure 2-20: Kr ion implantation of 6H-SiC with temperature and dose dependence. There appears to be very little difference between 14 and 70 peak dpa doses. Increasing temperature sharpens Si-Si and Si-C peaks while the D band of C-C becomes more intense than the G band. Room temperature irradiation amorphises SiC [129]

Reprinted from Nuclear Instruments and Methods in Physics Research Section B: Beam Interactions with Materials and Atoms, Vol 307, Hang Zang, Tao Yang, Daxi Guo, Jianqi Xi, Chaohui He, Zhiguang Wang, Tielong Shen, Lilong Pang, Cunfeng Yao, Peng Zhang, Modifications of SiC under high fluence Kr-ion irradiation at different temperatures, 558-561, Copyright (2013), with permission from Elsevier.

Figure 2-21: Swelling as a function of temperature for neutron irradiated SiC [143]

Reprinted from Journal of Nuclear Materials, Vol 367, L.L. Snead, Y. Katoh, S. Connery, Swelling of SiC at intermediate and high irradiation temperatures, 677-684, Copyright (2007), with permission from Elsevier.

Figure 2-22: Dimensional swelling of neutron irradiated SiC based on a model fitted to experimental data [50]

Reprinted from Journal of Nuclear Materials, Vol 499, Yutai Katoh, Takaaki Koyanagi, Joel L. McDuffee, Lance L. Snead, Ken Yueh, Dimensional stability and anisotropy of SiC and SiC-based composites in transition swelling regime, 471-479, Copyright (2018), with permission from Elsevier.

Figure 2-23: Thermal conductivity with temperature for unirradiated and irradiated REFEL [170]

Copyright UKAEA but reproduced with UKAEA permission

Figure 2-25: Nanoindentation hardness from Nogami et al. [182] note the large error bars overlapping unirradiated hardness.

Reprinted from Journal of Nuclear Materials, Vol 307, S. Nogami, A. Hasegawa, L.L. Snead, Indentation fracture toughness of neutron irradiated silicon carbide, 1163-1167, Copyright (2002), with permission from Elsevier.

Figure 2-29: Elastic modulus as a function of temperature for neutron irradiated SiC from Nogami et al. [182]. The legend refers to different neutron irradiation experiments

Reprinted from Journal of Nuclear Materials, Vol 307, S. Nogami, A. Hasegawa, L.L. Snead, Indentation fracture toughness of neutron irradiated silicon carbide, 1163-1167, Copyright (2002), with permission from Elsevier.

Figure 2-30: Indentation fracture toughness of neutron irradiated CVD SiC. Values are likely to be incorrect, but a reduction in fracture toughness with low temperature irradiation, and an increase in toughness at high temperatures can be seen [182].

Reprinted from Journal of Nuclear Materials, Vol 307, S. Nogami, A. Hasegawa, L.L. Snead, Indentation fracture toughness of neutron irradiated silicon carbide, 1163-1167, Copyright (2002), with permission from Elsevier.

Figure 2-31: Nanoindentation fracture toughness and out of plane strain of room temperature Xe implanted SiC. The dashed box marks amorphisation [188]

Reprinted from Materials Today: Proceedings, Vol 5, Issue 6, C. Jiang, L. Dagault, V. Audurier, C. Tromas, A. Declémy, M.F. Beaufort, J.F. Barbot, Strain buildup in 4H-SiC implanted with noble gases at low dose, 14722-14731, Copyright (2018), with permission from Elsevier.

Figure 2-32: Residual stress map in silicon regions of RB-SiC [189]

Reprinted from Acta Materialia, Vol 129, Phillip Jannotti, Ghatu Subhash, James Zheng, Virginia Halls, Measurement of microscale residual stresses in multi-phase ceramic composites using Raman spectroscopy, 482-491, Copyright (2017), with permission from Elsevier.

Figure 2-33: Outline of the IBL method from ref. [199]. (a) rectangular cross-section cantilever is released by cutting off the end and deflects upwards due to tensile residual stress in the film. (b) & (c) An area (section A) of the cantilever is thinned and the deflection of the cantilever as a function of thinned depth is measured.

Reprinted from Scripta Materialia, Vol 59, S. Massl, J. Keckes, R. Pippan, A new cantilever technique reveals spatial distributions of residual stresses in near-surface structures, 503-506, Copyright (2008), with permission from Elsevier.

Figure 6-4: XRD lattice strain in ion implanted 4H-SiC [188]

Reprinted from Materials Today: Proceedings, Vol 5, Issue 6, C. Jiang, L. Dagault, V. Audurier, C. Tromas, A. Declémy, M.F. Beaufort, J.F. Barbot, Strain buildup in 4H-SiC implanted with noble gases at low dose, 14722-14731, Copyright (2018), with permission from Elsevier.